NASA Contractor Report 3698

NASA-CR-3698 19840009180

Technology Needs of Advanced Earth Observation Spacecraft

James J. Herbert, J. R. Postuchow, and Wilfred A. Schartel

CONTRACT NAS1-16756
JANUARY 1984

NASA

NASA Contractor Report 3698

Technology Needs of Advanced Earth Observation Spacecraft

James J. Herbert, J. R. Postuchow,
and Wilfred A. Schartel

Martin Marietta Aerospace
Denver, Colorado

NASA

National Aeronautics
and Space Administration

Scientific and Technical
Information Branch

1984

Page Missing in Original Document

CONTENTS

Figure

Table

A	Ampere
ACS	Attitude Control System
ADAMS	Automatic Dynamic Analysis of Mechanical Systems
A-h	Ampere Hour
ALT	Altimeter
AMTS	Advance Meteorological Temperature Sounder
ANSYS	Analysis System Finite-Element Program
ASR	Atmospheric Sounding Radiometer
BPSK	Binary Phase-Shift Keying
BRDF	Bidirectional Reflectance Distributing Function
°C	Centigrade
c_B	Battery Capacity
CLIR	Cyrogenic Limb Scanning Interferometer
cm	Centimeter
CTE	Coefficient of Thermal Expansion
CZCS	Coastal Zone Color Scanner
dB	Decibel
deg	Degrees
DOD	Depth of Discharge
DC	Direct Current
EOL	End of Life
EOS	Earth Observation Spacecraft
EPM	Electric Power Module
ESMR	Electrically Scanned Microwave Radiometer
EIFOV	Effective Instantaneous Field of View
FET	Field Effect Transistor
FRUSA	Flexible Rolled-Up Solar Array
GHz	Gigahertz
GN&C	Guidance, Navigation and Control
GTD	Geometrical Theory of Diffraction
h	Hour
HPBW	Half-Power Beamwidth
Hz	Hertz
IFOV	Instantaneous Field of View
IMP	Integrated Mechanism Program
IMPS	Integrated Modular Power Subsystem
IMU	Inertial Measurement Unit
in.	Inch
IR	Infrared
ISP	Integrated Science Platform
K	Degrees Kelvin
kbps	Kilobits per Second
kg	Kilogram
kHz	Kilohertz
KSA	Ku-Band Single-Access

LANDSAT	Land Satellite
L_C	Loss in Conversion
LEO	Low Earth Orbit
LeRC	Lewis Research Center
LMR	Large Microwave Radiometer
m	Meter
MA	Multiple Access
Mbps	Megabits per Second
MeV	Megaelectron Volts
MIRI	Mid-Infrared Imager
MITAS	Martin Marietta Interactive Thermal Analysis System
MLA	Multispectral Linear Array
MRS	Multispectral Resource Sampler
M/S	Maintenance/Servicing
MSS	Multispectral Scanner
MTBF	Mean Time between Failure
N	Newtons
NASA	National Aeronautics and Space Administration
NASTRAN	NASA Structural Analysis Program
NiCd	Nickel Cadmium
NiH_2	Nickel Hydrogen
nm	Nanometer
NOSS	National Oceanic Satellite System
NRZ	Nonreturn to Zero
P_L	Power Load
PPT	Pulsed Plasma Thruster
PRF	Pulse Repetition Frequency
QPSK	Quadrature Phase-Shift Keying
R-C	Resistor-Capacitor
rf	Radio Frequency
rfi	Radio Frequency Interference
RMA	Remote Manipulating Arm
rms	Root Mean Square
R_R	Range Resolution
s	Second
SA	Single Access
SAR	Synthetic Aperture Radar
SCATT	Scatterometer
SMMR	Scanning Multichannel Microwave Radiometer
SNR	Signal-to-Noise Ratio
SOA	State of the Art
SPOT	Systeme Probatoire d' Observation de la Terre (a French Program Similar to LANDSAT)
SSA	S-Band Single Access
STS	Space Transportation System
T_B	Brightness Temperature
TDRSS	Tracking Data Relay Satellite System
T_E	Time of Eclipse

TEMINT	Temperature Interpolation
TM	Thematic Mapper
TPR	Total-Power Receiver
TRASYS	Thermal Radiation Analysis System
UARS	Upper Atmospheric Research Satellite
V_B	Battery Voltage
Vdc	Volts, Direct Current
W	Watt

1.0 INTRODUCTION

The Technology Needs of Advanced Earth Observation Spacecraft (EOS) study was commissioned by NASA to determine the advantages of including additional earth surface and/or atmospheric sensors on a large microwave radiometer (LMR) spacecraft. The study emphasized the selection and analysis of complementary sets of sensors for earth, oceanic, and atmospheric observation, and the development of the EOS spacecraft design in some detail. Technology development requirements were identified and classified regarding their value in enabling and enhancing multidiscipline missions. To accomplish these goals, the study focused on conceptual designs, system analyses, and performance evaluations of competing multidiscipline spacecraft concepts. EOS was to operate in low earth orbit (consistent with mission requirements), be deployable as a fully operational satellite from the shuttle orbiter, and be capable of a 10-year lifetime, including two- to three-year revisit periods for resupply, maintenance, and sensor changeout.

1.1 MISSION ANALYSIS

The mission analysis proceeded from the guidelines of first developing a baseline radiometer-only mission, and then developing missions with complementary sets of sensors for earth, oceanic, and atmospheric observation. We soon realized that even an elementary set of augmenting sensors so enhanced the radiometer mission that the radiometer-alone mission was not desirable. The baseline was then redefined, with NASA concurrence, to consist of the LMR, an atmospheric sounding radiometer (ASR) and a synthetic aperture radar (SAR). Earth, oceanic, and atmospheric missions and a combined mission were developed, sensors selected, and subsystems sized to provide the proper support of the entire spacecraft and sensors.

1.2 STRUCTURAL DESIGN AND ANALYSIS

A functional analysis was performed to determine the structural, mesh, feed, and surface design requirements. The resultant design used Martin Marietta box truss structural elements for the antenna support structure and for the integrated offset feed mast. The spacecraft design is shown in Figure 1-1.

The gold-plated molybdenum, tricot knitted mesh antenna surface is 120 x 60 m. The mast rises 116 m off the mesh surface and supports a 30-m feed beam on which is mounted 324 feeds in three rows, operating at 1.41, 5.5, and 10.68 GHz. A science beam extending off the front of the spacecraft supports the instruments discussed above. The spacecraft weighs approximately 6500 kg and is stowable in one orbiter cargo bay, along with its cradle and deployment system (discussed in detail in Section 5.0).
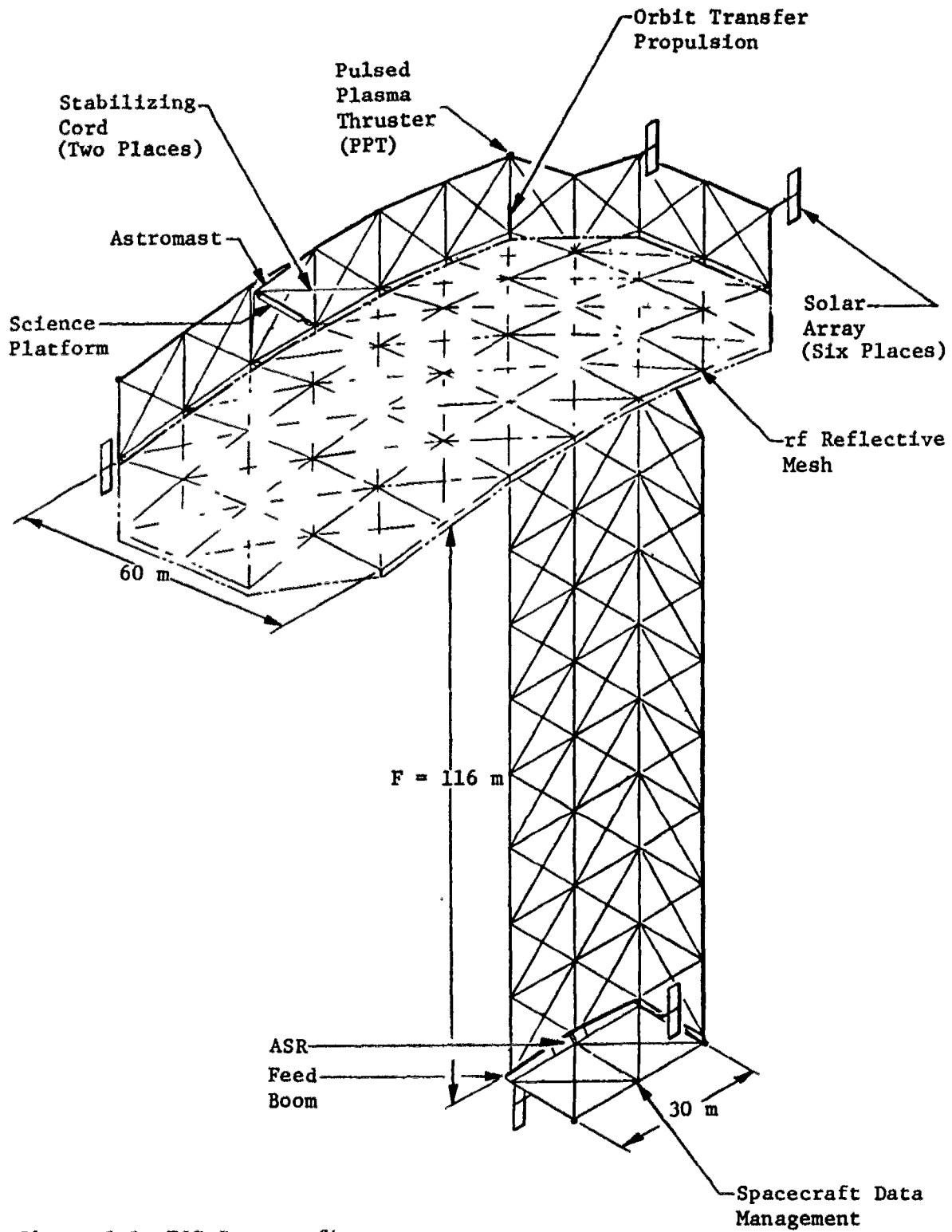
Figure 1-1 EOS Spacecraft

1.3 SUBSYSTEMS

The spacecraft is a fully autonomous vehicle capable of full operation for 10 years. The usual lifetime problems associated with solar array surface degradation and the exhaustion of attitude control system (ACS) propellant have been overcome in the EOS design. There are, however, problems that could dictate resupply and maintenance visits every two years or so. Certain scientific sensors require a cryogenic coolant that cannot be space-stored for much over 18 months (UARS experience). Gyroscope MTBFs are not consistent with a 10-year lifetime and neither are current data recording devices of the type necessary for the EOS missions.

Each of the support subsystems was designed and configured and the data are presented in Section 4.0. The orbital attitude control system, the transfer propulsion system, and the data management system all presented unique problems that were solved with state-of-the-art hardware.

1.4 TECHNOLOGY NEEDS

During the study, technology needs for the structure, the mesh feed combination, and certain of the ancillary sensors were identified in the areas of design, analysis, manufacturing, test, modeling, and on-orbit operation. The range of severity of the technology gaps identified varies from items merely requiring additional analysis to fundamental problems in radiometric operation with the EOS-type of feed horns and mesh surfaces, accurate sensor thermal control at very low temperatures, and confidence in deployment.

2.0 MISSION ANALYSIS

NASA planning has defined future missions that utilize radiometers and large microwave antennas. These large microwave antennas are physically capable of carrying additional sensors that could be used for earth surface and atmospheric observation. A mission analysis was therefore performed to determine the particular additional sensors, and groupings of sensors, that provide the most advantageous scientific returns within reasonable spacecraft constraints. The sensors (and missions) were categorized from a scientific user viewpoint into three families—land observation, oceanic observation, and atmospheric observation.

A multidiscipline mission was also developed to determine whether it was feasible to achieve combined land, oceanic, or atmospheric observation with a group of sensors sharing a large microwave antenna spacecraft in a single compromise orbit.

The focus of the study was on the generation of design and analysis data for the EOS spacecraft concepts and subsystems. Scientific issues were addressed only to the extent necessary to clearly understand the engineering requirements to be imposed on the various earth observation sensors, to compare the performance of state-of-the-art sensors with data requirements, and to define the technological advances needed.

The goals of the mission analysis effort were to formulate viable mission concepts, and to determine the technology requirements of the large microwave radiometer and the augmenting sensors. EOS represents a major advancement in the capability, completeness, and approach to earth orbiting remote sensing platforms that use a large microwave radiometer as the "core" instrument. The mission analysis also provided the requirements and criteria used in the hardware selection discussed in Section 4.0.

2.1 LARGE MICROWAVE RADIOMETERS

The technique of microwave remote sensing has become well established, with an inheritance going back to Skylab. Since that time, various instruments have flown, e.g., the electrically scanned microwave radiometer (ESMR) and the scanning multichannel microwave radiometer (SMMR). Both of these instruments, however, were small and had limited ground resolution.

The large microwave radiometer (LMR) considered in this study is almost 60 times larger than these instruments. Because the ground resolution is measured in a few kilometers at most, the utility of the measurements is greatly increased.

As part of a comprehensive remote sensing package, microwave remote sensing offers many unique advantages. This package should consist of

microwave radiometers providing day/night and near-all-weather observation in the 1- to 37-GHz region, sensors operating in the visible region, and sensors operating in the infrared (IR) region. This enables sensing both in the atmosphere and on the ground.

The microwave signals would be processed to provide data revealing the geometric and bulk-dielectric properties of a target (inferring its parameters) material, while the "color" discernible in visible and IR data would provide information about the target material surface. This combination of measurements enables a comprehensive description of a scene to be developed.

Passive microwave profiling of the atmospheric water content, which is a fundamental meteorlogical parameter, can also be done from space. Modification of the ground emission from absorption due to nonraining water in clouds and scattering from rain itself are used in the retrieval algorithms. The emission from oxygen can be used to measure atmospheric temperature.

The combination of simultaneously obtained data over a broad spectral range provides the opportunity to realize a quality of earth surface identification considerably beyond the present state of the art.

The mission analysis discussed in the following paragraphs considered groups of sensors sharing the spacecraft, operating together to gather information on a common target, and also considered sensors that ride on the spacecraft but sense their own targets independently.

2.1.1 Baseline Microwave Observations

Large microwave radiometers have wide utility fulfilling many user needs, and cover both land and ocean*; Table 2-1 illustrates some potential observations. The measurement frequencies cover two orders of magnitude that are not currently attainable in a single instrument of this size because it is not possible to maintain the required surface accuracy. Therefore microwave measurements were restricted to lie between 1 and 37 GHz, implying a primary emphasis on land and ocean observations.

---

*Wright, R. L., The Microwave Radiometer Spacecraft - A Design Study, NASA
RP-1079, 1981.

Table 2-1 Potential Microwave Observations

Application	Observable Frequency, GHz 1-37 Water Roughness Sea State (Winds)	1-2 Sea Surface Salinity	1-10 Water Pollutants	1-10 Soil Moisture	1-8 Sea Surface Temp	22 Atmos Water Vapor	30-40 Land Surface Imaging	10-50 Ice Mapping (Coverage & Age)	50-70 Atmos Temp Profile	130 140,183, 93, 118 Surface Image & Atmospheric Sounding
Agriculture	–	–	–	¶	–	–	+	–	–	0
Hydrology	–	–	–	¶	–	–	+	–	–	0
Weather & Climate	+	0	–	+	+	+	0	+	¶	+
Coastal Productivity	+	+	–	–	¶	–	–	0	–	–
Coastal Dynamics	+	–	–	–	+	–	¶	+	–	0
Water Quality	–	–	¶	0	–	–	0	–	–	0

Legend:

–   Not Applicable
0   Helpful
+   Important
¶   Critical

2.1.2   Ocean Observations

The retrieval of geophysical data over the ocean is a complex problem because the sensed brightness temperature is a function of sea surface temperature, salinity, and water roughness, which depends on wind speed. For instance, to infer sea surface temperatures from the SeaSat SMMR, a geophysical algorithm that used multiple linear regression was implemented to develop a relationship between physical variables and brightness temperatures (T_B). The multiple linear regression technique consisted of a data set with 90 surface models (10 wind speeds, 9 sea surface temperatures) and 81 atmospheric models (9 temperature profiles, 9 cloud models). Applying the technique yields the most probable function (equation) for each parameter, using as inputs selected T_Bs and polarizations. The brightness temperatures are measured at 6.6, 10.68, 18, 21, and 37 GHz. The measured brightness temperature from the spacecraft were substituted into the equation to yield retrieved geophysical parameters. Accuracy of the retrieval depended on the number of inputs provided.* For the accurate measurement of sea surface temperature, salinity, and wind speed (or sea state), T_B measurements at a number of frequencies is desired as inputs to the retrieval algorithm. But the single LMR operating at a few of the lower frequencies cannot provide all the inputs desired for the algorithms mentioned. The ancillary radiometer operating at 18, 21, and 37 GHz suggested to fulfill this need is described in Section 2.3.1.2.

*R. Hufer and E. Njoku: "Regression Techniques for Oceanographic Parameter Retrieval Using Spaceborne Microwave Radiometry," IEEE Trans GeoSci Remote Sensing, GE-19, No. 4, 1981, p 178.

2.1.3 Soil Moisture/Vegetation

An ideal application for passive radiometers is the soil moisture measurements necessary for agricultural and hydrological studies. The dielectric coefficient of the soil changes with water content, and the microwave emission is inversely related to these coefficients. A moist soil has a lower apparent temperature than that of a dry soil at the same physical temperature. This is the basis for passive microwave remote sensing of soil moisture.

The situation is more complicated when vegetation covers the soil one wishes to measure. For a dry field with vegetation cover, the microwave signature is similar to, or lower than, that of bare fields.[*] Modification of the microwave emission to account for the vegetation cover is based on the dielectric coefficient and volume-scattering models for the vegetative medium. The dielectric properties of the cover are related to the moisture content of the vegetation. The models that consider moisture content can range from relatively simple to more comprehensive, and consider moisture both by volume and by weight.[+] The variations in brightness temperature (T_B) due to different models can range up to 17K at a wavelength of 20 cm as shown in Figure 2-1. This graph indicates the response of the nadir brightness temperature as a function of vegetation depth for three different dielectric models. The complex dielectric coefficient for each model is given.

The need for an ancillary sensor to monitor vegetation canopies has therefore been suggested because it is difficult to establish what, if any, vegetation covers a test area with the LMR alone. The errors attributable to modification of the microwave emission by the vegetation can be appreciable and can exceed the soil moisture emission values.

[*]H. Burke and T. J. Schmugge: "Effects of Varying Soil Moisture Contents and Vegetation Canopies on Microwave Emissions, IEEE Trans GeoSci, Remote Sensing, Vol GE 20, No. 3, July 1982, p 268-274.

[+]G. P. DeLoor and F. W. Meijboom: "The Dielectric Constant of Foods and Other Material with High Water Contents at Microwave Frequencies," J. Food Technol, Vol 1, 1966, p 313.

Legend:

Dielectric Coefficient for Vegetation Layer

1 (1.8, 0.05)
2 (1.64, 0.04)
3 (1.3, 0.021)
ϵ_{Surf} 0.79
T_{Surf} 300 K
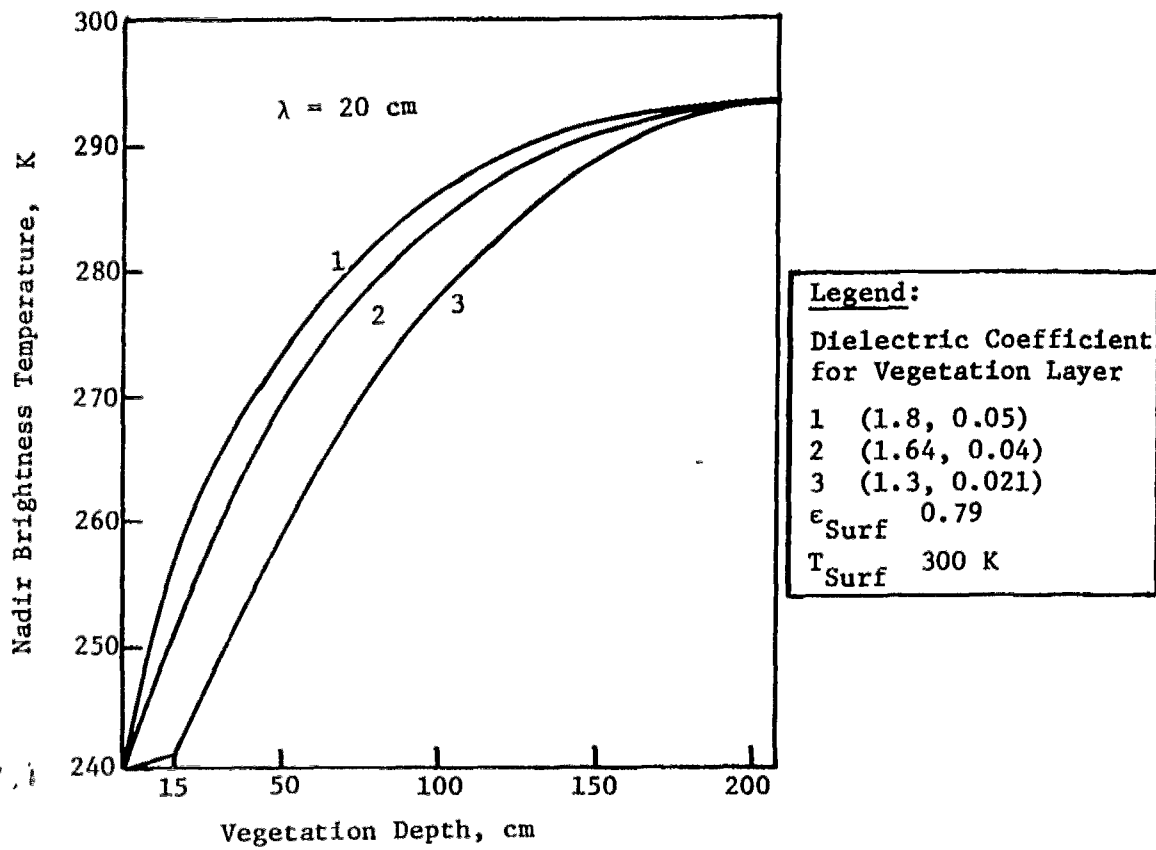
Note:

Response of nadir brightness temp at λ = 20 cm as a function of vegetation depth for three dielectric models of the vegetation layer.

Figure 2-1   Variations in T_B Due to Vegetation

2.1.4   Ice/Snowpack Conditions

Knowledge of mountain snow/icepack conditions is necessary to predict spring runoff and is important in both crop forecasting and hydrology. This information can also be ascertained in part with passive microwave radiometers. The microwave response (T_B) depends on the water equivalency of dry snow, and the grain size, structure, and degree of metamorphism of the snow field. However, the LMR alone is not completely capable of discriminating between various snow parameters under particular environmental conditions. For the types of surveys suggested, mapping the extent of snow fields and snowfree areas becomes very difficult when the snow becomes wet. It becomes difficult to discriminate between the changes in T_B due to soil moisture and vegetation or snow wetness and roughness.

To ease some of the ambiguity, recent work* has suggested optimum sensor specifications for the remote sensing of snow. A possible solution to the snow wetness problem is to use active instruments such as a radar scatterometer and measure the backscattering coefficient (σ). Snow wetness lowers T_6 and can yield high contrast between wet and dry snow or between wet snow and snowfree regions. For observation of the melting process, the active instrument would be used to map the extent of wet snow, while the LMR would be used to measure the water equivalency of the snow.

2.2 MISSION REQUIREMENTS

The missions described in this section were based on a large microwave antenna spacecraft primarily designed for soil moisture and ocean observations. The spacecraft includes compatible sensor sets used for remote sensing along four observational regimes—baseline, land, ocean, and atmospheric. These are known as EOS Missions I, II, III, and IV, respectively.

The baseline mission described in Section 2.1.1 represents a general radiometer mission with the minimum implied sensors of Section 2.1.1 (Table 2-1). EOS Mission II (land observation) is a comprehensive land resources mission using multispectral sensors and active imaging radar covering a broad range of disciplines.

The ocean mission, EOS Mission III, is primarily open ocean with the capability for coastal zone monitoring. This mission is similar to a NOSS-type mission, using primarily active/passive microwave sensors.

The final mission concentrates on atmospheric observations. Although the LMR does not directly contribute to these observations, it is a useful platform for the atmospheric sensors.

There are both scientific and technical advantages in providing the LMR with ancillary sensors. The mission requirements and sensors for the missions described in the following sections are organized around three main thoughts. An essential set of sensors that enable the LMR measurements described in Section 2.1 to be made are included first. If these sensors were not included, the LMR data would be degraded in accuracy and precision. Sensors that enhance the LMR measurements beyond the essential set are included next. Sensors that provide supplemental measurements to the LMR are also included to enhance the various earth observational science disciplines.

---

*C. Mätzler, E. Schanda, and W. Good: "Towards the Definition of Optimum Sensor Specifications for Microwave Remote Sensing of Snow." IEEE Trans GeoSci Remote Sensing, Vol GE 20, January 1981, p 57-64.

Including additional mission goals on a single spacecraft is motivated by the long mission lifetimes anticipated. A 10-year lifetime is desired to provide a long-lifetime observation platform so crop prediction studies can continue over many seasons. Also because optimum atmospheric conditions for surface observation times are not available every day, long mission lifetimes are required to obtain a reasonable data set.

2.2.1 EOS Mission I - Baseline Mission

The baseline mission for EOS constitutes a remote sensing platform capable of extensive observations in both the land and ocean sciences. This mission uses both active and passive microwave remote sensors with the LMR as the core instrument, and is intended to satisfy all the potential measurements of Table 2-1. The orbit could have either a 60-deg or near-polar orbit, depending on coverage requirements.

It would be advantageous to have a single radiometer provide a wide range of measurements from about 1.4 GHz to beyond 30.0 GHz. This instrument would cover land, sea, and atmospheric observations and provide its own support of auxiliary inputs. It would fulfill all the measurement needs described in Section 2.3.1. This configuration constitutes the "ideal" radiometer.

Primarily due to engineering considerations, the "ideal" radiometer must be revised and restricted in scope. These restrictions, discussed in Section 4.1, involve the inability to create reflector surfaces accurately enough to operate throughout the range. Our baseline radiometer mission includes the observations most suited for the LMR, and the addition of sensors that minimally satisfy the measurement needs. The orbit is either polar or a near-polar sun-synchronous orbit for maximum geographic coverage.

2.2.2 EOS Mission II - Land Observation Mission

The intent of EOS Mission II is to provide the next level of complexity beyond the baseline configuration. This ensemble of new sensors forms an integrated sensor package (ISP) for land observations that will provide multidisciplinary, multispectral observations that satisfy the needs of a wide range of users. The sensors were selected to provide cross-discipline information, facilitate geophysical parameter retrieval, support the LMR, and generally provide more information than isolated noncoordinated observations.

The observables selected for this mission were derived from a variety of sources. Land management, resource assessment and agricultural monitoring can all benefit from orbiting spacecraft observation. The area of predictive system modeling requires multifaceted inputs (to which remote sensing from space can make a marked contribution). Figures 2-2 and 2-3 illustrate models for food and crop production forecasting, respectively, and indicate the types of inputs required.

The technical requirements for the sensors were derived from the goals previously mentioned. These plausible mission objectives are meaningful in directing technology developments. The next subsections discuss the instruments' performance requirements.
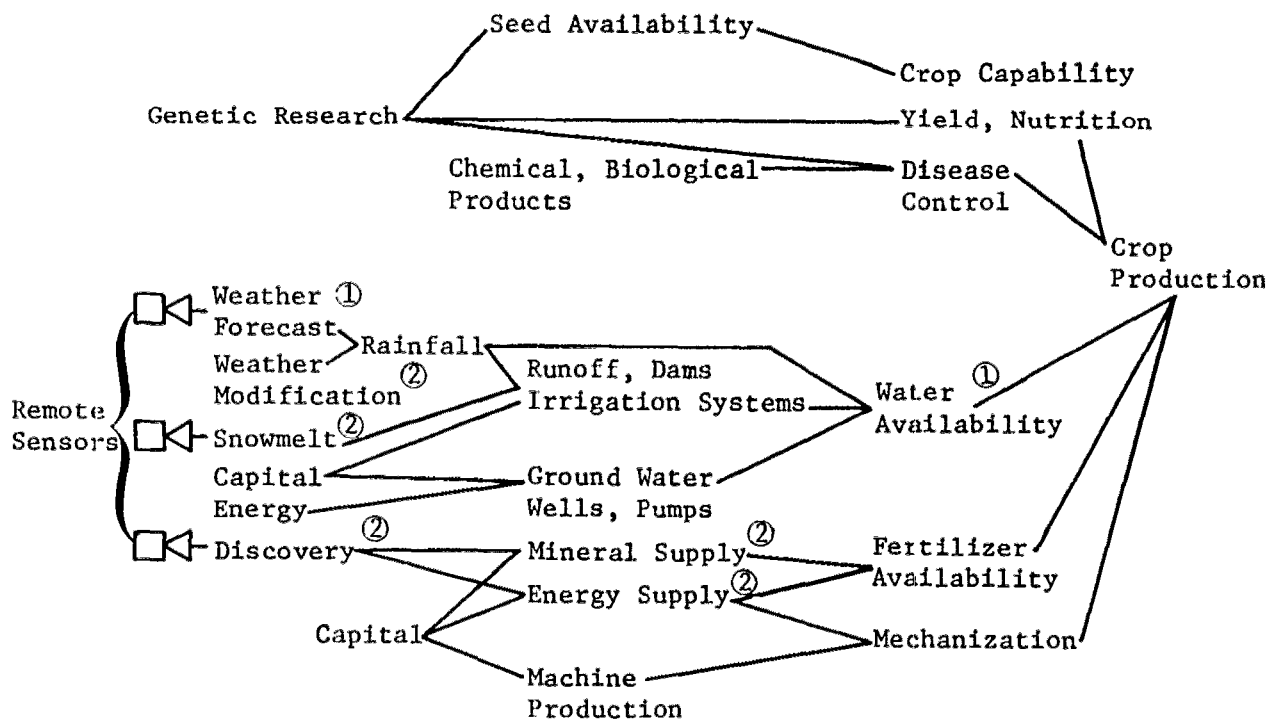
① Areas of Major Space Contribution ② Areas of Secondary Space Contribution

Figure 2-2 Model for Food Production
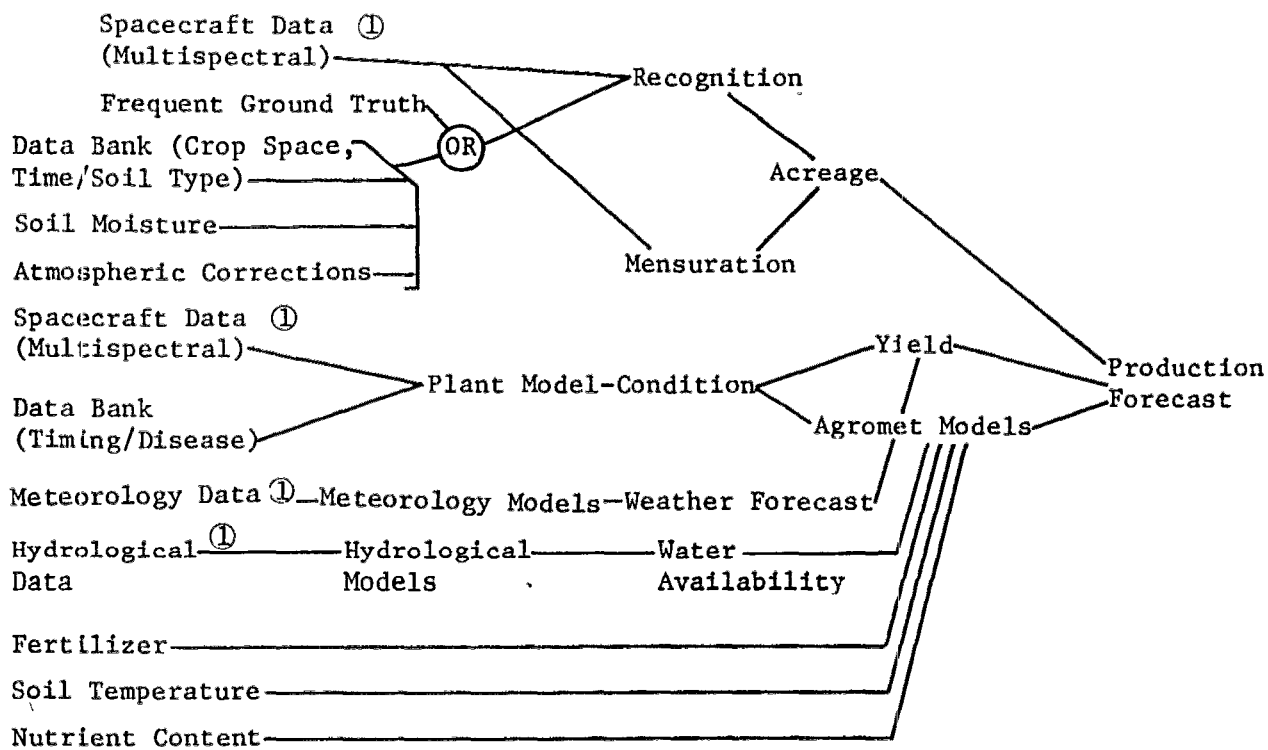
① Areas of Major Space Contribution

Figure 2-3 Model for Crop Production

11

2.2.2.1 <u>Spectral Resolution</u> -- The spectral bands and spectral resolution requirements are set by the observables. Such early scanners as the multispectral scanner (MSS) on LANDSAT 1-3 simply divided the visible spectrum into four regions. The spectral bands for the LANDSAT 4 thematic mapper (TM) flown in July of 1982 were based on considerably more experience and, with the exception of one spectral region, satisfy all known demands for spectral coverage.

The Mission II spectral bands identified as particularly useful for remote sensing applications are summerized in Table 2-2.

Table 2-2   Mission II Spectral Bands

Spectral Bandpass	Description
0.45 to 0.52	Peak transmittance of clear water, enabling mapping of coastal water areas.
0.52 to 0.60	Reflectance from healthy vegetation.
0.63 to 0.69	Differentiation between plant species, soil boundary, and geologic discrimination.
0.76 to 0.90	Biomass survey and water body delineations.
0.90 to 1.1	Agriculture.
1.55 to 1.75	Differentiate between clouds and snow.
2.08 to 2.35	Rock-type discrimination helpful to mineral and petroleum geologists.
10.4 to 12.5	Vegetation classification and crop stress locate geothermal activity.

Nearly all spectral requirements are satisfied with this assortment of spectral bandpasses.

2.2.2.2 <u>Spatial Resolution</u> -- Spatial resolution refers to the ability to discern detail on the ground. To increase the spatial resolution, the area imaged is divided into a large number of picture elements, or pixels. The system implication of increased resolving power is discussed in the following paragraph.

The ability to resolve finer ground detail will generally improve the usefulness of the data. The LANDSAT serves as an example. The MSS on LANDSATS 1-3 had a ground resolution of 80 m. The LANDSAT 4 TM has a ground resolution of 30 m. The French earth resources program called SPOT will also attain a similar resolution. Because experience has shown that such disciplines as agriculture, geology, and coastal zone studies benefit from greater resolution, a resolution of 30 m or better is a baseline requirement for imaging instruments. Table 2-3 illustrates the spatial resolution desired for various disciplines that use

space-acquired land observational data. The table also states related
geometric needs regarding field of view, pointing angle, and coverage.*

The effective instantaneous field of view (EIFOV) is defined as the
minimum linear dimension on the surface at which user specified
characteristics of the surface can be discerned.

Table 2-3 Scanner Geometrical Needs

EIFOV, m (Ground)	Field of Coverage, km (Ground)	Maximum Oblique Pointing Angle, deg	Sample (S) or Continental (C) Coverage
10			
— C	40	Nadir	(C)
— A, F, G (5-10)	15-30	6	(S)
10-30			
— H	50	15	(S)
— L (10-20)	13	45	(S)
30-50			
— H, C	200	Nadir	(C)
— C	200	45	(C)
— G, A, F	200	12	(C) or (S)
— L	200	12	(C)
50-100			
— H, C	200	Nadir	(C)
— C, O	200	30	(C)
— C	200	45	(C)
— G, A, F	200	12	(C) or (S)
— L	200	12	(C)
100-300			
— C	200	45	(C)
300			
— L (300)	400	20	(C)
— M (300-400)	1000x400	8	(S) (2 to 3-minute repeat)
— C, O (1000-10,000)	400	20	(C)
— L (1000-2000)	1300	45	(C)

Legend

A — Agriculture	F — Forestry	L — Geology	M — Meteorology
C — Coastal Zone	G — Geography	H — Hydrology	O — Global Oceanography

2.2.2.3 Classification Retrieval — A major goal for all EOS missions
is to ease and expedite the data reduction of imagery. This is done in
part by selecting sensors that will support the observations of other
instruments. This section is intended to provide the background and
example for such an opportunity.

The effect of the atmospheric haze on scene classification accuracy has
been studied by various investigators. Turner, et al.[+] investigated
the ability to classify wheat on successive days at different haze
levels. The classification accuracy decreased from 87 to 65% from day
1 to day 2, and improved from 65 to 78% when corrections were made. In

*Advanced Scanners and Imaging Systems for Earth Observation, NASA SP-335,
1973.

[+]R. E. Turner, W. A. Milila, R. F. Nalepka, and F. J. Thomson: "Influence of
the Atmosphere on Remotely Sensed Data," Proc SPIE, 51, 101, Scanners and
Imagery Systems for Earth Observation, 1975.

another work, Potter* artificially increased the upwelling atmospheric radiance for test and training (reference) over fields of corn and soybeans. When the optical thickness was increased to 0.2 over the test area, classification accuracies decreased from 97.4 and 99% to 60.2 and 83.3% for corn and soybeans. Inaccuracies were even more pronounced when the atmospheric radiance was increased over the training site, dropping to 45.4 and 73.8%. These examples suggest there is a reasonable need to correct for these effects.

A widely used procedure known as image rationing can help overcome the radiometer-associated problems. Corresponding images made from different spatial bands are combined and analyzed. This technique eliminates the effects of vignetting and variations in topography and reduces atmospheric effects. These images are considered normalized spectral signatures but are not, strictly speaking, compensated for atmospheric effects.

Various existing methods will compensate for atmospheric effects although many rely on participation of ground support and atmospheric models. In the multispectral resource sampler (MRS) technique,[+] the spectral radiance of a particular scene is repeatedly viewed at various angles off nadir and eventually used to evaluate the upwelling atmospheric-path spectral radiance. This method avoids ground dependence and should expedite and enhance the ability to identify scenes.

2.2.2.4 Orbit Considerations -- The primary objective of any earth remote sensing platform is to measure the spectral radiance of a geophysics feature in various spectral bands, and determine the soil, crop, or other physical characteristics. This seemingly simple measurement can be complicated by many factors. An example that affects the monitoring of crops grown in rows is discussed.

A perfectly diffuse surface (known as a Lambertian surface) is one for which the reflected radiance is constant for any angle to the surface normal. If a row of crops could be considered such a surface, the solar elevation angle (or the angle that the solar illumination strikes) would not affect the reflected radiance. Orbits could be considered that would yield various elevation angles, even for the same spot on various days, and not affect results. Most natural objects, however, exhibit what is known as a bidirectional reflectance distributing function (BRDF). In other words, the reflectance from a surface depends on both the solar elevation angle and the angle that the sensor views the ground. Crop classification attempts would be further complicated with varying radiances.

In various land-monitoring studies, it is desirable to have approximately the same lighting conditions and length of shadows. Because shadows provide topographic relief and can significantly modify the spectral signatures from a forest, it is desirable to control these

---

*J. F. Potter: Haze and Sun Angle Effects on the Automatic Classification of Satellite Data--Simulation and Correction, Proc SPIE, 51, 78, 1975.

[+]P. N. Salter: Remote Sensing, Chapter 11, Addison-Wesley, 1980.

shadow variations as much as possible. Alternatively, shadows provide the topographic relief necessary in some applications.

The preferred orbit characteristics for land missions is known as a sun-synchronous orbit and enables data to be collected at the same local time of day over the same region. In this type of orbit, the orbit plane precesses 0.95 deg per day to the east to compensate for the earth's eastward revolution of 360 deg per year around the sun. Only specific combinations of orbit inclination and altitude can be used.

The large radiometer mission and land mission using optical imaging sensors present conflicting orbital parameters. Optical imaging sensors have special illumination demands and dictate specific orbital parameters such as being in a sun-synchronous orbit. A microwave radiometer is not so constrained and has more flexibility. For instance, a microwave radiometer mission could effectively operate in a 60-deg inclination orbit and cover the temperate zones of the earth. A microwave radiometer mission specifically designed for such observation would not have the complement of sensors used for regular monitoring of crops because of orbit incompatibility.

The available ground coverage is another problem. Currently, optical sensors obtain ground resolutions of 30 m with a crosstrack swathwidth of almost 200 km. A microwave radiometer achieves much lower spatial resolution but, depending on design, has a much wider crosstrack swathwidth. A LMR mission employing wide swaths would cause gaps in the ground coverage of an optical sensor.

2.2.3   EOS Mission III - Oceanic Observation Mission

The intent of EOS Mission III is to combine the measurement capability of the LMR with instruments designed for ocean-type missions. Microwave radiometers are well suited for the monitoring of ocean parameters. The microwave signal is influenced in part by ocean roughness (surface winds) and water temperature. These parameters are useful inputs in meteorology and climate models but are not regularly collected over vast extents of the ocean. The relatively homogeneous nature of the ocean enables the swath and medium resolution of the LRM to provide synoptic views of the ocean.

The sensors used in ocean missions generally must have higher performance than land sensors because the radiances are weaker, implying a need for high S/N ratios in the detectors.

The coastal zone measurements differ from both open ocean and inland areas in a number of ways:

1)   Generally the scenes are more dynamic, requiring a short revisit time;

2)   Coastal zone areas have a more intricate geomorphology, requiring resolution greater than achieved in the past;

The determination of a possible sensor complement began with a survey of needs. The measurement needs listed in studies by JPL and NOAA are shown in Table 2-4. The requirements for the open ocean measurements are similar to those of the SeaSat mission and described by Darnell.* A sun synchronous orbit is suggested.

Table 2-4 Oceanic Measurement Needs

Measurement Parameter*	Pollution	Bioresource	Weather	Physical Oceanography	Shoreline
Water Color	X	X			X
Plankton	X	X			X
Salinity	X	X		X	X
Bioassay	X	X			
Nutrients	X	X			
Particulates	X				
Metals	X				
Oil	X				
Water Temperature		X	X	X	X
Bathymetry		X		X	X
Vegetation		X			X
Fish Schools		X			
Wind Direction & Velocity	X	X	X	X	X
Precipitation			X		
Water Density		X	X		
Currents	X	X		X	X
Freshwater Inflow	X	X			X
Ice				X	X
Tides	X			X	X
Waves				X	
Sea Topography				X	
Land Use					X
Sediments	X				X
*Measurement parameters listed according to major user interests.					

2.2.4 EOS Mission IV - Atmospheric Observations Mission

Atmospheric remote sensing covers the altitude regime from the lower troposphere to the mesosphere (approx 100 km). The wide range of observables requires a multitude of instruments and operating modes. In general, atmospheric observations involve the most difficult, numerous, and highest variety of sensor operating modes of all remote sensing applications. A comprehensive observation package includes sensors for measurement of the multiple gaseous chemical species involved in the complex and highly coupled nature of atmospheric photochemistry. In addition to gaseous chemical species, temperature, aerosols, and pressure are other observables.

---

*W. L. Darnell: Mission and Sensor Concepts for Coastal and Ocean Monitoring Using Spacecraft and Aircraft, NASA TM-80103, 1980.

2.2.4.1 <u>Orbits and Sensor Performance</u> – The variety of instrument/orbit combinations complicates mission design. The objective of this section is to identify constraints and select instruments and orbits that are compatible with general LMR mission constraints. Including the most desirable atmospheric sensors on the LMR mission may require sensor technical improvements because the atmospheric sensors will no longer operate in their design orbit. The four operating modes for atmospheric sensors are described in the following paragraphs.

<u>Limb View, Solar Occultation</u> – Limb instruments using the sun as a source have the potential for monitoring stratospheric trace species with good resolution and sensitivity. Using the sun as a source realizes high signal/noise ratios and simplifies instrument design.

Limb instrumentation is not compatible with all orbits. Sun-synchronous orbits limit performance in the range of latitudes sampled, and each latitude is seen only four times each year. Diurnal and seasonal sampling of various latitudes is not practical because the measurement period is only 0.5 to 3.0 minutes during each orbit.

<u>Reflected Solar</u> – These nadir-viewing instruments use reflected solar light and require the local solar elevation angle to be greater than 45 deg for adequate illumination. This stipulation limits the latitude coverage.

<u>Nadir View, Thermal Emission</u> – Instruments that measure the emission features of a species are not restricted by the location of the sun. They provide day/night observations but are limited in their vertical profiling capability.

<u>Limb View, Thermal Emission</u> – Limb emission instrumentation is also not restricted by the location of the sun and provides day/night observations. Vertical profiling can be accomplished in the upper troposphere and stratosphere. High demands are placed on the instrument in the areas of sensitivity, cooling, and resolution.

Selection of instrumentation for an atmospheric mission depends on the sensors' mode of operation. The solar modes have restricted geographic coverage because of the location of the sun. This is particularly severe with solar occultation. The major asset of the solar occultation mode is its high signal-to-noise ratio, and it is employed for sensing the very tenuous gaseous species and aerosols. Emission modes are not limited in geographic coverage, but in the lower troposhpere are limited in a vertical profiling capability. Atmospheric measurements, like land and ocean measurements, are not particularly sensitive to orbit altitude, and specific altitudes are selected to obtain the desired sampling repeat (revisit) cycles. Orbit inclinations are also selected to obtain the desired periodic geographic coverage and the desired solar illumination. Consequently, atmospheric measurements will probably not change the orbit parameters selected for the baseline mission.

2.2.4.2 <u>Observables</u> – Because atmospheric photochemistry, transport processes, and chemical transformations are complex and highly coupled, the investigation of many chemical species with adequate temporal, global, and altitude resolution is necessary to verify photochemical models.

The principal measurands for stratospheric chemical species include CH_4, N_2O_4, H_2O, CO_2, NO, NO_2, HNO_3, and O_3. It would be desirable for these species to be observed, either nadir or limb view, with species-specific instruments. The necessary technology to develop these sensors exists.

The final report of the science working group for the upper atmospheric research satellite (UARS) also recommended measurements for which emission instrumentation is not available. Table 2-5 summarizes these recommendations for species, along with the desirability for such instruments.

Table 2-5 Species and Impetus of Instrument Development

Species	Remarks
HCl	Variability or Response to Perturbations
HF	Good Tracer for Transport Studies
CF_2Cl_2, $CFCl_3$, CH_3Cl	Emission Instrument Would Provide Saving in Weight and Data Rate Over a Spectrometer
H_2, N_2O_5, $ClONO_2$	Evaluate Roles as Reservoir Species
OH, ClO	Need to Monitor Diurnal Variation of Important Radical Species
O (mesosphere)	No Instrument Exists
O_3	Requires Understanding of High-Altitude Processes

Some recommendations regarding measurements and sensor developments made by the workshop in tropospheric passive remote sensing* are:

1) Development of sensors for a potential list of measurands for a tropospheric research program that includes dual-layer measurements of O_3, CO, CH_4, CO_2, HNO_3, H_2O, NO, NH_3, SO_2, CH_3CCL_3;

2) For multilayer measurements of a wide range of species, a nadir-viewing instrument in the 3- to 15-um spectral region with a resolution of less than 0.1 cm^{-1} is desired.

---

*Tropospheric Passive Remote Sensing, NASA CP-2237, Lloyd Keafer, Ed, 1982.

2.2.4.3 <u>Summary of Atmospheric Missions</u> – Emission instruments have
been considered as primary or "core" instrumentation of the LMR/atmos-
pheric mission. These satisfy most user needs and are compatible with
both 60-deg and sun-synchronous orbits. Limb emission instrumentation
includes spectrometers and radiometers. Spectrometers are generally
configured to be broad band and are sensitive to a large number of
species, while radiometers are generally limited by filters to the
spectral band associated with one or a small number of species. Each
has its own set of desired sensitivity and resolution requirements.

The required accuracy of the sensors is to be within 5%, or about dou-
ble the present capability. Increased sensitivity may necessitate
cooling of detectors and, in some instances, the entire instrument.
This presents a formidable problem because of the long desired lifetime
of the refrigeration system.

2.3   MISSION FORMALIZATION

The mission formalization derived from the mission requirements is de-
scribed in the following subsections.

2.3.1   EOS Mission I – Baseline Configuration

Some of the operational problems associated with passive microwave
radiometry and the accurate retrieval of earth surface characteristics
via remote sensing were summarized in Section 2.1. To reduce the ambi-
guity of remote sensing, general minimal requirements for the baseline
LMR mission are suggested:

1)   Inclusion of an ancillary passive microwave radiometer that
      operates at higher frequencies than the LMR;

2)   Use of a calibrated radar system to measure the radar scattering
      coefficient and derive additional surface characteristics.

2.3.1.1 <u>Large Microwave Radiometer</u> – Figure 2-4 illustrates the sensi-
tivity of microwave emission to geophysical parameters. The measure-
ments range is between 1 and 37 GHz. This complete range of bands can-
not be included on a single LMR because of surface inaccuracy at the
higher frequencies. Section 6.6.1 discusses the problem of surface ac-
curacy to a greater extent.

The LMR operates at three frequencies—1.4, 5.5, and 10.68 GHz. These
bands were selected for their usefulness in radiometry and also to min-
imize the effects of radio frequency interference (rfi) from other
ground transmitters. In particular, the 1.4 and 10.68 frequencies are
within protected radio astronomy bands in which no transmitters are al-
lowed.

Specific details of the antenna design, rf electronics, and performance
requirements are covered in Section 4.1.
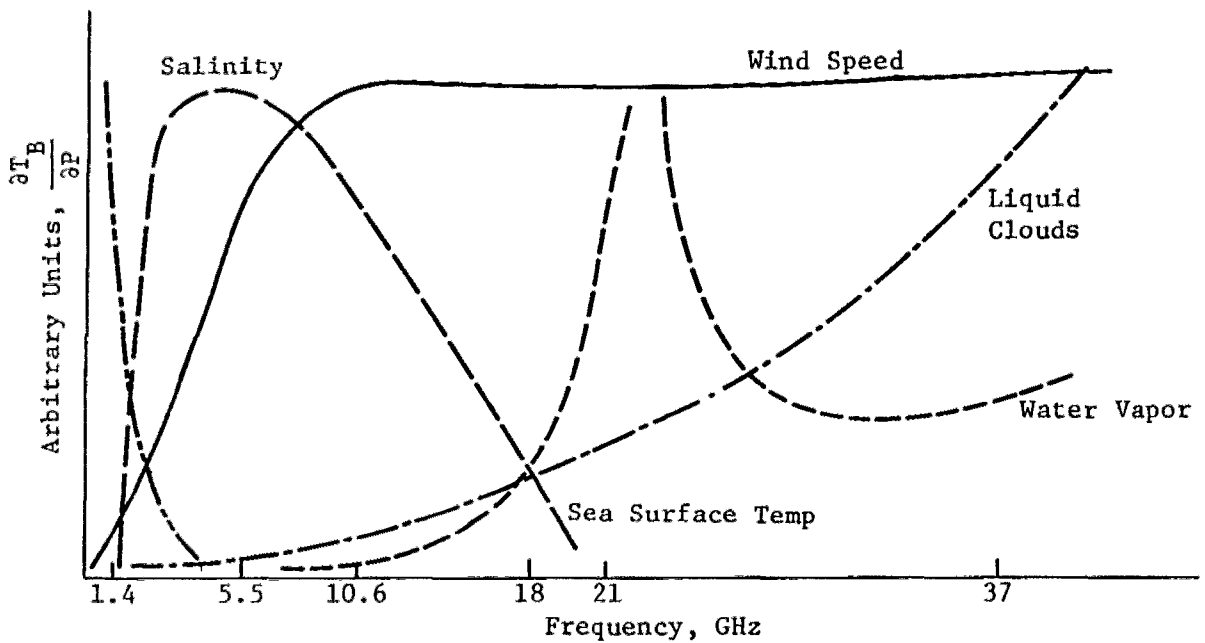
Figure 2-4   Microwave Sensitivity

2.3.1.2 <u>Atmospheric Sounding Radiometer (ASR)</u> — The ASR is a smaller radiometer used to provide higher frequency inputs to the retrieval algorithms. It can also provide additional measurements not possible with the LMR.

Section 2.1.1 presented the background for recommending implementation of the ASR. The conclusion was that the effects of water vapor, liquid water, and oxygen on T_B must be included in the measurements. A three-frequency approach using 18, 21, and 37 GHz can provide the necessary information on the atmospheric modifications of upwelling microwave energy. In addition, dual polarization and an incidence angle of between 40 to 70 deg is preferable. In this way, atmospheric effects can be separated from the contributions from ground conditions (i.e., soil moisture).

Because the ASR will provide data along the same ground swath as the LMR, this further complicates the system design. Space limitations will preclude an ASR pushbroom configuration, necessitating scanning either mechanically or electronically. The aperture of the radiometer must be approximately 4 m in diameter to provide a 10-km ground resolution (on the order of average storm cells). The hardware system design tradeoff study was between electronically scanned planar arrays and a mechanically scanned offset-fed paraboloid. Table 2-6 summarizes this study. The alternatives were evaluated from both mechanical and radiometer performance perspectives.

Table 2-6 ASR Concept Comparison

Concept	Remarks
Sweeping	Antenna must be rotated back and forth every 1.5 s. Torques produced by ASR/vehicle crosscoupling must be compensated for by attitude control system. The duty cycles of the drive mechanism and loads imposed on structure are a major concern.
Rotating	Must complete one rotation every 1.5 s or angular rate of 4.2 rad/s (40 rpm). Momentum compensation requires use of counterrotating wheel.
Electronically Scanned	Requires antenna and supporting structure on planar surface. Easy to integrate on structure. Little or no impact on attitude control system.

2.3.1.3 Synthetic Aperture Radar (SAR) – The SAR is used to provide high-resolution (25-m) radar imagery of both land and ocean surfaces. The SAR is also used to provide ancillary measurements that directly support the LMR and its primary mission. The SAR advantages and contributions include:

1) Radar backscatter coefficient can be used to estimate sea surface roughness, which is a function of surface wind speed. Because a direct correlation exists between microwave emission and sea state, the SAR and LMR are combined to yield wind velocities of lower ambiguity;

2) The SAR is capable of identifying wet snow areas and enables the LMR to map these areas at 5.5 GHz;

3) The SAR will differentiate surface vegetation and will be used to correct for vegetation canopies.

The specific design and functional requirements for this instrument are covered in Section 4.2.3.

2.3.1.4 Mission I Science and Summary – Table 2-7 shows the science/ observables supported by EOS Mission I. These represent a synthesis of minimal sensor requirements for an efficient and functional microwave radiometer.

Table 2-7 Science on EOS Mission I

Observable	Large Radiometer	Atmospheric Sounding Radiometer	Synthetic Aperture Radar
Soil Moisture	X		
Sea Surface Temperature	X		X
Sea State = Winds	X		
Salinity		X	
Ice/Snow Pack	X		X
Atmospheric H_2O		X	
Atmospheric Liquid H_2O		X	
Rain Rates		X	
Correction for Models		X	
Land Surface Imaging Geology			X

2.3.2 EOS Mission II – Land Observation

The needs for land observation missions were presented in Section 2.2.2, and are based on:

1) Continuity of data from past missions;

2) User needs;

3) LMR complementing;

4) Cross-sensor support – atmospheric haze correction.

The sensor complement presented here is from a catalog of many similar sensors. The salient features of the instruments are described in the following paragraphs.

2.3.2.1 **Multispectral Linear Array (MLA)** – The MLA operates primarily in the visible spectrum and is usually configured for crop prediction and land survey applications. Unlike the thematic mapper and past United States sensors, the MLA will use a linear array of detectors operating in the pushbroom mode, permitting improved geometric precision of pixels, a smaller instrument, and a higher SNR, which enables it to operate over a greater range of conditions. Such an instrument does not exist although the French are developing a similar instrument for their SPOT program. The MLA is intended to obtain global data routinely for general use. Table 2-8 summarizes the MLA characteristics.

Table 2-8 Multispectral Linear Array Specifications

Spectral Bands, μm	0.52 to 0.60
	0.63 to 0.69
	0.76 to 0.90
	0.90 to 1.11
	1.55 to 1.75
Sensor Field of View, km	180
Instantaneous FOV, m	30
Orbit Altitude, km	705

2.3.2.2 <u>Multispectral Resource Sampler (MRS)</u> — The MRS system selected for this mission is the same as that detailed by Schnetzler and Thompson.* It is intended to be a research instrument as opposed to a general survey like the MLA, and is intended to work with the MLA to provide:

1) Higher resolution spot data taken concurrently with the MLA;

2   A means of correcting for atmospheric haze as described in Section 2.2.2.3 and as an aid in classification accuracy;

3) The ability to scan crosstrack to review objects more frequently than in the normal orbital progression; with this technique it is possible to reduce revisit time to two or three days instead of 16;

4) Command pointing capability, permitting stereo imagery.

Table 2-9 summarizes the salient system specifications.

Table 2-9 Multispectral Resource Sampler Specifications

Spectral Bands, μm	4 Selectable from 12
Sensor Field of View, km	15 (Prime Mode) or 30
Instantaneous FOV, m	15 (Prime Mode) or 30

Like the MLA, the MRS utilizes a linear array.

2.3.2.3 <u>Midinfrared Imager (MIRI)</u> — The MIRI operates in the IR and is not covered by the previous instruments. It is intended to provide rock discrimination, vegetation classification, crop stress detection, and mapping of thermal gradients.

---

*C. C. Schnetzler and L. L. Thompson: "Multispectral Resource Sampler: an Experimental Satellite Sensor for the Mid-1980s," <u>Proc SPIE</u>, 1983, 34, 1979.

Table 2-10 summarizes the instrument specifications.

Table 2-10 Mid-IR Imager Specifications

Spectral Bands, μm	8.1 to 9.1
	9.5 to 10.5
	11.0 to 12.0
Sensor Field of View, km	180
Instantaneous FOV m	30

In general, the 10.5- to 12.0- m band is useful for vegetation classi-
fication and crop stress detection. The three discrete bands have been
identified as optimum thermal IR bands for mapping general rock types
and temperature from space.

2.3.2.4 <u>Synthetic Aperture Radar (SAR)</u> - The SAR for Mission II is more
comprehensive in its remote sensing capability than that of Mission I.
The instrument provides multispectral observations in both the X and
L-band enabling enhanced surface identification capability with varying
angles of incidence. Separate antennas are used for each frequency.

The varying incidence angles enhance the information content of the
images. Low angles of incidence (< 25 deg) emphasize topographic fea-
tures because a ground slope of a few degrees can change the strength
of the backscattered energy by a factor of 2 or more. The signal
strength at angles of approximately 50 degrees is influenced primarily by
surface roughness, and can delineate boundaries of rock strata and the
type of rock. L-band is most sensitive to roughness in the range
2.5-25 cm while X-band extends that range to between .3 and 3 cm. and
improves the discrimination capability.*

2.3.2.5 <u>Mission II Science and Summary</u> - Table 2-11 summarizes the
science and utility of EOS Mission II for land observation. The com-
plement of sensors is derived from the operating considerations of
Section 2.2.2.

2.3.3 <u>EOS Mission III - Ocean Observation</u>

The instruments selected for this mission satisfy the majority of user-
expressed needs presented in Section 2.2.3.

2.3.3.1 <u>Coastal Zone Color Scanner (CZCS)</u> - The CZCS is a spectrometer
specifically designed for imaging over water bodies. The radiances are
generally less than those over land, requiring increased dynamic range
and greater signal/noise ratios in the detectors. Its purpose is to
map chlorophyll concentration, sediment distribution, gelbstoffe (yel-
low substance) concentration, and water temperature. The CZCS satis-
fies the biological and imaging needs expressed in Section 2.2.3.

---

*Elachi, C., "Spaceborne Imaging Radar: Geologic and Oceanographic
Applications", <u>Science</u> Vol 209, pp 1073-82

Table 2-11 EOS Mission II Science

Disciplines	LMR	SAR	ASR	MLA	MRS	MIRI
Crop Yield Forecasting						
— Soil Moisture	3					
— Multispectral Imaging				3	3	2
— Water Availability	2	1		3		
Geology						
— Mineral Identification		2				3
— Subsurface Imaging		3				
Ice/Snow Pack						
— Snow Metamorphosis	3	2	1			
— Extent			2	2		
— Wet/Dry Conditions		3	3			1
Support Observations						
— Multispectral Imaging Atmospheric Haze				1	3	
— Soil Moisture Vegetation Canopies		2		3		2
— Microwave Radiometry Retrieval Input		3	3			

Legend

3 — Primary Observation
2 — Contributing Observation
1 — Helpful Observation

2.3.3.2 <u>Radar Scatterometer</u> — A scatterometer measures the scattering of radar signals from the surface of either the ocean or land. The varying signal strength of the return pulses is used to measure surface conditions and the wind speed over oceans at specific resolution cells on the surface.

2.3.3.3 <u>Science Summary</u> — Table 2-12 summarizes the relevance of the instrument complement to some observable parameters.

Table 2-12 EOS Mission III Ocean Science

	LMR	ASR	CZCS	MRS	ALT	SCATT
Physical						
— Salinity	3					
— Water Temperature	2		3			
— Wave	2				3	
Bioresource						
— Plankton			3	2		
— Chlorophyll			3	2		
Weather						
— Winds (Direction, Velocity)	3				2	3
— Precipitation		3				
Coastal Zone						
— Imaging			3	3		
— Pollutants				3		

Legend

3 — Primary Observation
2 — Contributing Observation

2.3.4 EOS Mission IV — Atmospheric Observations

Table 2-13 presents the sensors required to satisfy a majority of the observational needs for an atmospheric monitoring science package. The sensor complement in this section is based on limb viewing, emission, and species-specific instrumentation. Limb viewing instruments offer relative superiority over the other operating modes discussed in Section 2.2.4.1.

Table 2-13   EOS Mission IV - Atmospheric Science

Instrument	Observable
Correlation Interferometer	CH_3Cl, $CFCl_3$, N_2O_5, H_2, CF_2Cl_2, $ClONO_2$, ClO, OH, H_2O_5
Grating/Interferometer	CO, SO_2, CH_4, NH_3, NO_2, H_2O, O_3, CO_2, HNO_3, NO, CH_3
Filter Radiometer	O_3, H_2O, CH_4, N_2O, HNO_3, NO_2, HCl
Advanced Meteorological Temperature Sounder (AMTS)	Temperature Profiles

2.3.4.1   Filter Radiometer - Table 2-14 summarizes the atmospheric trace species measured by the filter radiometer. A third column has been included to facilitate comparison with the state of the art.

Table 2-14   Trace Species - Filter Radiometer

Species	Desired Measurement		Currently Available	
	Altitude, km	Accuracy, %	Altitude, km	Accuracy, %
O_3	60 to 90	10	--	--
H_2O	Tropopause, 70	10	10 to 80	15
CH_4	Tropopause, 60	20	10 to 50	15
N_2O	Tropopause, 40	20	10 to 50	20
HNO_3	20 to 30	10	10 to 40	15
NO_2	20 to 60	10	10 to 40	15
HCl	20 to 50	10	--	--

2.3.4.2   Correlation Interferometer - This instrument is a limb scanning interferometer to observe emission spectra in the stratosphere. It is intended to make observations both day and night and operate with a duty cycle of 50%. Some of the species that can be measured are indicated in Table 2-13. To achieve high sensitivity and SNR, the entire instrument needs to be cooled to 10 K for detectors and 30 K for the optics. The long-term cyrogenic requirement is not available with current space technology.

2.3.4.3   Advanced Meteorological Temperature Sounder (AMTS) - The AMTS uses 28 appropriately selected IR channels. It will be capable of making the following measurements from 800 km as reported by Hinkley:*

1)   Obtain temperature profiles through three layers of broken clouds with 1.5 K rms error;

---

*E. D. Hinkley: "Advanced Instrumentation for Remote Sensing," Journal Astronautical Sciences, Vol XXIX, No. 2 1981, p 97-111.

2) Simultaneously obtain humidity profiles to accuracy of 20%;

3) Day and night ocean and land surface temperature ± 1.5 K;

4) Map fractional cloud cover;

5) Determine location of tropopause to 0.5 km.

2.3.4.4 <u>Grating/Interferometer</u> - This instrument is a combination grating/interferometer for profiling chemical species in the troposphere. A similar sensor was suggested by the Sensing Technology Panel of the Tropospheric Remote Sensing Workshop previously referenced.

2.4 CROSS-DISCIPLINE UTILITY

The previous sections have described sensor sets and observables germane to a single-discipline mission concentrated on either land, ocean, or atmospheric measurements. A wide range of possible observations have been described. Even though these sensors were configured for a particular mission, they present a considerable cross-discipline utility.

Table 2-15 illustrates the span of ocean and atmospheric observations and disciplines possible with the sensors configured for land observation. The approximate spectral overlap and compatible ground resolution enable this discipline synthesis. The sensors also cover a broad range of spectral bands, permitting substitute observations if the primary band is not possible with the present sensor set. The multispectral linear array (MLA) has not been included for an area such as ocean color because, as presently configured, its dynamic range is not sufficient to measure spectral radiances over water.

Table 2-15 Cross-Discipline Utility for Land Sensors

Disciplines	LMR	SAR	ASR	MRS	MIRI
Ocean					
— Sea State	3	3	RI		
— Surface Temperature	2				3
— Ocean Color				3	
— Coastal Studies		2		3	
Atmospheric					
— Precipitation			3		
= Storm Cell ID			3		
Legend					
3 — Primary Observation 2 — Contributing Observation 1 — Helpful Observation RI — Retrieval Algorithm Input					

Table 2-16 depicts a possible range of land observations for the ocean mission. Its major contributor is active radar sensors that enable this sensor set to map and characterize ice and snowpack conditions over both land and polar sea ice. The coastal zone color scanner (CZCS) did not find much utility in crop studies because of poor resolution and the poor match of spectral bands with those specifically required for crop studies.

The atmospheric instruments, except possibly the AMTS do not directly support the basic observations of the LMR. The spectral regimes and operating modes as discussed in Section 2.2.4 do not lend themselves to either land or ocean observations. If atmospheric sensors are included on a LMR mission, they must be considered as using the LMR as a stable long-term observation platform only while operating independently of the LMR and its observations.

The weather and climate disciplines, however, are necessary inputs in earth radiation budget monitoring and validation of earth climate models. These observations when integrated with other climate dependent observables (soil moisture, ocean surface wind velocity) do form a complete climate model. Although the atmospheric sensors do not directly aid in the interpretation of LMR data, they can be effectively combined for broader modeling capability.

The relative success of the land and ocean missions in achieving a cross-discipline utility suggests a possible synthesis of the missions. The easiest method of producing a composite mission is to combine sensors such as the CZCS, SCAT, and the ALT to the land observation sensors (Mission II). The science platform can be reconfigured to accommodate these additional sensors, although the SAR and SCAT antennas will present packaging difficulties.

Another alternative is to combine the functions of several instruments into a single advanced instrument. This idea was the basis for the thematic mapper flown on Landsat 4, which had greater capability than its predecessor, the Multispectral Scanner (MSS). A candidate synthesis might be between the MLA and the CZCS. Figure 2-5 compares the spectral bands of the MLA with the CZCS and a summary of restrictive spectral cutoffs. The restrictions described should be compared with Table 2.2 that describes the use of each band. The combined visible spectrum converge suggest a maximum of 9 bands are required.

The prospective orbit design for the combined mission is an attempt to reconcile various diverse sensor operating requirements. An important factor to consider with optical sensors is to have proper surface illumination and sufficient solar elevation of greater than 30° to provide good surface radiances. The suggested orbit is sun-synchronous with mid morning equatorial crossing. Mid morning reduces the possibility of surface coverage by clouds and sun synchronous ensures constant illumination. Sun synchronous orbits are a mandatory requirement for land observation, and must be included as the baseline requirement for any anticipated combined mission.

MLA

CZCS

.4   .5   .6   .7   .8   .9

Wavelength um
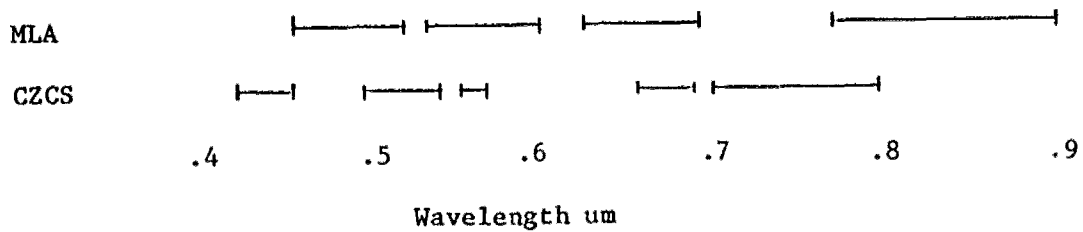
Band	Restrictions
0.45-0.52	Below 0.45 µm ground radiances are reduced by atmospheric scattering
0.63-0.69	The absorption of red light by chlorophyll occurs in this region. The reflectance crossover for vegetation occurs in the 0.68 µm to 0.75 µm region, thus the upper cutoff should be below 0.69 µm.
0.76-0.90	The lower cutoff should be above 0.75 µm for the reasons described above. The 0.90 µm edge is not critical.

Figure 2-5 Spectral Band Comparison

Table 2-16 Cross-Discipline Utility for Ocean Sensors

Disciplines	LMR	ASR	CZCS	MRS	SCATT	ALT
Ice/Snowpack						
— Metamorphosis	3	1			2	2
— Extent				2		3
— Conditions	2	2			3	1
Land						
— Surface Temperature			3			
— Special Crop Investigations	2			3		2
Legend						
3 — Primary Observation 2 — Contributing Observation 1 — Helpful Observation RI — Retrieval Algorithm Input						

3.0   STRUCTURAL DESIGN AND ANALYSIS

The antenna design selected for the EOS is a pushbroom radiometer as
shown in Figure 3-1. To achieve adequate stiffness, stability, and
packaging efficiency, box truss structural elements with an integrated
offset feed mast are used. The following sections describe the antenna
requirements and tradeoff studies that resulted in the antenna geometry
and use of the box truss. This section also describes in detail the
resulting EOS antenna design.
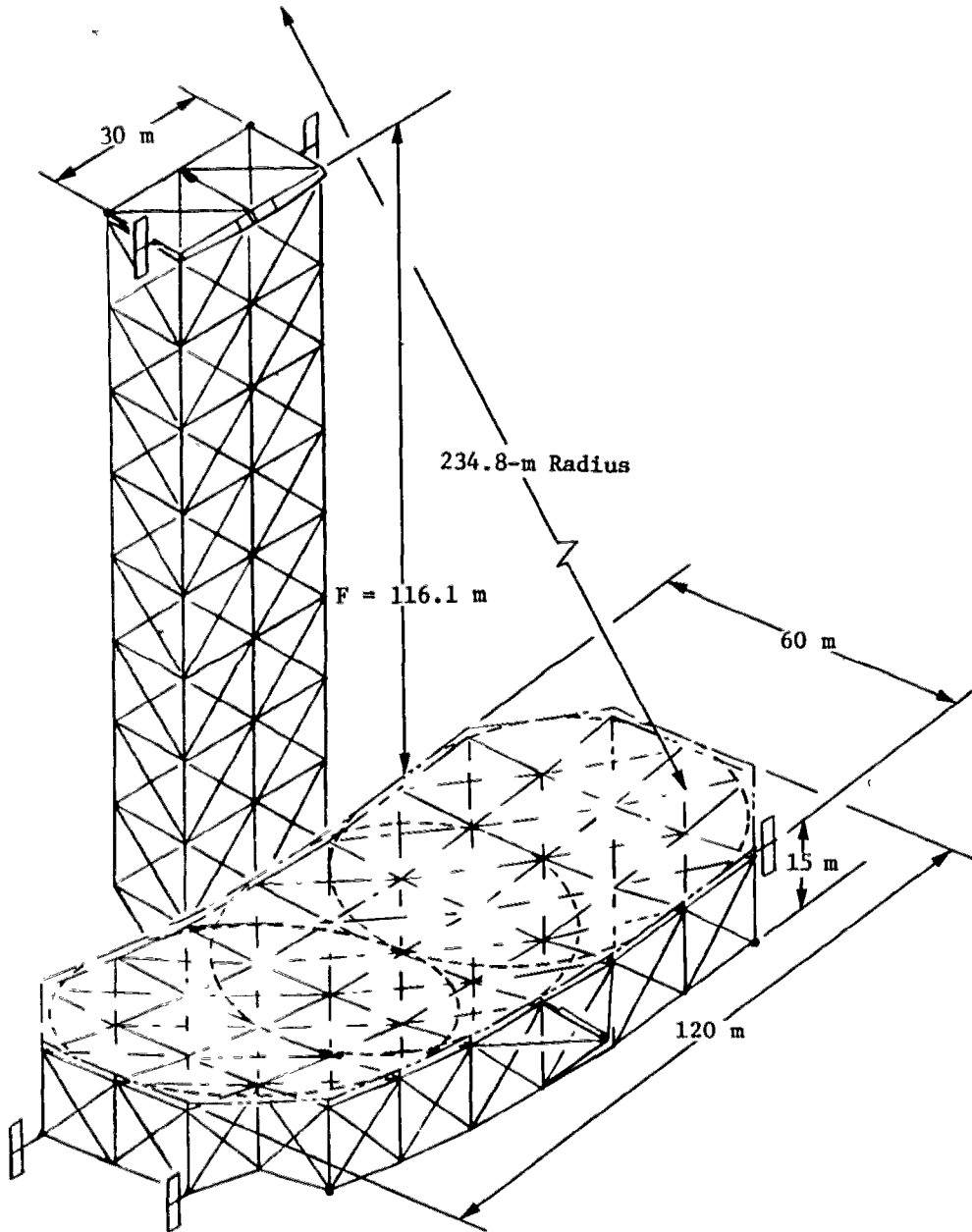
Figure 3-1 EOS Configuration

3.1 ANTENNA REQUIREMENTS AND GEOMETRY

Microwave radiometry imposes stringent requirements on the antenna system. The radiometer functional requirements presented in Table 3-1, along with STS payload constraints, are the predominant drivers of the large radiometer antenna design.

Table 3-1   Antenna System Performance

Functional Requirements	Derived Requirements
Beam Efficiency, 90%	Total Phase Errors $\lambda/16$ to $\lambda/30$, Surface Errors $\lambda/30$ to $\lambda/100$, Offset-Fed Reflector, Optimum Feed Design
Radiometric Resolution, 1 K, in Combination with Revisit and Coverage Requirements	Long Integration Time, Multibeam Concepts
Spatial Resolution in 1- to 10-GHz band	
10 km Mandatory	Large Reflectors in the 50- to 200-m
1 km Desirable	Range

The main beam efficiency is defined as the integral of power over the main beam (first minimum) divided by the total power received. The radiometer samples the microwave emissions from specific areas on the earth's surface. Contributions, via sidelobes to the signal from areas outside the desired area, must be accurately known and should be minimized. The larger the beam efficiency, the easier it is to correct for these contributions. Maximum main beam efficiency is synonomous with minimum sidelobe levels. The offset-fed reflectors reduce aperture blockage and minimize scattered radiation, thereby helping to minimize the sidelobe levels. In an offset-fed reflector system, the beam efficiency is governed by the feed illumination taper and the surface errors.

The size of the large radiometer antenna system is defined by the operating frequencies, radiometric resolution requirements, and number of beams. For radiometer systems, the radiometric resolution is inversely proportional to the dwell time for the particular scene. To achieve adequate radiometric resolution and spatial resolution, a 58-m spot size is needed. To obtain the necessary ground coverage and revisit times, multibeam systems are required.

Based on these considerations, the antenna design selected was an offset-fed reflector operating in a pushbroom mode. A spherical/parabolic reflector is used instead of a paraboloidal reflector because the spherical/parabolic reflector provides a line focus for multiple beams. In this configuration wide swaths and multibeams are obtained simultaneously by aligning multiple feeds in a circular arc subtending the spherical curve of the reflector. Each feed sees an independent spot on the reflector and, consequently, an independent footprint on the ground.

The use of spherical reflectors for multibeam antennas was suggested by Ashmead and Pippard in 1946.[*] The principal drawback is the effect of spherical aberration, which must be minimized. The approach used in this study involved using a restricted aperture and a reflector with a long radius of curvature. Other methods using multisource feeds, correcting lenses, or auxiliary reflectors were not considered.

The maximum phase error produced by a spherical surface is a function of the radius of curvature of the reflector and the aperture size. Relationships given by Li^{+} were used to derive the phase error interrelationships shown in Figure 3-2.
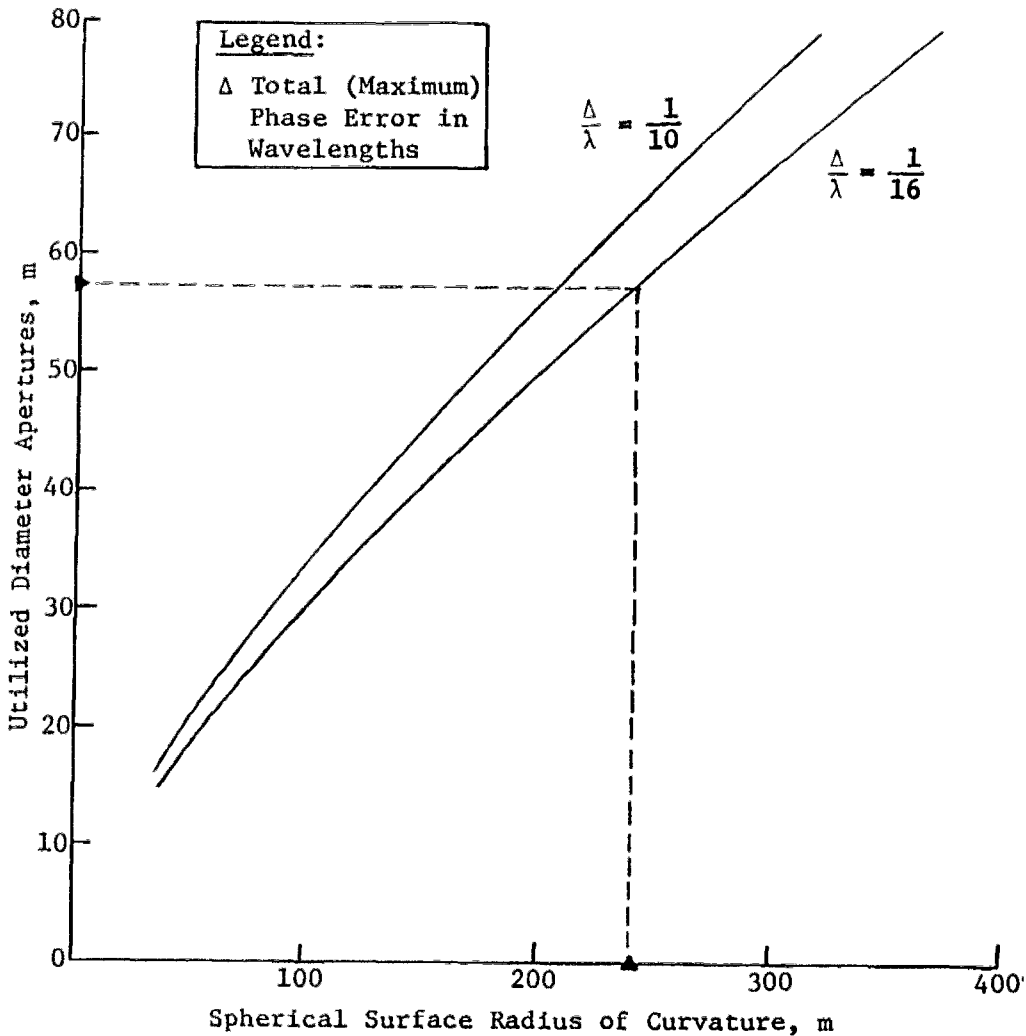
Figure 3-2
Phase Errors As a Function of Aperture Diameter and Spherical Surface of Curvature

[*]J. Ashmead and A. B. Pippard: "The Use of Spherical Reflectors As Microwave Scanning Aerials," J. Inst Elec Eng, Vol. 93, Part III-A, 1946, p. 627-632.

[+]T. Li: "A Study of Spherical Reflectors As Wide-Angle Scanning Antennas," IRE Trans Antenna Propag, Vol. AP-7, July 1959, p. 223-226.

Spatial resolution requirements dictate use of 50- to 60-m apertures at the lower operating frequencies. If good design practices (i.e., using total, not rms, phase errors on the order of $\lambda/16$) are adhered to, Figure 3-2 tells us that the main reflector's radius of curvature must be on the order of 250 to 300 m.

The size of the shuttle orbiter bay clearly influences the largest aperture possible. The largest design possible that still allowed feeds and other subsystems to be packaged was a reflector with a radius of curvature of 232 m and a reflector spot size of 58 m with a total aperture of 120 x 58 m. As shown in Figure 3-3, the feed arc is a section of a concentric circle whose radius of curvature is approximately the same as the paraxial focus of the larger reflector. Cargo bay constraints restricted the design to a single articulated feed array with a deployed length on the order of 30 m.
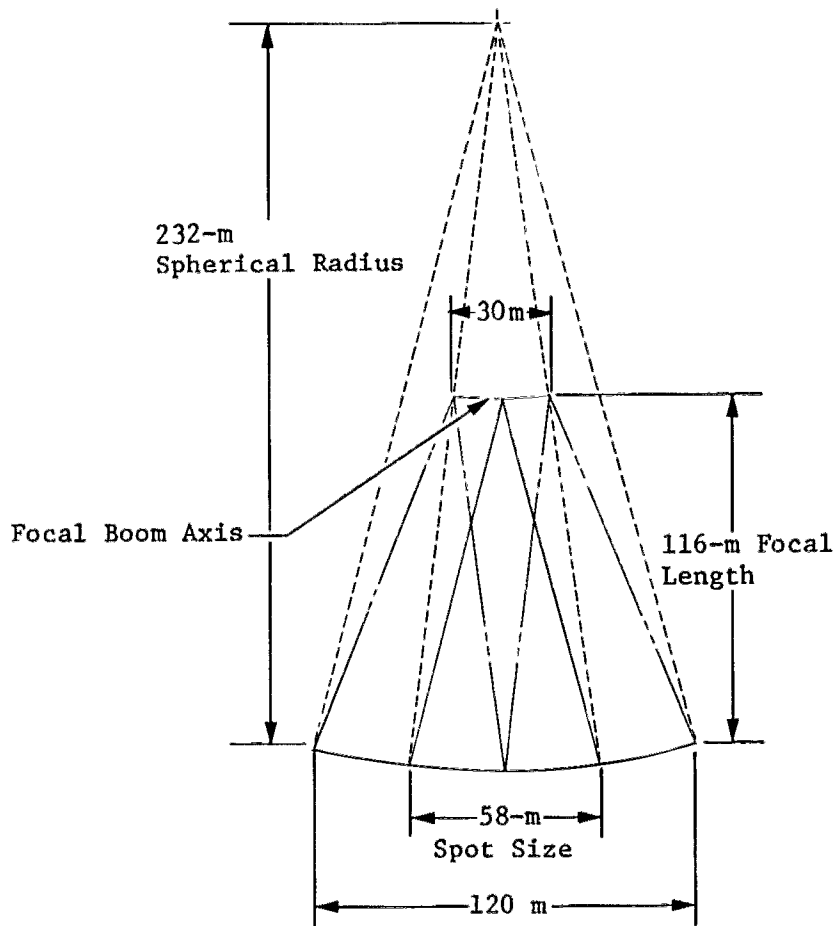
Figure 3-3   Antenna Geometry

The length of the main reflector is determined by the feed array length and the reflector's radius of curvature. Feeds at the edge of the array need to illuminate a full 58-m spot. As shown in Figure 3-3, the resultant reflector length is 120 m.

33

The final reflector design shown in Figure 3-1 has a dual curved sur-
face. It is spherical in the long dimension and parabolic in the other.
The parabolic surface is intended to reduce phase errors compared to a
purely spherical reflector in the radius of curvature of 232 m. The
focal length of the parabola is 116.1 m, the same as the paraxial
focus, giving each beam an f/D of 2.

3.2 CONCEPTUAL DESIGN

Selection of the EOS structural configuration involved the evaluation
of several structural systems compatible with the mission parameters,
with sensor payloads and STS orbiter packaging as constraints. To sat-
isfy this objective, six structural approaches were evaluated: (1) box
truss ring, (2) box truss oval, (3) wrap radial rib, (4) hoop/column,
(5) tetrahedral truss, and (6) box truss.

Early in the program, two requirements were placed on the structural
system:

1)   Use an offset-fed antenna configuration to eliminate blockage
     effects;

2)   The antenna configuration will be a pushbroom type with a line feed.

Both of these constraints/requirements became obvious based on the
sidelobe level requirements of a radiometer and the desire to achieve
maximum ground/ocean coverage with the required resolutions. In addi-
tion to the above two requirements, a third (attachment of added sen-
sors and subsystems) was a driver in selection of the spacecraft struc-
tural design.

The seven configurations evolved from existing structural concepts
(Fig. 3-4) were modified, when possible, to satisfy the offset feed and
pushbroom line feed requirements. One new configuration (Fig. 3-5) was
developed combining some advantages of existing concepts. Table 3-2
summarizes the results of the tradeoff study. The first three consid-
erations in Table 3-2--offset feed, pushbroom line feed, and 50-m or
greater diameter--were mandatory design requirements. The Figure
3-4(a) design was eliminated because it was a center-fed system. The
Figure 3-4(b) and (e) designs were eliminated because of their smaller
apertures (~ 25 m). The Figure 3-4(f) design was eliminated because it
could not satisfy the pushbroom line feed requirement.

This left four structural configurations for further evaluation. These
systems were compared on the basis of relative dynamic stability,
structural complexity, structural mass, achievable surface precision,
and sensor attachment compatibility. As can be seen in Table 3-2, the
structural masses of the four systems were not sufficiently different
so this parameter was not a driver in concept selection. The contin-
uous box truss antenna with an offset-fed mast was selected as the best
structural configuration for this study. This configuration offers ex-
cellent dynamic stability characteristics and provides abundant attach-
ment points for subsystems and additional instruments while maintaining
packaging efficiencies and low mass.
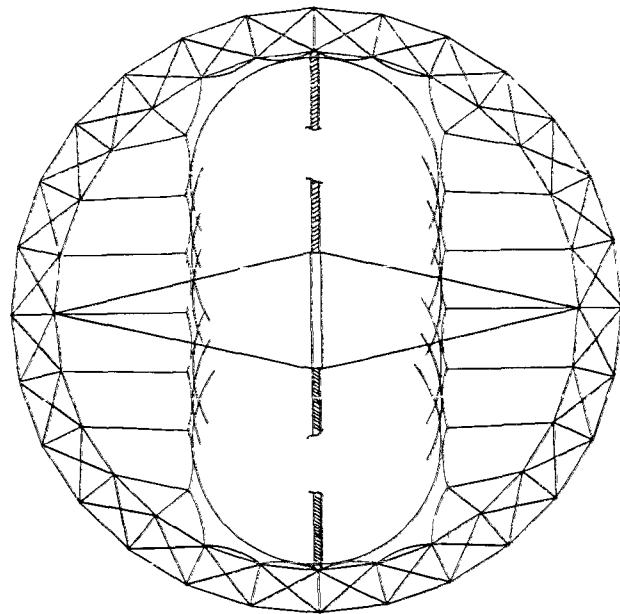
(a) Center-Fed, 50-m Subapertures, Reflector
Restricted to Active Area Only
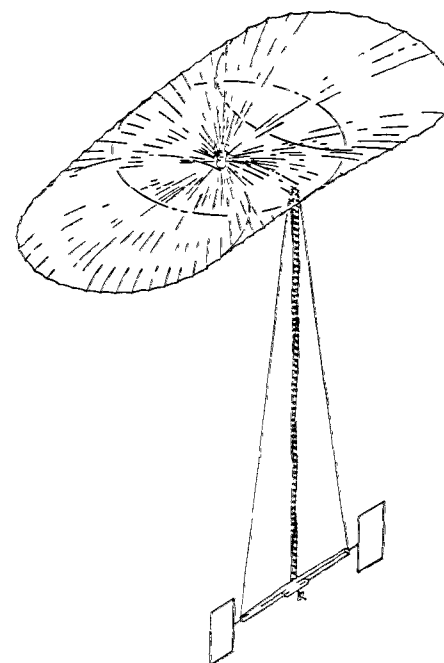
(d) Wrapped Radial Rib, Single Row
of Offset-Fed 25- to 50-m
Subapertures
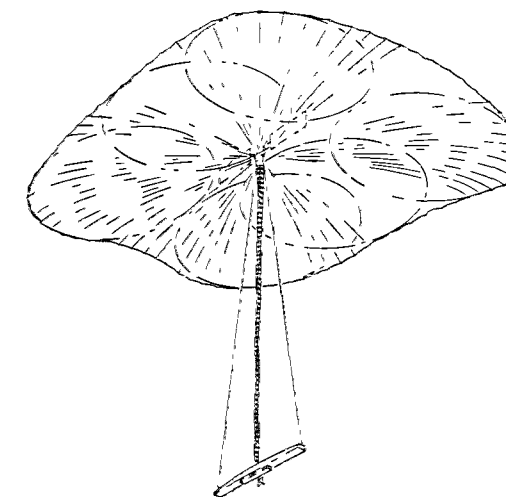
(e) Wrapped Radial Rib, Two Rows of
Offset-Fed 25-m Subapertures
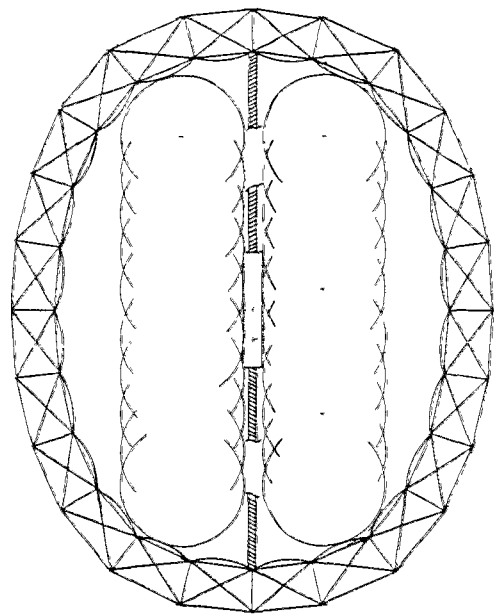
(b) Oval Hoop, Two Rows of Offset-
Fed 25-m Subapertures
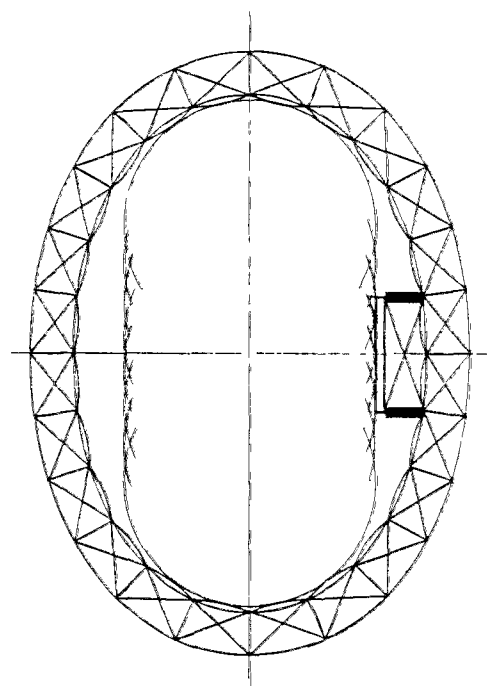
(c) Oval Hoop, Single Row of Offset-
Fed 50-m Subapertures
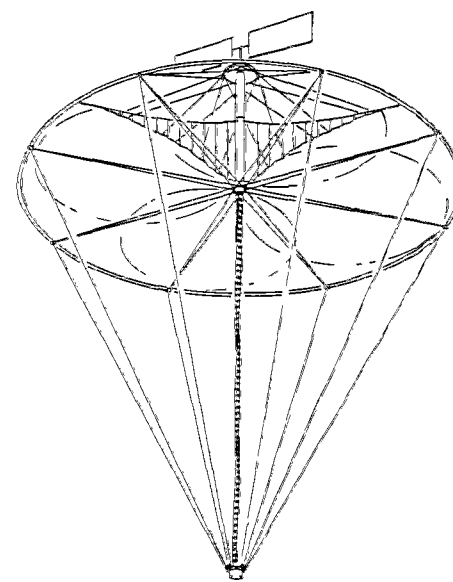
(f) Hoop/Column, Offset-Fed
50 to 100-m Subapertures
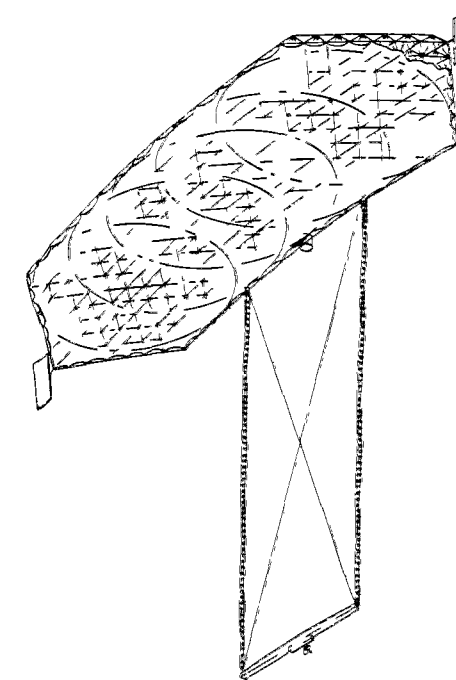
(g) Tetrahedral Truss, Single Row of
Offset-Fed 25- to 50-m Subapertures

Figure 3-4 Potential EOS Configurations
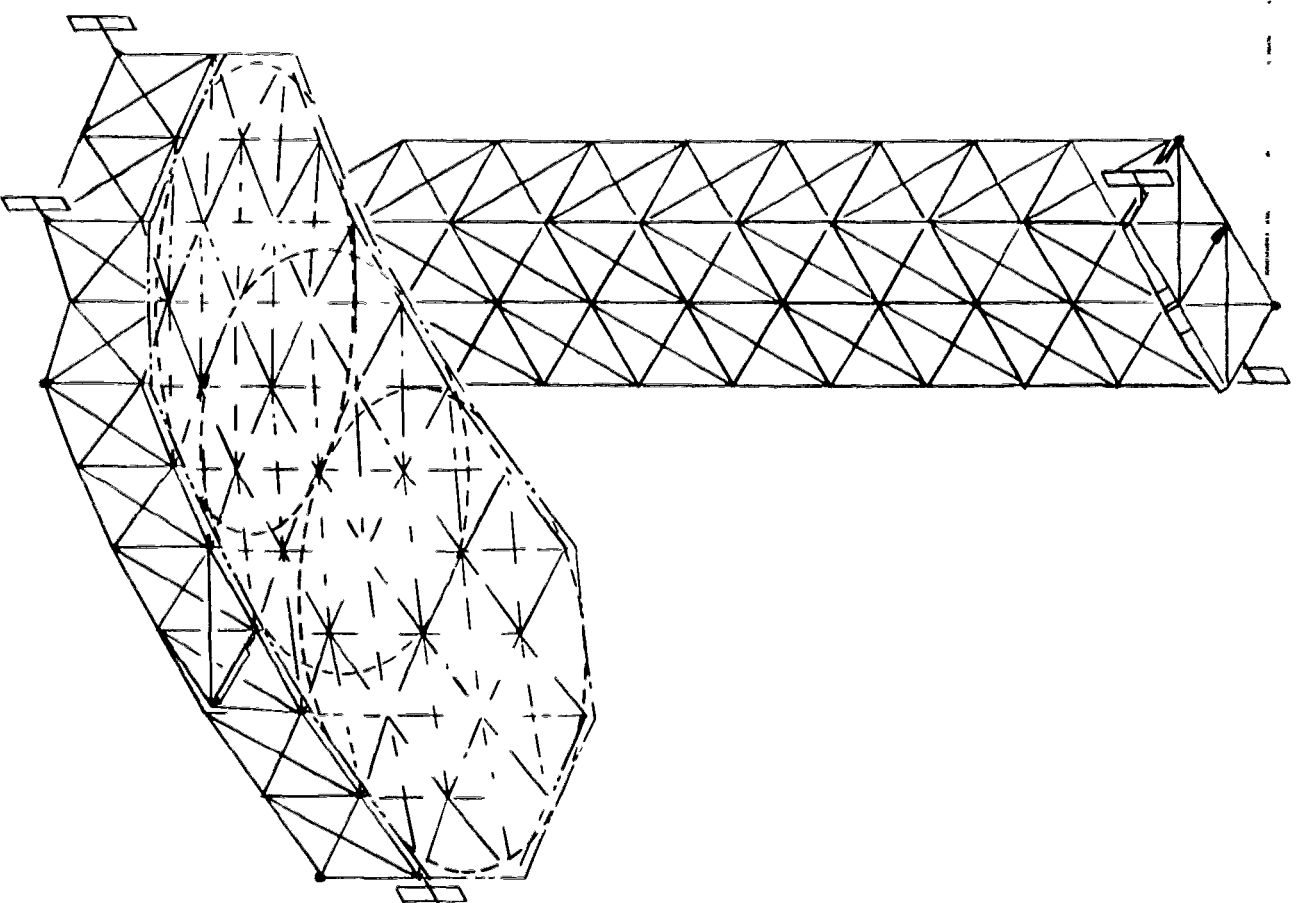
Figure 3-5 Box Truss Offset-Fed Antenna

Table 3-2 Structural Configuration Comparison

	Mandatory Requirement			Selection Criteria for Final Candidates				
	Offset Feed	Pushbroom Line Feed	50-m Dia Structural	Relative Dynamic Stability (10 - best)	Structural Complexity	Structural Mass, kg	Surface Precision, mm	Comments
Box Truss Ring Center-Fed Large Aperture [Fig. 3-4(a)]	No	Yes	Yes	--	--	--	--	Design cannot be readily modified to an offset reflector
Box Truss Oval Smaller Offset Aperture [Fig 3-4(b)]	Yes	Yes	No	--	--	--	--	In an offset reflector configuration, does not produce the required resolution
Box Truss Oval Offset-Fed Large Aperture [Fig 3-4(c)]	Yes	Yes	Yes	4	Reflector— Medium Mast— Medium	2400	5 to 7	Low surface accuracy and relatively low dynamic stability are the drawbacks of this system
Wrap Radial Rib Offset-Fed Large Aperture [Fig. 3-4(d)]	Yes	Yes	Yes	1	Reflector— Low Mast—High	2300	6 to 8	Design is lowest mass and has low reflector complexity However, dynamic stability and surface accuracy are low
Wrap Radial Rib Offset-Fed Small Aperture [Fig 3-4(e)]	Yes	Yes	No	--	--	--	--	Smaller apertures do not produce the desired resolution
Hoop/Column Offset-Fed Large Aperture [Fig. 3-4(f)]	Yes	No	Yes	--	--	--	--	Hoop/column design is not compatible with both offset-fed and pushbroom line feed requirements.
Tetrahedral Offset-Fed Large Aperture [Fig 3-4(g)]	Yes	Yes	Yes	8	Reflector— Medium Mast—High	2600	3 to 4	Good surface accuracy, dynamic stability, and multiple attachment points.
Box Truss Offset-Fed Large Aperture [Fig 3-5)	Yes	Yes	Yes	10	Reflector— Medium Mast— Medium	2500	3 to 4	Good surface accuracy, dynamic stability, and multiple sensor attachment points.

3.2.1 Box Truss Oval Hoop

The box truss oval offset-fed antenna [Fig. 3-4(c)] was a derivative of the center-fed antenna [Fig. 3-4(a)] that was developed as a part of the NAS1-16447 studies concerning advanced space system analyses. The oval structure reduced the unused aperture with respect to the ring structure, and also reduced the length of the surface support cords between the structure and the surface. When compared to the selected box truss offset-fed configuration, its disadvantages are:

1) Low dynamic stability caused by the root stiffness of the feed mast. This is because when the central boxes of the contiguous truss are removed (Fig. 3-6), the reflector structure behaves as a torsion bar;

2) Surface accuracy is degraded because of the long distance between the attachment points of the surface to the structure.
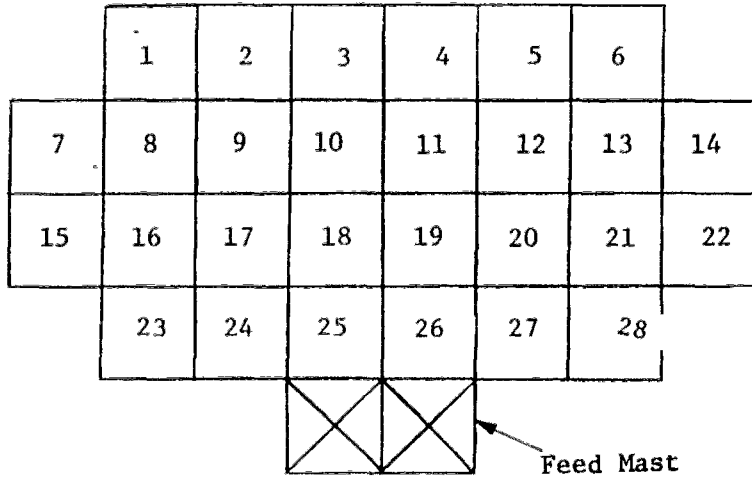
(a) *Contiguous Box Truss Reflector*
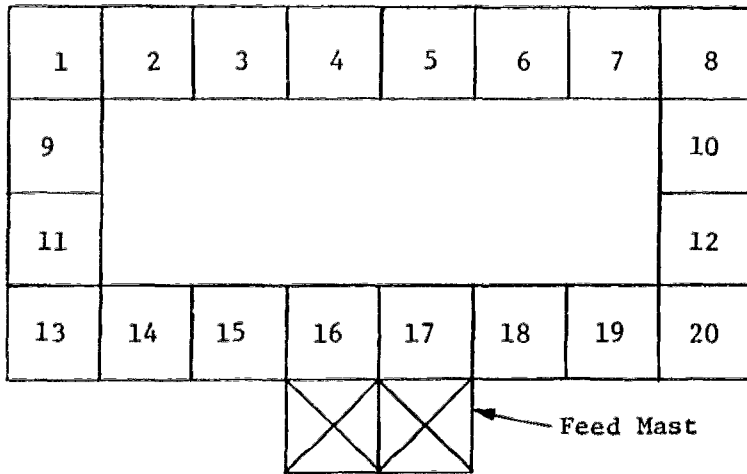
(b) *Box Truss Oval Hoop*

*Figure 3-6
Comparison of Contiguous Box Truss and Box
Truss Oval Hoop*

The primary advantage of the box truss oval is the low piece parts.
However, this was not a dramatic advantage for this design. The con-
tiguous box truss has 28 boxes in the reflector and 16 boxes in the
feed mast structure. The box truss ring has 20 boxes in the reflector
(Fig. 3-6) and 16 boxes in the feed mast. The net reduction in piece
parts was 1 vertical member, 8 sets of surface tubes, 8 sets of in-
terior diagonals, and 8 sets of exterior diagonals. The percentage of
piece parts reduction from the contiguous truss was less than 10%.

3.2.2 Wrap Radial Rib

The primary advantage of the wrap radial rib concept is its relatively simple reflector surface and lower weight. However, its surface accuracy and dynamic stability are the poorest of all the concepts. The stiffness of the dogleg feed mast is very low. Estimates showed greater than 20 times lower fundamental frequency relative to the box truss offset-fed system. The wrap radial rib system was projected to have a 6- to 8-mm rms surface accuracy, which was twice that projected for the box truss system. This system also has limited attachment points for the subsystems and sensors.

3.2.3 Tetrahedral Truss

The tetrahedral truss was very similar in performance to the selected box truss design. It was relatively stiff, had equivalent surface accuracy, similar masses, and multiple attachment points. The reasons for selection of the box truss design over the tetraheral truss were the former's orthogonal-sequential deployment and integrated offset feed mast.

3.2.4 Box Truss

The box truss concept was selected based on its high dynamic stability, a 3- to 4-mm surface accuracy, multiple attachment points that could easily support the sensors and subsystems, and the fact that the integrated offset-fed mast was the most efficient stowed mast of all concepts considered. Because the mast was essentially an extension of the reflector surface, no new mast design was required. The same structure that would be qualified for the reflector would be used for the mast.

The dynamic stability (structural frequency) of the integrated offset feed mast and reflector combination was estimated to be 5 to 50 times stiffer than the other concepts. The box truss frequency was estimated to be approximately 1 Hz while the other concepts were estimated as tabulated.

Box Truss Oval Hoop	0.2 Hz
Tetrahedral Truss with Astromasts	0.2 Hz
Wrap Radial Rib with LMSC Mast	0.02 Hz

Relative stowage efficiency for the box truss was equal or superior to the other concepts. The estimated stowage efficiencies (stowed volume for reflector and feed mast) were as tabulated.

Box Truss and Integrated Feed Mast	Reflector	31 m^3
	Mast	19 m^3
Box Truss Oval Hoop	Reflector	24 m^3
	Mast	19 m^3
Tetrahedral Truss with Astromasts	Reflector	38 m^3
	Mast	20 m^3
Wrap Radial Rib with LMSC Mast	Reflector	24 m^3
	Mast	48 m^3

The 60 by 120-m earth observation spacecraft is designed using the deployable box truss structure to form the parabolic dish and feed mast. Because of the collapsible nature of the box truss configuration, the structure easily stows within the STS. The truss is parabolic in the 60 x 120-m antenna support structure, with a focal length of 116.1 m (Fig. 3-7).

The rf surface is made spherical, with a radius of 232 m, in the 120-m direction by using appropriate vertical standoff heights (above the truss's parabolic shape). The truss itself was designed to be parabolic because of the geometric restrictions imposed by an orthogonal, sequential deployment. The following section describes the truss and its component parts. This truss comprises a deployable frame consisting of two equal-length structural members ("verticals"), two structural members hinged in the middle ("surface tubes") that connect the ends of the verticals and fold inward to stow between the adjoining verticals, and telescoping diagonal braces that lie in, and control the shape of, the deployed frame (Fig. 3-8). Prototype hardware has been fabricated with all-composite tubes and fittings, and low-cost manufacturing processes are being developed for all repetitive components.

The shape of each truss frame in the reflector support structure and feed mast is controlled by the length of its diagonal tension braces. The manufactured length of each diagonal is slightly shorter than its deployed length, thus creating a pretension in each diagonal brace when the box truss is fully deployed. The pretension load levels prevent diagonal slack under any combination of thermal and dynamic load levels. (This is discussed further in Section 6.4.)

A key feature of the truss is the hinge and latch in the middle of each folding surface tube. All moving parts in the hinge and latch are contained in the tube's interior. This eliminates protuberances that could interfere with the diagonal braces or an antenna surface during deployment. Redundant coil springs in the hinge are sized to produce the desired deployment rate. The spring-driven overcenter latch starts increasing its mechanical advantage significantly when the deploying tube is approximately 10 deg from full deployment (Fig. 3-9). The latch spring is sized to meet diagonal brace and antenna surface tensioning requirements. A redundant mechanical latch functions in parallel with the overcenter latch.

The structure is deployed in a controlled sequence of steps. The feed mast is deployed one pair of cubes at a time and the reflector support structure is deployed one row of cubes at a time. In the latter case, the steps are accomplished in a preselected sequence in the two orthogonal deployment directions. Section 5.2 includes a further discussion of deployment.

Spacecraft
Management
and Control
Module

ASR Array
Panels

Feed Boom

Pulsed
Plasma
Thruster
Two Places

Battery
Pack – Two
Places

Solar Array
(Rotated 45 deg)
Two Places

Pulsed Plasma
Thruster –
Two Places

View A (Rotated 90 deg)

Feed Boom

Rf Reflectivity Mesh

SAR

Astromast

Stabilizing
Cord – Two
Places

Solar Array – Six Places

SAR Mount
Located on
Center Vertical

Rf Reflective
Mesh

Battery Pack
Four Places

Solar
Array
Four Places

60 m
(120-m Long)

Hydrazine
Thruster
System –
Four Places

Ku-Band
Antenna –
Two Places

Pulsed
Plasma
Thruster –
Four Places

116-m Focal
Length

15 m

Pulsed
Plasma
Thruster

Feed Boom

Solar
Array

Battery
Pack

Pulsed
Plasma
Thruster

119 m
Deployed EOS Structure

15 m

Figure 3-7 EOS Structural System

41

Truss

Cube

Exterior
Diagonal

Mesh
Support
Posts

Frame

Surface
Tube

Stowage

Vertical
Member

Diagonal
Tape

Midlink Hinge
End Fitting
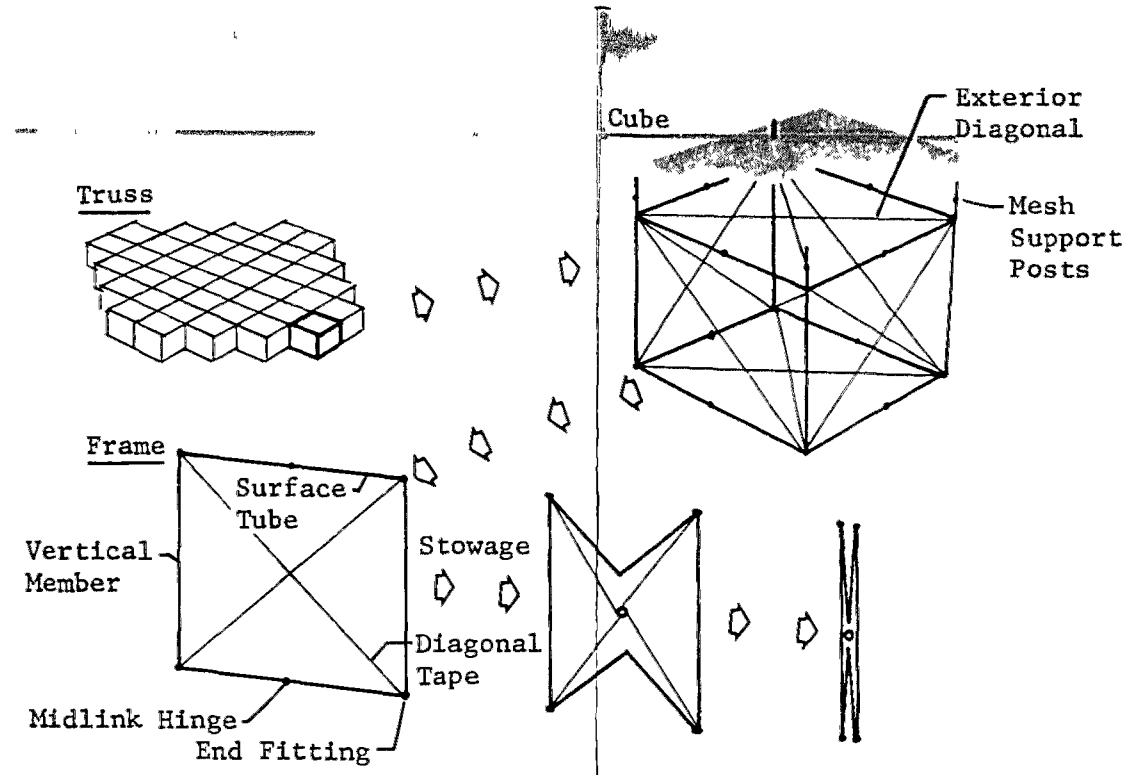
Figure 3-8   Deployable Box Truss Structure

Surface
Tube
Halves

$\frac{\theta}{2}$

θ

Mechanical Advantage of Overcenter Latch

14:1

12:1

10:1

8:1

6:1

4:1

2:1

Deployment

30   26   22   18   14   10   6   2   0

θ, deg
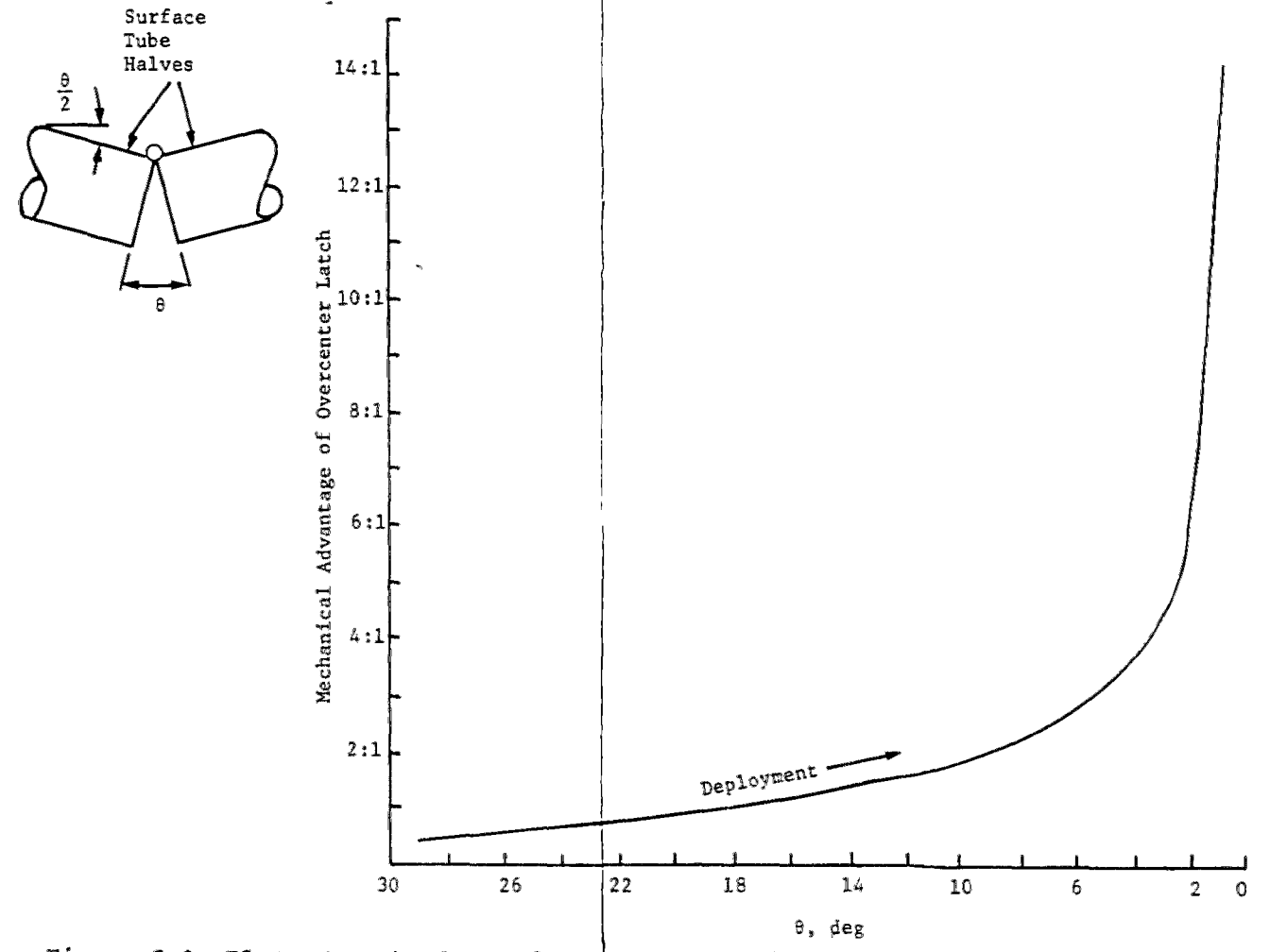
Figure 3-9   Plot of Mechanical Advantages vs Deployment Position

42

The 4-bay by 8-bay antenna support structure has an extremely high stiffness-to-weight ratio. The structure is made thermally stable by using low coefficient of thermal expansion (CTE) graphite/epoxy composite layups. The dynamic stability created by integration of the feed mast and antenna support structure is the basis for the high 1.08-Hz fundamental frequency of this structure. The key feature of this unique design is that the feed support mast is an extension of the reflector truss structure rather than an added appendage. This design features efficient stowage, simple integration with the reflector structure, excellent thermal stability, light weight, and very high stiffness and dynamic stability. These features are directly attributable to the efficiency and features of a deep truss structure. Previous offset-fed masts were appendages added to the reflector structure and had less efficient packaging, more difficult integration, and substantially lower dynamic stability. Because of the high strength and stiffness of the selected design, the mast can easily accommodate more complicated and massive advance feeds (e.g., line feeds, array feeds, and multifrequency multibeam feeds).

3.3.1 Member Properties

Table 3-3 lists the section and material properties of the box truss structural members. The locations in the structure for the different member types are shown in Figure 3-10. At all member locations, member properties were optimized to achieve maximum overall dynamic performance at minimum weight (see Section 6.0). This produces minimum members at the periphery of the structure and high-stiffness members near the feed mast/reflector interface. The graphite/epoxy layups and cross-section dimensions for the members are contained in Appendix A. As can be seen in Table 3-3, because many different member types exist, only a general description of each major class will be provided. All surface and vertical members were designed with a factor of safety of 1.25, and a 0.9 knockdown factor for nonstraightness of members (manufacturing and thermal). Each member was designed based on the most demanding of the following:

1) Deployed stiffness of the antenna system;

2) Strength;

3) Individual member fundamental frequency (hinged-hinged) of 1 Hz.

Table 3-3 Section and Material Properties

Member Type	Section Type No.	Material Type No.	Area, cm^2	IY, cm^4	IZ, cm^4	Torsional Constant, cm^4
Surface						
— 8.33-cm Dia	1	1	1.72	14.7	14.7	29.3
— 8.33-cm Dia	51	51	3.27	27.6	27.6	55.1
— 5.9x5.9-cm^2	59	59	3.27	18.1	18.1	36.2
Verticals						
— 5.08x4.23-cm Rectangular	60	60	6.64	17.3	23.3	40.6
— 2.54x2.54-cm Square w/5.08-cm Fins	2	2	3.81	27.5	27.5	55.1
Channel						
— 6.05x7.35 cm	53	53	13.53	112.1	48.8	2.57
— 7.62x5.66 cm	54	54	4.24	22.3	25.3	0.026
Feed Mast Brace						
— 5.08x5.08-cm Square	58	58	5.34	20.6	20.6	30.8
Diagonals						
— 0.66-cm Dia	5	11	0.348	—	—	—
— 0.81-cm Dia	6	11	0.52	—	—	—

Note: All properties are in member coordinate system.

Material Type	E_L, N/m^2 10^{12}	E_T, N/m^2 10^{12}	G_{LT}, N/m^2 10^{12}	V_{LT}	Density, kg/cm^3	CTE, $m/m/°C$ 10^{-6}
1	0.166	0.0291	0.0131	0.193	0.0087	-0.252
2	0.182	0.0219	0.0143	0.35	0.0087	-0.522
11	0.234	—	—	—	0.0087	-0.4
51	0.188	0.0251	0.0105	0.154	0.0087	-0.335
53	0.187	0.0242	0.0155	0.198	0.0087	-0.378
54	0.189	0.023	0.0117	0.225	0.0087	-0.414
58	0.196	0.0237	0.0096	0.136	0.0087	-0.36
59	0.187	0.024	0.012	0.198	0.0087	-0.5
60	0.196	0.0237	0.0096	0.136	0.0087	-0.36

3.3.2 Cube Corner Fitting

The EOS cube corner fittings (Fig. 3-11 and 3-12) form the structural ties between the vertical members, surface tubes, and diagonal braces. As many as 13 members may be connected to a cube corner fitting. The cube corner fitting is made of 1.25-cm chopped graphite-fiber compression-molded in an epoxy matrix to give rigidity and thermal stability. An early prototype graphite/epoxy cube corner fitting is shown in Figure 3-13. Because the cube corner fitting is a repetitive identical part, the part can be molded at low cost. Pin locations are drilled depending on the location of the cube corner fitting in the structure. Since some pin locations in some corner fittings require less depth, excess material will be trimmed from fittings to save weight. To save additional weight in edge areas of the antenna structure where only partial fittings are needed, the cube corner fitting is trimmed to the needed size. The shear pins are provided to handle shearing loads during the launch.

44
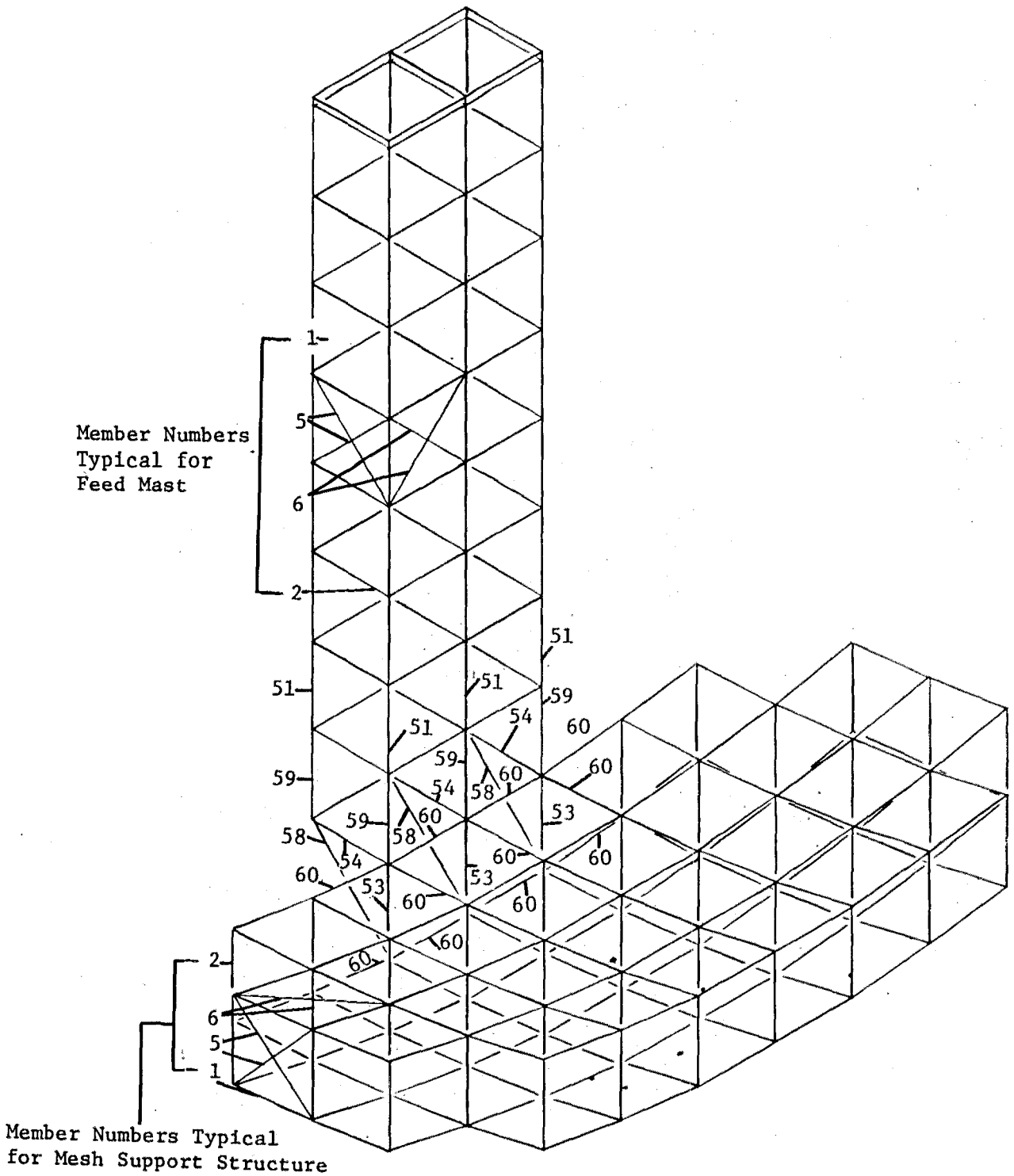
Member Numbers
Typical for
Feed Mast

Member Numbers Typical
for Mesh Support Structure

Figure 3-10   EOS Section Types
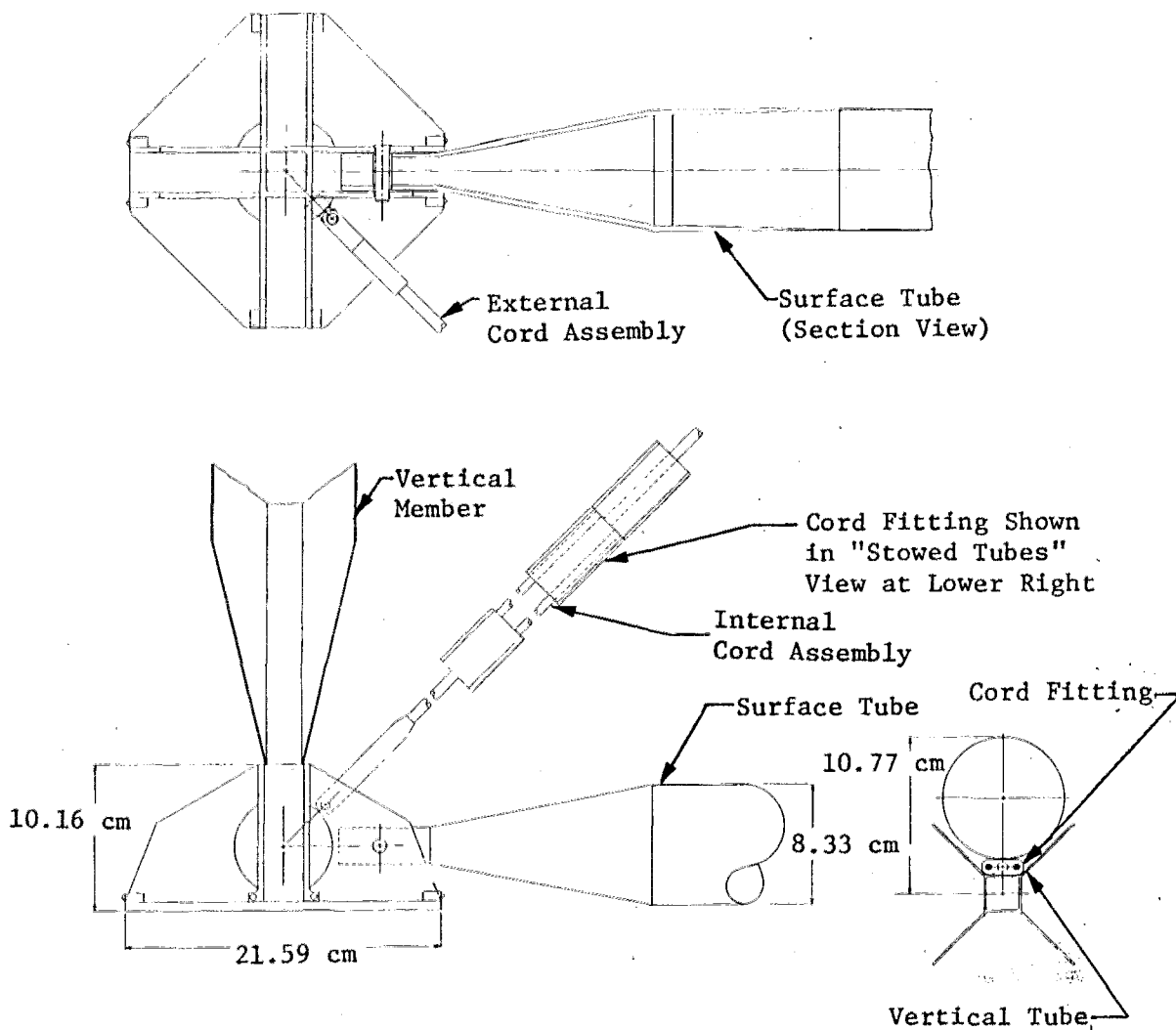
Figure 3-11 Lines of Forces Through Cube-Corner Fitting

The parabolic box truss design is an accurate truss, i.e., with all force lines of action passing through a coincident point. This design feature is shown in Figure 3-14. The cube corner fitting attachment point for the surface tube is positioned so the surface tube line of action goes through a coincident point with all the other surface tubes and diagonal members of that particular cube corner fitting. The line of action of the diagonals is through a coincident point with the line of action of the vertical and surface tubes. This is accomplished with a spherical surface molded into each cube corner fitting.

If the attachment points are not positioned as described to eliminate end moments on the vertical members, the fundamental mode frequency of the entire structure will be dramatically reduced. Along with positioning surface tube attachments, specific surface member lengths must be kept identical in any row or column of the structure to ensure that the structure remains orthogonal during sequential deployment in either direction.

Interior
Diagonal
Interface

Vertical
Member
Interface

Surface
Tube
Interface

Stowage
Shear
Tie

Exterior
Diagonal

Stowage
Shear
Tie
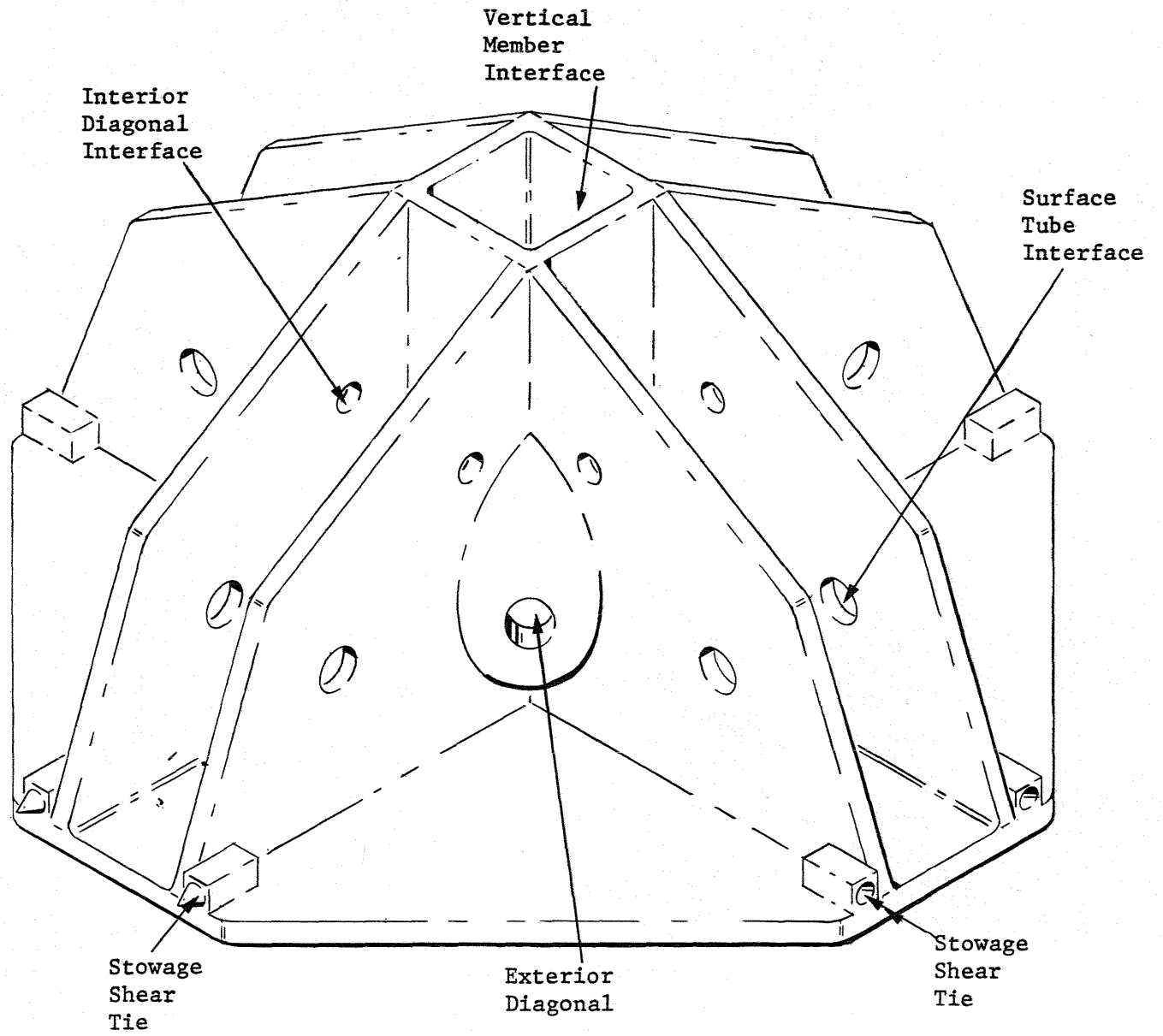
Figure 3-12   EOS Truss Corner Fitting
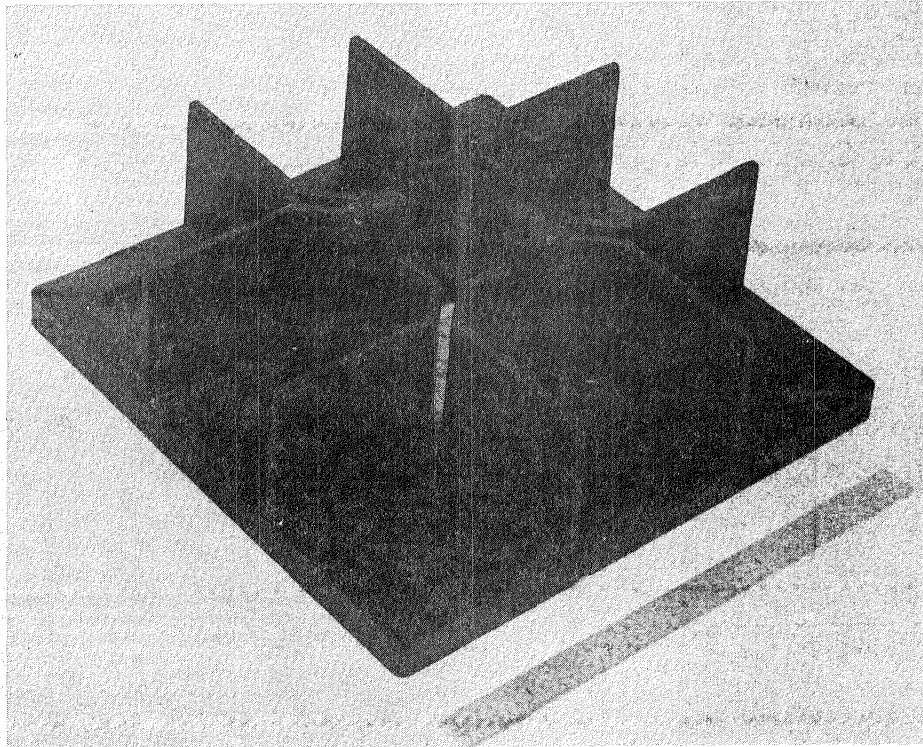
Figure 3-13   Prototype Cube Corner

Vertical Member

Note:

All force vectors (lines of action) intersect at a single point of action. This eliminates end moments on the vertical members, thus increasing the structure's overall natural frequency.

Diagonal Force Vector

Surface Tube Force Vector

Single Point of Action
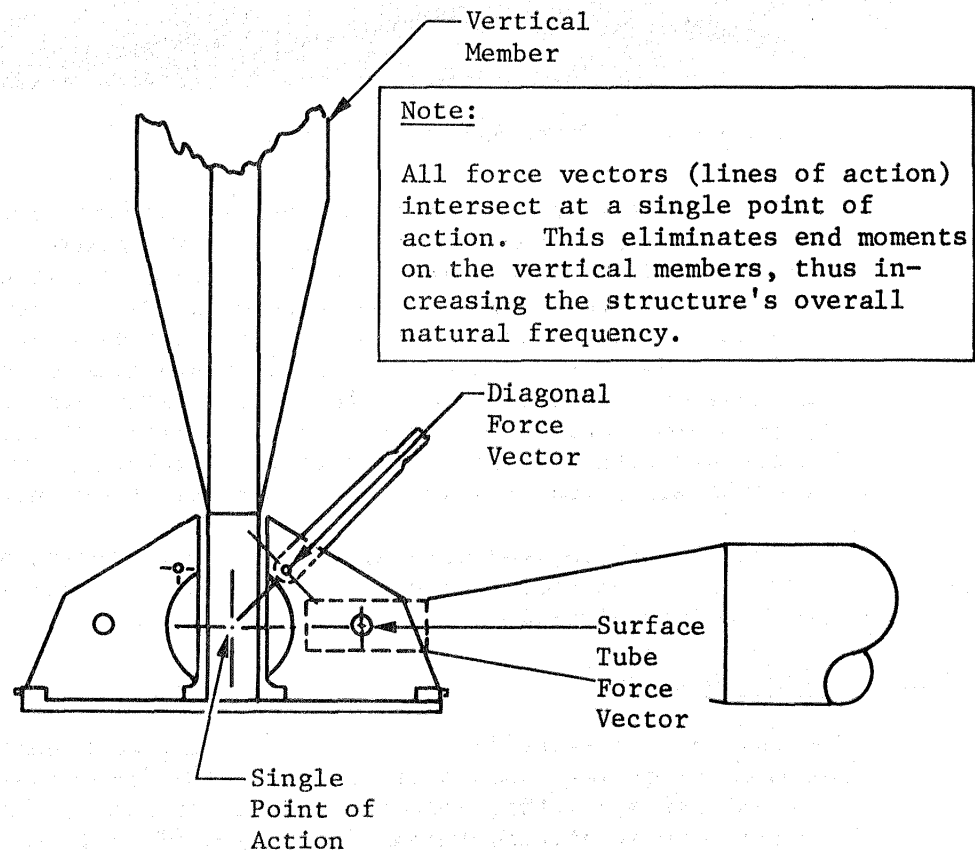
Figure 3-14   Lines of Force Through Cube-Corner Fitting

3.3.3 Vertical Members

These structural members are called "verticals" because they span from top to bottom in the box truss bays. A similar member is shown in Figure 3-15.

Figure 3-15 Graphite/Epoxy Vertical Member

The EOS members are a 2.54-cm square with 5.08-cm fins at 45 deg to the square. The fin member design was selected to maximize the packaging efficiency of the truss while maintaining the required stiffness and strength characteristics of the verticals. The members are 0.121-cm thick and are Type 2 in Table 3-3. They are made of a graphite/epoxy laminate. Most verticals are closed sections, with the exception of the feed support structure at the antenna/structure interface where channels are used. The vertical members are bonded in the cube corner fitting and extend through the fitting on the top surface to create 2-m standoffs above the box truss structure for the mesh tie system.

The lengths of the standoffs are varied to arrive at a 116.1-m focal length in the parabolic direction and a 234.8-m radius of curvature in the spherical direction.

3.3.4 Surface Members

The surface tubes lie in the top and bottom surfaces of the antenna support structure. Tube diameters are 8.33 cm and vary in wall thickness according to their location in the structure. Most of the surface members have a wall thickness of 0.066 cm (Type 1 in Table 3-3). The wall thickness is increased in the area of interface between the feed mast and the antenna support structure. The tube diameter decreases in the area where it interfaces with the corner fitting (Fig. 3-11). This

49

is done to reduce the size of the cube corner fitting. A constant material cross-sectional area is maintained in this taper to maintain axial stiffness. The surface tubes contain a graphite/epoxy hinge and deployment mechanism located at midspan that allows them to fold for stowage. The length of each surface tube is approximately 15 m, but varies slightly depending on its location in the structure.

3.3.5 Interior Diagonal Members

The interior diagonals span the interior faces of the box truss bays. These tension members are a two-part design made of rods and slides as shown in Figure 3-16. This unique construction scheme is used to permit the member to telescope for stowage.

Rod/Cord
Fitting (C)   Cord   Rod
Graphite Rods   Fitting (B)   Fitting (A)
Graphite   Graphite
Cord   Cord

(Assembly Shown Deployed)
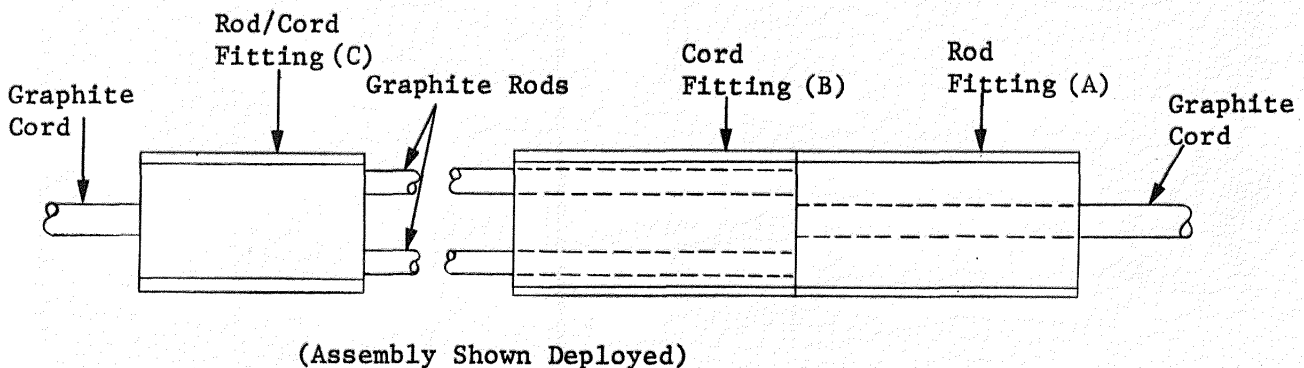
Figure 3-16   Telescoping Interior Diagonal Member

A rod assembly consists of two parallel rods bonded on one end to a rod fitting (A) and on the other end to a rod/cord fitting (C). A graphite cord that runs back to the cube corner fitting is also bonded to the rod/cord fitting (C).

A cord is composed of individual graphite/epoxy strands. The cord strands are individually pretensioned and then bonded into a sleeve fitting. This tensioning process guarantees equal load distribution among the cord strands and should not be confused with the box tensioning process discussed in the next paragraph. The cord strands are then encased with shrink tubing. The shrink tubing protects the cord strands from damage during handling and stowage. The graphite cord bonded to cord fitting (B) is locally stiffened with wraps of fiberglass cloth tape for a length that is slightly greater than that required for telescoping. This provides a good sliding fit for deployment. Shrink tubing is not used over this length but does cover the rest of the cord.

The interior diagonals are pretensioned from 80 to 150 N in the deployed configuration (depending on location within the structure). The pretension level is selected to maintain tension in all diagonals under the combined effects of thermal distortions, manufacturing errors, and operational dynamic loads. The lengths of the interior diagonals set

the deployed box truss to a parabolic shape in space. During its manu-
facture, the box truss is first assembled without the diagonals. Next,
the truss is deployed and positioned to the desired shape and the diag-
onals are installed and tensioned. The diagonals are then bonded while
under tension. This procedure minimizes manufacturing tolerance buildup
and ensures proper tension levels.

The unique abilities of this cord design to bend, twist, and telescope
facilitate stowage as depicted in Figure 3-17(a). The rod and slide
assembly (fittings A, B, and C) is twisted 90 deg to minimize stowage
volume, and nests between a stowed surface tube and a vertical tube.
The vertical tube position is schematically represented as a square box
on the corner fitting. The cord then bends around the stowed surface
tubes and runs up to the opposite corner fitting. Only one telescoping
section per cord is required.

For deployment as shown in Figure 3-17(b), fitting B slides along the
rods to butt against fitting A. The cord has now rotated 90 deg back
to its equilibrium position to provide maximum surface area in the
plane of the box truss. This position optimizes heat transfer within
the cord assembly while minimizing shadowing effects.
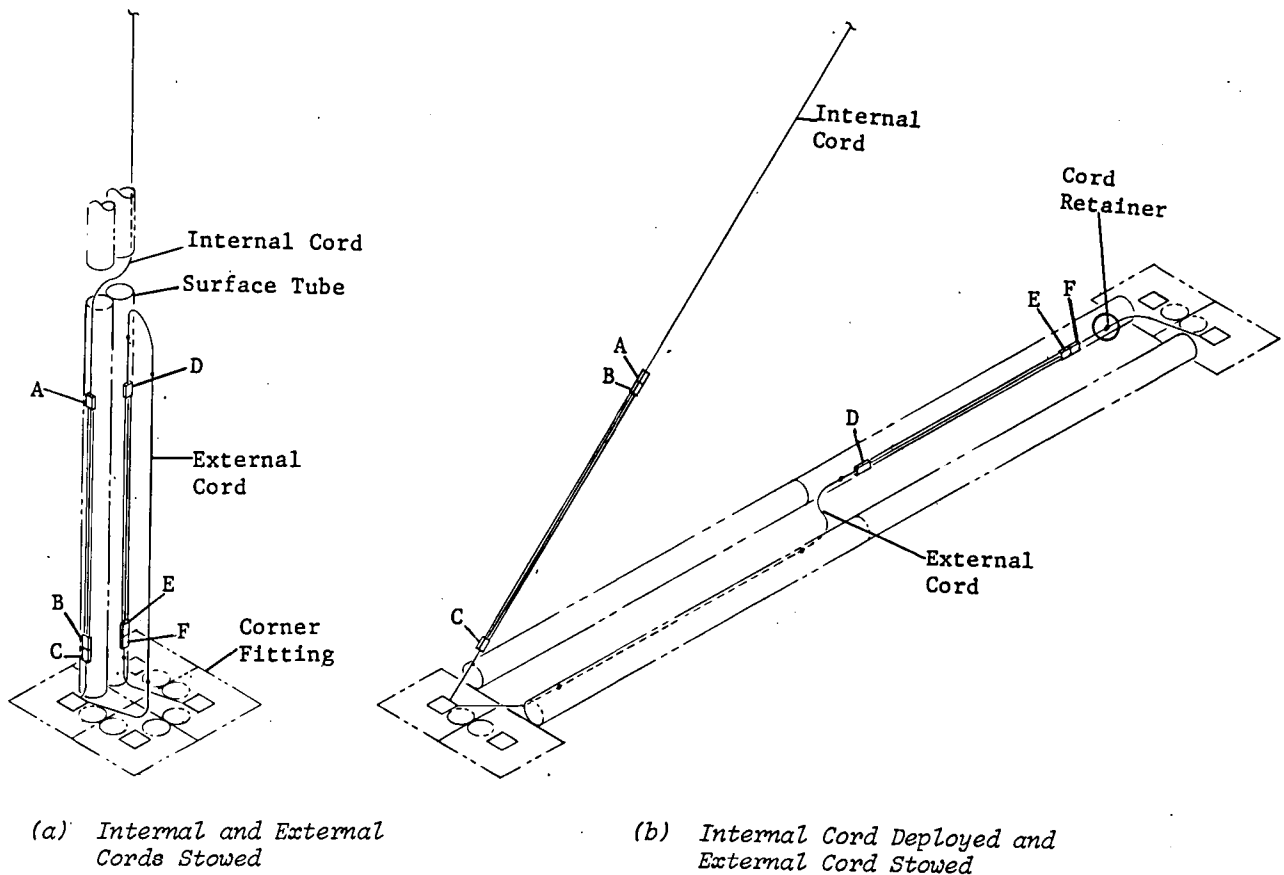
(a) Internal and External   (b) Internal Cord Deployed and
    Cords Stowed   External Cord Stowed

Figure 3-17 Stowage of Diagonal Members

3.3.6 Exterior Diagonal Members

The exterior diagonal members lie in the surface faces of the box truss bays. These members must deploy in both directions and yet be fabricated of a very high modulus of elasticity material. The basic exterior diagonal is a rod and cord configuration similar to the interior diagonals. These members are installed and pretensioned in a manner similar to that of the interior diagonal members. The exterior diagonals have 1 1/2 times more cross-sectional area than the interior diagonals to provide greater stiffness in the plane of the surface tubes.

The exterior diagonals stow in a manner similar to the internal diagonals [Fig. 3-17(a)]. During stowage the exterior diagonal cord runs across the corner fitting, up the side of one surface tube, then bends to run down the opposite side along a surface tube and across to its respective corner fitting. Cord retainers on the surface tubes hold the cord assembly in place until deployment.

The external cord deployment is a two-step sequence, whereas the internal cord requires only a single step. At the first step of deployment, one row of frames have deployed but the external cords are still stowed. Notice that the positions of fittings D, E, and F in views (a) and (b) along the surface tubes have not changed during the first stage of deployment. The circles on the corner fittings in view (b) schematically represent surface tubes. These surface tubes deploy in the second stage of deployment. The external cords are pulled free from their cord retainers, and cord fitting E slides to butt against fitting D. These cords also rotate 90 deg to lie flat in the plane of the truss.

3.3.7 Midlink Hinge

Each surface member uses a midlink hinge that allows the surface tube to fold for stowage. The midlink hinge must meet three requirements: (1) hinge action for stowage and deployment, (2) torsion springs to supply deployment drive torques, and (3) a rigid structural link between the deployed tube halves. Figure 3-18 is a photograph of the all-graphite/epoxy (except springs and pins) midlink hinge assembly. The torsion spring driving the overcenter latch has a high mechanical advantage. This assists in overcoming static and startup resistance forces, and the completion impulse provides the force required to tension the reflector surface and truss diagonal members. The deployed structural link across the midlink hinge consists of the bearing surfaces on the hinge halves that are held in place by the hinge axis pins and the overcenter links and pins.
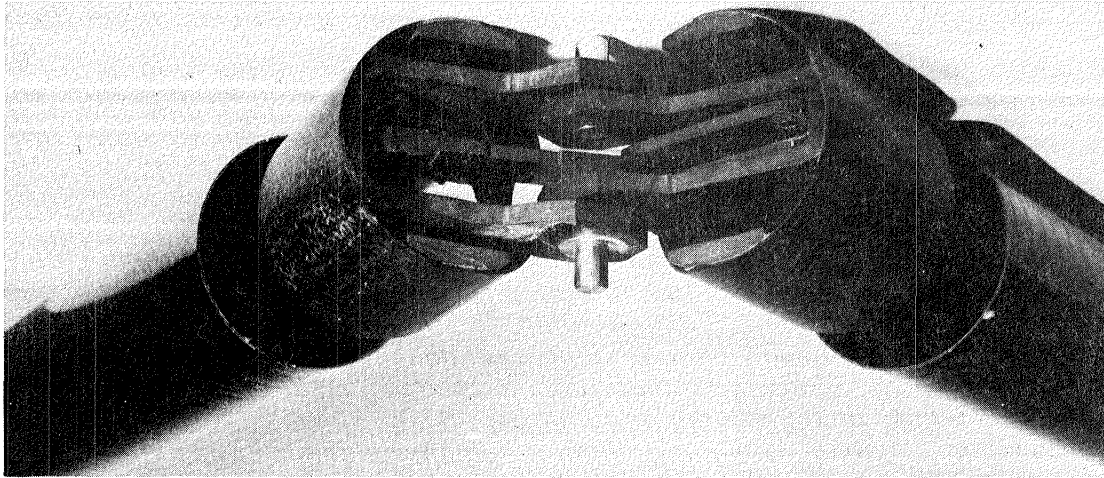
Figure 3-18 Midlink Hinge Design

3.3.8 Offset Feed Support Hinge

The connection point between the feed mast and the antenna support structure is a unique design because 15 different members' lines of force must converge through a coincident point. The fitting assembly (Fig. 3-19) is a three-dimensional joint with feed box trusses rotating out and up during deployment. The brace structural members fold up inside the interlocking vertical channels during stowage. The channels are of different thicknesses in the flanges and web so their centroidal planes intersect at deployment, maintaining a true truss configuration. The end fitting for the surface tubes in the feed mast is bonded to the back of the feed mast vertical channel. This complex fitting is fabricated from several smaller graphite/epoxy laminates that are bonded and mechanically fastened into a single, unique, hinged, cube corner fitting. The structural members in this region have an increased cross-sectional area to provide local stiffness. The increased cross-sectional areas were determined in an iterative process using the strain distribution in the structural modes obtained from the finite element dynamic computer runs. This process optimized member sizes by defining high-stiffness members in areas of high-strain energy and low-stiffness (weight) members in areas of low-strain energy.

Feed Mast

V3
T2
T1
T3
V2
T4

S2

Mesh
Reflector

T5

V1

Schematic Showing Super-
joint-Related Members
Deployed

22 cm

Overcenter
Latch

Mesh Standoff

T5

T2

T4

Stowed Superjoint

V1

S1
T1 T2
V2
S2
V3
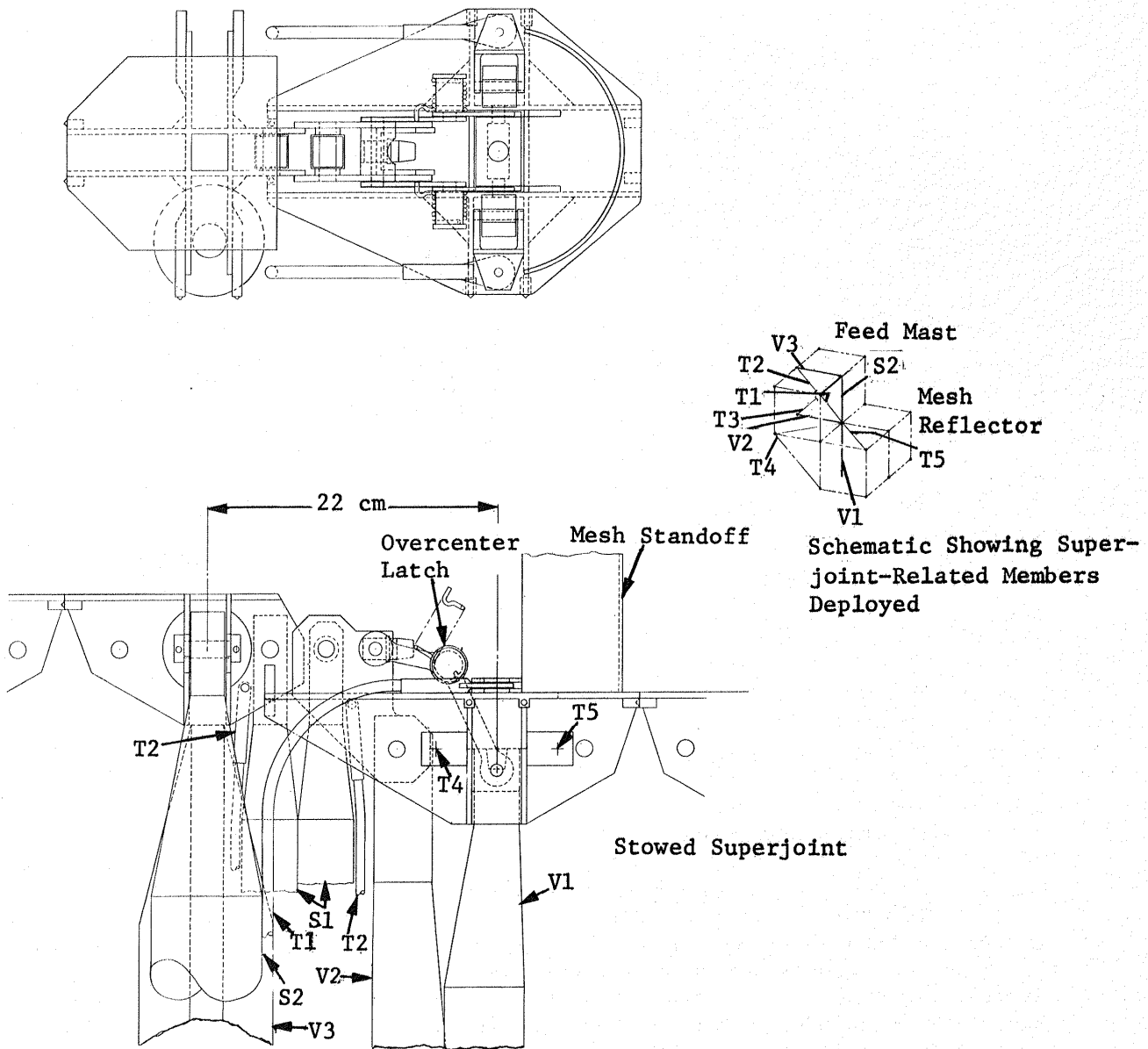
Figure 3-19   Offset Feed Support Hinge Design

3.4.   MESH TIE SYSTEM DESIGN

The mesh shaping system design proposed for the EOS radiometer is a
direct tieback cord system as shown in Figure 3-20.

Surface Cross Cords

Surface Cords

Tieback Cords

Note:

Drawing simplified for clarity.

Truss Standoff (Vertical Member Extension)
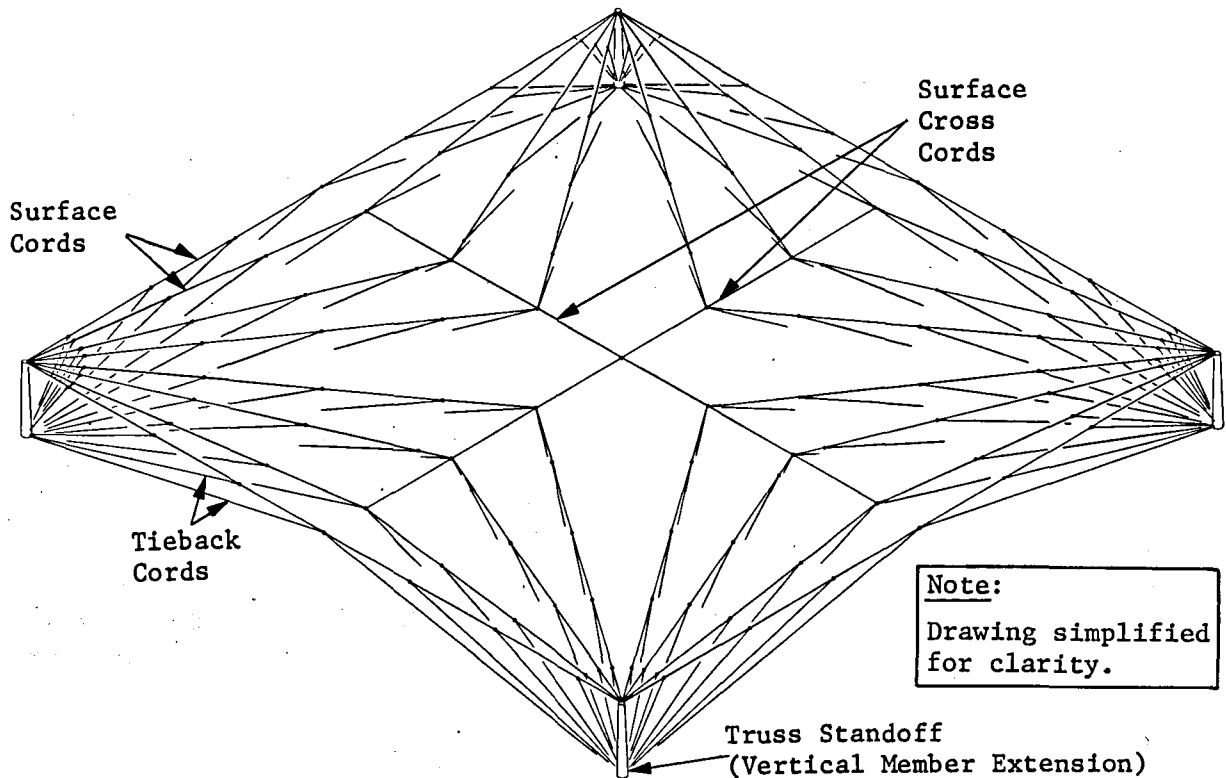
Figure 3-20   EOS Mesh Tie System

This cord system uses two types of cords—upper surface cords and tie-back cords. The upper surface cords rest on the mesh in a radial pattern from each standoff, and intersect at a surface cross cord. At incremental lengths of the surface cords, the surface cord is pulled back into shape with tiebacks that attach to the base of a truss stand-off. For each box section, the tieback spacing can be optimized for the particular box truss standoff geometry because the surface cords are independent from box to box. The total mesh surface is formed by individually tensioning mesh panels on a table (each panel is sized for compatibility with a truss cube) and then sewing them together. The mesh is then attached to the deployed truss standoffs. The standoffs are approximately 2-m long. The mesh attachment points are located and marked while the mesh panels are on the mesh stretching table. The surface cords with attachment beads and tieback cords are then strung across the surface of the mesh. At this point, mesh shape setting is started.

During the setting process, a constant force is maintained at the surface cord-to-standoff interface. Each surface cord attachment point will be adjusted to match the parabolic-spherical shape required. Figure 3-21 shows the plan view location of the points for a typical 15-m box section.
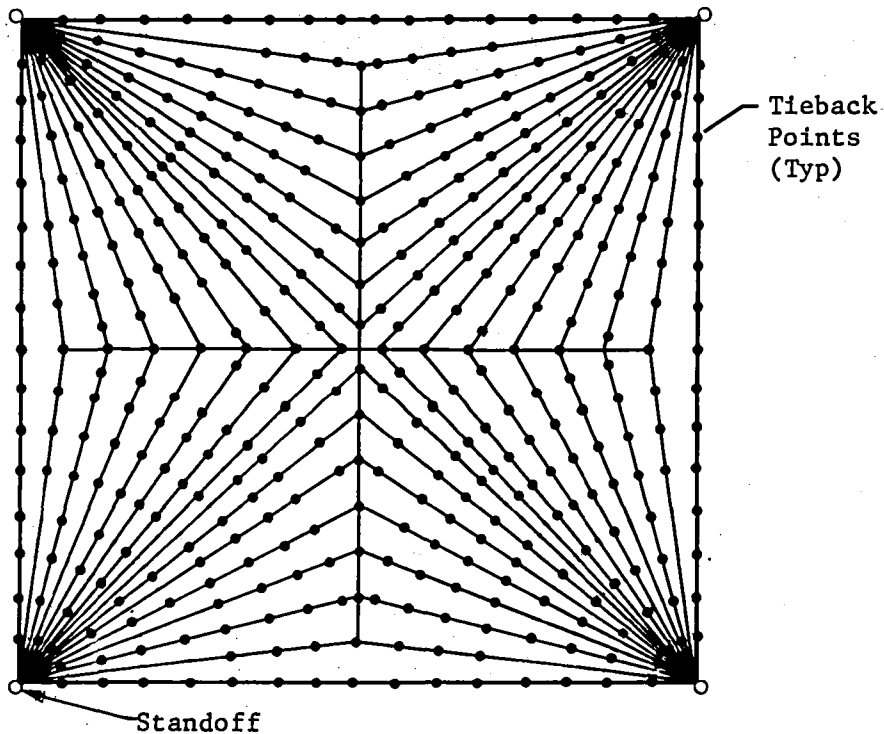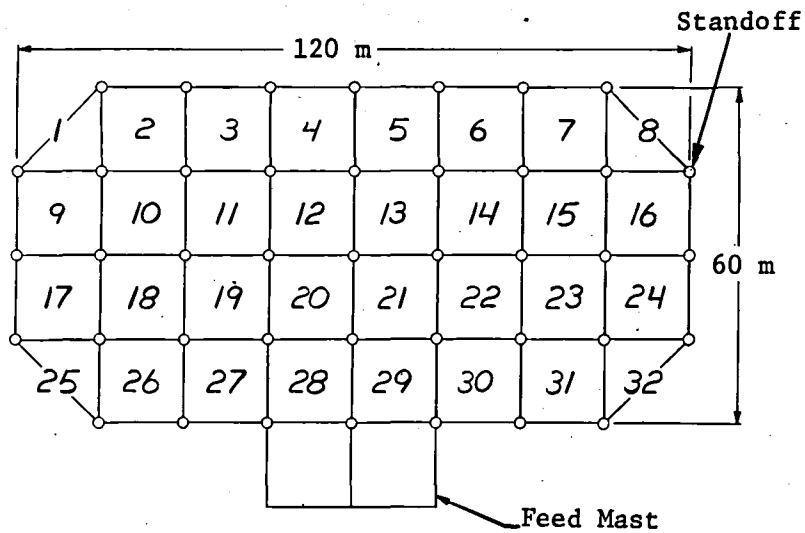
Figure 3-21   Mesh Box Numbering System and Plan View of Typical 15-m Box Section Tie Points

Manufacturing processes for tensioning mesh and adding tie cords and attachment beads have been established using previously designed models of different tie-system configurations, such as the tie-system model shown in Figure 3-22.*

---

*Built under Denver Aerospace IR&D project D-54D, 1981.

56
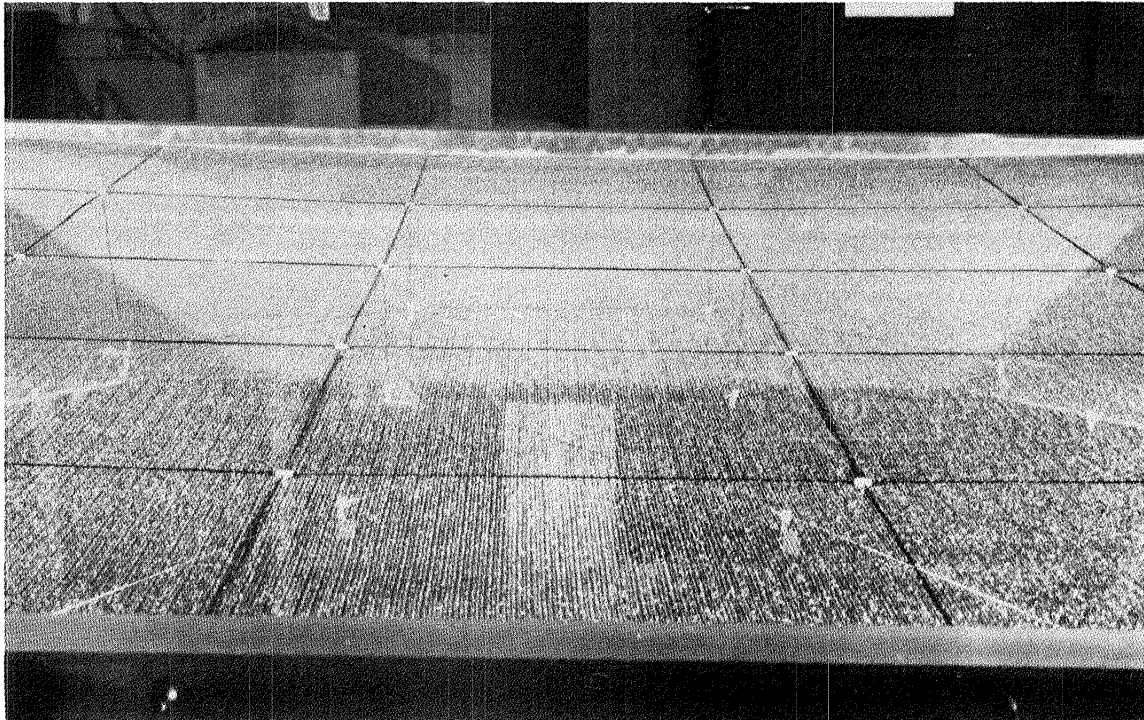
Figure 3-22 Prototype Mesh Tie Model

The direct tieback design for an EOS-size reflective surface requires a standoff height of 2 m, and some of the tiebacks are attached to the vertical members below the corner fittings, giving an effective stand-off height of 3 to 4 m. The standoff height causes no critical packaging or strength/stiffness problems.

3.4.1 Mesh Surface Pillowing

The shape of the reflector surface is defined by several factors--mesh tension and compliance; upper surface cord pattern (spacing), tension and stiffness; tieback stiffness and length; and local radius of curvature. Further, the geometric saddling effects (pillowing) caused by biaxially tensioned mesh and the upper surface cord pattern cause local deformations. Figure 3-23 shows a test model of a biaxially tensioned surface incorporating deliberate scale exaggerations. Measurements were made to determine pillow shape versus mesh tension and cord tension. When the panel's shape is duplicated and scaled to a mesh surface on a 58-m reflector with a 116.1-m focal length and average drop-cord spacing of 0.7 m, the rms surface errors (best-fit mesh saddles relative to an ideal parabola) are 0.021 cm, and the worst-case deflections (at the tieback attachment points) are 0.10 cm behind the ideal parabola. Figure 3-24 shows how the rms surface error will vary by changing the tie-spacing. Assuming 50% of 1/55 of a wavelength can be assigned to rms mesh distortions, the proposed mesh surface design will perform well at the EOS high operating frequency of 10.68 GHz.
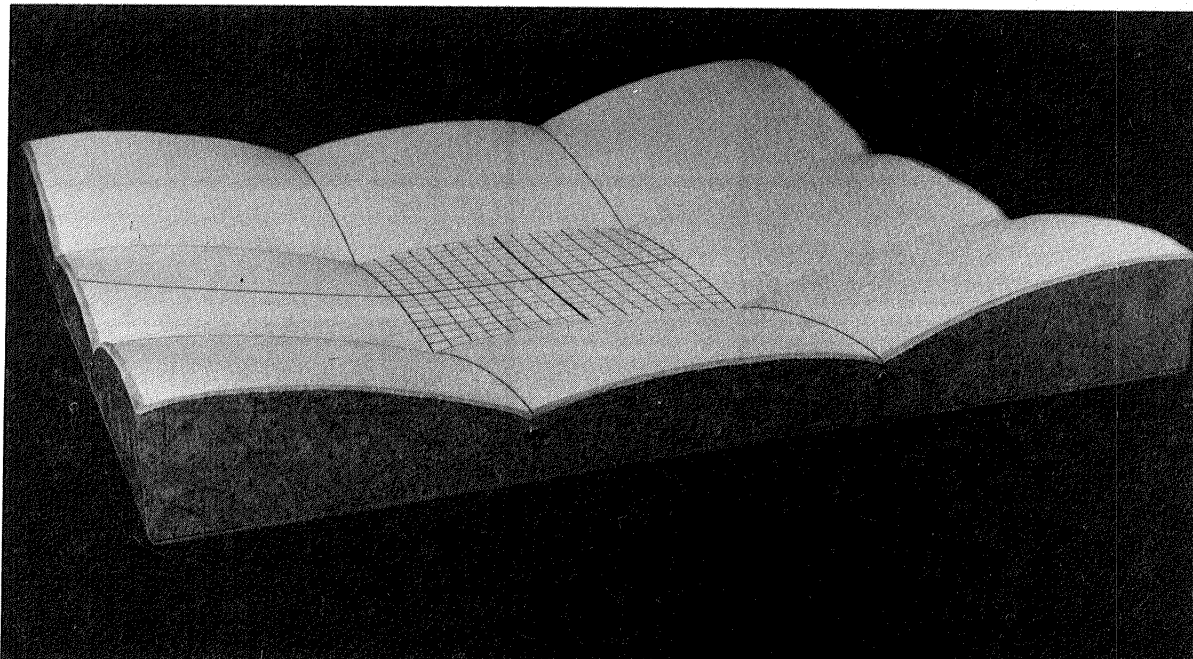
Figure 3-23   Mesh Pillowing Model

Tieback Cord Spacing, m
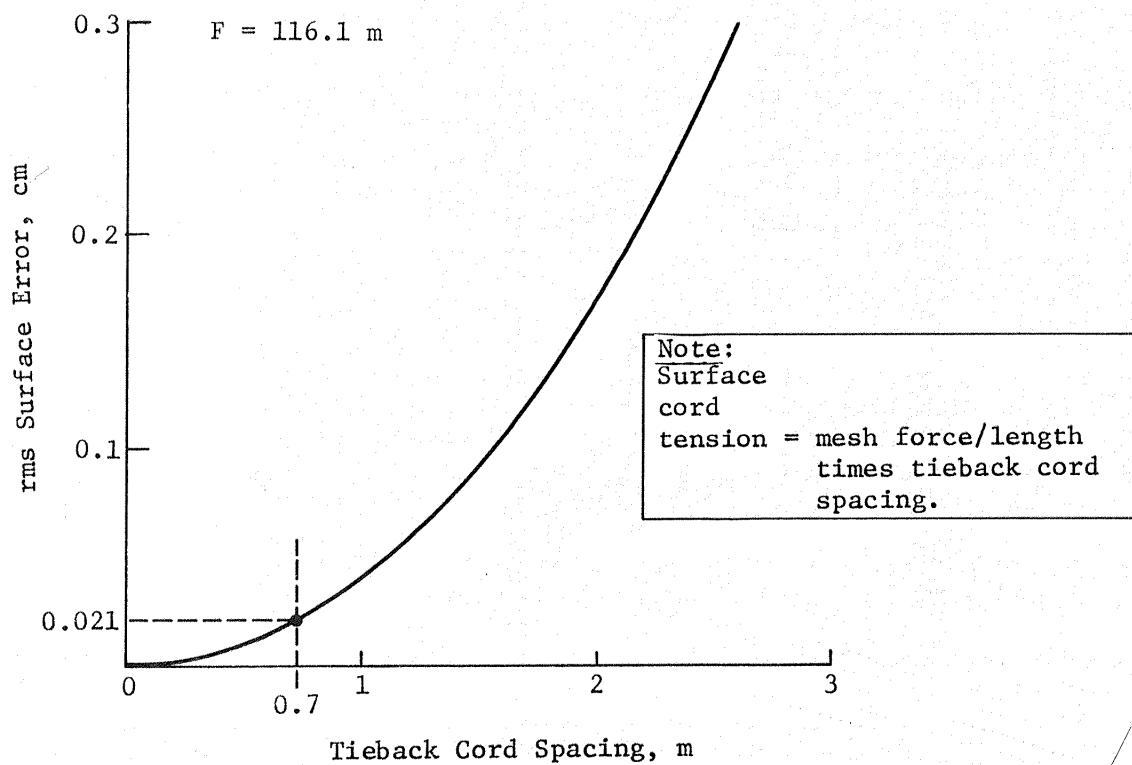
Figure 3-24   rms Surface Error vs Mesh Tie Spacing

3.4.2 RF Reflective Mesh

The radio frequency (rf) reflective surface is formed by using a tricot-knitted, 0.003-cm diameter, gold-plated, molybdenum monofilament wire mesh. This design has the desirable properties of high rf reflectivity, corrosion resistance, low weight, wrinkle resistance, low spring rate, puncture resistance, and radiation resistance. Figure 3-25 illustrates the mesh knit. The weave size is varied depending on the frequency of operation to ensure acceptable rf loss. Figure 3-26 presents an estimate of mesh rf loss for a mesh with 5.5 openings per centimeter versus operating frequency.* Operational mesh tensions were not specified but typical values of 1.5 to 3.0 N/m were assumed. Mass of the mesh also depends on the weave size. For the mesh with 5.5 openings/cm, the mass/area is equal to 21.96 gm/m^2. The mass of mesh with different size openings is a ratio of the square of the mesh openings/cm.
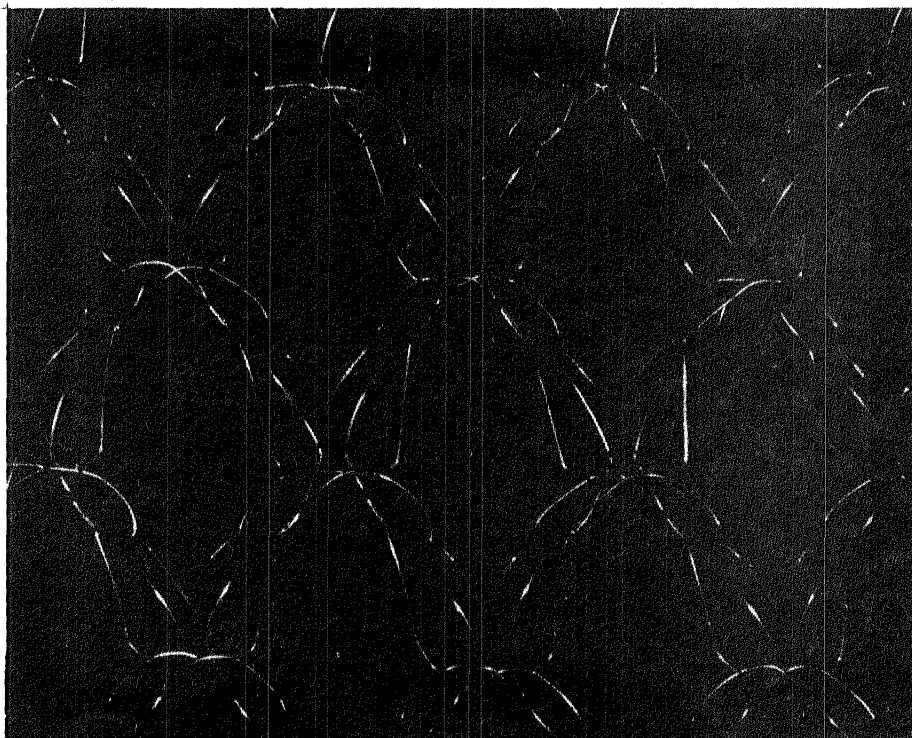
Figure 3-25   Tricot Knit Weave

*AAFE Large Deployable Antenna Development Program, NASA CR-2894, 1977.

59
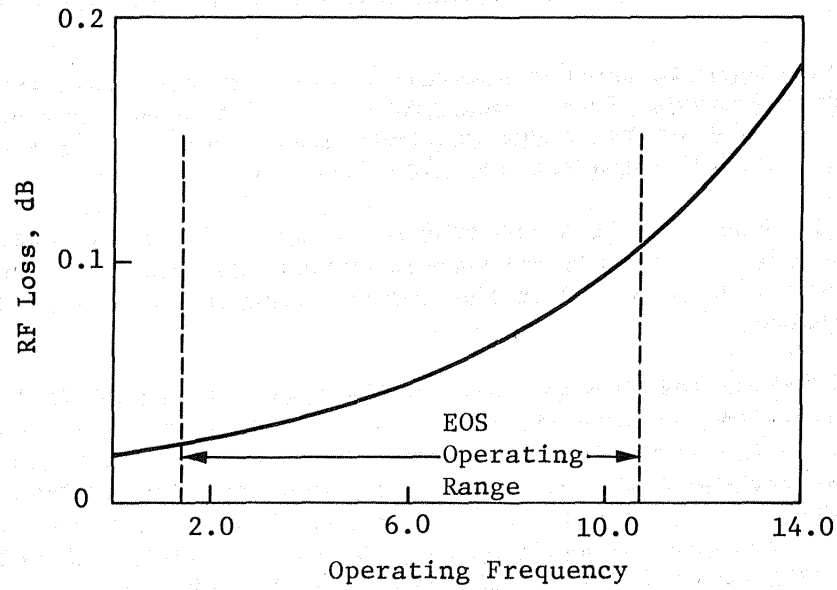
Figure 3-26   rf Reflectivity Loss of 5.5 Openings/cm Tricot Mesh

The subsystems unique to the EOS spacecraft are discussed in this section. The EOS subsystems (i.e., solar/battery and transfer propulsion) comprising state-of-the-art components that were significantly repackaged to suit the EOS constraints are also discussed.

When the EOS is separated from the orbiter's bay it is an autonomous spacecraft capable of complete structural deployment and, with an orbital transfer system oriented in the nadir direction, is prepared for on-orbit operation.

The 10-year lifetime requirement imposes the greatest burden on technology and subsystem development, e.g., the thermal control system for the IR cyrogenic spectrometer instrument. Because the anticipated heat load for this instrument exceeds the storage cooling capability of stored cryogens, it requires mechanical coolers that cannot last 10 years. A possible solution is to specify a two- or three-year resupply period. Resupply would involve installing new cryogens to cool certain atmospheric sensors if a stored system were used, replacement of the IRU, and replacement of electromechanical data storage devices if they are used instead of solid-state recorders.

4.1   RADIOMETER SYSTEM

The EOS pushbroom radiometer employs 324 receivers. Both a total power radiometer (TPR) receiver and the Dicke* receiver design have been considered for this application. Although analysis is not complete enough to recommend selection of a final design, the two approaches are discussed.

4.1.1 Radiometer Receiver Candidates

The TPR receiver illustrated in Figure 4-1 has the best sensitivity and simplest configuration of any radiometer receiver. The TPR, however, has no provision to compensate for receiver power gain fluctuations ($\Delta G/G$). These variations will appear as random changes in the receiver output and are indistinguishable from changes in scene characteristics. Small changes in gain will produce significant output variations. For example, a system with a temperature of 250 K and an 0.1 dB receiver change produces a variation of about 6 K, which is 10 times the allowable.

---

*R. H. Dicke: "The Measurement of Thermal Radiation at Microwave Frequencies," Rev Sci Instr, 17, 1946, p 268-275.
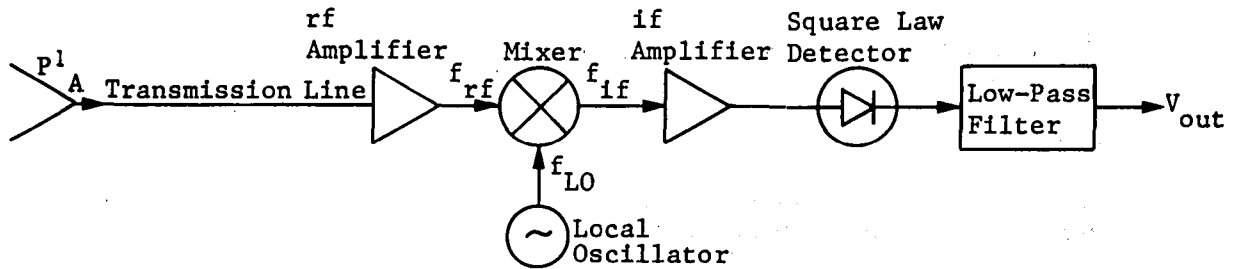
Figure 4-1 Total Power - Radiometer

The radiometric resolution (ΔT) for a TPR is given by

[1] $$\Delta T = T_{sys}\sqrt{\frac{1}{B} + \frac{\Delta G}{G}^2}$$

where

B   = predetection bandwidth,
t   = integration time,
T_{sys} = temperature of the system.

This expression provides a qualitative relationship for ΔT incorporating both noise and gain variations. The $\Delta G/G$ term dominates the radiometer sensitivity and must be on the order of 10^{-4} to achieve acceptable ΔT, which is difficult to maintain because of power supply and environmental temperature variations. For these reasons, the TPR is usually not considered suitable as a precision radiometer receiver when the design is analyzed in a simplified manner.

Hersman and Poe* developed an expression for ΔT that characterizes the gain fluctuations in terms of such radiometer calibration parameters as calibration period and integration time.

[2] $$\left(\frac{\Delta T_{SE}}{T_{sys}}\right)^2 = \frac{1}{B\tau_S} + \frac{1}{B\tau_C} \sum \omega^2(t - Kt_C) \left(\frac{\Delta G}{G}\right)^2$$

where

T_{sys} = system noise temperature,
B   = bandwidth,
t_S = scene integration time,
t_C = calibration scaling factor,
w   = calibrator weighing function, K/V,
c   = radiometer scale factor,

*M. S. Hersman and G. A. Poe: "Sensitivity of the Total Power Radiometer with Periodic Absolute Calibrating," IEEE Trans Microwave Theory Tech, Vol MTT-29, January 1983, p 32-40.

and

$$\left(\frac{\Delta G}{G}\right)^2 = \left(\frac{c}{T_{sys}}\right)^2 \int_0^\infty df \; S_g(f) \; H(f)$$

where

S_g = gain fluctuation spectrum,

$H(f)$ = unitless transfer function.

This equation provides some insight into the tradeoffs between calibration interval and other parameters required to obtain optimum performance. A preliminary analysis indicates that short integration times with calibration periods of a few seconds are satisfactory. Therefore, the TPR should not be dismissed from further consideration as a receiver system.

Dicke was the first to alleviate the gain variation problems by using modulation techniques. The expression for variations in V_{out} of the Dicke receiver due to gain, noise, and noise variations between reference temperature and receiver is given by

[3]
$$\Delta T = \left[\frac{2\left(T_a + T_{rec}\right)^2 + \left(T_{ref} + T_{rec}\right)^2 + \frac{\Delta G^2}{G} \left(T_a - T_{ref}\right)^2}{B\tau}\right]^{\frac{1}{2}}$$

where T_a = apparent temperature of the antenna,

T_{ref} = temperature of an external temperature reference.

If the value of T_a equals T_{ref}, the radiometer is said to be balanced and the effects of gains of varying complexity are eliminated entirely. A variety of techniques can be employed to maintain this balance. Significant performance and design analysis is required before a particular receiver design can be judged to be most advantageous.

4.1.1.1 Thermal Control of Receivers - A thermal control system is required for the EOS feed array to maintain the feed electronics to within +0.1 K for each receiver and minimize the temperature differential between receivers. This is especially true if TPR are used because the receiver temperature coefficient of gain is on the order of 10^{-3}. The individual receiver electronics will be enclosed in thermally insulated boxes. The absolute temperature requirement within each box has not been determined, but will probably be near 285 K.

Because the EOS uses low-power electronics, there will be minimal heat dissipation in each receiver. Heat pipes can be designed into each box to distribute the heat evenly, and should be able to maintain the +0.1 K requirement. The receiver-to-receiver differential heating will be minimized by using active electronic control as well as passive control through wrapping with a multilayer insulation blanket. Detailed analysis of this approach to a thermal control system should be pursued. The analysis would consist of modeling the radiation and conduction heat flow using TRASYS and MITAS.

4.1.1.2 System Noise Temperature – A brief study was undertaken to relate the specific characteristics of the radiometer receiver to the ultimate achievable performance of the radiometer, and to expose potential problems in receiver characteristics. Section 4.1.1 indicated that the radiometric precision (ΔT) is influenced by the temperature of the receiving system (T_{sys}). The output voltage from the receiver is proportional to the noise power delivered by the antenna to the receiver input, and the noise generated within the receiver. A convention used in receiver analysis is to consider the receiver as noise free and reference its noise (power) as an additional input. Thus, the noise power of the feeds, waveguides, and receiver can be related to a temperature that a resistor would be at to generate the equivalent amount of noise. This noise represents the temperature (T_{sys}) of the receiver system.

The noise equivalent temperature of the system is essentially equal to that of the first rf amplifier. This will probably contain a FET amplifier. Figure 4-2 illustrates the relationship between frequency and currently available device noise temperatures. FET and bipolar transistors have temperatures around 300 to 500 K. The minimum detectable change at the radiometer output caused by system noise is given by [1] without the $\Delta G/G$ term. For the plot in Figure 4-2, a predetection bandwidth of 250 MHz and an integration time of 1 second is assumed. Although it will always be desirable to have low-temperature devices, they, in themselves, do not represent a technology obstacle in the further development of the LMR.

4.1.2 Feed Array

The EOS operates in a pushbroom mode. In this configuration, wide swaths and multibeams are simultaneously obtained by aligning feeds in a circular arc in front of a spherical reflector. The angular separation on the arc between adjacent feeds is the same as the angular separation between adjacent ground footprints. The physical feed spacing along the feed beam are given by

[4] $L = r\theta$

where

r = distance from centers of curvature to feed arc, 116 m,
θ = beamwidth of antenna, radians.

The mission definition study by Keafer, et al.* suggests both optimistic and conservative criteria for defining the required beamwidth of the antenna. The beam size for the optimistic criterion is the half-power beamwidth (HPBW), or 1.22 λ/D. The conservative criterion states that the maximum dimension of the main beam should be equal to or smaller than one-half the resolution requirement. The relationship between the required radiation pattern of the antenna and the conservative and optimistic criteria is illustrated in Figure 4-3. The beam size, 3 λ/D, is the full main beam. Using these two criteria, the EOS feed spacing is summarized in Table 4-1.

---

*L. S. Keafer Jr., P. Swanson, and J. Eckerman: Radiometer Mission Requirements for Large Space Antenna Systems, NASA TM-84478, (1982).
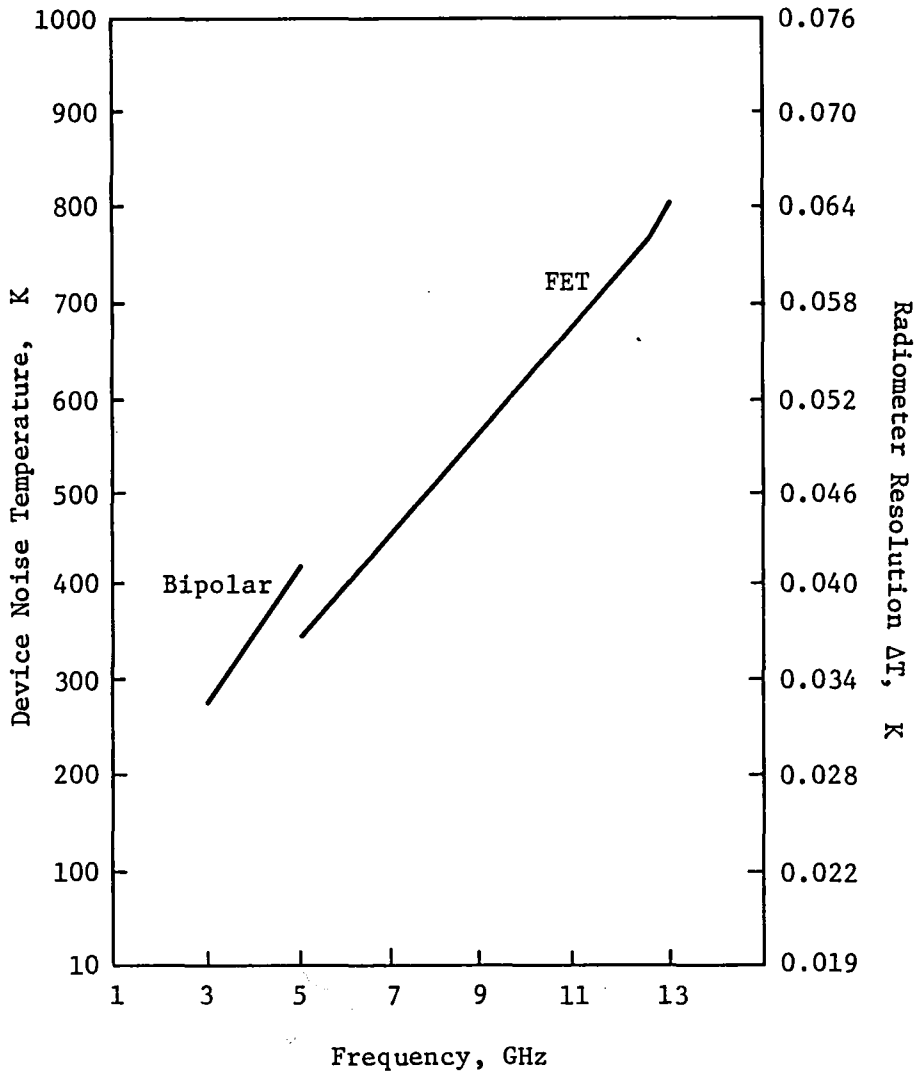
Figure 4-2   Device Noise Temperature

Table 4-1   Feed Spacing, EOS Structure

Frequency, GHz	Conservative, m	Optimistic, m
1.41	1.21	0.51
5.5	0.36	0.15
10.68	0.168	0.07

Figure 4-4 illustrates the feed spacing configured for the optimistic criteria. The feeds are designed to view a spot on the reflector sur-face that corresponds to an individual ground footprint on the earth. The detail for the 1.4-GHz array has been omitted for clarity. For this band, each spot is formed by a 5 x 5-element array. The four outer columns of elements are shared with adjacent arrays so the cen-ters of the arrays may be spaced at 0.51-m intervals. The 1.4-GHz band cannot use single feed horns for the reasons developed in the following paragraphs.
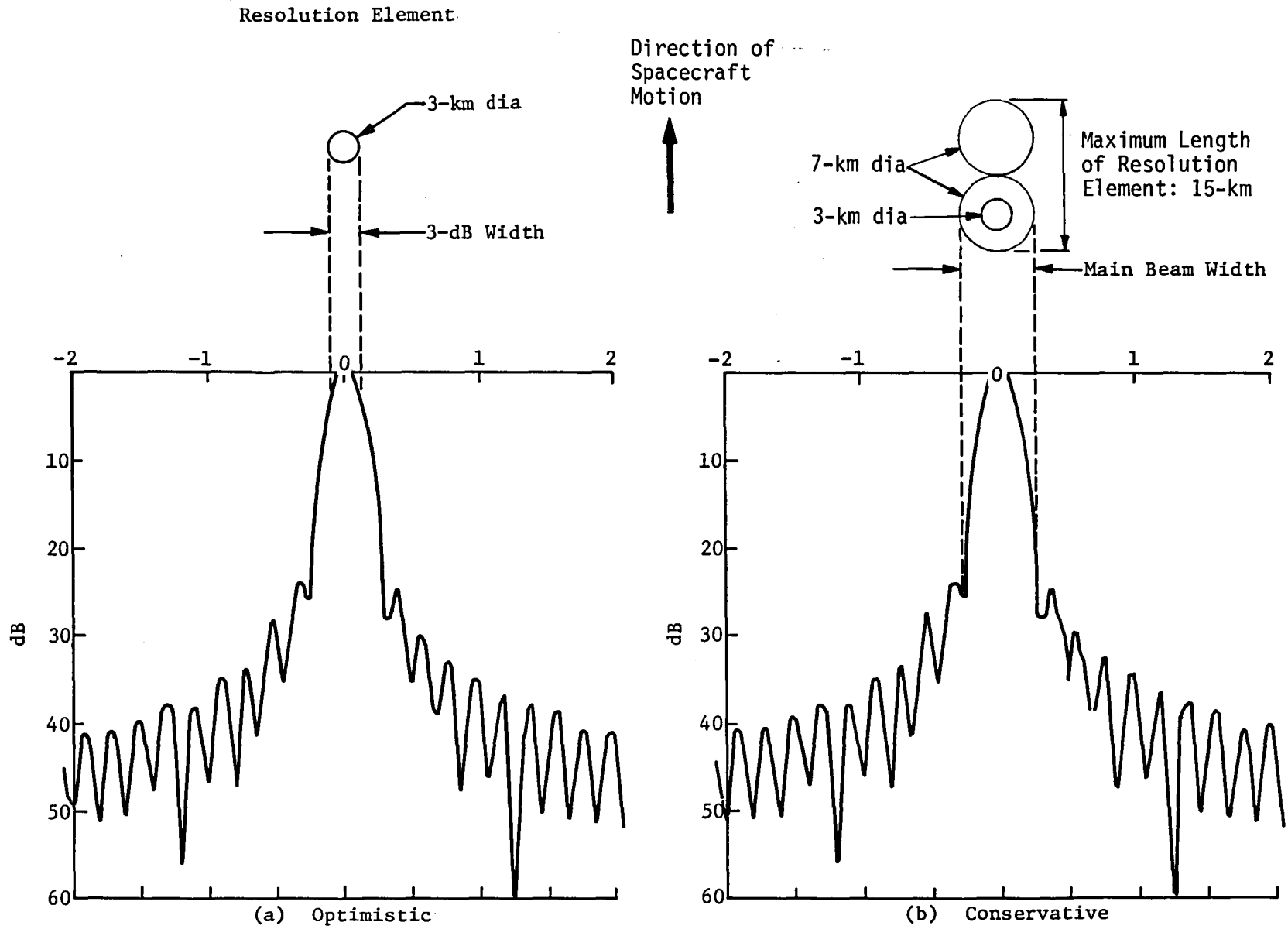
Figure 4-3 Ground Resolution

Linear Bearing
Shaft

Linear
Bearing
Shaft

Hinge.

1.52 m

Honeycomb
Panel

Epoxy/Graphite
Support Structure

Motor
Mount

Horns

1.4-GHz Feed Array

88 per Boom Half
(10.68 GHz)
41 per Boom Half
(5.5 GHz)

Horn Locations
(Structure Not
Shown)
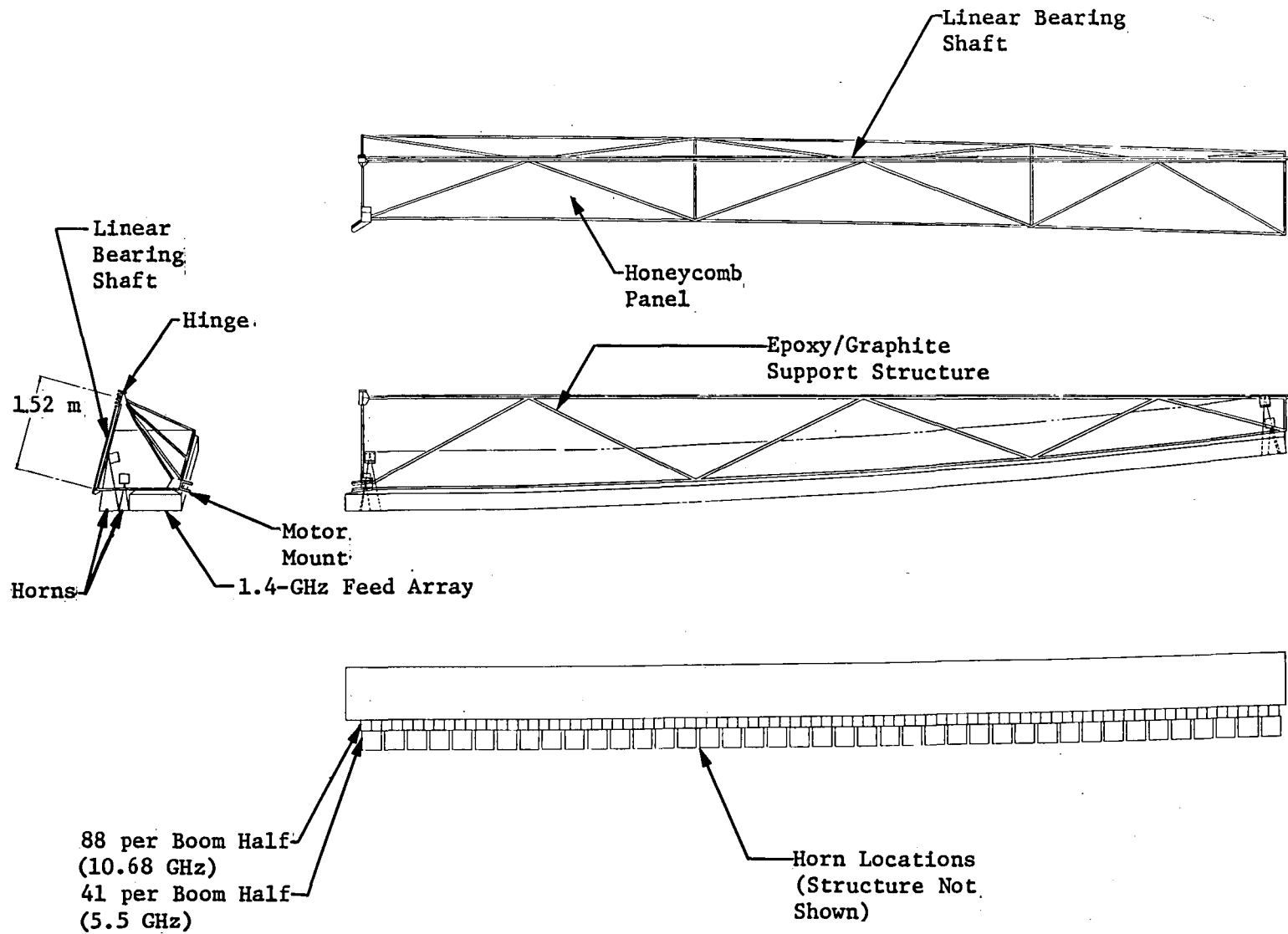
Figure 4-4 Feed Geometry

The desired feed horn performance also influences their size. A feed horn illumination taper of approximately 15 to 20 dB is required to achieve the beam efficiency requirement of > 90%. To determine the compatibility of horns with general volume restrictions, a preliminary analysis was performed using flat-walled rectangular horns. The physical dimensions of such horns depend on wavelength (λ) and the desired edge illumination at an angle ϕ.

Figure 4-5 illustrates the relationship between the angle ϕ and the f/D ratio of the reflector. The inset figure illustrates the geometry with one 58-m spot on the reflector illuminated. As the focal length becomes less, ϕ becomes greater.
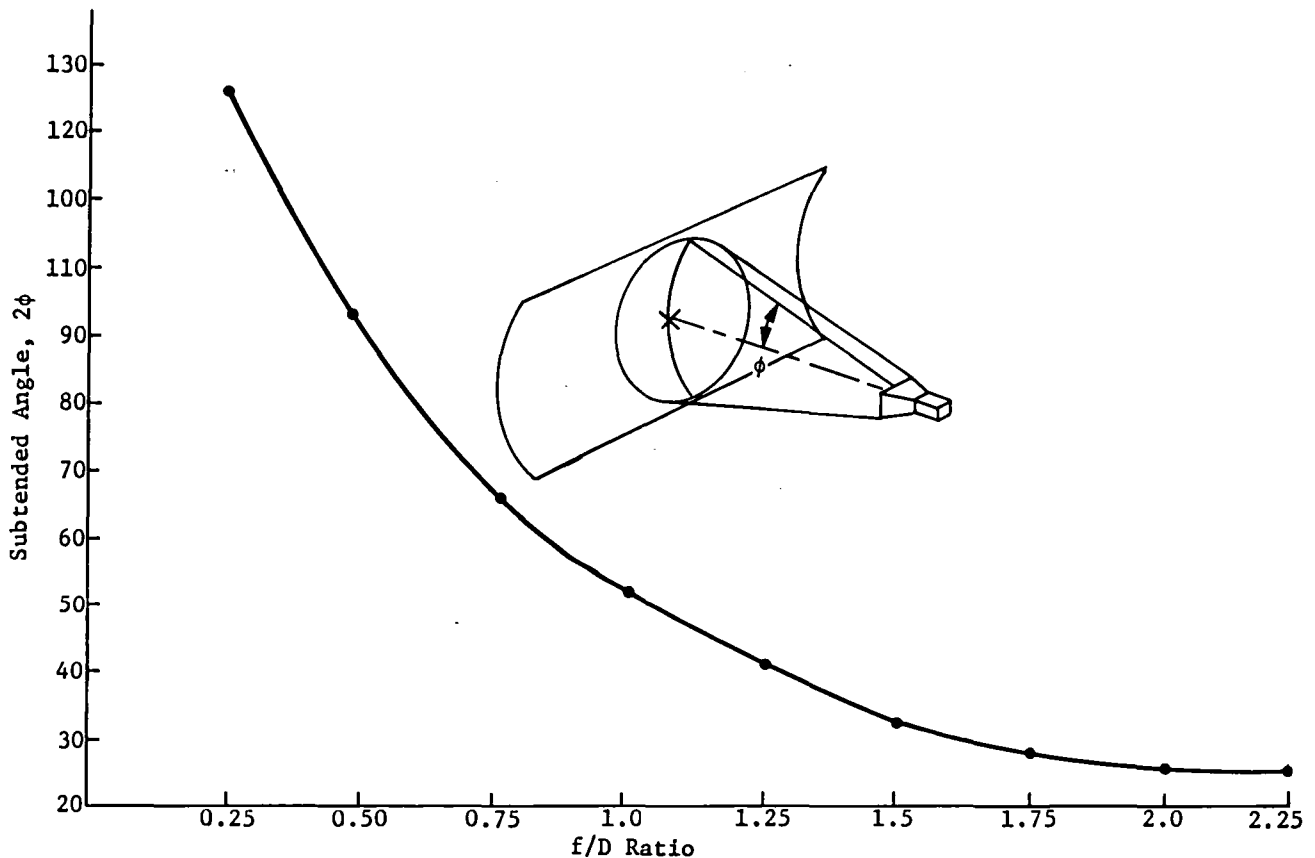
Figure 4-5   Feed Horn Subtended Angle

The horns are designed using the universal patterns for E-plane sectoral and pyramidal horns. The value of ϕ for the EOS configuration is approximately 14 deg. Therefore the aperture dimension (b_1) of the horn is determined if the solutions are constrained around (b_1/λ) sin $\phi = 1$. The horn length is determined by the desire to have S (the maximum phase deviation in wavelengths) so the edge illumination is approximately -20 dB and achieves high beam efficiencies.

Figure 4-6 illustrates the relationship between p_1 and b_1 with increasing f/D. A fundamental problem for all LMR designs using long f/Ds is the dimensions for the lowest frequency horn. A horn length of 3.6 m is required for an f/D = 2. The requirement for so many of these large horns when used in a pushbroom mode therefore becomes incompatible with shuttle limitations. Section 6.6 discusses a partial solution.

4.1.3 Receiver Calibration

Instruments such as microwave radiometers must be periodically calibrated to maintain their high accuracy. This will be true, regardless of the radiometer system ultimately selected, because the initial characterization of the radiative transfer function for the radiometer may alter with time and varying conditions. Should this occur, a means must be available to recalibrate the receiver.

Because most radiometer receivers are linear devices, the output voltage is directly proportional to the input power. Therefore two temperature references near the limits of the dynamic range of the radiometer can be used to determine the calibration line. It is usually desirable to have a "cold" source below 100 K and a "hot" source near 300 K.

The hot calibration load is usually easy to produce. This becomes particularly important when hundreds of elements may be required in a pushbroom radiometer feed array. The source could be a passive blackbody radiator maintained in a temperature-controlled enclosure, or an active source. These sources can be small and easily packaged.

The cold source represents a problem for large radiometers of the pushbroom type. Past satellite borne systems have used an auxiliary antenna to view space and its characteristic cosmic background radiation of 2.7 K. This approach becomes impractical, even if a single horn were to service multiple receivers, because of the losses incurred and volume and packaging problems. Another alternative uses FET-produced output noise temperatures much lower than the FET's physical temperature. This is an active circuit that behaves like a cold noise source and could be used as a cold reference load. Frater and Williams* have demonstrated effective temperatures approaching 50 K at 1.4 GHz. The use of the cold FET represents an adequate minimum temperature for calibration and a feasible solution.

---

*R. H. Frater and D. R. Williams: "An Active 'Cold' Noise Source," IEEE Trans on Micro Theory and Techniques, Vol MTT-29, No. 4, April 1981, pp 344-347.
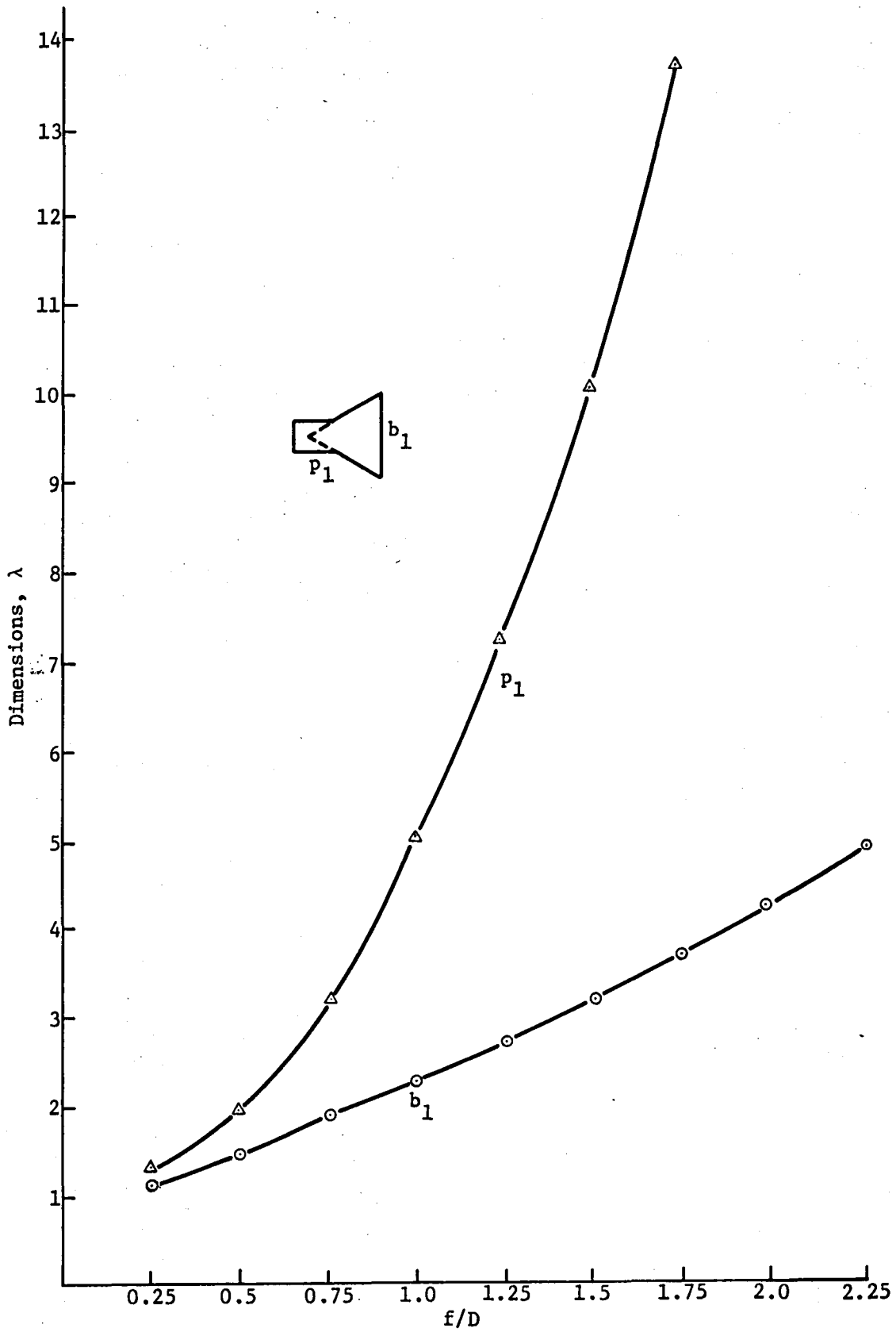
Figure 4-6   Horn Dimensions

70

4.2   REMOTE SENSORS

This section summarizes the design developments for the sensors speci-
fied in Section 2.3. Because large deployable space structures normal-
ly have limited space and attachment points for ancillary sensors and
subsystems, the idea of an integrated science platform (ISP) capable of
being deployed from the main structure was developed. A lightweight,
pentahedral structure, with a honeycomb base where needed, was designed.
This structure provides a common strongback carrier for the science in-
struments, and greatly eases the problem of integrating sensors with a
deployable LSS.

Many of the sensors have stringent mounting requirements that can be
easily satisfied with the science platform. A sensor such as the MLA
of Mission II requires the capability of fine pointing and vibration
isolation to achieve the necessary arc-s stability. This can be ac-
complished for individual instruments, or for the entire beam when an
appropriate isolation device is mounted at the spacecraft attachment
interface.

4.2.1   EOS Mission I - Baseline

The sensors for EOS Mission I represent a complement of active and pas-
sive microwave sensors. These instruments are used for land and ocean
observations and were selected to satisfy the mission definition of
Section 2.2.1.

4.2.1.1   Synthetic Aperture Radar (SAR) - The SAR is an active imaging
radar operating in the L-band. The ground resolution for this instru-
ment is designed to be 25 m, making it compatible with optical imaging
sensors. The SAR is intended for high-resolution imagery of land and
ocean features, both day and night and through most types of weather.

The antenna and sensor electronics are mounted on the ISP as shown in
Figure 4-7, which illustrates the salient features of the integration
with the spacecraft. Unlike previously flown SAR antennas, the present
design is fully deployed along the science beam making the design very
rigid. An active array in which physical distortions of the antenna
are electrically compensated is not anticipated to be needed.

4.2.1.2   Atmospheric Sounding Radiometer (ASR) - The ASR is a passive
microwave radiometer operating at 18, 21, 37 GHz. The instrument is
intended to make supporting observations and provide additional inputs
to the ground parameter retrieval algorithms. The anticipated radio-
metric precision (ΔT) is 1.5 K. This value should be acceptable as
auxiliary retrieval inputs.

The antenna design options for the ASR are constrained by packaging and
engineering considerations. A separate array is necessary for each
frequency. The proposed antenna is a microstrip, series fed, 4x4 m
square array. The series feed microstrip array is inherently low loss
because the transmission lines are kept to a minimum. The panels can

be fabricated on a dielectric honeycomb core. Mechanically scanned dishes would probably offer better performance, but they are difficult to implement because of the high scan rates necessary.

The ASR is mounted on the LMR feed beam because a large area for the array panels and an unobstructed view of the earth is available. In addition, the ASR is required for all LMR observations, thus the ASR is included as an integral feature of the spacecraft and permits the science platform to be configured with a greater variety of sensors.

4.2.1.3 <u>Spacecraft Integration</u> – The SAR antenna is supported on a truss structure known as the Science Platform. The basic platform concept is used for the instrumentation on all EOS missions. Although the truss is relatively stiff, motion of the linear platform is anticipated and platform motion sensor is required.

This subsystem will consist of star trackers located on the platform to obtain attitude information and a position reference for the platform. An optical autocollimination technique is used to provide information on angular rotations and displacements about the three orthogonal axis. An overall accuracy of about 0.25 arc sec is attainable for displacements and an order of magnitude greater for twist.
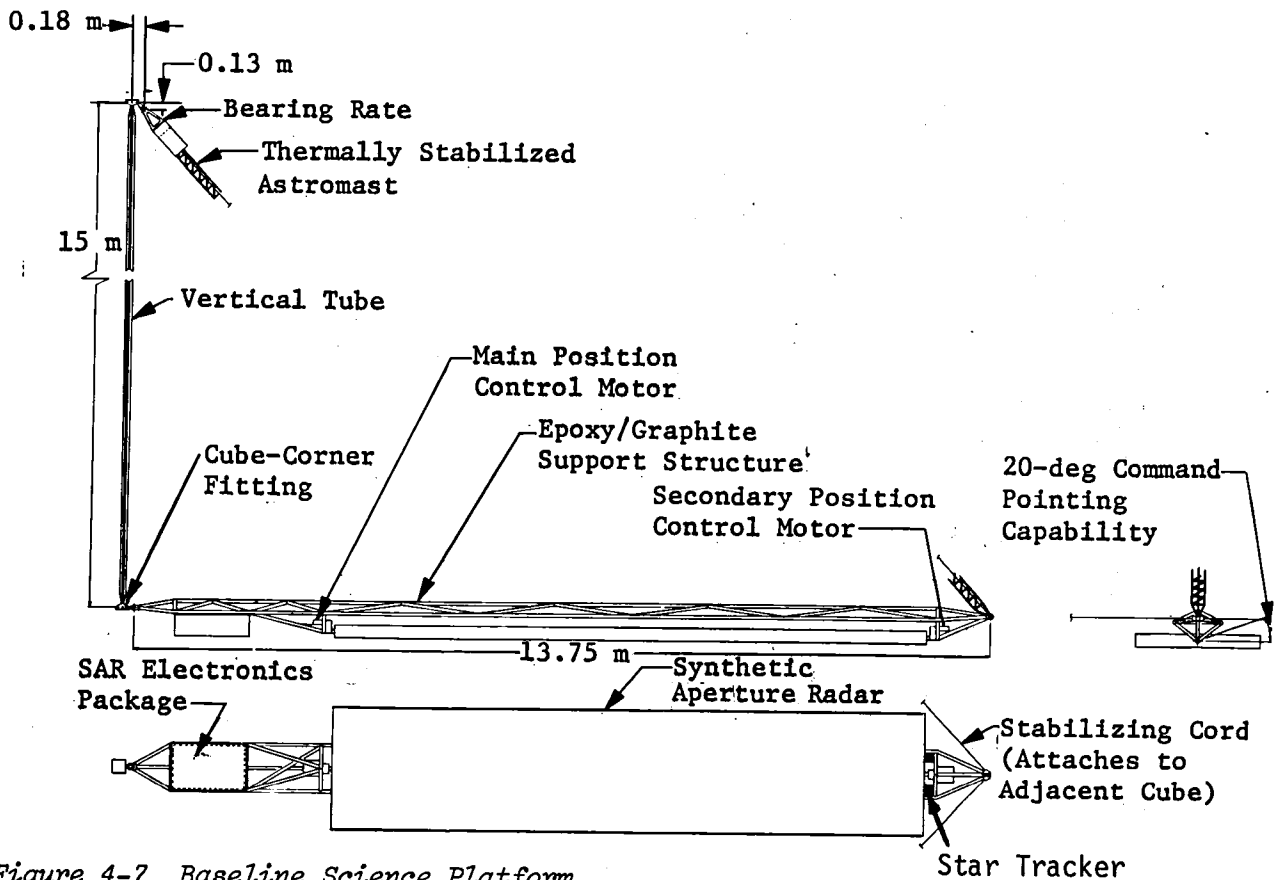
Figure 4-7 Baseline Science Platform

72

4.2.2   EOS Mission II - Land Observation Sensors

The sensors in this sector are required to satisfy the user needs suggested in the mission planning for land missions. They also represent a comprehensive complement of sensors capable of a diverse range of observations.

4.2.2.1   Multispectral Linear Array - Mechanically scanned sensors employing an articulated object plane mirror have been the only types flown on spacecraft. Instruments of this type include the multispectral scanner (MSS) and thematic mapper (TM) of LANDSAT 1-3 and LANDSAT 4, respectively. The TM represents the state of the art for mechanical scanners. New user demands for imaging systems will make improvements in mechanical scanners very costly because of the extreme construction precision required.

The self-scanned linear array operating in the pushbroom mode offers significant improvement in performance over mechanical systems and can be implemented with minimal technology advances. In this device, the array is oriented in the crosstrack direction, with the forward motion of the satellite providing the single-axis scanning motion. This offers improvement in the integrated circuit fabrication technology used to manufacture the arrays and permits improved detector-to-detector and band-to-band registration. The smaller detector size enables ground resolution improvement. A further improvement may be possible using a planar focal plane array such as CCDs.

4.2.2.2   Mid-IR Imager (MIRI) - The MIRI is intended to satisfy the IR imaging needs of the land observation mission and to measure emitted thermal fluxes. Two possible designs exist, one employing mechanical scanning and one employing linear array pushbroom scanning. The electromechanical version is well within present capability, and the means to implement the IR pushbroom version is a near-realizable technology. Implementing the pushbroom scanner eliminates complex mechanical scan mechanisms and allows a longer dwell time on a scene, which results in significant improvements in the signal-to-noise ratio.

The optical design for the MIRI is within the state-of-the-art capability. The sensor would employ reflecting and IR transmitting optics, with the IR beam focused on HgCdTe detectors cooled to 115 K.

4.2.2.3   Multispectral Resource Scanner (MRS) - The MRS concept has been presented by Schnetzler and Thompson*. The emphasis on this instrument has been to define phase A-type system specifications and designs. This instrument, as conceived, could be used with the EOS as an integral part of the land science complement.

4.2.2.4   Synthetic Aperature Radar (SAR) - The two SARs used for this mission operate in the L- and X-band and use separate antennas for each. These sensors use available technology. Section 2.3.2.4 gives a fuller description.

4.2.2.5 <u>Spacecraft Integration</u> - The complement of sensors included in Mission II are contained on a single science beam or pallet (Fig. 4-8). Table 4-2 summarizes the salient features of these sensors.
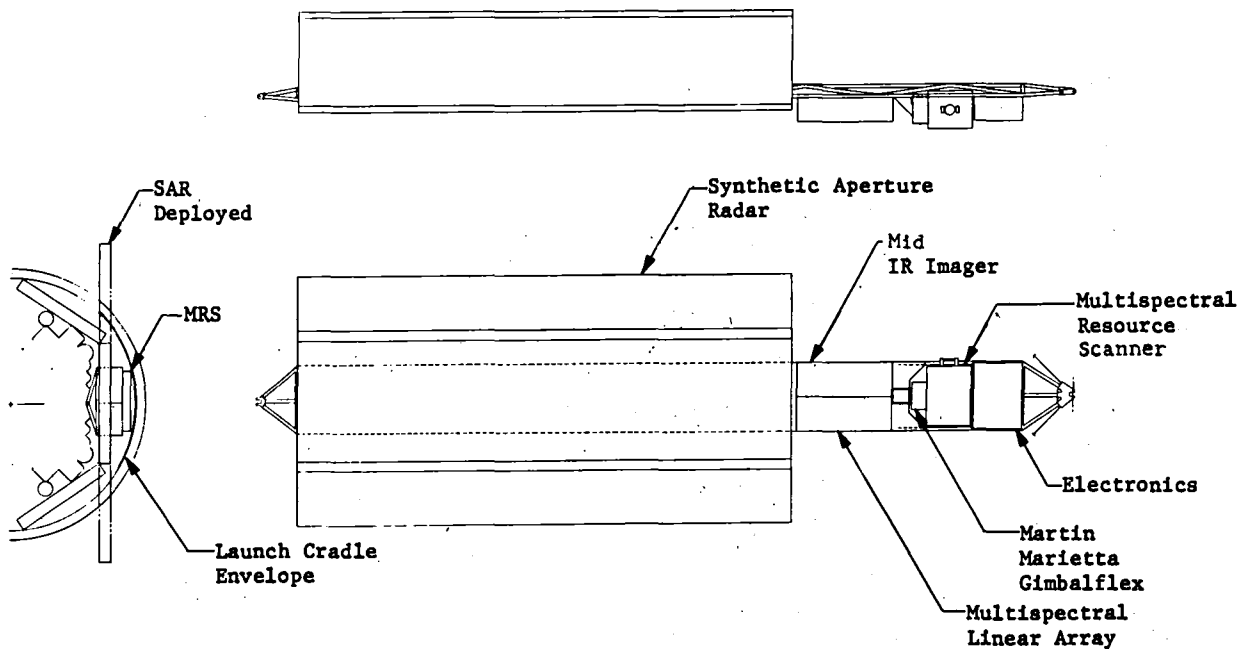
Figure 4-8   Land Mission Science Platform

Table 4-2   Sensor Characteristics

	MLA	MRS	MIRI
Mass, kg	70	65	60
Power, W	50	75	50
Dimensions, m	1.6 x 0.6 x 0.4	---	1 x 0.5 x 0.5
Spectral Range, μm	5 Bands, 0.52-1.75	Visible	2.08-2.35 8.1-12.0
Data Rate, mbps	44.9	15	11
IFOV, mrad	0.042	0.021	0.042
On surface, m	30	15	30
Bit Quantization	8	8	8

*C. C. Schnetzler and L. L. Thompson: "Multispectral Resource Sampler: An Experimental Satellite Sensor for the Mid-1980's," <u>Proc SPIE</u>, p 183, 34, 1979.

4.2.3 EOS Mission III - Ocean and Coastal Zone

This section summarizes the design paths and developments required for the sensors specified in Section 2.3.

4.2.3.1 Ocean Zone Color Scanner (CZCS) - The CZCS is used to provide estimates of phytoplankton concentration by measuring the spectral radiances backscattered out of the water. This senses in bands centered on 443, 520, 550, 670, and 750 nm with a thermal band covering 10.5 to 12.5 m. Due to the lower radiances over water, the detector noise equivalent power should be on the order of 1×10^{-11} with a SNR of 100:1.

This instrument will be similar to an instrument flown on Nimbus 7, but is anticipated to use a linear array in a pushbroom mode instead of being mechanically scanned.

4.2.3.2 Radar Altimeter (ALT) - The ALT is an X-band radar altimeter used to measure altitude and infer wave height. The measurement accuracy of the oceanic backscatter coefficient has to be within ± 1.0 dB. The parabolic antenna is 1 m in diameter. Table 4-3 summarizes the engineering details.

Table 4-3   Radar Altimeter Specifications

Frequency	X-Band
Transmitted Power, W	1500
DC input power, W	150
Data Rate, kpbs	8
Weight, kg	90

The performance specifications required in Section 2.4.3 are well within the state of the art.

4.2.3.3 Scatterometer (SCATT) - The microwave scatterometer operates in the X-band and is used to determine wind speed and direction over the ocean. While such information is not extensively collected, it significantly influences the ability to forecast continental weather.

Four fan beam antennas are aligned 45 deg to the satellite ground track and separated by 90 deg in azmiuth. This "star" pattern is required because wind vector determinations require two measurements for each resolution cell. The scatterometer has provisions for a fifth and sixth antenna to be oriented parallel to the satellite motion. These additional antennas will reduce the possibility of the scattering coefficient being influenced by unknown effects. Grantham et al.* has described the development of the SeaSat scatterometer based on user requirements.

The placement of these sensors on the ISP is depicted in Figure 4-9.
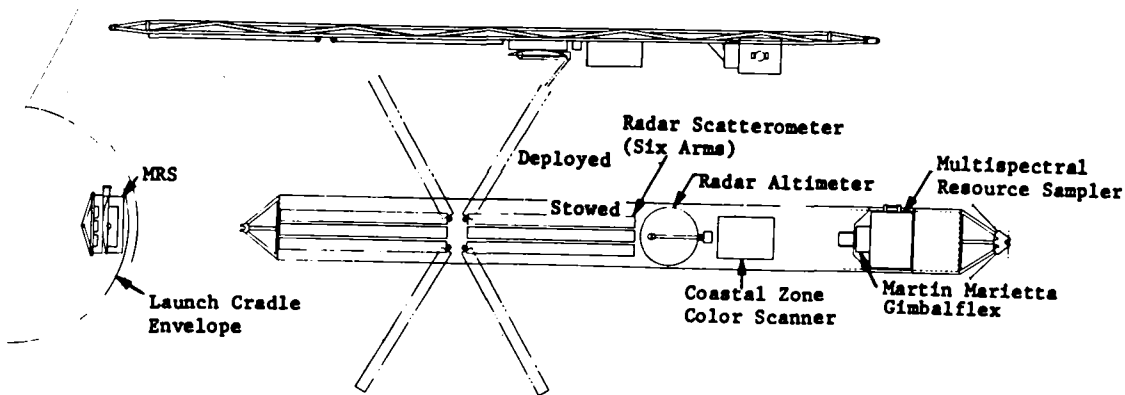
Figure 4-9   Ocean Mission Science Platform

4.2.4   EOS Mission IV - Atmospheric Observations

Figure 4-10 illustrates the atmospheric mission science platform.

4.2.4.1   Correlation Interferometer - This instrument has two channels, one operating in the nonthermal infrared from 2.0 to 2.4 m, and another in the thermal IR from 4 to 9 μm. The interferograms produced are correlated with interferograms of known species. The instrument may be configured for nadir or limb viewing. An interferometer-type instrument was selected because it contains many desirable characteristics, including high sensitivity and high spectral resolution.
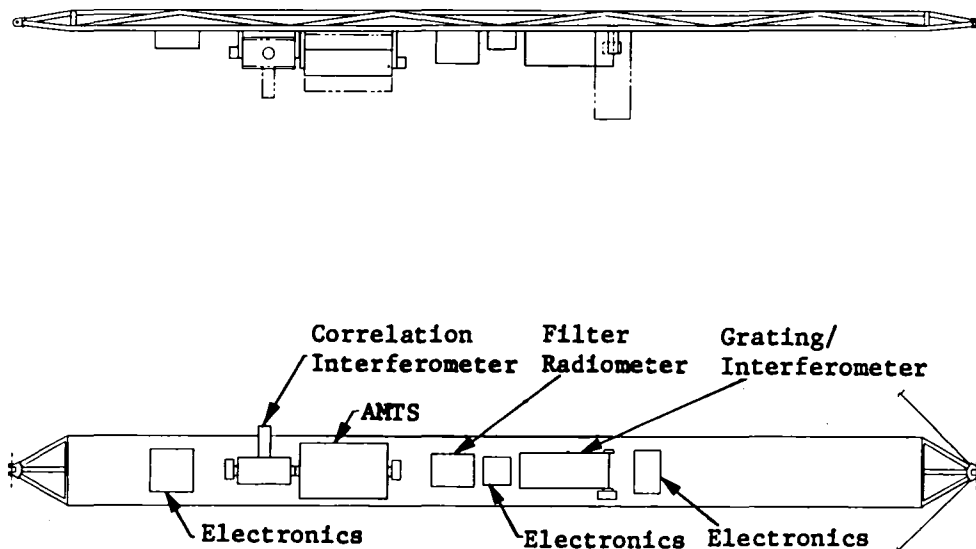
Figure 4-10   Atmospheric Mission Science Platform

*W. L. Grantham, E. M. Bracalente, L.W. Jones, and T. W. Johnson: "The SeaSat-A Satellite Scatterometer," IEEE Journ Oceanic Eng, April 1977, p 200-206.

4.2.4.2 <u>Filter Radiometer</u> - The filter radiometer used optical filters
for selection of atmospheric species. It is a species-specific instrument intended to measure some of the more abundant tropospheric species, including H_2, O_3, N_2O, and HNO_3.

4.2.4.3 <u>Advanced Meterological Temperature Sounder (AMTS)</u> - AMTS is an infrared sounder for the measurement of atmospheric temperature profiles. This instrument uses several CO_2 channels in the CO_2 4.3-um and 15-μm bands.

4.2.4.4 <u>Grating/Interferometer</u> - This instrument is a hybrid composed of a grating spectrometer with approximately 8 channels 100 wave numbers wide. Each channel is then resolved to 0.1 cm^{-1} with a Fabry Perot interferometer.

4.3 ELECTRIC POWER SYSTEM (EPS)

The electric power system provides electric power to all loads throughout the 10-year mission. Key concerns in its design are proposed lifetime, reliability, and redundancy. These problems have significant design implications that are discussed in this section.

4.3.1 <u>Solar Arrays</u>

The solar arrays convert sunlight into electrical energy and are susceptible to radiation degradation. The long mission lifetime requires special consideration of the space radiation environment because of damage to solar cells, covers, and adhesives. The operating altitude for most radiometer missions will be in the 450- to 1000-km range where geomagnetically trapped electrons and protons of varying energies will primarily be encountered.

4.3.1.1 <u>Integrated Radiation Burden</u> - The concept of damage equivalent fluence is used to characterize particular radiation effects on cell current and voltage. The damage produced by multienergy electrons is related to monoenergetic electrons at 1 MeV. Similarly, proton damage is normalized to 10 MeV. It is possible to convert 10-MeV proton damage to 1-MeV electron damage by a single conversion factor. One 10-MeV proton does the equivalent damage of 3000 1-MeV electrons.

During a 10-year mission, the total 1-MeV equivalent fluence is the summation of the annual contribution summed over 10 years. At an altitude of 700 km, the combined annual fluence is approximately 1.1 x 10^{14} electrons/cm^2, or 1.1 x 10^{15} total. Figure 4-11 illustrates the cumulative degradation of the junction short circuit current (J_{SC}) due to the radiation fluence. In addition to these well-modeled population models, unpredictable solar flare proton events can occur. One particularly large event on August 4, 1972 was estimated to be equivalent to a dose of 4.7 x 10^{13} electrons/cm^2.
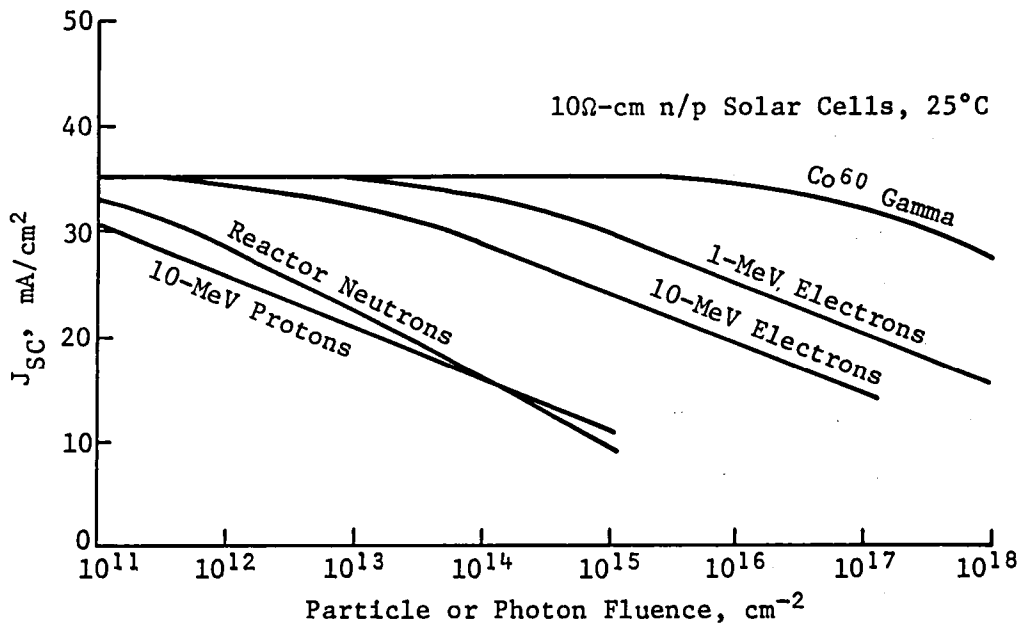
Figure 4-11   Radiation Degradation

Solar arrays are designed to provide the required power at end of life (EOL) by conservative design that incorporates these degradation effects. The design expedient of increasing array size is commonly used, but results in considerable oversizing when both radiation degradation and redundancy for failures are considered.

4.3.1.2   Array Design — A design and sizing of the solar arrays was undertaken for the EOS configuration. It was intended to determine if technology deficiencies could adversely affect satisfying the power loads.

The power produced by the array at EOL is given by

[5] $P_A = S \times \cos\beta \times n \times (1 - F) \times A_A$

where

S = intensity of solar constant, 1353 W/m^2,
F = array degradation factors,
A_A = area of array, m^2,
n = cell efficiency, 0.13,
β = angle between sun and array, 0 deg.

78

The degradation factors calculated for the arrays are tabulated.

Assembly Loss	2%
Diode Insertion Loss	3%
Radiation	20%
Ultraviolet	2%
Cell Packing	10%
Thermal Cycling	6%
Total	43% = 0.43

The power/m^2 over mission lifetime is 100 W/m^2.

Table 4-4 summarizes the power sinks in the feed area.

Table 4-4   Power Sinks in Feed Area

Component	Power (Orbit Average), W
Attitude Control Subsystem	
Inertial Reference Units	35
Fixed-Head Star Tracker	
Star Tracker	20
Shutter	3
Computers	50
Power Conditioning	10
Communications	100
Command and Data Handling	50
Radiometer Feed Electronics	1620
Pulsed Plasma Thrusters	720
Power Losses in Electric Power Module (EPM)	150
Atmospheric Sounding Radiometer	60
Additional Losses	100
Total	2918

Two solar arrays located on the feed beam each produce 1800 W and require 18 m^2. Four arrays are also located on the antenna structure. Assuming a specific performance of about 30 W/kg, each array weighs 50 kg.

The size and performance of the designed arrays are well within the state-of-the-art technology capability. This is because the total power production is distributed among six arrays, but an array of 10 kW is still technically feasible. A parameteric analysis of the terms in equation [5] does not reveal glaring deficiencies in solar array technology.

4.3.2 Energy Storage

The batteries provide a means of energy storage during eclipses. A battery consists of individual cells with each cell having a nominal discharge voltage of 1.25 V. The storage capacity of each cell is usually between 30 A-h to 50 A-h. Thus a battery can be configured with any capacity and voltage with the cells in appropriate series or parallel combinations.

Nickel-cadmium cells have essentially been the only storage devices used despite the fact that NiCd can be a major lifetime-limiting subsystem component. The principal degradation modes are hydrolysis and oxidation of the separation material, cadmium migration, and electrolyte redistribution. These aging effects can be slowed through careful thermal and recharge management. Nevertheless NiCd poses a limitation to long-duration missions.

An alternative energy storage device is a nickel hydrogen cell. These cells are expected to have a much longer operational life than NiCd and operate at a higher depth of discharge (DOD). Figure 4-12 illustrates the advantages of NiH_2 versus NiCd with regard to cycle life.

Little practical flight experience concerning the capabilities of these cells has been gained. Additional work needs to be done to characterize them. Nevertheless NiH_2 cells have been assumed for the spacecraft subsystem design.

4.3.2.1 Battery Sizing - During eclipse, batteries are required to supply the housekeeping and spacecraft loads. The power loads were divided into those in the feed, science platform, and around the reflector areas. Because operation of the LMR is not affected by night and will operate continuously, the feed area represents the greatest power consumption during all times in orbit (Table 4-4). The fraction of sun time per orbit was calculated for sun/spacecraft angle $\beta = 0$ and a 720-km altitude. The eclipse period lasts 35 minutes (0.58 h).

The battery capacity model is

[6] $\qquad C_B \times V_B \times DOD \times L_C = P_L \times T_E$

where

C_B = battery capacity, A-h,
V_B = battery voltage,
DOD = depth of discharge,
L_C = losses in conversion,
P_L = power of loads, W,
T_E = time of eclipse, h.

80
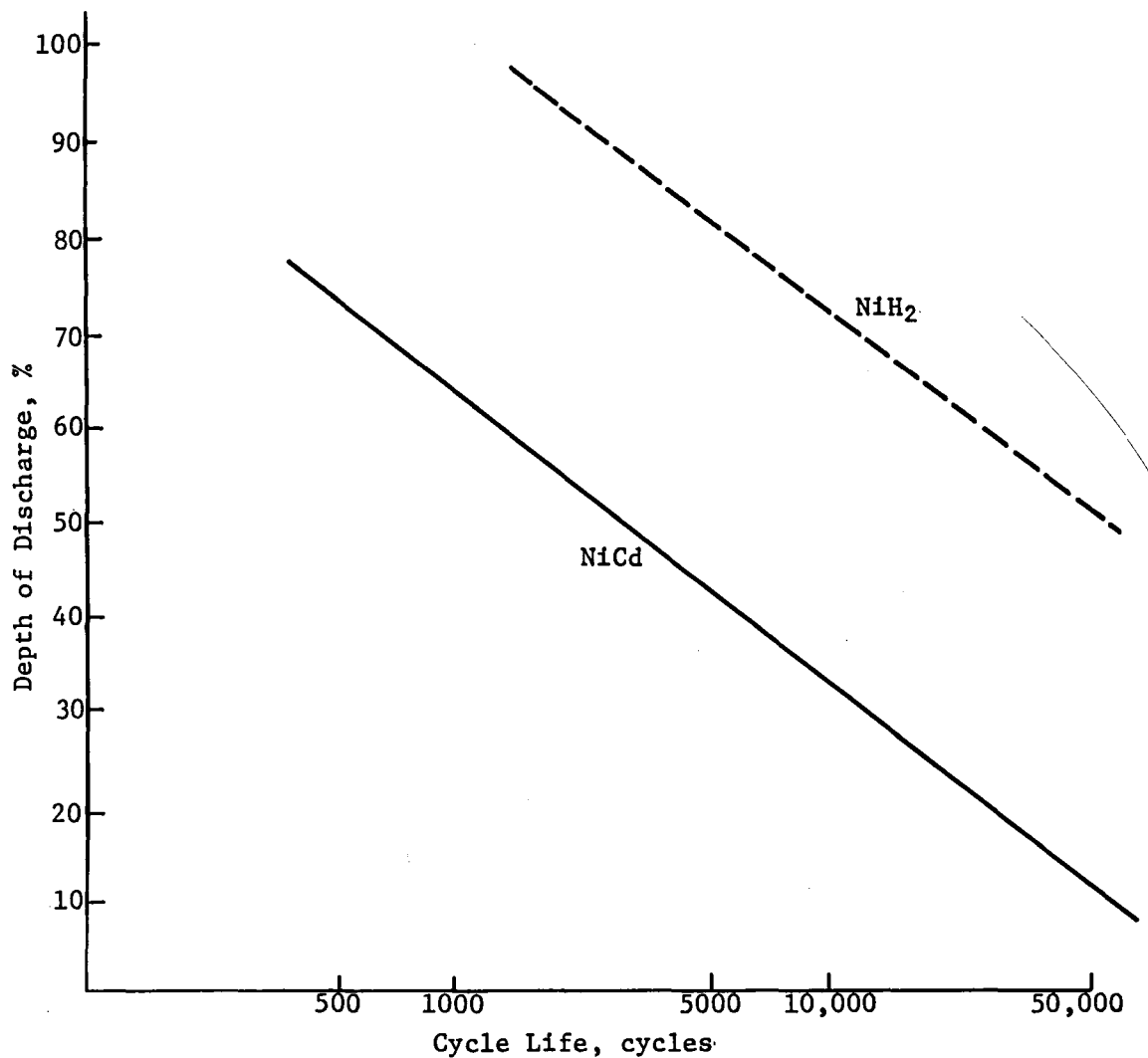
Figure 4-12 Lifetime vs Depth of Discharge

To size the required battery capacity

[7] $$C_B = \frac{P_L \times T_E}{V_B \times DOD \times L_C} = \frac{1/2 \ (2918) \times 0.58}{[30 \times 0.55 \times 0.90]}$$

$$= 57.0 \ A\text{-}h.$$

The half value is introduced because the total power load is divided between two EPMs. This value represents the maximum possible requirement. A possible solution is to use two 30-A-h batteries yielding 60 A-h of capacity.

Configuring the batteries in series for higher voltage (125 V) usually imposes packaging and weight penalties over a lower voltage configuration and later inversion to 125 volts. A battery with 60 A-h capacity and 30 volts (before inversion) has a mass of 42.7 kg. An equivalent series configured battery has almost 100 cells. Although the required capacity of each cell would be less the,difference in the pressure vessel, internal hardware and seal assemblies would only be reduced 10%.

Battery Selection - The tentative battery selected is NiH_2 composed of 24 cells. NiH_2 was selected because:

1) It has a longer expected lifetime than NiCd;

2) It has a higher DOD;

3) There is no need for reconditioning;

4) It has greater tolerance to temperature changes, overcharge, or reversal.

The primary design variable for the required battery capacity is the possible depth of discharge for the battery. A parametric analysis of equation[6]for DOD, and normalized battery capacity with respect to fixed V_B, L_C, P_L and T_E, is presented in Figure 4-13. It indicates that the total battery capacity can be reduced when the DOD is increased.

Permitting a higher DOD has several advantages, primarily savings in both weight and volume. The volume savings is important for deployable structures because attachment volume is limited and the savings increases the ratio of available energy to volume. The superiority of NiH_2 (DOD = 0.60) to NiCd (DOD = 0.30) is evident and should receive further consideration in the future.

4.3.3 Electric Power Conditioning and Management

The total spacecraft power requirements for LMR missions are on the order of 10 kW. Designing the electric power subsystem requires these considerations:

1) The power sinks, which are distributed in many different places and each has individual power requirements and load profiles, and the distances between sources and sinks may be 30 m or greater;

2) Large deployable space structures, which limit the packageability of electric power conditioning electronics because of attachment point availability and the size of both the electronics and energy storage;

3) The long mission lifetimes, which require particular consideration of reliability, redundancy, and failure mode management.
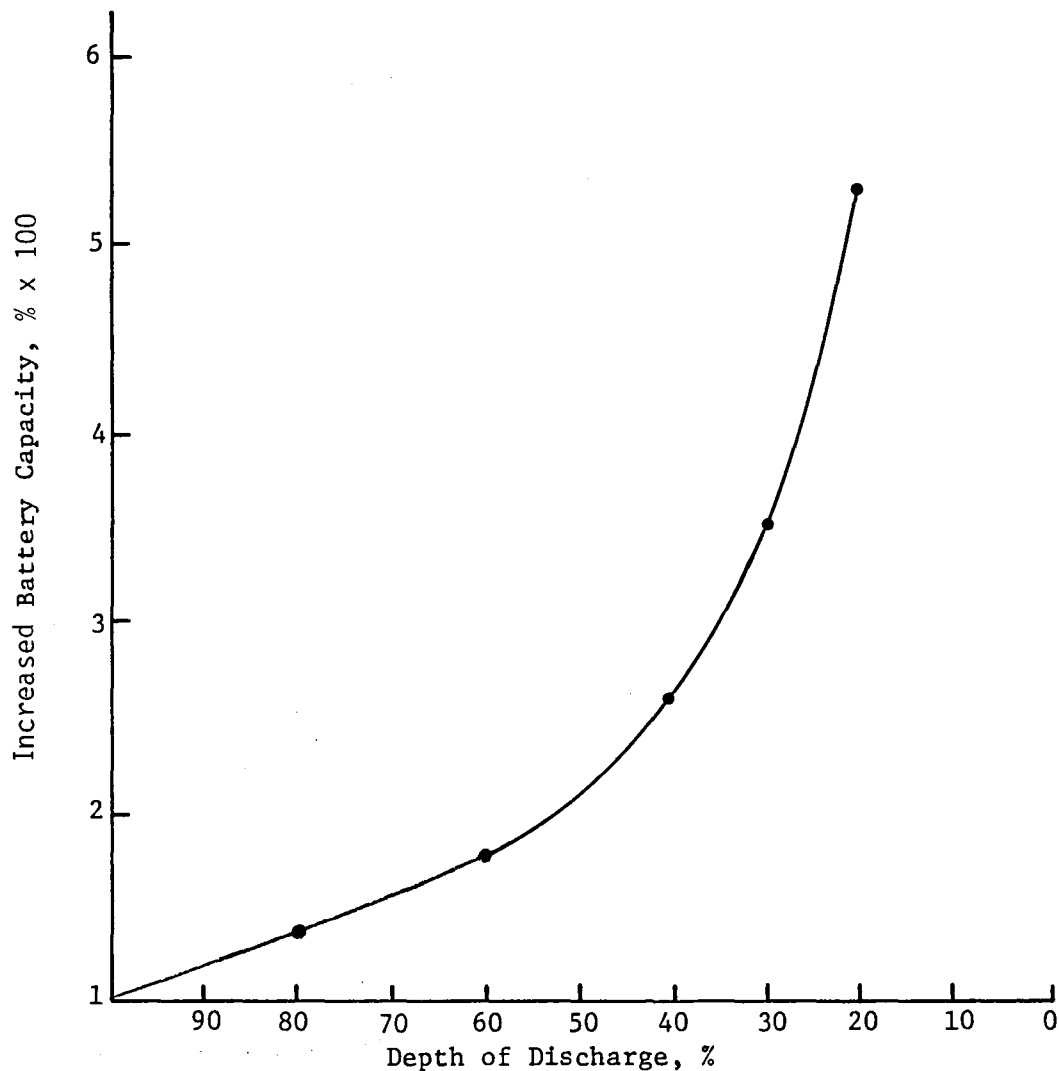
Figure 4-13   Battery Capacity for Various Depths of Discharge

Conditions 1) and 2) suggest that the electric power modules and their solar arrays should be distributed about the spacecraft as indicated in Figure 1-1. The long lifetimes require new techniques for onboard system monitoring employing microprocessor control.

The integrated modular power subsystem (IMPS) is designed to be integrated with the spacecraft structure and is located along an outer vertical of the box truss, as shown in Figure 4-14. The length for each of these subsystems may be 15 m, although a cross-sectional area is limited to 0.25 x 0.3 m. Therefore most standardized electric power components must be reconfigured.

The IMPS will contain the following subassemblies:

1) Microprocessor-controlled power conditioner;

2) NiH$_2$ energy storage;

3) Solar arrays.

Table 4-5 summarizes the approximate mass breakdown for the IMPS.

The electric power bus for EOS will be at least 125 Vdc and is required to reduce the current-handling capability for the power distribution cabling. A dc-to-dc converter of high reliability will be required. A high converter switching frequency (100 kHz) is used, enabling significant reductions in size and weight.

Inboard

4.18 m

Mounting Plate

0.24-m Cube

7.32 m

Stowed

Deployment Latch

Deployed

Battery Pack

Vertical Tube

Integrated Modular Power Subsystem Cross Section

Cube Corner Fitting (Feed Mount)

- FRUSA-Type Solar Array
- Total Area = 24 m^2
- Area per Panel = 12 m^2
- Panel Dim = 4.9x2.45 m (Two per Array)

Integrated Modular Power Subsystem

Uses Two 30-Ah NiCd Batteries

Local Microprocessor

Surface Tube Diagonal Cord Vertical Tube

15 m

Mesh Reflector

Pulsed Plasma Microthruster (Fairchild Republic)

Figure 4-14 Feed Mast Solar Array, PPT, and Integrated Modular Power Supply

Table 4-5   IMPS Mass Summary

Component	Mass, kg
- Power Regulator Unit	12
- Telemetry Interface Units	5
- Cell-Mounting Hardware	10
- Two Batteries (30 Ah, 24 Cells Each)	62
- Cabling and Miscellaneous	10
Total	99 kg

4.4   ORBIT TRANSFER SYSTEM

The orbit transfer requirements call for an altitude change from 240 to 700 km, no inclination change, and a maximum permissible acceleration of 0.01 g. A spiral transfer orbit is used with a transfer time of 6.6 h and a ΔV of 275 m/s. During this period spacecraft yaw and pitch are controlled through off-modulation of the primary propulsion thrusters. Roll is controlled by separate roll control thrusters fed by the primary propulsion propellant tanks.

Two propellant system types were examined—monopropellant N_2H_4 and bipropellant N_2O_4/MMH. The primary drivers behind these choices were system simplicity and the availability of flight-qualified components. Packaging of the propellant system was dictated primarily by the stowed configuration of the EOS in the shuttle payload bay, and is basically the same for the two candidate systems. Four thruster/tank assemblies are located on the periphery of the spacecraft antenna dish assembly at outside corners, two inboard and two outboard, as shown in Figure 4-15. Two thrusters for redundancy are mounted in the ends of the mesh reflector standoffs at these corners, providing a rigid mounting platform for the thrusters and positioning them to minimize exhaust impingement on the spacecraft structure and the antenna reflective mesh. The propellant tanks are mounted on the finned vertical structural members as shown. A separate roll thruster is mounted on a modified corner cube fitting. Tables 4-6 and 4-7 show a breakdown of the final system masses and component sizes for the monopropellant and bipropellant systems.

A preliminary survey was made of potential thruster candidates. A TRW MRE-4 thruster was chosen for the monopropellant hydrazine system outboard positions. This thruster, in a blowdown system, has a vacuum thrust range of 18.2 to 3.1 N with an inlet pressure range of 428.1 to 34.0 N/cm^2. A Rocket Research Corporation MR-50A was selected for the in-board positions. This thruster in a blowdown system has a vacuum thrust range of 44.5 to 9.8 N with an inlet pressure range of 344.7 to 48.3 N/cm^2.

A Marquardt R-6C thruster was chosen for the in-board location on the bipropellant N_2O_4/MMH system. This thruster displays a thrust range of 13.3 to 35.6 N for a feed pressure range of 69.8 to 275.6 N/cm^2 and a corresponding mixture ratio range of 1.0 to 2.4. An Aerojet AJ10-181-1 thruster was chosen for the outboard location. This thruster displays a thrust range of 9.8 N to 26.7 N for a feed pressure range of 68.9 N/cm^2 to 275.8 N/cm^2 and a mixture ratio range of 2.0 to 1.2.
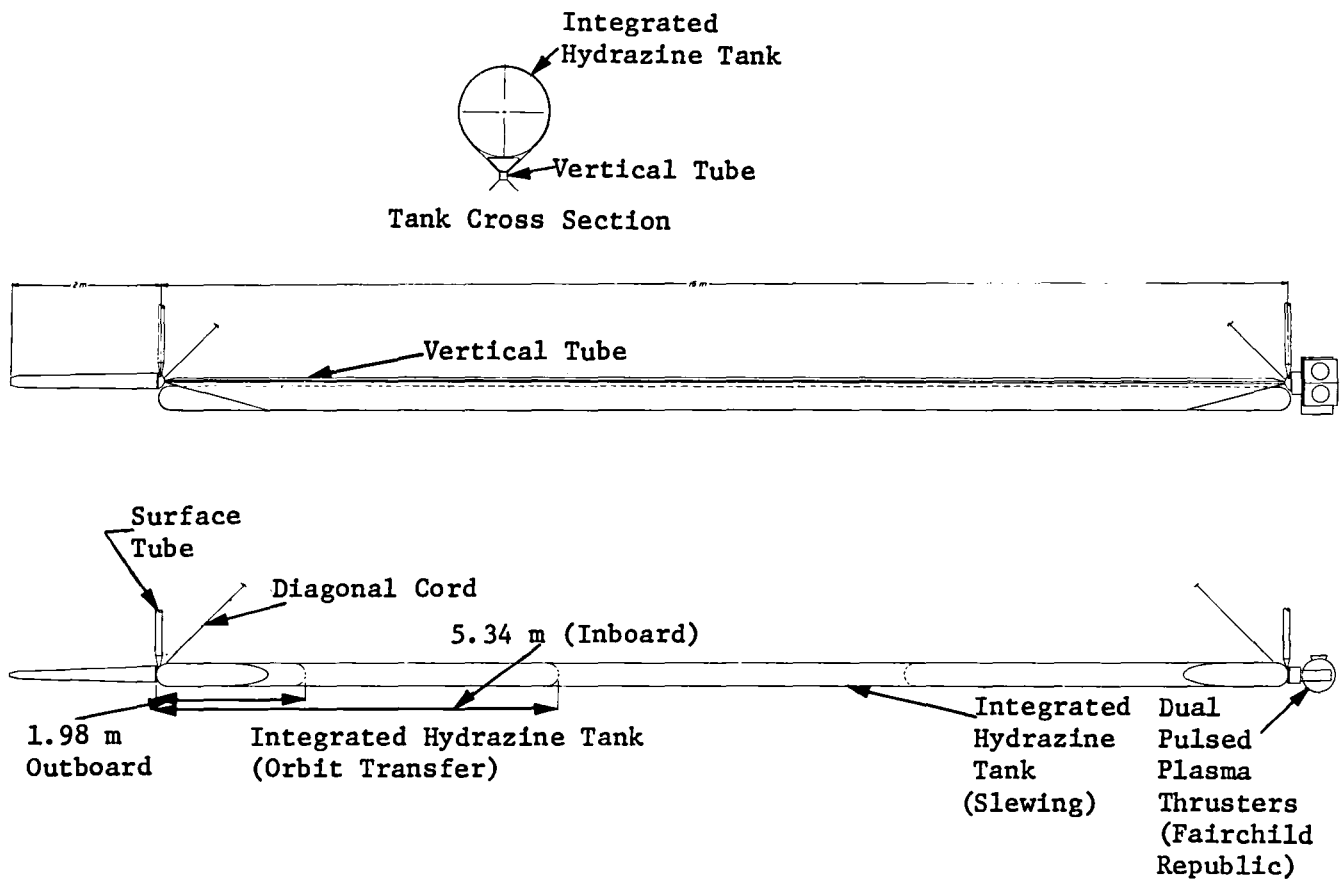
Figure 4-15   Integrated Hydrazine Tanks

Table 4-6   Monopropellant System

	Thrusters Outboard	Thrusters Inboard	System Total
Average Thrust, N	9.3	26.3	71.2
N_2H_4, kg	106.2	299.7	811.8
N_2, kg	1.0	2.8	7.6
Fluids Total, kg	107.2	302.5	819.4
V_{Tank}, m^3	0.13	0.37	1.00
Tank, kg	6.6	18.4	50.0
Components, kg	4.2	4.3	17.0
System, kg	118.0	325.2	886.4

Table 4-7 Bipropellant System

	Thrusters Outboard	Thrusters Inboard	System Total
Average Thrust, N	9.4	26.2	71.2
N_2O_4, kg	53.4	149.7	406.2
MMH, kg	22.3	62.4	169.4
N_2, kg	1.6	4.6	12.4
Fluids Total, kg	77.3	216.7	588.0
N_2O_4 Tank, m^3	0.04	0.11	0.30
MMH Tank, m^3	0.03	0.08	0.22
N_2 Tank, m^3	0.01	0.02	0.06
N_2O_4, kg	1.1	3.3	8.8
MMH Tank, kg	0.7	2.2	5.8
N_2 Tank, kg	1.7	5.1	13.6
Tank Total, kg	3.5	10.6	28.2
Components, kg	13.2	13.3	53.0
System, kg	94.0	240.6	669.2

Both the monopropellant and bipropellant systems studied for this project met the packaging and performance requirements for the earth observation satellite. Largely because of its significantly lower I_{sp}, the monopropellant system proved to be somewhat heavier and required a greater volume than the bipropellant system. However, this disadvantage was offset by the poorer reliability of the bipropellant system because of its greater complexity. The monopropellant system was selected for the EOS design and its integration with a vertical member is shown in Figure 4-15.

4.5 ATTITUDE CONTROL FOR SENSING

The orbit maintenance, attitude control, and position of the spacecraft vary with each mission. The inclusion of imaging sensors places strict requirements on the LMR structure when it is used as a platform for other sensors. The specific requirements for both radiometry and optical sensing have been reviewed.

4.5.1 Radiometry

The image and, consequently, attitude tolerances are expressed in terms of ϵ, which is a specific fraction of the assigned resolution element. In this definition, ϵ is the largest dimension of the smallest rectangle containing 50% of the total power collected. For all EOS microwave radiometer missions, $\epsilon = 0.6$ mrad (0.033 deg).

The attitude control system is designed to maintain the following image tolerances;

1) Changes in the X-axis (roll) shall not exceed ϵ to maintain cross-scan contiguity or to minimize gaps or overlaps;

2) Changes about the Y-axis (pitch) shall not exceed 2ϵ to maintain along-scan displacement;

3) Changes about the Z-axis (yaw) shall not exceed 2ϵ to minimize geometric distortions.

4.5.2 Optical Imaging Missions

The orbit determination accuracy and the attitude control capability become significantly more stringent if the LMR is used as a platform for high-resolution imaging sensors. While the improved orbit ephemeris and attitude jitter requirements are independent, both must be resolved if the proposed EOS missions are to be implemented.

4.5.2.1 Orbit Determination — Knowledge of the orbit trajectory and the cartographic position of the subsatellite point at a particular time is necessary for the multispectral resource scanner included in Missions II and III. This instrument has a command-pointable capability permitting it to image scenes of interest off axis. This pointing capability requires frequent spacecraft position data, making it desirable to have ephemeris updates generated onboard to minimize ground control interaction.

The required knowledge of spacecraft position in both the along-track and crosstrack vary with ground resolution and altitude. The required accuracy of orbit elements when the ground resolution is normalized to 1 m is given by $1 + h/R$, where h is the orbit altitude and R is the radius of the earth. This is plotted in Figure 4-16 (NASA 1973).* The error is on the order of 30 m or less (one sigma) for the EOS altitude of approximately 700 km.

The regularity of satellite motions have enabled positions to be calculated on the order of 100 m using equations of motion and compensation for perturbations. A large space structure such as EOS, however, may not exhibit such regular motion because of a smaller ballistic coefficient and its greater susceptibility to drag and other disturbances. Therefore EOS will need to use orbit ephemeris updates from either the global position satellites or TDRSS.

---

*Advanced Scanners and Imaging Systems for Earth Observation, NASA SP-335, 1973.

4.5.2.2 <u>Attitude Control</u> – The short-term changes in spacecraft atti-
tude (jitter) are particularly detrimental to imaging systems. Errors
in pitch and roll distort the frame and affect spatial registration of
scene pixels. Errors about the vertical (yaw) affect the cartographic
positioning. Short-term perturbations are more significant in image
deterioration than slow ones. Perturbations with long periods repre-
sent systematic errors that can be corrected.
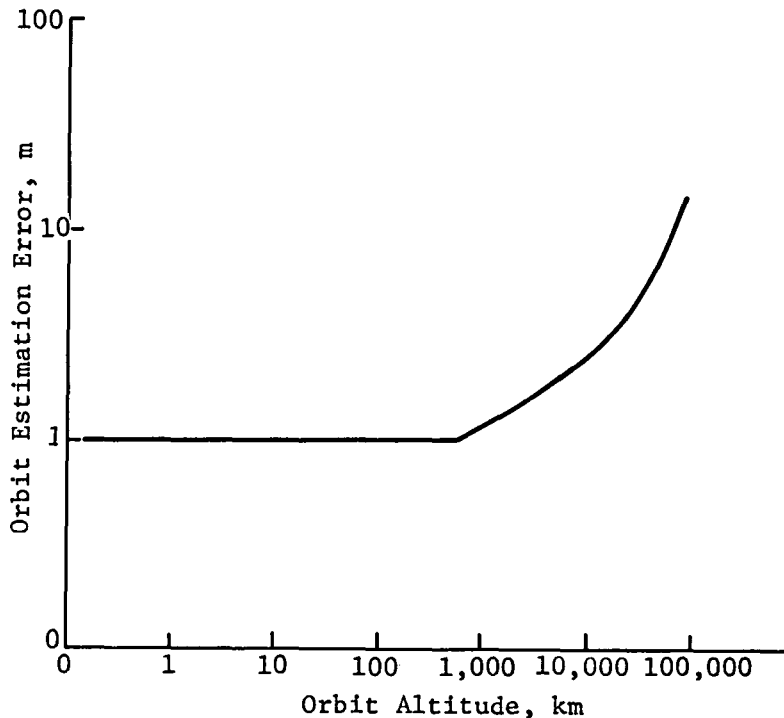
Figure 4-16 Position Error

Strict platform stability requirements are imposed on scanners that use
the motion of the spacecraft to produce images. This includes all the
sensors on EOS Mission II. The short-term stabilization in roll and
pitch should be maintained to 1/6 of the instantaneous field of view
(IFOV). The multispectral linear array (MLA) has an allowable error of
5 m, or approximately 0.2 arc-s (0.003 deg). Figure 4-17 illustrates
the stability error requirement, or, alternatively, the attitude deter-
mination accuracy for a remote-sensing platform. These tolerances must
be maintained during the 27 seconds required to record a scene.

The problem with attitude determination is compounded when structural
dynamics are included. The attitude sensors, i.e., star tracker, may
be at a different location than the earth remote sensor. The differen-
tial flexure of past spacecraft has been minimal, but not negligible.
Large space structures are anticipated to have considerably more flex-
ure than their rigid-body predecessors, necessitating new solutions and
much better structural definition.

The star tracker provides the platform attitude reference. Current
technology such as the NASA Standard Star Tracker used on the
Multimission Modular Spacecraft is adequate for this application,
although star trackers using solid state detectors might be substituted
to increase lifetime. Such a device is being developed by Ball
Aerospace Systems Division and uses a charge injection device (CID) as
the detecting and scanning element. These devices are relatively small
(approximately .170x.180x.31 m) such that they can easily be integrated
onto the forward part of the science platform.

An integral component of the flexure monitoring system is the
autocollimator and remote alignment reflectors. This system will
permit three axis angular deviations to be measured with an overall
accuracy of approximately 0.25 arc-s in the two axes orthogonal to the
long axis (x) of the platform and about 2.25 arc-s in the measurement
of roll.* The optical path for the laser light beam, and the prism
reflectors are inside the unused portion of the truss. This technology
is also within current capability.

The attitude information obtained with the platform monitoring system
is transmitted via the high speed data bus to the onboard computer and
communication system. The information will be included as part of the
annotation tapes that are transmitted with the sensor telemetry. These
tapes also provide satellite ephemeris and other data required to
process images and remove geometric and other distortions caused by
image motion.
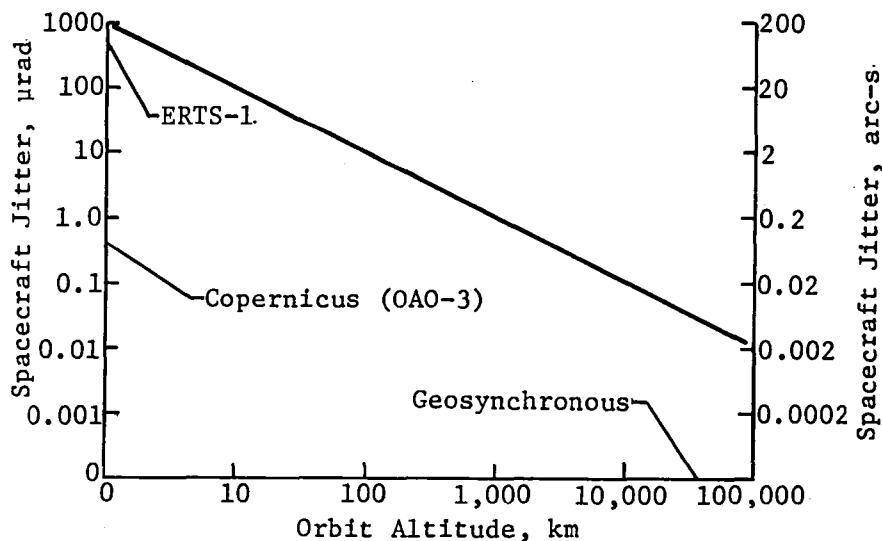
Figure 4-17 Stability Error Requirement

*Collyer, P. W., "Flexture Monitor System for Spacecraft," AIAA Guidance and
Control Conference, August 14-16, 1972, AIAA Paper pp72-855.

The expedient of placing all sensors on a single beam, or pallet, as
detailed in Section 4.2, permits using such advanced isolation devices
as the Gimbalflex fine-pointing system developed at Martin Marietta.*
The Gimbalflex concept, or other high-order controllers, provide high
pointing accuracies and platform stabilities even in severe disturbance
environments. An active isolation-controlled platform will be included
on an LMR carrying imaging sensors.

4.6 DATA MANAGEMENT

The data management subsystem is intended to control all spacecraft
operations. The information manipulated by the data management system
includes scientific data, GN&C housekeeping, and commands to the space-
craft. The goal was to use the instrument sets previously described to
arrive at a strawman design. Technology needs could be identified,
with the final result being an efficient end-to-end system.

4.6.1 Data Rates

This section explores the magnitude of the data rates possible for
these types of missions. Obviously these cannot be final tallies, but
are representative of those anticipated. The sensors used are those
defined in Section 2.3.

4.6.1.1 Scientific Data Rates - An initial survey of the gross data
rates for imaging sensors can be staggering. The rates for these in-
struments nominally reach 50 Mbps or more, while the EOS Mission II
(land observation) has three such instruments. The capacity of many
data storage and transmission systems would be quickly exhausted. Cal-
culating the data rates moderated with the duty cycles for the instru-
ments presents a more realistic assessment of the situation. This is
the method used in this report.

Microwave Radiometer - The data rates for a microwave radiometer depend
on altitude, swathwidth, ground resolution, quantization and the number
of bands used. The radiometer operates in the pushbroom mode with the
feeds arranged in a linear array, as described in Section 3.1. The
ground swath is composed of contiguous parallel footprints moving along
in parallel because of the forward motion of the spacecraft. The data
rate for such an instrument is not excessive as shown in the example.

The ground swath is composed of the contiguous ground footprints shown
in Figure 4-18. The solid circles represent the diameter of one foot-
print on the earth's surface at the start of a time interval. The
dashed circles represent the number of footprints of the higher fre-
quency bands that are contained in the lowest frequency footprint, and
is the "factor" term.

---

*Osborne, N. A., "Gimbalflex 5 Degree of Freedom Inertially Stabilized
 Platform," AAS Paper No. 80-015, AAS Guidance and Control Conference,
 February 17-21, 1980, Keystone, CO.
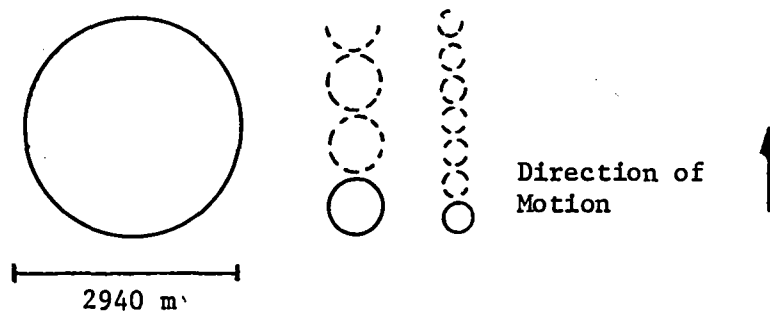
Figure 4-18   LMR Ground Footprints

The ground track velocity V_g = 6700 m/s. Therefore, the time required to cross the lowest frequency footprint element is

$$\frac{2940}{6700 \text{ m/s}} = 0.435 \text{ s.}$$

During this time, the 5.5-GHz footprint covers 3.34 footprints and the 10.68 GHz covers 7.13 elements when referenced to the largest element. This is summarized in Table 4-8.

Table 4-8   Swath Data Summary for LMR

Frequency, GHz	Wavelength	Ground Resolution, km	No. Horns	Factor	No. Samples*
1.4	0.2	2.94	58	1	58
5.5	0.06	0.88	90	3.34	300
10.68	0.028	0.41	176	7.13	1267

*Total number of samples per swath = 1644.

To provide an upper limit to the data rate, the bit quantization per sample footprint is 18. This might include 12 bits for signal and 6 bits for other telemetry. The total data rate then is

$$\text{Radiometer data rate} = \frac{\text{(total samples/swath) (bits/sample)}}{\text{time/swath}}.$$

Ideally we like to have dual polarization so the total rate is now

$$\text{Radiometer data rate} = \frac{2(1644)(18)}{0.435} \text{ kbps}$$

$$= 136.055 \text{ kbps.}$$

92

Synthetic Aperture Radar - Synthetic aperture radars have the potential
of generating data rates over 100 Mbps. The data rate out of the
radar, N, may be expressed as

[8]
$$N = \frac{2N_b (T + t)c (PRF)}{R_r}$$

where

N_b = number of bits per sample,
T = required sample interval,
t = pulsewidth,
c = speed of light,
R_r = range resolution,
PRF = pulse repetition frequency.

Although the data rates are highly design dependent, data rates on the
order of 110 mbps are anticipated.

Atmospheric Sounding Radiometer (ASR) - The ASR operates at three fre-
quencies—18, 21, and 37 GHz. Table 4-9 is similar to that shown for
the LMR. The data rate for this instrument is well within the capabil-
ity of state-of-the-art data management systems.

Table 4-9 Swath Data Summary for ASR

Frequency, GHz	Wavelength, cm	Ground Resolution, km	No. Spot	Factor	No. Samples
18	1.7	10.0	20.0	1.0	20
21	1.4	8.6	23.0	1.16	27
37	0.81	5.0	40.0	2.0	80
				Total	127

The maximum scan time across the swath is restricted by the time for
the spacecraft to cross the smallest footprint in the along-track
dimension, or about 0.75 second. The data rate for the ASR is

Radiometer data rate = 2 x $\frac{\text{(samples/swath)} \times \text{(bits/sample)}}{\text{time/swath}}$

= 7034 bps.

Because the instrument has dual polarization, the data rate = 7034 bps.

Table 4-10 summarizes the total scientific data rates for the EOS base-
line mission not modified by duty cycles.

Table 4-10 EOS Baseline Data Summary

Sensor	Data Rate, bps
Large Microwave Radiometer (LMR)	136,055
Atmospheric Sounding Radiometer (ASR)	7034
Synthetic Aperature Radar (SAR)	110,000,000
Total	110,143,089

EOS Mission II, Land Observation - Table 4-11 shows the gross data rate summary for this mission. Included are the new sensors specifically provided for land remote sensing and those of the baseline configuration.

Table 4-11 EOS Mission II Scientific Data Rates

Sensor	Data Rate, Mbps
Multispectral Linear Array (MLA)	44.90
Multispectral Resource Scanner (MRS)	15.00
Mid-IR Imager (MIRI)	11.38
Synthetic Aperture Radar (SAR)	110.0
Atmospheric Sounding Radiometer (ASR)	0.007
Large Microwave Radiometer (LMR)	0.136
Total	181.423

EOS Mission III, Ocean and Coastal Zone - Table 4-12 presents the gross data rate for this mission.

Table 4-12 EOS Mission III - Ocean and Coastal Zone

Sensor	Data Rate, Mbps
Coastal Zone Color Scanner (CZCS)	1.000
Multispectral Resource Sampler (MRS)	15.000
Radar Altimeter (ALT)	0.0085
Scatterometer (SCATT)	0.00054
Microwave Radiometer (LMR)	0.136
Atmospheric Sounding Radiometer (ASR)	0.0074
Total	16.1524 Mbps

EOS Mission IV, Atmospheric Observation - Table 4-13 presents the gross scientific data rate for the atmospheric mission.

Table 4-13 EOS Mission IV - Atmospheric Observations

Sensor	Data Rate, Mbps
IR Scanning Radiometer	0.008
Correlation Interferometer	0.003
Filter Radiometer (FR)	0.006
Advanced Meteorological Temperature Sounder (AMTS)	0.003
Large Microwave Radiometer (LMR)	0.136
Atmospheric Sounding Radiometer (ASR)	0.0074
Total	0.1634

The total data rate for these missions represents the greatest burden on the data management system. To fully exploit the full remote sensing capabilities of the mission, it is conceivable that such rates be sustained for the time required to record a scene frame of 180x180 km. This requires approximately 30 seconds and represents 5400 Mbps of information. A useful characterization of the data management problem is to specify an interval between these data spurts. Section 4.6.3.2 uses this perspective to discuss multiplexing, storage and transmission of the data.

4.6.1.2 Engineering Data Rates - The engineering data rates represent a considerable increase in volume over past satellites. The data consist of housekeeping to be downlinked with the scientific data, and uplink commands to the spacecraft. The engineering telemetry was determined primarily from the LMR and spacecraft subsystems. The change from one mission to another does not appreciably alter the total.

The engineering data rate for the LMR is 15.5 kbps. This number represents the data stream required if engineering data are continuously needed for the 324 receivers. The exact amount has not been finalized because the sampling frequency has not been fully determined. An additional 10 kbps is used to monitor the other subsystems.

4.6.2 TDRSS Capability

The data produced by the satellite must be returned to the ground. The purpose of this section is to determine the nature of the problems required for this transmission. The return link services of the tracking data relay satellite system (TDRSS) are assumed to be the primary link to the ground. Analysis of these services was undertaken to determine if an intractable data bottleneck exists, and perhaps stimulate the need for a more elaborate data management system.

4.6.2.1 Services Available - The TDRSS has several return link telecommunication devices available to users.

MA Service - The multiple-access (MA) service can provide dedicated service to users at data rates up to 50 kbps during the time the TDRSS is visible (typically 85% of the time).

SA Service - The single-access (SA) service can provide high data returns of up to 300 Mbps. This service cannot be used for dedicated mission support and is used on a priority-scheduled basis. This channel might provide the data link for high-speed dump of recorded data.

The SA service is further divided into the S-band single access (SSA) and the Ku-band single access (KSA). These return communication links have different operating characteristics.

Cross Support - The cross support service can provide dedicated MA support with periodic SSA service of 3.15 Mbps.

Two signal designs are available to return link service users, and are defined as either Data Group 1 (DG1), modes 1, 2, 3, or DG2 signals. These operating modes specify the way the signals are encoded. The reader is urged to consult the original document for a thorough description of TDRSS characteristics.*

Table 4-14 summarizes the return link signal parameters for the two data groups (DG1 and DG2).

Table 4-14 TDRSS Return Link Services

Parameter	Definition MA	SSA	KSA
DG1			
Mode 1 Data Rate Restrictions			
Total	0.1–50.0 kbps	0.1–300 kbps	1–600 kbps
I-Channel	0.1–50.0 kbps	0.1–150 kbps	1–300 kbps
Q-Channel	0.1–50.0 kbps	1.0–150 kbps	1–300 kbps
Mode 2 Data Rate Restrictions			
Total	1–50 kbps/s	1.0–300 kbps	1–600 kbps
I-Channel	1–60 kbps	1.0–150 kbps	1–300 kbps
Q-Channel	1–50 kbps	1.0–150 kbps	1–300 kbps
Mode 3 Data Rate Restrictions			
Total	I + Q	I + Q	I + Q
I-Channel	0.1–50.0 kbps	0.1–150 kbps	1–300 kbps
Q-Channel	1.0 kbps–1.5 Mbps	1 kbps–3 Mbps	1 kbps–150 Mbps
Carrier (F₁) Reference, Hz			
Modes 1 and 3	−	−	−
Mode 2	Spacecraft Oscillator	Spacecraft Oscillator	Spacecraft Oscillator
DG2			
Carrier (F₂) Reference, Hz	NA	Carrier Frequency or Spacecraft Oscillator	Carrier Frequency or Spacecraft Oscillator
Data Format	NA		
Without Convolutional Coding		NA	NRZ-L, NRZ-M, NRZ-S
With Convolutional Coding		NRZ-L, NRZ-M, NRZ-S	NRZ-L, NRZ-M, NRZ-S
Data Rate Restrictions			
Total	NA	I + Q	1 kbps–300 Mbps
I-Channel	NA	1 kbps–3 Mbps	1 kbps–150 Mbps
Q-Channel	NA	1 kbps–150 kbps	1 kbps–150 Mbps
Symbol Interleaving	NA	See para 3.3.2.3a(4)*	NA
Data Modulation	NA	QPSK or BPSK	QPSK or BPSK

*Tracking and Data Relay Satellite System (TDRSS) User's Guide, STDN No. 101.2, Goddard Space Flight Center, 1980, Rev 4

---

*Tracking and Data Relay Satellite System (TDRSS) User's Guide, STDN No. 101.2, Goddard Space Flight Center, 1980, Rev 4.

4.6.3 LMR Data Rates and Operational Protocols

The large microwave radiometer produces a constant 140-kbps science data plus 20 kbps of engineering telemetry. This does not tax the present system in throughput, but will present scheduling and priority conflicts because a dedicated link through TDRSS cannot be established for it. Two possible options exist:

1) Record the data in real time onboard the spacecraft and play the information back at high speed through TDRSS;

2) Continually multiplex and route data through TDRSS channels as they become available.

4.6.3.1 Operating Protocols/Duty Cycles for Imaging Sensors - The complexity of the data management system is compounded by the potential for simultaneous operation of three or more high data rate sensors. To take maximum advantage of the synergistic benefits afforded by the sensor sets, concurrent observations must be made with various instruments. The sensor grouping of Mission II (land observation) contains multiple multispectral imaging sensors, each with approximately 30-Mbps data rates. It is the most difficult of all missions and is considered in detail here.

It is difficult to extrapolate the expected duty cycles for these imaging systems although an initial point might be the image throughput capability of the image processing facility at Goddard Space Flight Center for LANDSAT 4. Plans call for a potential of processing 100 thematic mapper images per day by 1985, with each scene containing 1.78×10^9 bits. The maximum throughput for MSS imagery is 200 scenes/day with 1.68×10^8 bits/scene although the average user demand is 89 images/day.

Table 4-15 summarizes the possible operating protocols for telemetry transmission options discussed in this section.

Table 4-15   Data Telemetry Protocols

Option	Sensor	Date Rate, Mbps	Duration, s	Imaged Area, km	TDRSS Service
1	MLA	45	26	180 x 180	DG2, KSA
2	MLA	45	26	180 x 180	DG2, KSA
	MRS	15	2	30 x 30	
3	MLA	45	26	180 x 180	DG2, KS
	MRS	15	2	30 x 30	
	MIRI	11	26	180 x 180	

The simplest operating mode for the sensors is to consider them working individually at regular intervals during the orbit. This is a reasonable assumption and similar to the single scenes taken by LANDSAT-type spacecraft. However, maximum benefit, as demonstrated in Section 2.4, requires simultaneous observations.

The multispectral linear array for EOS contains 1.18 x 10^9 bits/scene, which is comparable to the present-day telemetry images of LANDSAT 4. Assuming a rough correlation in image processing complexity, the maximum limit is 100 scenes/day, which can only be taken during daylight portions of the orbit because there is no IR imaging capability

$$\frac{1 \text{ day}}{14.5 \text{ orbits}} \quad x \quad \frac{100 \text{ images}}{1 \text{ day}} \quad = \quad 6.89 \frac{\text{images.}}{\text{orbit}}$$

The MLA can only record data during daylight so

$$\frac{1 \text{ orbit}}{6.89 \text{ scenes}} \quad x \quad \frac{1/2 \ (5880 \text{ s})}{1 \text{ orbit}} \quad = \quad 426 \text{ s/orbit.}$$

Each scene requires approximately 26 s to take the MLA data through TDRSS and transmit them in real time. The transmission interval has a period of 400 s. This does not represent a problem.

The multispectral resource scanner is not intended to provide global coverage like the MLA, but to provide specific high-resolution imagery for selected areas. These images contain 3.2 x 10^7 bits/scene. For this analysis it was assumed that the MRS would provide ancillary images to the MLA during every second scene, or a duty period of 800 s. The data produced by the MRS could easily be transmitted in real time. When data are concurrent with MLA, the same TDRSS service can be used (protocol 2).

The concurrent data sampling of the same scene by the mid-IR imager (MIRI) is handled in a similar manner. This is protocol 3 of the data protocol table. The data throughput capability for this TDRSS service is not taxed by this scenario. It does, however, require a complex data controller or multiplexer, and a high-speed high-capacity buffer. Such an instrument does not exist although the technology for its development does.

An alternative is to use separate TDRSS channels for each of these sensors. The primary problem is not the data rates themselves, but the duration of time that a TDRSS channel is burdened. The SSA and KSA links are scheduled on a priority basis, and it is impossible to determine the user demands at this time. The data return problem is quite manageable if the high data rate links can be dedicated for approximately 30 s every 400 s.

4.6.3.2 Operating Protocols for Data Management - The missions presented in this study constitute four separate data management problems because of the diverse sensor complement and imaging requirements. The data management designs, and the technology needs required to implement them, are for typical, but nonetheless complex, remote sensing observation scenarios for each mission.

The data output for the LMR does not burden the input or storage capability of current magnetic tape read/write storage devices. The primary disadvantage is the short lifetime relative to the anticipated EOS

mission. These devices are limited to three- to five-year lifetimes, and would require two or three levels of redundancy to complete the mission.

A promising alternative to magnetic tape is to use solid-state magnetic bubble memories. This memory technology offers high density, high re-liability, and good radiation characteristics. Toussan, et al.* has described a magnetic bubble recorder with 60 Mbits of storage, serial data transfer at 500 kbps with parallel possible, and a reliability of R = 0.9 over five years. The predicted MTBF for another prototype re-corder described by Steury[+] was 41,000 hours.

With further development, solid-state data recorders will have suffi-cient capacity to store all LMR data for an entire orbit and read at rates of 50 Mbps. The lifetimes demonstrated are encouraging.

---

*M. Toussan, J. C. Gidrol, and M. Poirier: "A Magnetic Bubble Recorder for Space Applications," Proc Internl Conf on Spacecraft Onboard Data Management, ESA SP-141, Nice, 24-27 October 1978.

[+]T. M. Steury: "Bubble Memory Technology," Proc Internl Conf on Spacecraft Onboard Data Management, ESA SP-141, Nice, 24-27 October 1978.

5.0   STOWAGE AND DEPLOYMENT

Stowage and deployment are covered in the following three subsections concerning the stowed configuration, the cradle assembly (including ejection of EOS from the STS payload bay), and deployment.

5.1   STOWED CONFIGURATION

Many of the design constraints of the EOS were driven by the dimensions of the cargo bay, which is approximately 4 m in diameter and 18 m long. Other factors such as center of gravity locations and hatch doors also had to be considered. Figure 5-1 shows the stowed EOS package. When viewed end-on, the stowed box truss elements form an inverted T. The thin leg of the T is the feed mast on which the folded feed array beam, two battery packs, two solar arrays, the spacecraft management and control module, and two single-unit stationkeeping thrusters are mounted. The ASR panels and two more single-unit stationkeeping thrusters are mounted on the feed array beam. The mesh support structure forms the fattened arm of the T. On this is mounted a science pallet, four battery packs, four solar arrays, four twin unit stationkeeping thrusters, two Ku-band antennas, and the orbit transfer/slewing subsystem, the nozzles for which are mounted to mesh standoffs directly in front of the tanks. The feed mast and the mesh support structure are structurally linked through three offset feed support hinges, three knee braces, and three cross braces. See Section 3.3.8 for a more detailed discussion of this interface region.

The overall length of the stowed EOS is 17.8 m. 15 m of this length is taken up by the stowed box truss elements. Another 2 m was allotted for the mesh support standoffs. The remaining 0.8 m is taken up by subsystems located on the backside of the spacecraft. The overall width is 3.75 m. The stowed feed array beam, not the stowed antenna support truss elements, drive this dimension. The stowed height measured from the backface of the feed mast battery packs to the mounting surface of the stowed science pallet is 3.53 m. Another 0.6 m of height is available for instrument stowage on the science pallet. A cross-sectional view of the effective stowage area available for science pallet instruments is shown in Figure 5-2.

In the stowed configuration, the box truss cube corner fittings butt against each other forming a plane at the top and bottom surfaces. The plane formed by the cube corner fittings provides a load path for loads incurred during launch, with inplane shearing loads handled by interlocking pins between fittings.
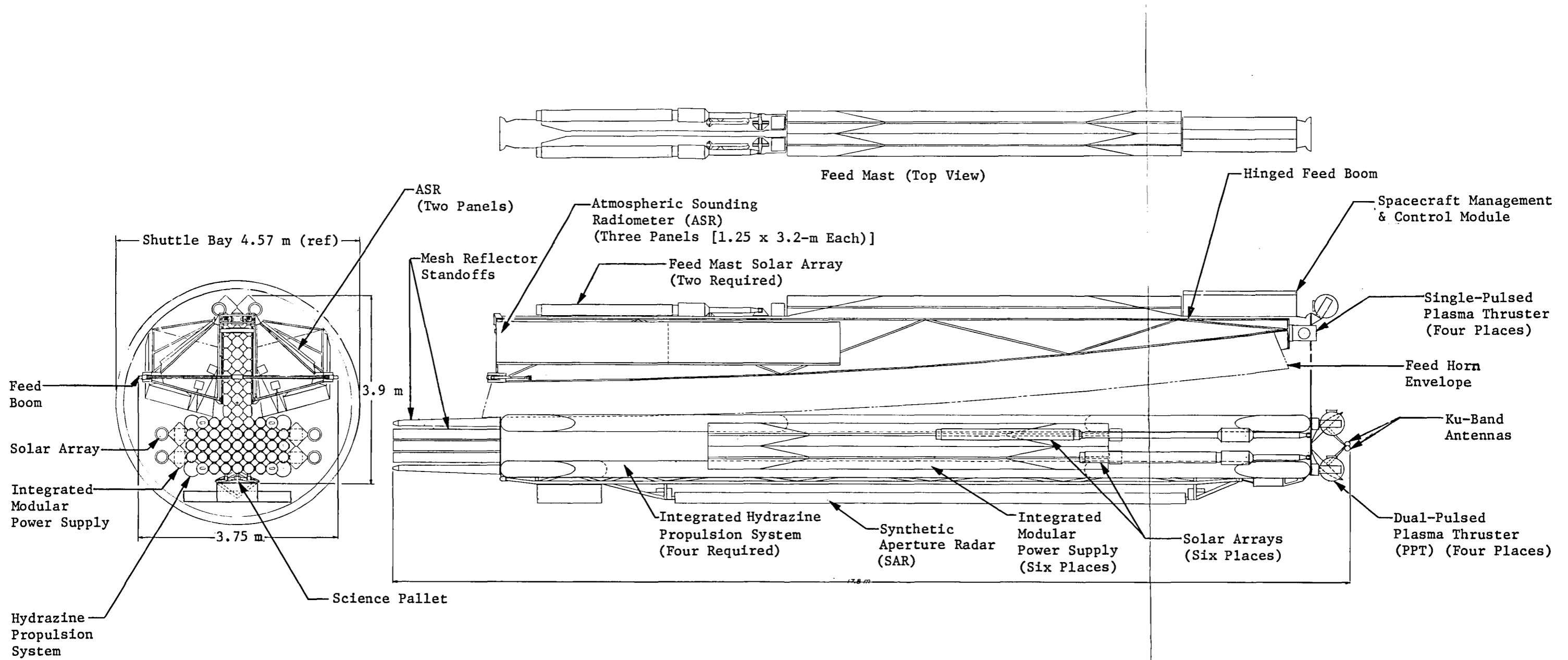
Figure 5-1 Stowed EOS Configuration
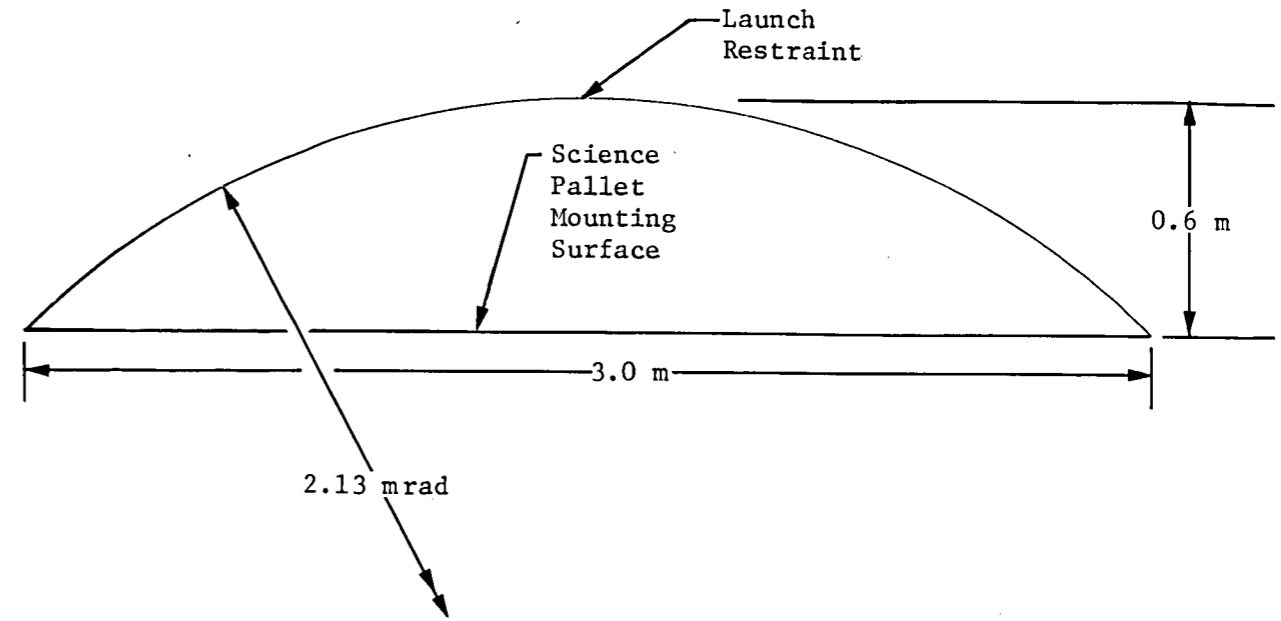
Figure 5-2 Stowage Area Available for Science Pallet-Mounted Instruments

5.2   CRADLE ASSEMBLY

The cradle assembly will be used in flight operations, ground handling, and ground transportation. The stowed spacecraft is installed in the cradle assembly at the manufacturing facility and remains there until the spacecraft is injected into its deployment orbit.

The cradle assembly consists of a launch cradle and two yoke assemblies. Each yoke assembly contains two telescoping arms that connect to the cradle. Figure 5-3 shows the cradle assembly positioned in the orbiter bay.

During launch, the cradle is secured to the orbiter bay by a four-point determinant mounting pattern. The yoke assemblies are also mounted to the orbiter bay and are decoupled from the launch cradle to protect them from damage during launch. The ejection sequence is started by lifting the cradle out of the orbiter cargo bay with the telescoping arms. The cradle door is then opened and the spacecraft is guided out of the cradle assembly by the remote manipulator arm (RMA).

The 17.8-m stowed length of the EOS spacecraft was the determining factor in the selection of this design approach. An alternative approach, lifting the spacecraft out of the cradle with the RMA while the cradle remains in the bay, was rejected because only ±0.25 m would be available for spacecraft pitch motion. This clearance envelope was determined to be insufficient for a successful manipulator arm-powered deployment from the orbiter bay.

Spacecraft
Ejection
Path

¢ Launch Cradle
Deployed for
Spacecraft
Release

Cradle
Deployment
Mechanism
Stowed.

5.08 m

Cradle Deployment
Mechanism Fully
Extended

¢ Launch Cradle
Stowed

Yoke

View F-F
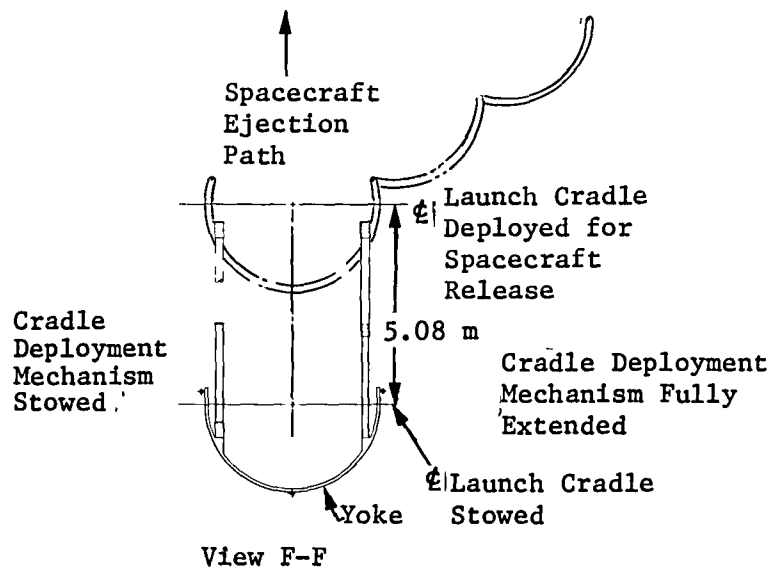
Legend:

A   Cradle Longeron Retention Trunnion

B   Cradle Keel Retentention Trunnion

C   Yoke Longeron Retention Trunnion

D   Yoke Keel Retention Trunnion

Cradle Deployed

F

17.8-m Launch Cradle

18.29-m Dynamic Envelope

4.57-m Dia
Dynamic
Envelope

C

¢ Cradle

A

A

C

B

D

F

D

Power Bus

Signal and Control
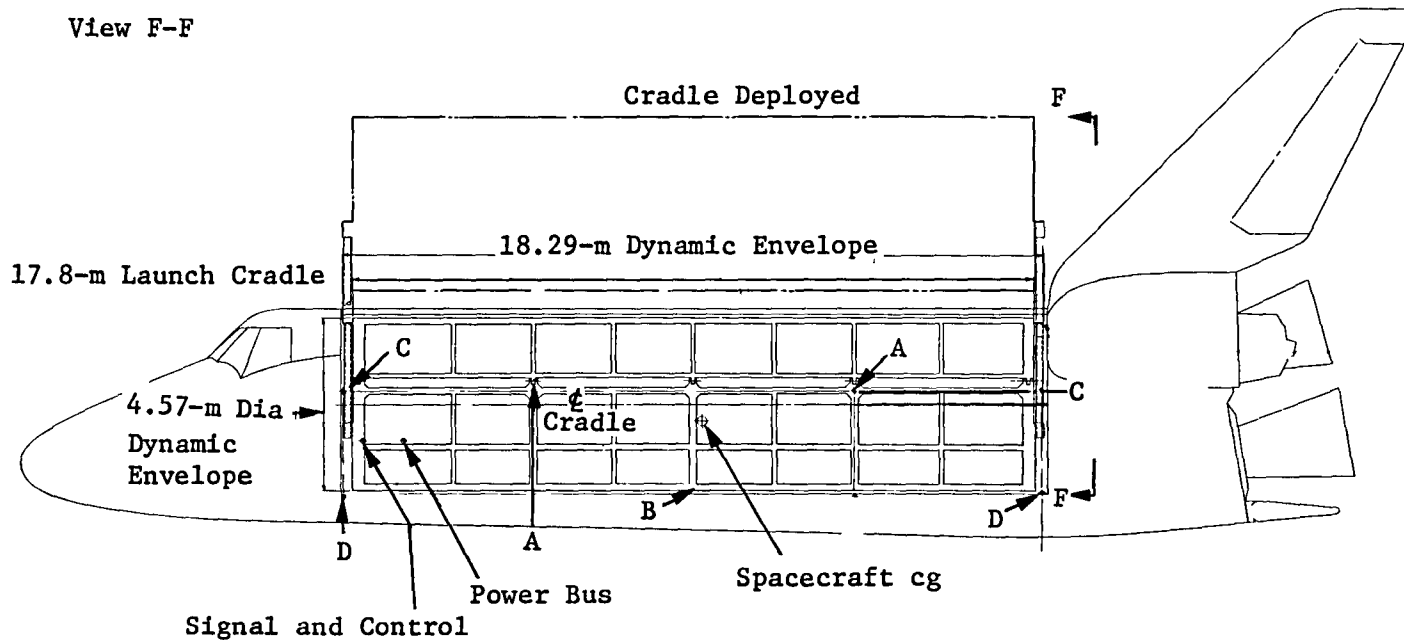
Spacecraft cg

Figure 5-3   Launch Cradle

Figure 5-4 shows the ejected but undeployed EOS spacecraft. The stowed feed mast is sandwiched between the folded feed beam. The gap between the feed beam halves is approximately 66 cm (the width of three cube corner fittings). The cube corner fittings that will support the feed beam are located in the top two rows.

Linear
Bearing

Hinge Arms

A

Feed
Half

Arm Containing
Linear Bearing

B

Motor
Drive

Nut

Five-Element
1.4-GHz
Feed
Horns

5.5-GHz Feed
Horns

10.7-GHz Feed
Horns

Feed
Mast
Structure

Main
Reflector
Structure
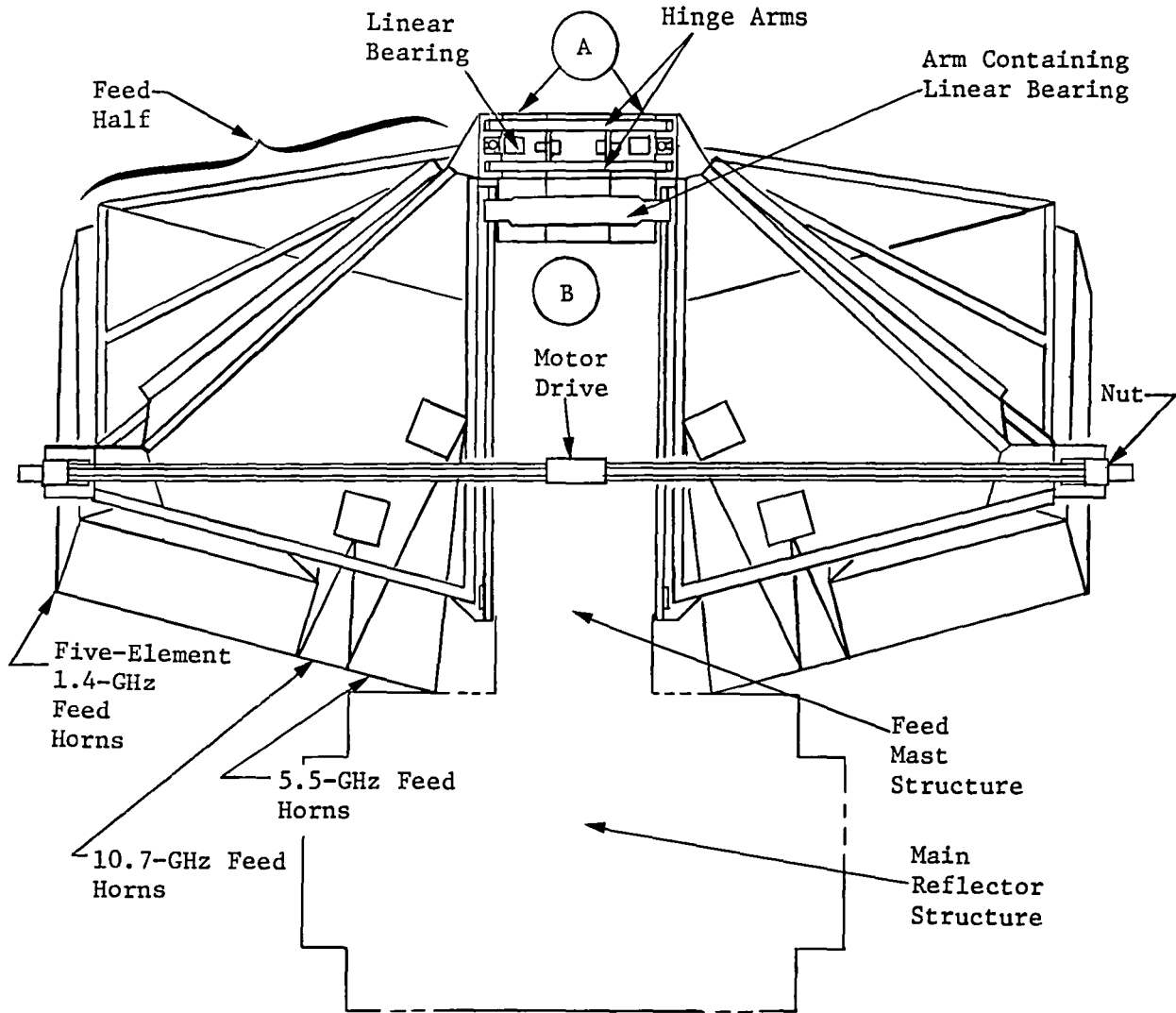
Figure 5-4   Stowed EOS (End View)

A pair of arms that form a hinge with a fitting located on the back of each feed beam half extend to the cube corner fitting located on the center of the top row. When deployed, this fitting will be at the top center of the feed beam.

In the top row of the stowed cube corner fittings, lying on either side of the center fitting, are the cube corner fittings (A) that will support the outermost ends of the feed beam. A linear bearing is mounted to the top face of each of the two corner fittings. During deployment this bearing will slide along a shaft that runs the length of the beam. These two fittings are disengaged from the feed beam when stowed.

An arm extends out to the feed beam from the cube corner fitting in the center of the second row. A linear bearing engaged with a shaft on the feed beam is located at each end of the arm. When deployed, this fitting will be at the bottom center of the feed beam.

The two feed halves are connected by a motor drive (B). The motor drives a screw shaft containing a right- and left-hand thread. This shaft engages a nut mounted to each half of the feed beam. The motor is mounted on a stiff square tube that is also mounted to the nut. This tube guides the feed during deployment and acts as a load-carrying member between the feed halves when deployed. When stowed, this member can be seen lying approximately three-fourths of the way down the width of the beam.

Truss deployment is controlled by latches between the cube corner fittings. These latches release by remote control in proper sequence, initiating deployment of each section of the antenna support structure. Deployment is powered by the stored energy in the midlink hinges of the surface tubes. The sequential nature of the deployment process dissipates the deployment energy in an incremental manner, thereby reducing the possibility of producing structural failure in the deploying truss. The sequential steps of deployment are shown in Figures 5-5 and 5-6.

The first step is linear deployment of the 1.5-m box truss supporting the feed beam. This is done by first deploying the tubes that will anchor the center section of the feed. The hinged corner cube remains stationary as the bearing mounted to the second row of cubes travels the height of the feed. The linear bearings that will anchor the far ends of the feed have not moved, and are still disengaged.

The second step is the linear deployment of the outermost 15 x 15-m box truss cube of the support mast. This will allow the feed beam to clear subsystems mounted to the stowed mesh support cubes during deployment. The screw drive motor is then started and the feed halves are rotated to their deployed position. The feed is rotated about the deployed linear bearing at the bottom of the feed and the hinged fitting at the top of the feed. A shaft at the top of the feed that runs its full length is now aligned with the disengaged linear bearings. This step is completed when two overcenter latches connected to the square guide tube (motor mount) and the feed beam lock up. The motor is now shut off. Deployment can be stopped and restarted during this step if necessary.

Page Missing in
Original Document

Hinge

Disengaged Linear Bearing Now Aligned with Shafts

Deployed Tubes

Linear Bearing Arm

View A

Disengaged Linear Bearing

Motor

Linear Bearing Arm

View B

65 m

1.94 m

1.08 m

15 m

Stowed

Step 1

View A

1

View B

Step 2

2
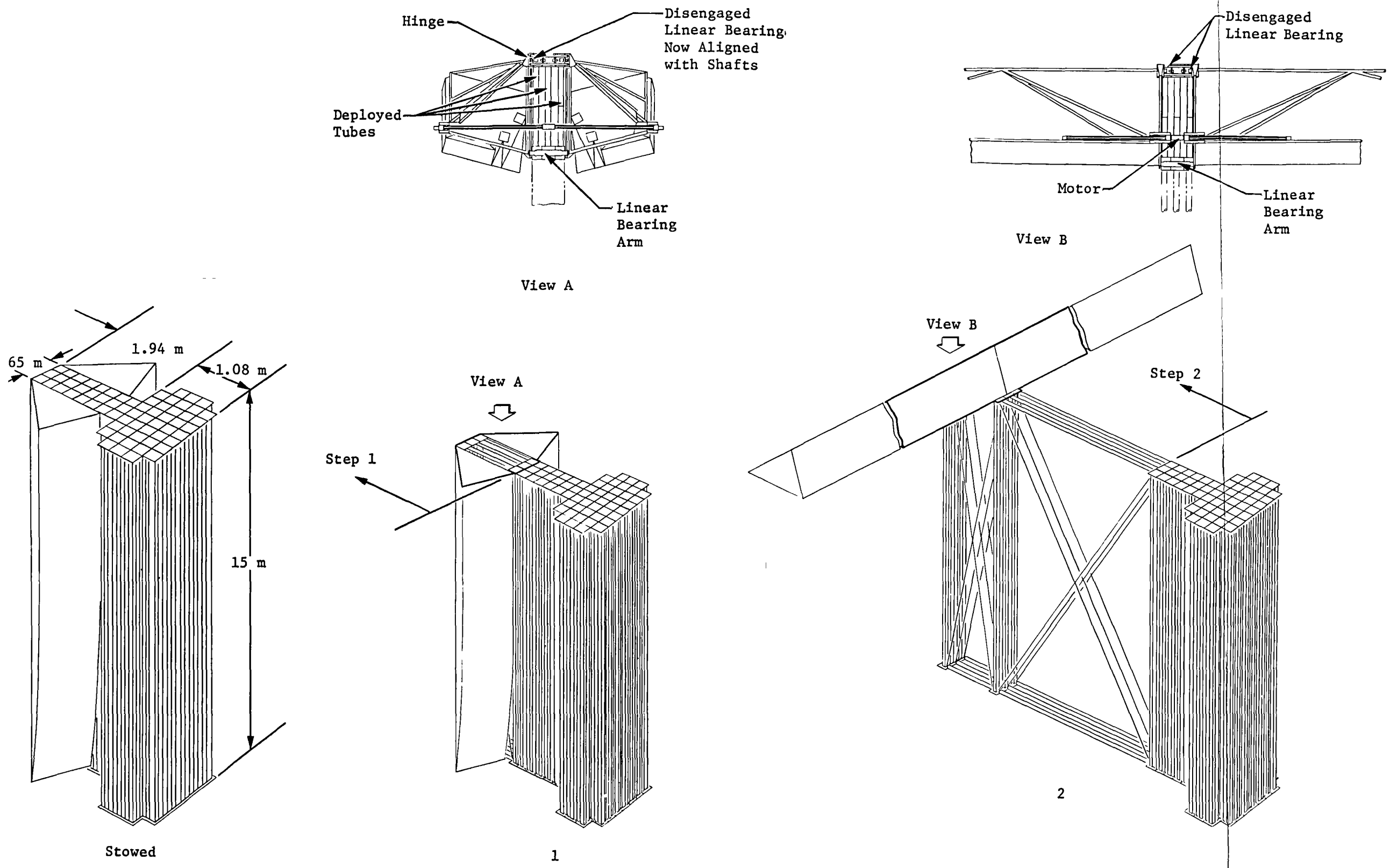
ʒure 5-5 *Structure Deployment Sequence*

Page Missing in
Original Document

Linear Bearing Engages
Shaft and Travels to
Here

Step 3

3

Step 4

4

Fully Deployed
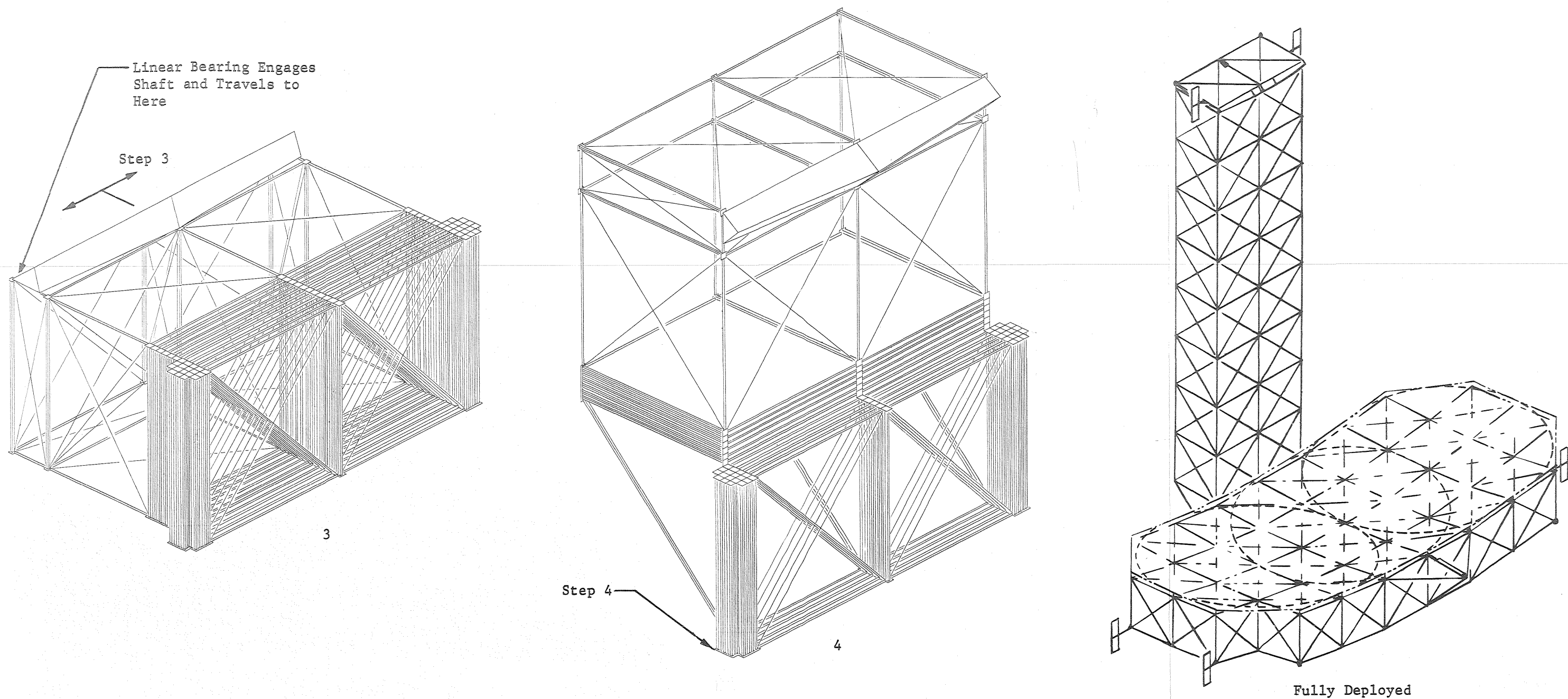
Figure 5-6 Structure Deployment Sequence, Steps 3 and 4

Step three is now started. The two unengaged linear bearings now engage the aligned shafts and travel out to the ends of the feed beam. This is accomplished by allowing the feed mast cubes and the second centermost rows of the antenna support structure to deploy sideways. This anchors the ends of the feed beams in place. The feed beam is now fully deployed.

The entire feed mast is rotated 90 deg relative to the antenna support structure in the fourth step.

The remainder of the deployment sequence is to deploy the feed mast one row of cubes at a time and then the mesh support cubes one row at a time. The final structure will measure 120 by 60-m wide x 120-m high, and is depicted in low earth orbit with the STS vehicle in Figure 5-7.
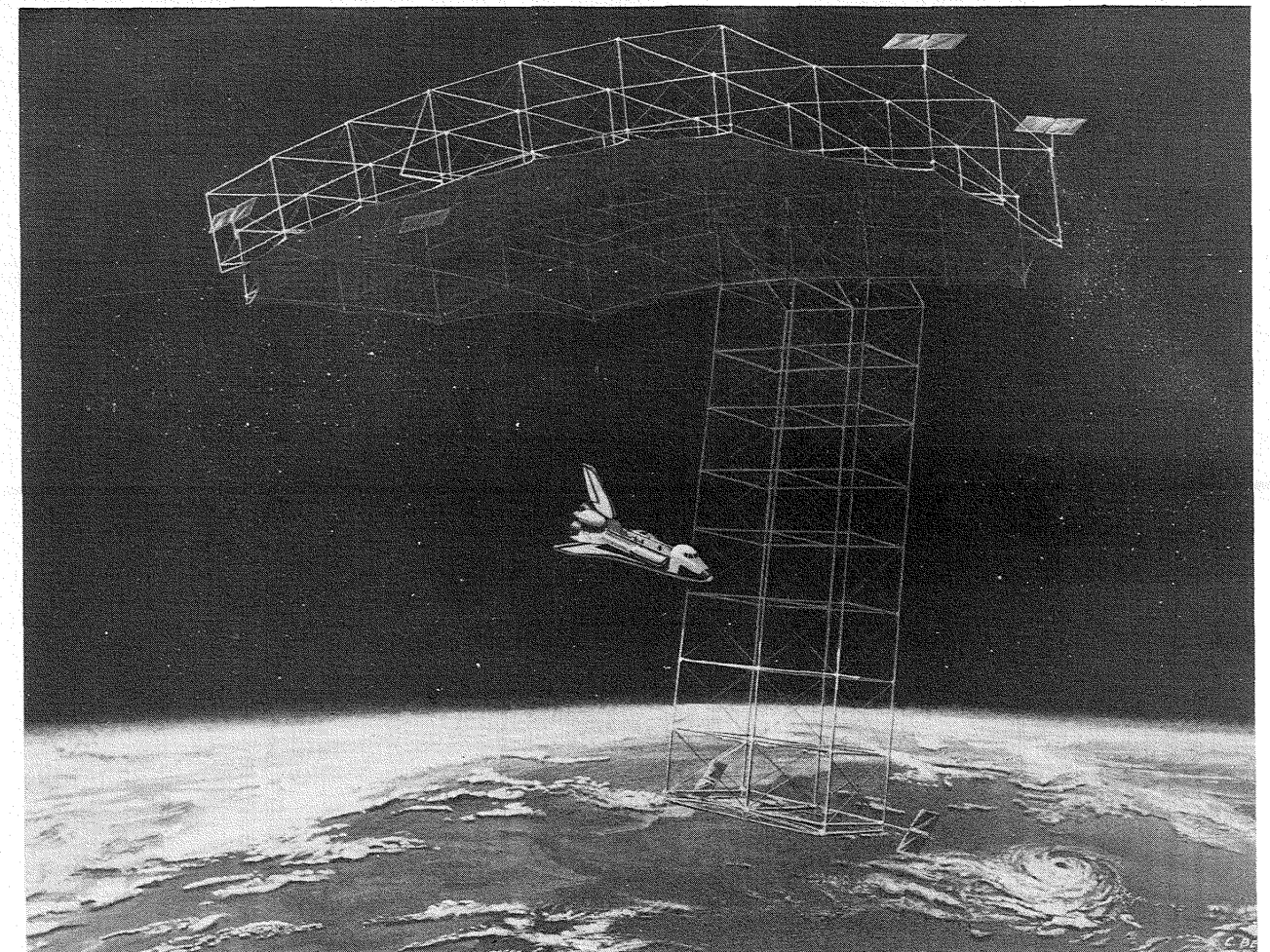
Figure 5-7 Deployed EOS

6.0 SUPPORTIVE ANALYSIS

The analyses supporting the EOS design are arranged in seven major groups—dynamics, thermal, thermoelastic, static rigid-body controls, rf performance, and slewing feasibility.

6.1 DYNAMIC ANALYSIS

This section details the EOS spacecraft structural dynamic analyses performed. The basic geometry and structural components are detailed in Section 3.3. These analyses identified the frequencies and mode shapes for the EOS structure, including the effects of subsystem masses. A NASTRAN finite-element technique was used to determine these modal characteristics. A total of 720 two-dimensional structural finite elements were used to model the spacecraft (Fig. 6-1). The surface members and the vertical members were modeled with beam elements, while the interior and exterior diagonals were represented by rod elements. Because the surface members are pinned at either end, this degree of freedom was released in the rotational direction along the axis of these pins to rigorously model the structure. The diagonal members were modeled with rod elements that have no bending stiffness, which is representative of their operational behavior. The diagonal members are pretensioned to a level high enough that they never go slack under all operating conditions. This eliminates any nonlinearities in the structure caused by slackening of the diagonal members. For this reason the diagonal members in this analysis were allowed to take a compressive load, which represents the mathematical behavior of the stiffness of tensioned members.

A lumped mass was placed at all the nodal locations to simulate the cube corner fittings, the mesh standoffs, and the rf mesh system. The model's nodal locations are depicted in Figure 6-2. The midlink hinge's mass was distributed along the length of the surface member because no node existed at that point. The masses of the power system, scientific platform, orbit transfer and slewing fuel, electronic housekeeping, and feed beam system were distributed as nonstructural mass. The pulsed plasma thruster, the ASR and the SAR masses were lumped at their respective nodes. Figure 6-3 also shows the location of many of these subsystems on the spacecraft. Table 6-1 summarizes the masses of the various subsystems and component parts of the EOS. Appendix B contains a listing of the NASTRAN input deck. Member numbers used in other sections of this report can be determined using the node numbers in Figure 6-2 and the NASTRAN input deck.

The dynamic computer model was run several times in an iterative process to optimize the stiffness of the structure at minimum weight. This was done by increasing the axial stiffness of the members with the largest strain energies in the structure. The modal extraction was performed using the fast Eigenvalue extraction routine in COSMIC NASTRAN. The boundary conditions were free-free and the model contained 834 deg of freedom. As one would expect, the area of the structure containing most of the strain energy was the interface region between the antenna support structure and the feed mast.

111
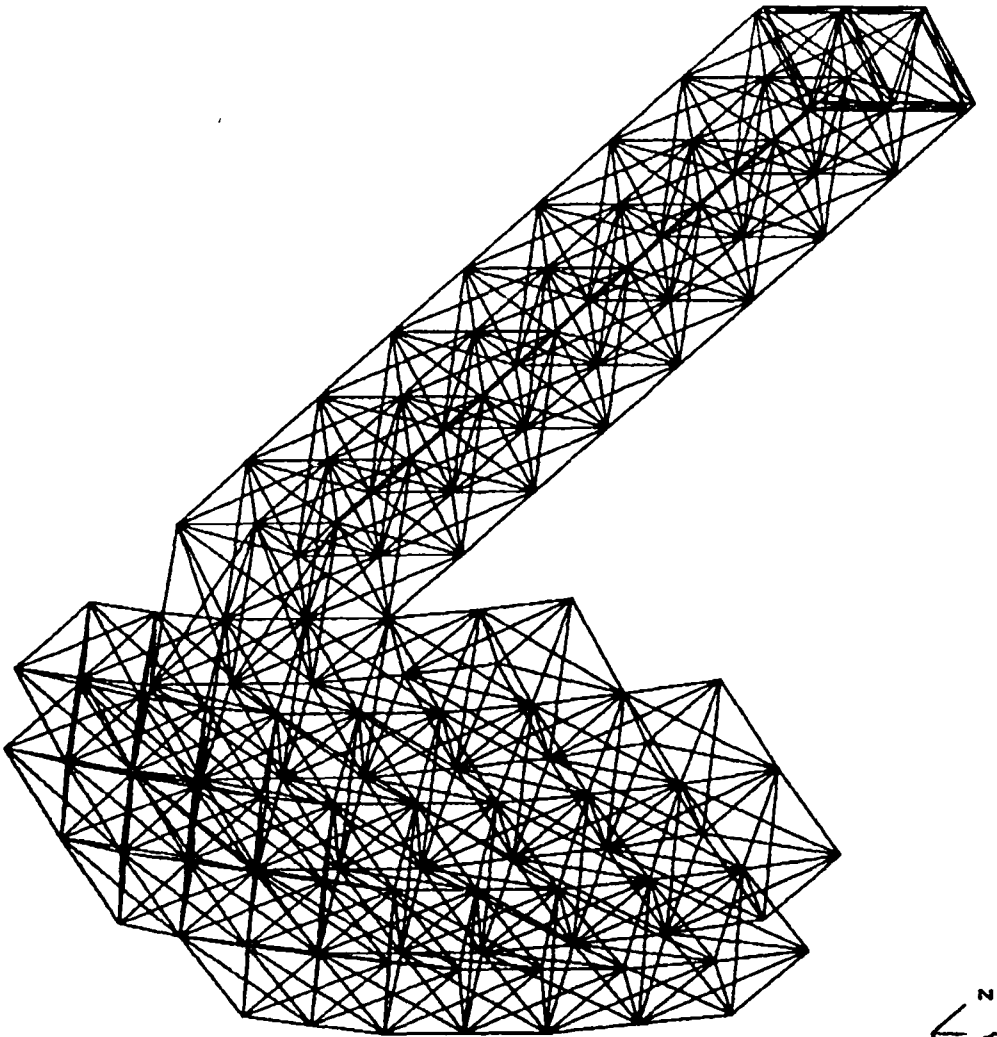
Figure 6-1 EOS Finite-Element Model

Three different mission situations that defined mass characteristics
were analyzed for EOS. The first case was at a 700-km orbit without
any slewing propellant. The second case was identical to the first ex-
cept for the addition of 1265 kg of slewing propellant and hardware.
The third case occurs just after deployment at a 200-km low earth orbit.
This case also includes both slewing and orbit transfer propellant.
Table 6-2 summarizes the first six modes of the three cases. Figures
6-4 thru 6-9 contain the first two mode shapes of the three cases. Ap-
pendix C contains additional modes shapes.
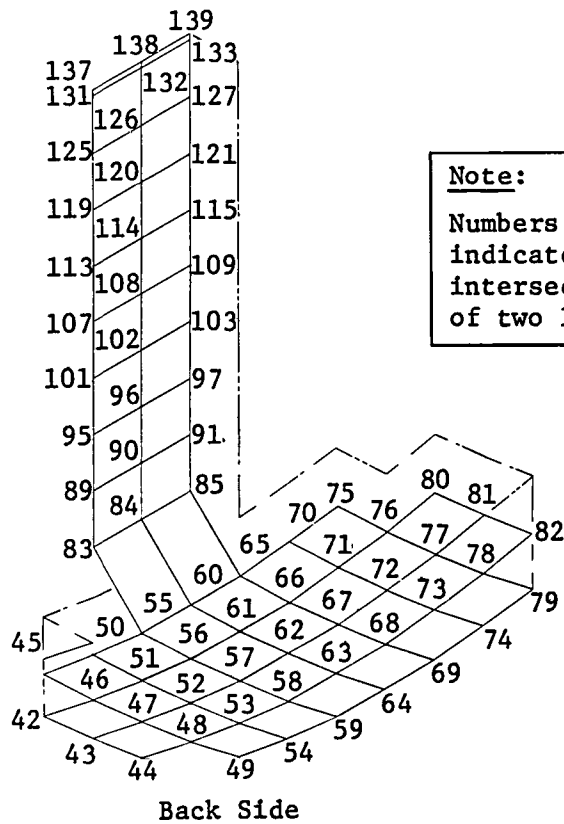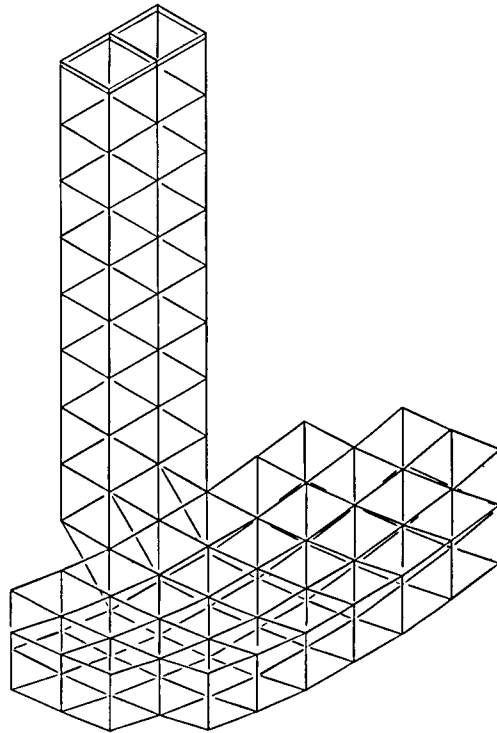
Note:

Numbers
indicate
intersection
of two lines.

Back Side

Mesh Side
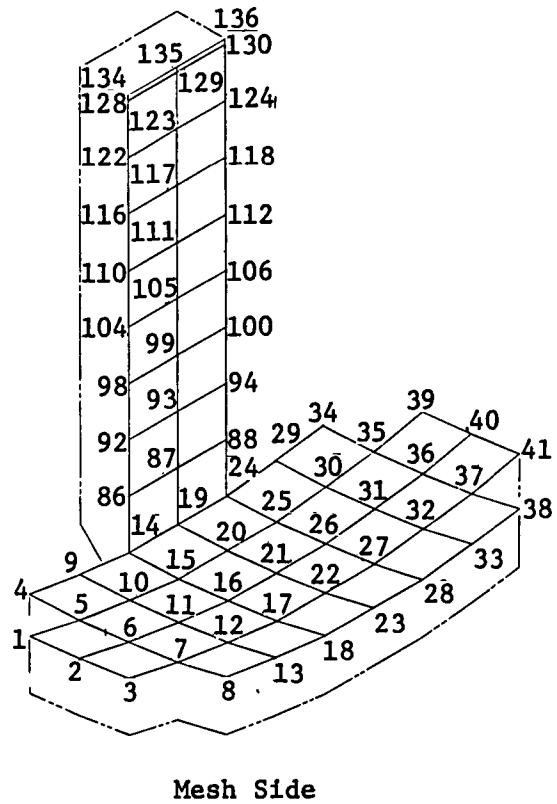
Figure 6-2 EOS Finite-Element Node Numbers

113
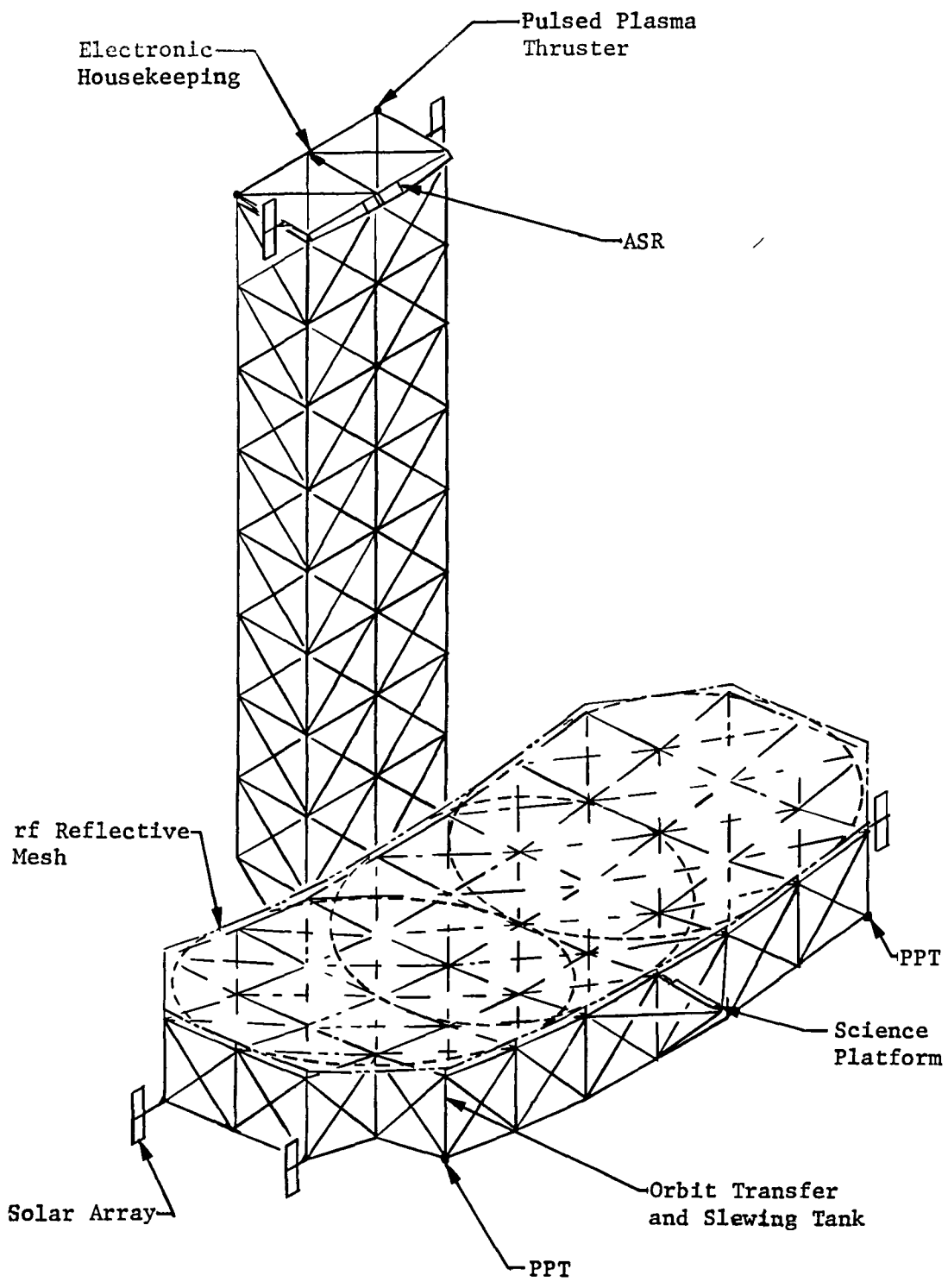
Figure 6-3   EOS with Subsystems

Table 6-1 Subsystem and Structural Mass Summary

Subsystem	Unit	Mass, kg/Unit	Total, kg
Feed Boom System	1	717	717
Electronics (GN&C, Communications & Data Processin	1	110	110
Atmospheric Sounding Radar	1	70	70
Mesh and Tie System	6750 m²	0 044	297
Science Pallet (SAR & Structure)	1	169	169
Twin PPTs	4	84	336
Single PPT	4	44	176
Power — Solar Panels — Battery Packs	 6 6	 50 90	 300 540
Orbit Transfer System — Inboard Propulsion System — Outboard Propulsion System	 2 2	 325 118	 650 236
Slewing Propulsion System	4	316	1265
Total Subsystem Mass			4866
Structural System			
Cube Corner Fitting — Full — 3/4 — 1/2	 67 52 20	 0 479 0 332 0 222	 32 17 4
Midlink Hinge	231	0 452	104
Mesh Standoff	42	0 8976	38
Structural Members			2574
Total Structure Mass			2769
Total Spacecraft Mass*			7635
*With slewing and orbit transfer			

Table 6-2 Modal Summary of EOS Propellant Mass Cases

Mode	Without Slewing and Orbit Transfer, Hz	With Slewing without Orbit Transfer, Hz	With Slewing and Orbit Transfer, Hz
1	1.09	0.911	0.711
2	1.13	0.963	0.736
3	1.14	0.969	0.766
4	1.32	0.972	0.782
5	1.38	0.990	0.844
6	1.39	0.998	0.900
Mass; kg	5547	6812	7635
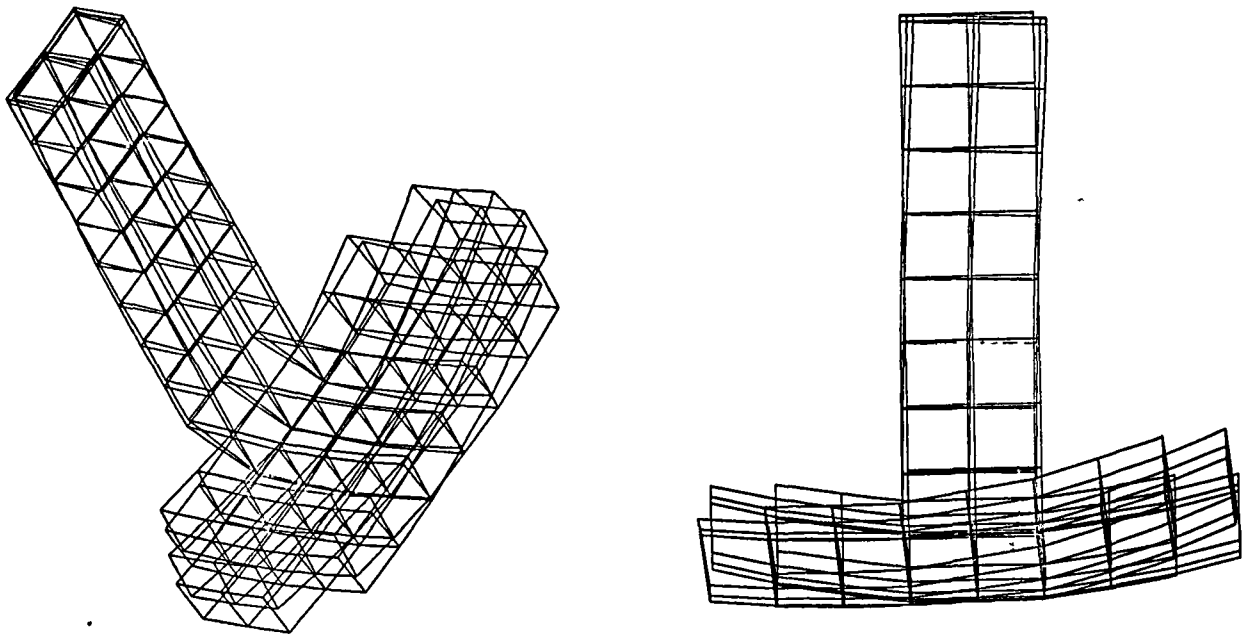
Figure 6-4   First Mode Shape without Slewing or Orbit Transfer (Freq of 1.09 Hz)
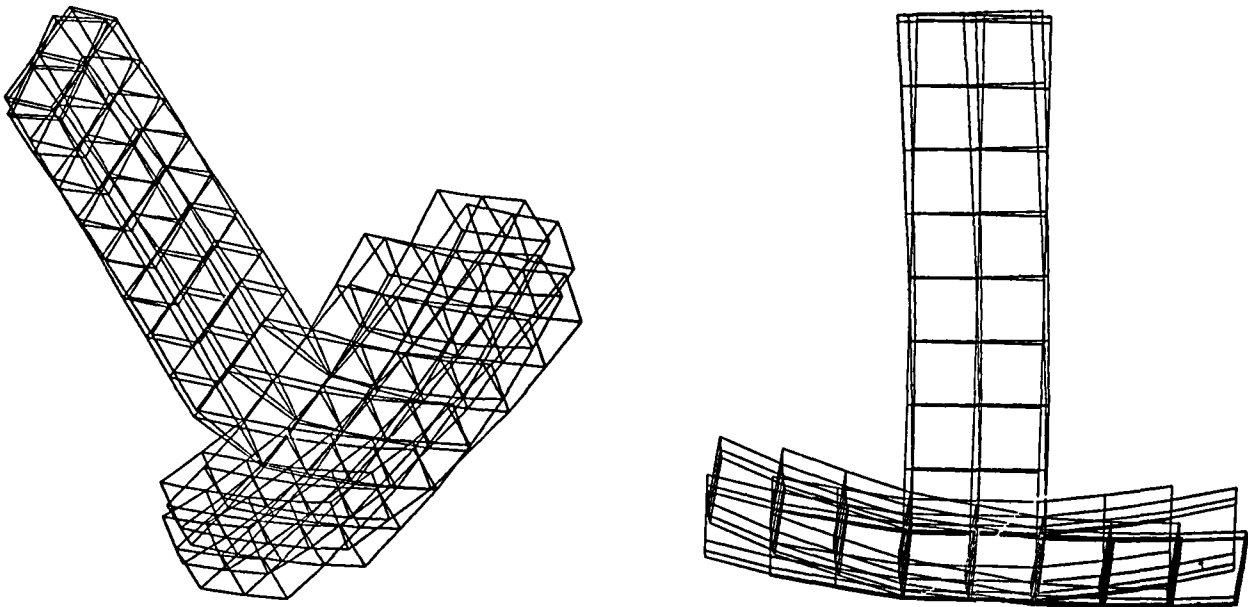
Figure 6-5
Second Mode Shape without Slewing or Orbit Transfer (Freq of 1.126 Hz)
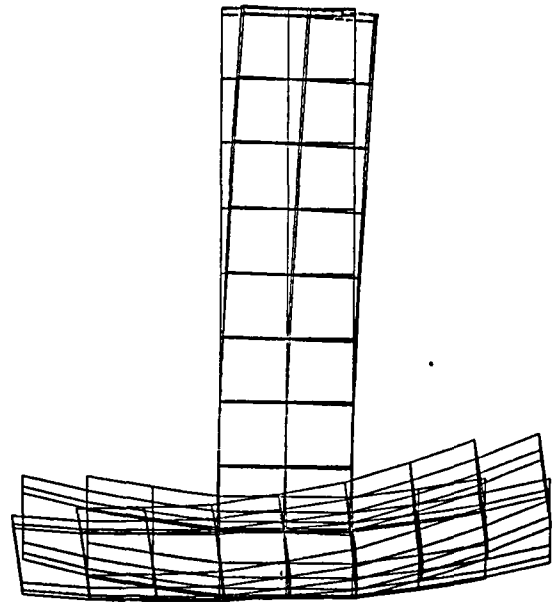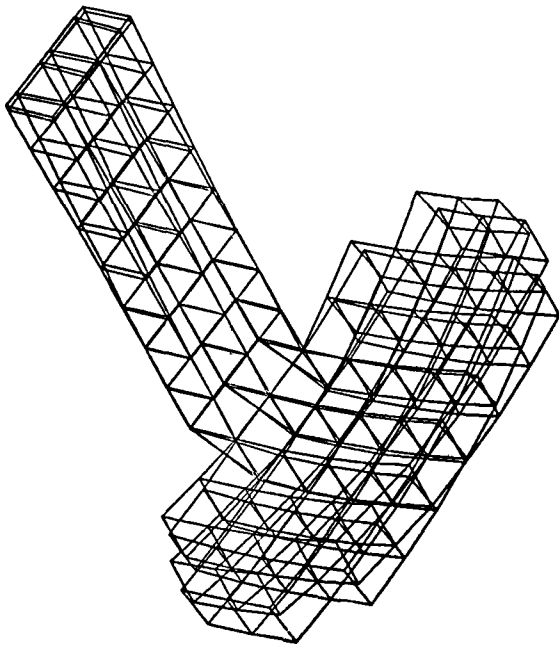
Figure 6-6
First Mode with Slewing and without Orbit Transfer (Freq of 0.911 Hz)
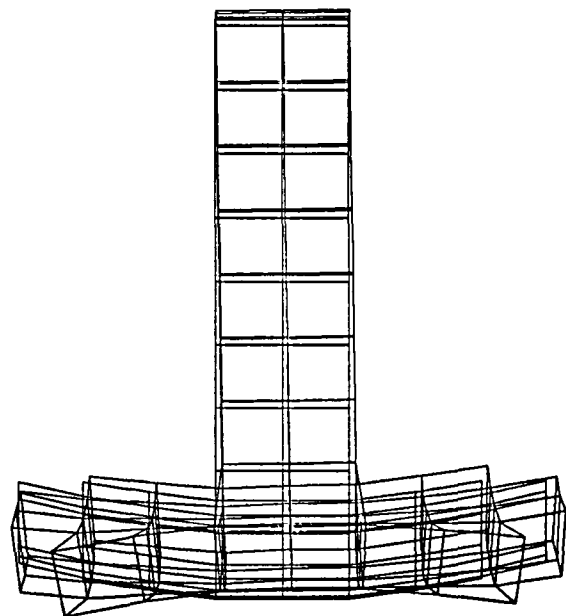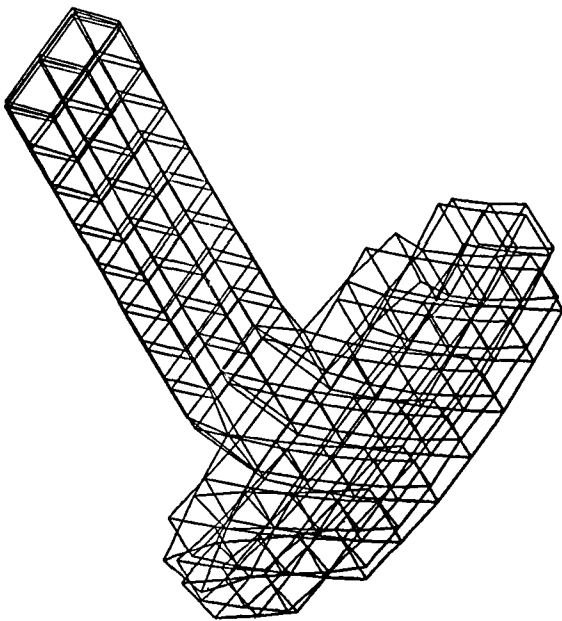
Figure 6-7
Second Mode with Slewing and without Orbit Transfer (Freq of 0.963 Hz)

117
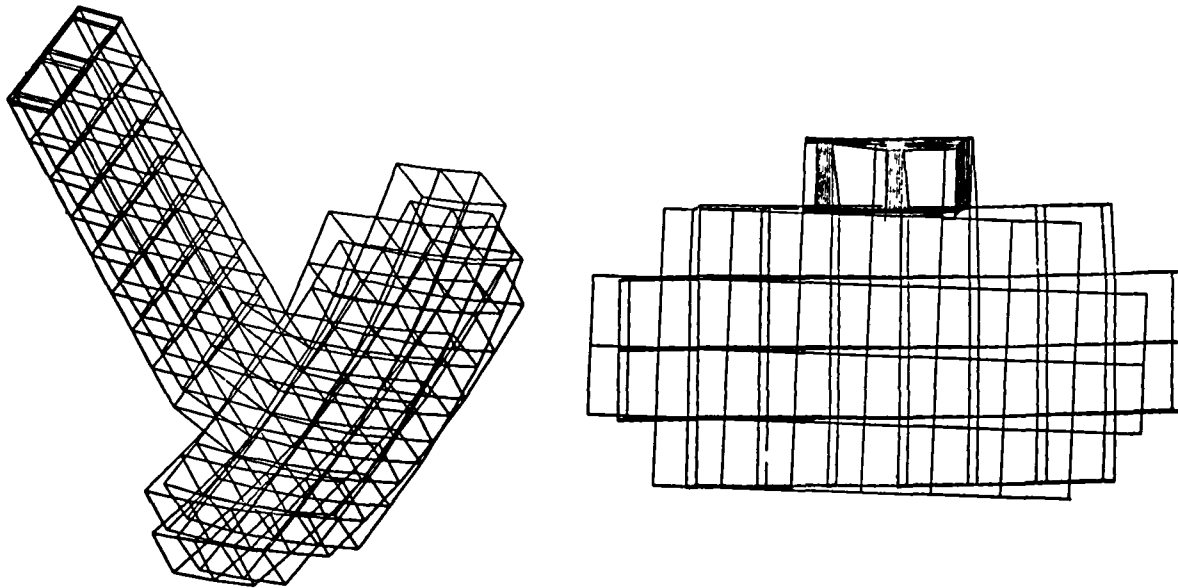
Figure 6-8
First Mode Shape with Slewing and Orbit Transfer (Freq of 0.711 Hz)
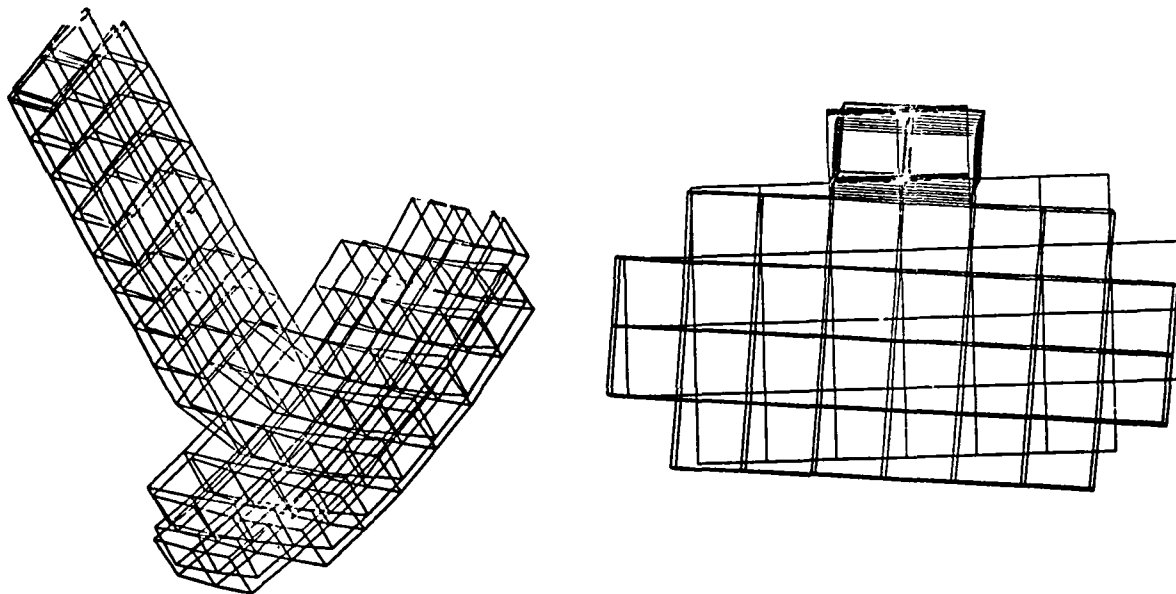
Figure 6-9
Second Mode Shape with Slewing and Orbit Transfer (Freq of 0.737 Hz)

The results indicate that the integrated offset mast box truss design produces a rigid and stable base for the large microwave radiometer and its ancillary sensors and subsystems. Higher structural frequencies reduce the potential for control instabilities and ensure that the dynamic response to the environmental forcing functions will be relatively small.

118

6.2 THERMAL ANALYSIS

A thermal analysis of the EOS structure and rf mesh was performed to obtain the temperatures throughout the structure for use in determining the thermoelastic distortion. Finite-element math models were developed using the two standard thermal analysis programs at Martin Marietta, the thermal radiation analysis system (TRASYS II) and the Martin Marietta interactive thermal analysis system (MITAS II). The TRASYS program provided the radiation interchange factors, along with the absorbed solar and earth albedo fluxes. The MITAS program used the TRASYS results to generate the steady-state temperature solutions for the EOS model.

Because of structure size (720 members and cords), the thermal analysis was broken into two separate models, one for the structure and one for the mesh. The structural model consisted of detailed modeling of the members, cords, feed beam, solar panels, and synthetic aperture radar system with coarse modeling of the mesh, while the mesh model provided the detailed mesh pillowing and tiedown system.

6.2.1 Structure Thermal Analysis

When modeling large space structures, the computer costs become quite high because of the large number of elements involved. For the EOS structure, an approach that significantly reduced the thermal analysis costs was used. Because the structure does not spin as the spacecraft proceeds in orbit and the solar vector remains in the orbit plane at all times, the incident solar fluxes will be parallel to, and symmetric about, the center plane of the structure. This allows the modeling of planar slices throughout the structure as depicted in Figure 6-10. In addition to these slices, the mesh was modeled as a single node, as were the feed beam, synthetic aperture radar, and each of the Hughes Aircraft Company FRUSA solar panels. The data obtained from the planar slices were used to interpolate the remaining temperatures throughout the structure employing Martin Marietta's geometric temperature interpolation program, TEMINT, a program specifically designed for large space structure thermal analysis. TEMINT interpolates temperatures for a box truss structure defined on a Cartesian coordinate system. It groups members into types according to their cross section and nearness to the rf reflecting mesh, and into families of types where each family member has approximately the same angle between its axis and the solar vector. Separate interpolations are done for each family.

The nodal network for the structure was defined in the same manner for both TRASYS and MITAS. Nodal plots for the three planar slices are shown in Figure 6-11. This network used a single node representation for the entire mesh, each solar panel, element, and cord in the three slices modeled. The feed beam was modeled as two nodes, one on each side of element 320. Each graphite/epoxy member was modeled as a single node, thus defining each member as an isothermal surface. The TRASYS/MITAS results defined an average member temperature for each element. The thermoelastic deformation analysis used these average temperatures in conjunction with the member geometry to approximate the circumferential thermal gradients within a single member while the structure is deployed in space.

119
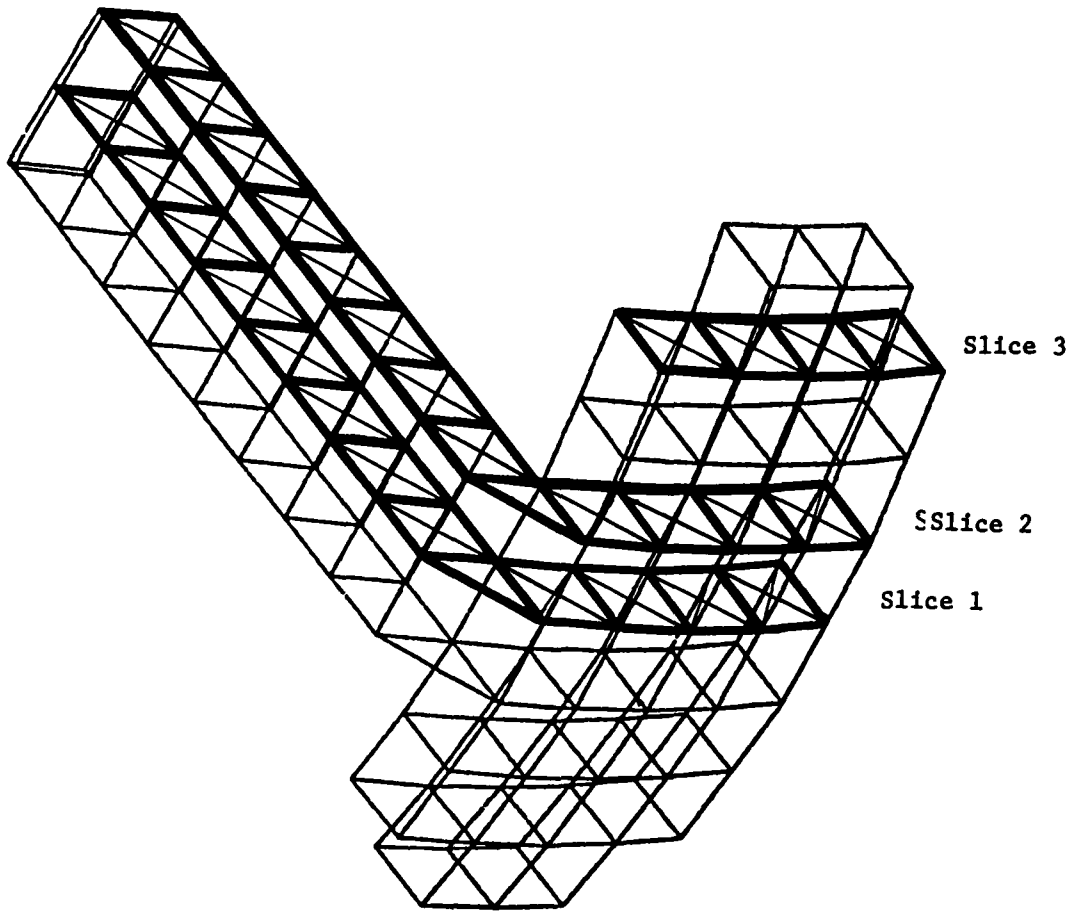
Figure 6-10   Planar Model Slices Used for Thermal Analysis
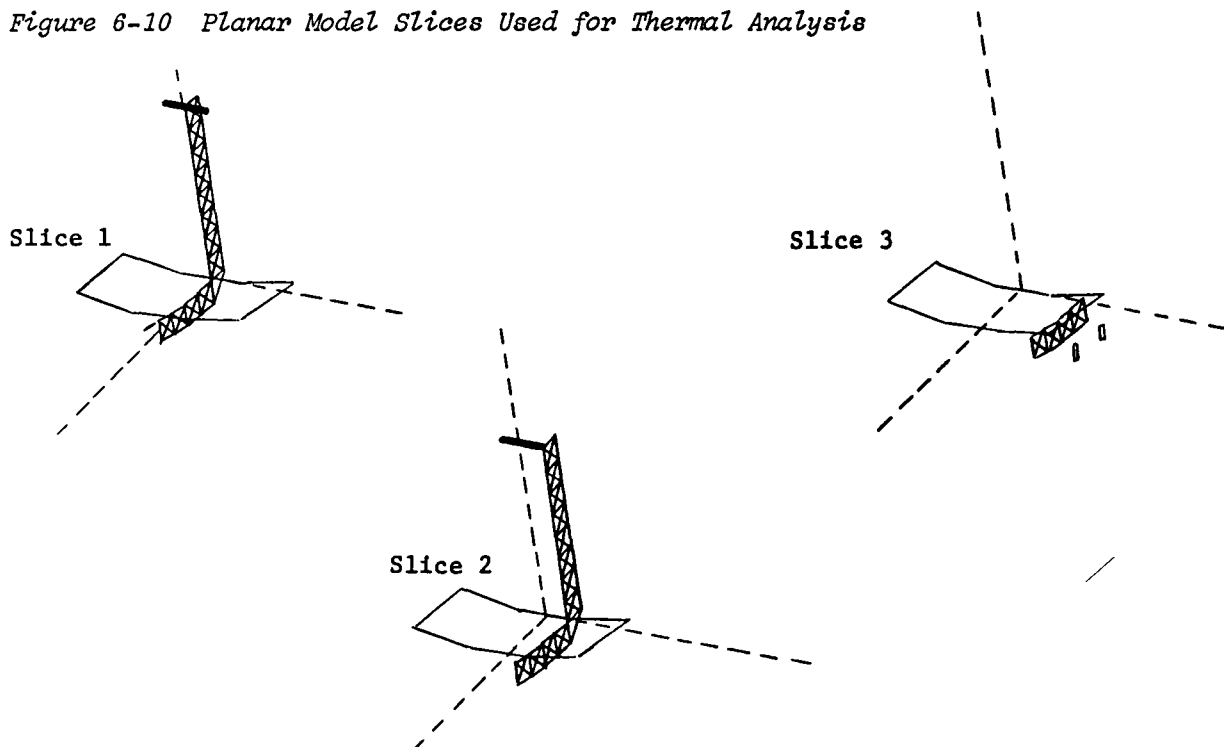
Figure 6-11   TRASYS Surface Plots of Structural Model

120

When creating the radiation math model utilizing TRASYS, all cords and members were assumed to be cylindrical tubes. For elements with square, finned square, or 7-channel cross sections, the radii characteristics of the surface area were calculated. The members and cords were all defined as "elements," which TRASYS treats in a unique manner compared to all other surface types. The optical properties for these graphite/epoxy members were defined as solar absorptivity (σ) = emissivity (ϵ) = 0.875. The rf mesh properties were σ = 0.304, ϵ = 0.04 and the transmissivity (τ) ranging from 0.88 at an incident angle of 0 deg to 0.0 at 89.0 deg.

During the radiation interchange factor calculation link of TRASYS, all elements are assumed to possess interchange factors to only nonelement-type surfaces, i.e., mesh, feed beam, solar panels, SAR and space. Based on the data in Figure 6-12, elements were assumed to not possess view factors to other elements. For a nonelement node (e.g., the mesh), interchange factors were calculated for all defined surfaces including the mesh. All surfaces except the members and cords were allowed to shadow during these calculations.
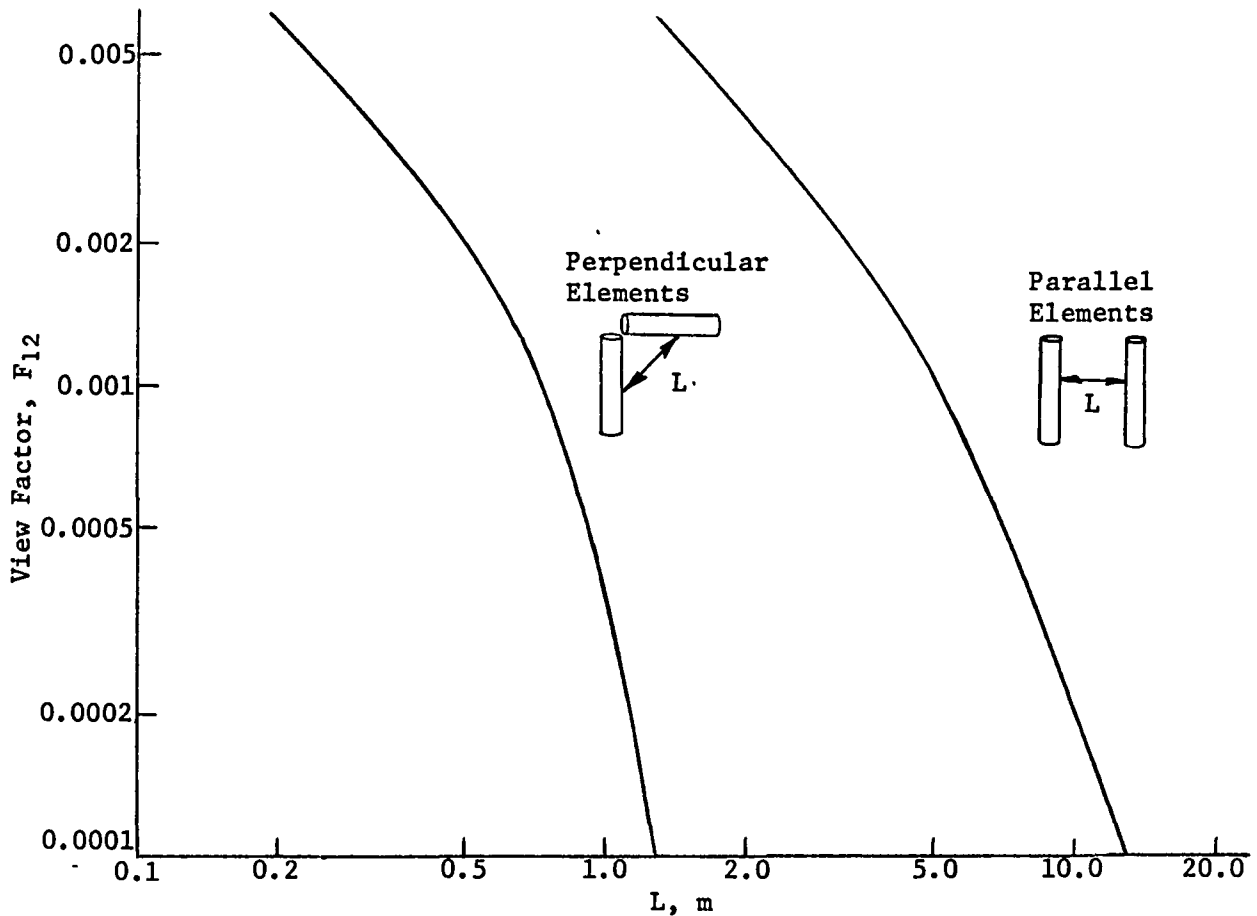
Figure 6-12   Interelement Radiation Exchange

Absorbed solar planetary and earth albedo fluxes were calculated for 12 points in orbit as defined in Figure 6-13(a). All surfaces were defined as potential blockers for solar shadowing except for the diagonal cords. TRASYS will account for the shadowing of a surface by any other defined surface. The shadowing routine uses a point source for the sun, resulting in either full or no shading of a surface. By defining members and cords as "elements," a disc sun is assumed so partial shading can exist. This provides the temperature accuracy needed when modeling large box truss structures.

The structure's orbit has been defined as being sun-synchronous with an altitude of 700 km, inclination of 98.2 deg, and an equatorial cross-over time of 12:00 noon. Figure 6-13(b) is a TRASYS plot of the slice model in the defined orbit. Note that TRASYS does not distinguish the difference between a polar orbit and an equatorial orbit. This will not affect the thermal results.

(a) Flux Calculations Points, deg   (b) TRASYS Orbit Plot
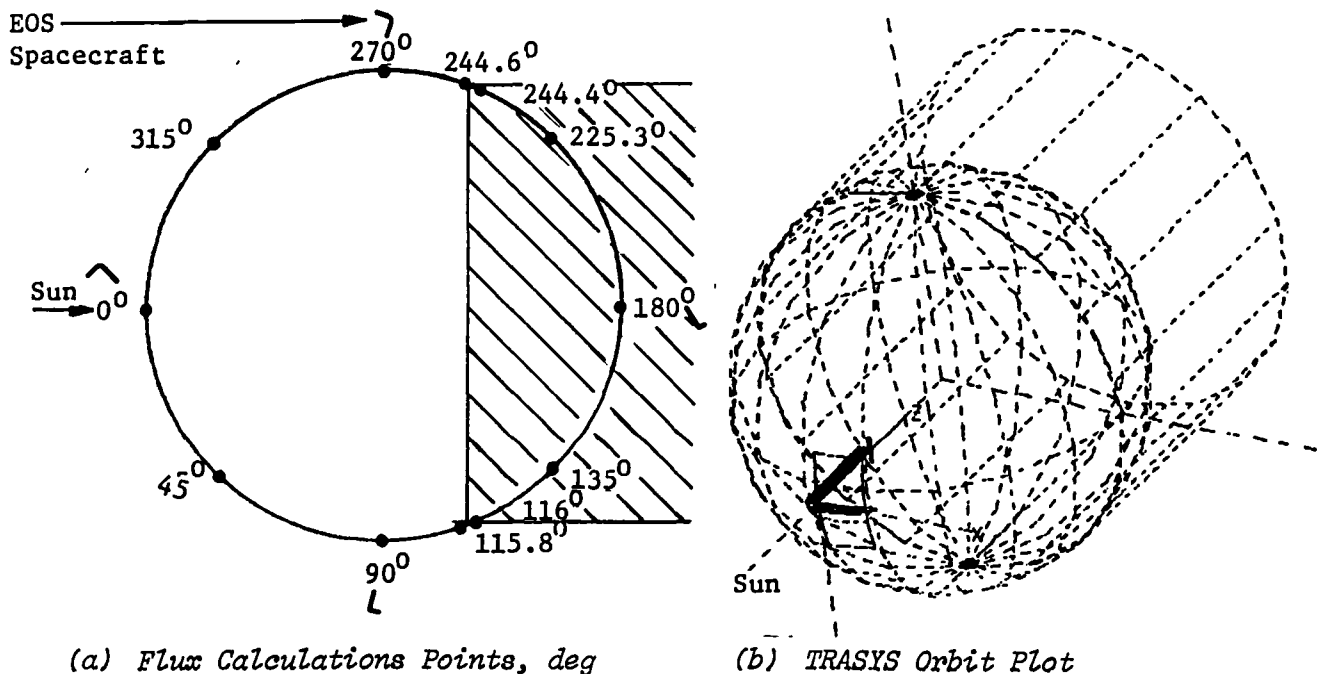
Figure 6-13   Orbit Definition for Thermal Analysis

Using the previously defined nodal network, the MITAS program was used to create and solve a resistor-capacitor (R-C) network analog of the three-slice model. Thermal capacitances were defined for all nodes in the structure model. For all graphite/epoxy members, the specific heat (c_p) was defined to be temperature-dependent as depicted by the function plotted in Figure 6-14. The function is nearly linear ranging from c_p = 364.3 J/kg-°C at -147 deg to c_p = 1214 J/kg-°C at

176.7°C.* The rf mesh is woven of gold-deposited molybdenum wire. Because the feed beam, SAR and solar panels were represented as single nodes, composite thermal capacitances were calculated for each based on the weight of the various materials in each component.

In large space structure applications, the majority of all heat transfer is through radiation exchange between nodes and to space. Circumferential conduction in the graphite/epoxy members was calculated by hand based on the average node temperature and using empirically determined relations. Conduction between members was assumed negligible because of the very long heat flow paths involved.
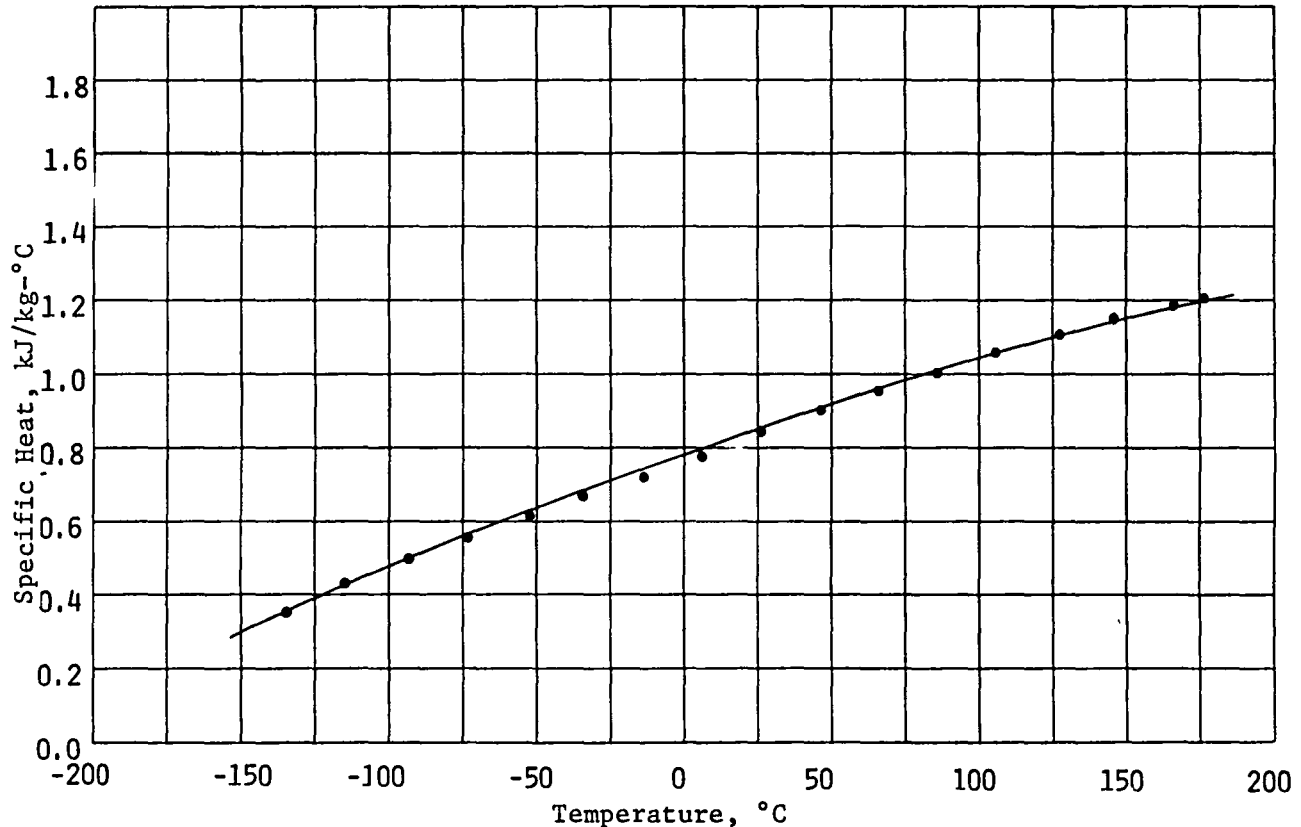
Figure 6-14 Specific Heat of Graphite/Epoxy

The resulting temperatures for the three planar slices were used as a basis for interpolating the remaining temperatures utilizing TEMINT. TEMINT fits a smooth curve to the known element temperatures using the X, Y, and Z coordinates as the independent variables. The various member types (e.g., members near or away from the mesh, vertical members, diagonals, etc) are grouped into families and each family is curve-fit and interpolated independent of all others. Table 6-3 displays the minimum and maximum temperatures and the maximum temperature differential for each point in orbit. Figure 6-15 represents typical steady-state temperatures of various element types as the structure travels

*Rockwell Internal Report TD-75-46, Determination of Graphite/Epoxy Thermophysical Properties, 1977.

through orbit. The largest thermal gradient, 136°C, through the struc-
ture occurs just as the structure enters and leaves the earth's shadow.
These temperatures were then applied to the structure in the NASTRAN
finite-element model to determine thermoelastic distortions of the
spacecraft (Section 6.3.1).

Table 6-3 Structural Temperature Extremes

Orbit Position, deg	Maximum Temperature, °C	Minimum Temperature, °C	Temperature Gradient, °C
0	54.2	−56.7	110.9
45	42.9	−60.2	103.1
90	28.8	−70.8	99.6
115.8	30.0	−93.6	123.6
116.0	−13.6	−96.0	82.4
135.0	−80.3	−117.0	36.7
180.2	−80.3	−117.0	36.7
225.3	−80.3	−117.0	36.7
244.4	−80.3	−117.0	36.7
244.6	30.0	−93.6	123.6
270.0	28.8	−70.8	99.6
315.0	42.9	−60.2	103.1
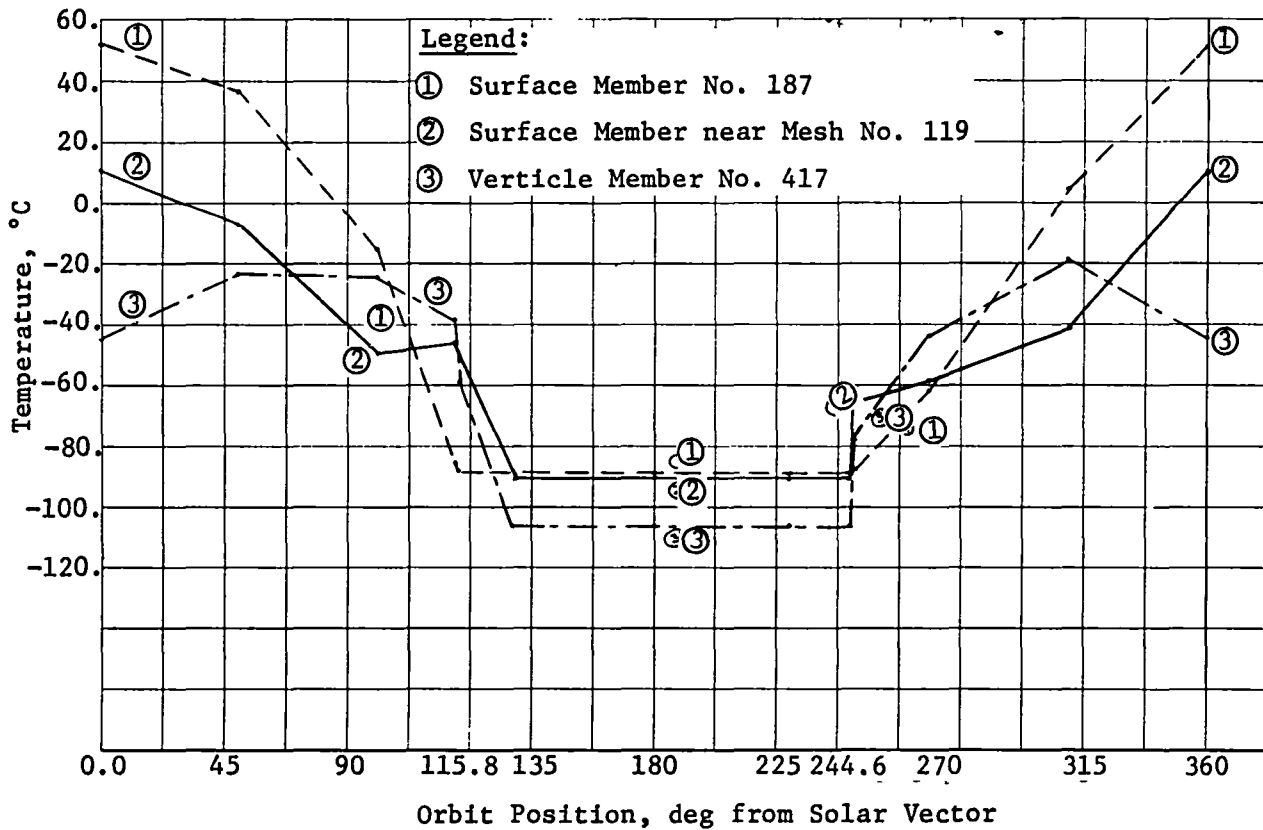
Figure 6-15 Steady-State Structural Member Temperatures

6.2.2 Mesh Thermal Analysis

The purpose of the detailed mesh thermal model was to determine the maximum distortion expected in the mesh's parabolic shape. This was achieved by calculating the minimum and maximum mesh box temperatures in the cold and hot orbits, respectively, and defining the point in orbit where the widest variation in flux distribution across a single mesh box exists. This flux gradient would be caused by shadowing of the box by other surfaces.

To minimize computer costs, an exploratory model was designed to represent only the mesh (no structure, standoffs, or tie strings). The nodal breakdown of this rough model is depicted in Figure 6-16(a). This model was used to locate the point(s) in orbit where the maximum flux variation on a single mesh box would occur. The only potential mesh shadowers were the feed beam solar panels (on the mast only), the SAR, and the mesh itself. Preliminary geometric computations determined that the solar panels, and similarly the feed beam, will never shadow the mesh because the orbital point at which shadowing will begin is 165.8 deg from the solar vector. Because the EOS will be in the earth's shadow from 116 to 244.4 deg, the solar panels and feed beam were eliminated as potential shadowers. The SAR and mesh itself were determined to shadow between 270 and 285 deg in orbit.

(a) Exploratory Mesh Model   (b) Detailed Mesh Box
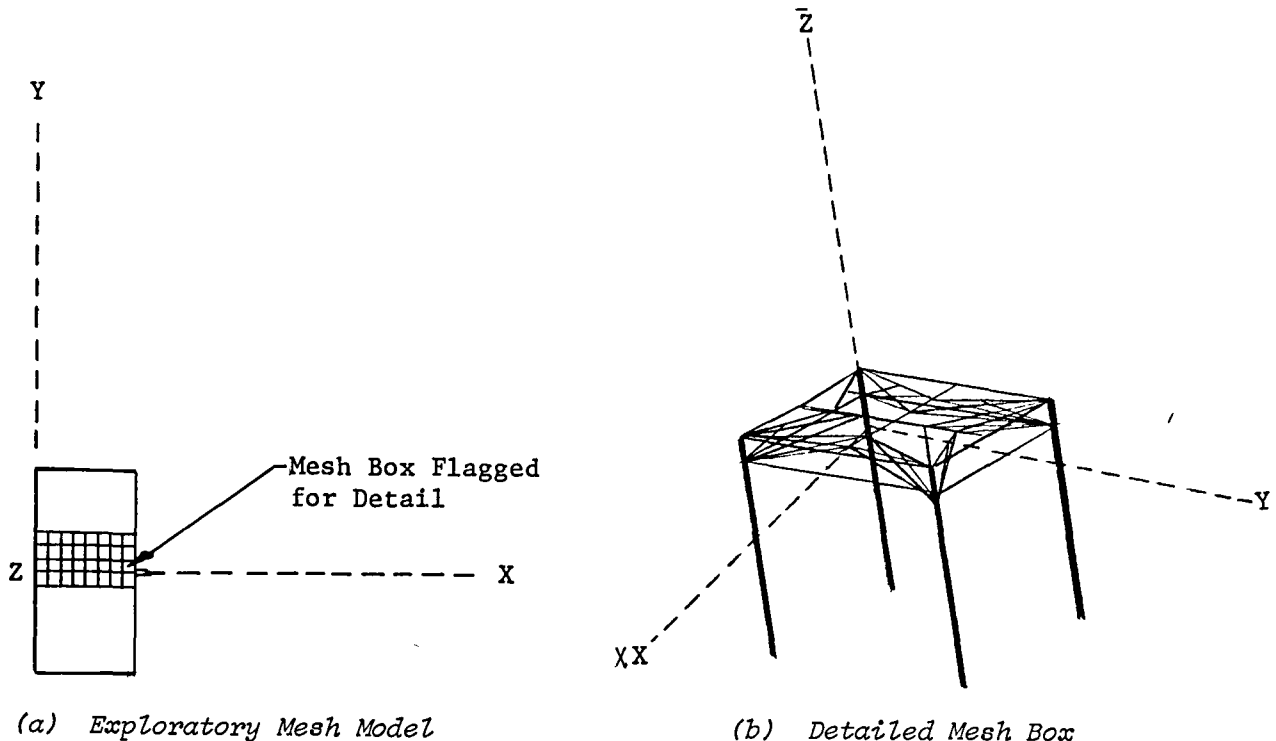
Figure 6-16 Mesh Thermal Model Definition

The orbit for the exploratory mesh model was defined as identical to the structure's orbit. Absorbed fluxes were calculated using TRASYS for the orbit position of 270 deg from the sun. This point is where the worst-case shadowing is expected. The results defined the particular mesh box that would be typical of a worst-case flux distribution.

125

This box was then modeled in detail as depicted in Figure 6-16(b). The detail consisted of adding the four standoffs and the partial box truss corresponding to the mesh box. Eight back tie strings were modeled for each standoff, along with 18 surface strings, resulting in a total of 50 mesh tie strings. The mesh, truss members, and standoffs were modeled as regular cylinders and plates, allowing them to both emit and receive thermal radiation from other nodes. The strings were defined as elements that prevented them from exchanging heat with each other. This detailed box and the remainder of the mesh nodes were modeled to obtain steady-state absorbed fluxes and therefore average surface temperatures for five points in orbit (0, 180, 270, 275, and 285 deg from the solar vector). These results are defined in Tables 6-4 and 6-5. The maximum thermal differential between surface cords was 85.08°C, which occurred at 270 deg. The maximum gradient for the rear cords was 107.6°C, which occurred at 285 deg in orbit. Figures 6-17 and 6-18 show the results of a transient simulation of the mesh tie cords traveling from 270 to 285 deg in orbit. The plot in Figure 6-17 shows the variation of the rear cords for a single quadrant. This particular quadrant received shadowing from the SAR between 275 and 285 deg in orbit. This shadow effect is represented by the dip in the temperature plots of cords 1727 and 1728.

Table 6-4   Mesh Tie System Thermal Data for Hot and Cold Orbits

Surface	Minimum Temperature, °C	Maximum Temperature, °C	Temperature Differential, °C
Mesh - Hot	187.2	191.4	4.2
- Cold	-103.0	-102.7	1.3
Surface Cord			
- Hot	41.9	47.0	5.2
- Cold	-93.0	-82.8	10.2
Rear Cord			
- Hot	32.6	47.9	15.3
- Cold	-97.1	-89.1	8.0

Table 6-5   Shadowed Thermal Results for Mesh Tie System

Orbit Position	Element	Minimum Temperature, °C	Maximum Temperature, °C	Temperature Differential, °C
270	Surface Cord	-54.5	30.6	85.1
	Rear Cord	-25.2	29.8	55.0
	Mesh	129.3	139.0	9.7
275	Surface Cord	-42.8	31.7	74.5
	Rear Cord	-28.1	29.4	57.5
	Mesh	153.7	161.9	8.2
285	Surface Cord	-15.0	34.6	49.6
	Rear Cord	-74.6	33.0	107.6
	Mesh	156.9	162.5	5.6
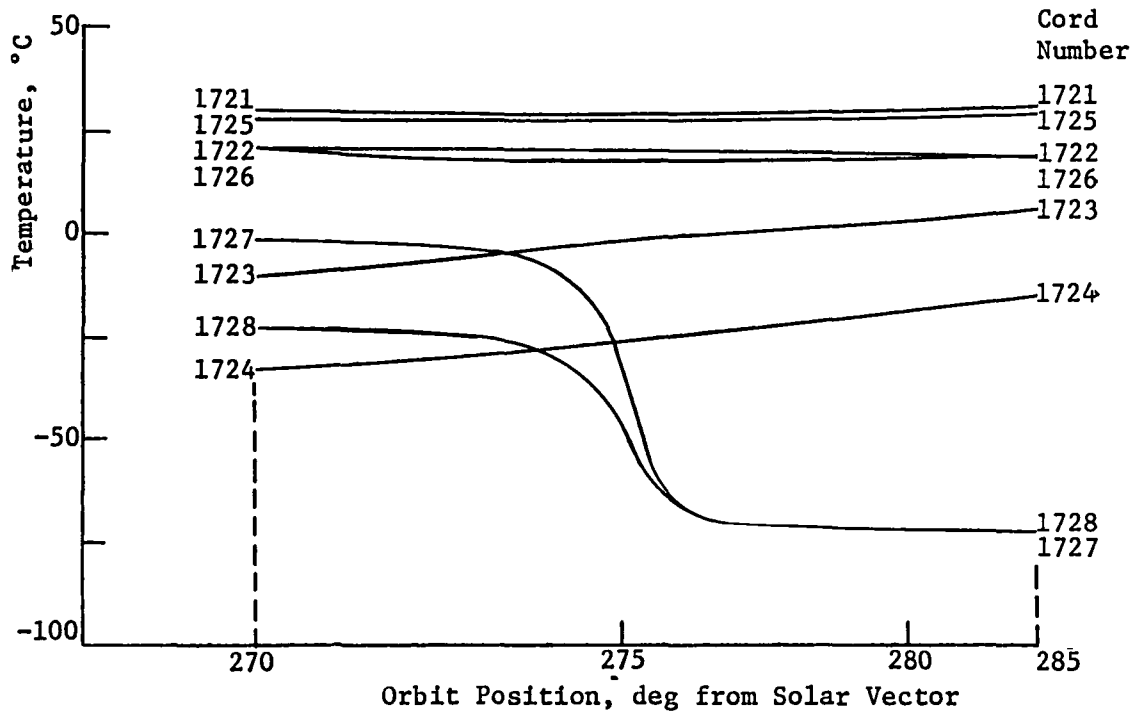
Figure 6-17   Mesh Tie Cord Transient Results
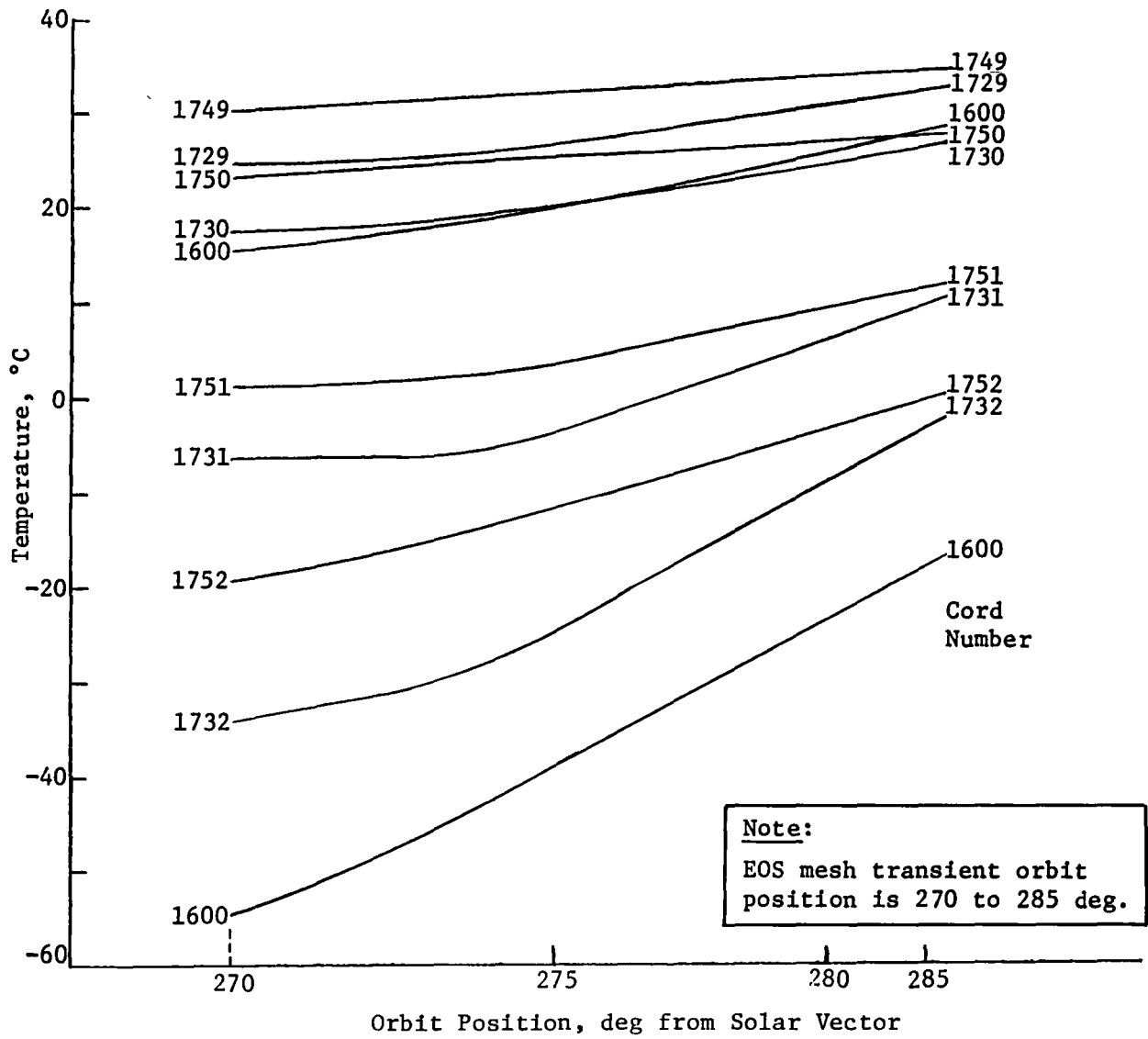
Figure 6-18 Surface Tie Cord Temperatures

6.3 DISTORTION ANALYSIS

A thermoelastic analysis of the EOS structure and mesh tie system was performed to determine their distortions. The distortions were used in an overall surface error and feed misalignment budget in determining rf operational performance. The temperatures used in this analysis came from the thermal analysis discussed in Section 6.2. A major concern was the effects of shadows on the dimensional integrity of the structure. The manufacturing error distortions were also analyzed in this section. Section 6.3.4 summarizes the various distortions.

6.3.1 Box Truss Thermoelastic Behavior

A static finite-element technique was used in the thermoelastic analysis. The NASTRAN computer model developed for the dynamic analysis described in Section 6.1 was used to predict thermoelastic behavior. Nine thermal load cases were run in this analysis. The thermal cases are of the nine orbital positions depicted in Figure 6-13(a). Orbital positions 135, 225, and 244.4 deg were eliminated because the temperatures are the same as 180 deg. This occurs because the albedo and planetary fluxes remain constant as the structure travels through the earth's shadow. Temperatures derived from the thermal analysis were assigned to all 720 members. The reference temperature of the structure was 22.22°C, which is the temperature of the spacecraft during manufacturing. The resulting thermally induced change in length of the members causes overall deflections and loads in the structure. Table 6-6 lists the maximum and minimum temperatures of the various component members.

Table 6-6 Structural Component Temperatures

Orbit Position, deg	Surface		Vertical		Interior Diagonal		Exterior Diagonal	
	Min	Max	Min	Max	Min	Max	Min	Max
0	−50	55	− 52	21	− 44	40	−49	49
45	−55	68	− 51	0	− 43	58	13	71
90	−55	55	− 71	26	− 62	47	23	46
115.8	−86	41	− 70	27	− 94	46	28	40
116	−89	− 5	− 72	−17	− 96	−18	−39	−31
180	−98	−72	−106	−80	−100	−72	−95	−82
244.6	−89	21	− 79	− 9	− 96	17	7	30
270	−77	41	− 72	32	− 89	33	9	27
315	−47	41	− 68	26	− 65	43	16	51

The finite element model used in the dynamic analysis was modified for the thermoelastic analysis by constraining all six degrees of freedom of node 19 of that model (Fig. 6-2).

The thermal distortions of the feed and reflector surface were then calculated using the modified computer model. These distortions are used in determining rf performance and as inputs in the mesh thermoelastic analysis. Table 6-7 gives the feed distortions.

Figure 6-19 shows the distortion of the box truss structure at orbit position 90 deg. Notice the structure distorts toward the sun because of its negative CTE members. In contrast, the feed and antenna distort toward each other in the 270-deg orbital position, but the magnitude of the deflection is an order of magnitude less than the 90-deg position. The antenna support structure tends to flatten slightly by about 2 mm in the 0-deg orbital position because of the solar flux. The effects of these distortions on rf performance will be discussed in Section 6.6. The antenna support structure distortions were used as input boundary conditions in the thermoelastic distortion analysis of the mesh tie system. These distortions are more significant in how they interact with the mesh tie system pretensions.

Table 6-7   Displacements of Feed Beam Due To Thermal Environment

Orbital Position, deg	Direction					
	X, mm	Y, mm	Z, mm	Rotation About X, rad 10-5	Rotation About Y, rad 10-5	Rotation About Z, rad 10-5
0	− 4.21	−0.056	−0.214	2.67	− 3.11	−0.515
45	−10.5	−0.080	0.221	1.03	−13.6	−0.134
90	−15.3	0.154	−1.52	−1.52	−19.4	0.633
115.8	−13.1	0.073	−0.814	0.738	−14.2	0.145
116	−7.79	0.177	1.42	−0.944	− 8.44	−0.248
180	−1.26	−0.422	4.11	−2.09	− 0.503	−0.372
2.44.6	−5.15	0.095	2.62	−2.58	7.95	0.241
270	3.80	−0.006	1.31	−1.61	7.64	−0.004
315	−4.20	−0.009	1.99	−1.01	9.94	0.185
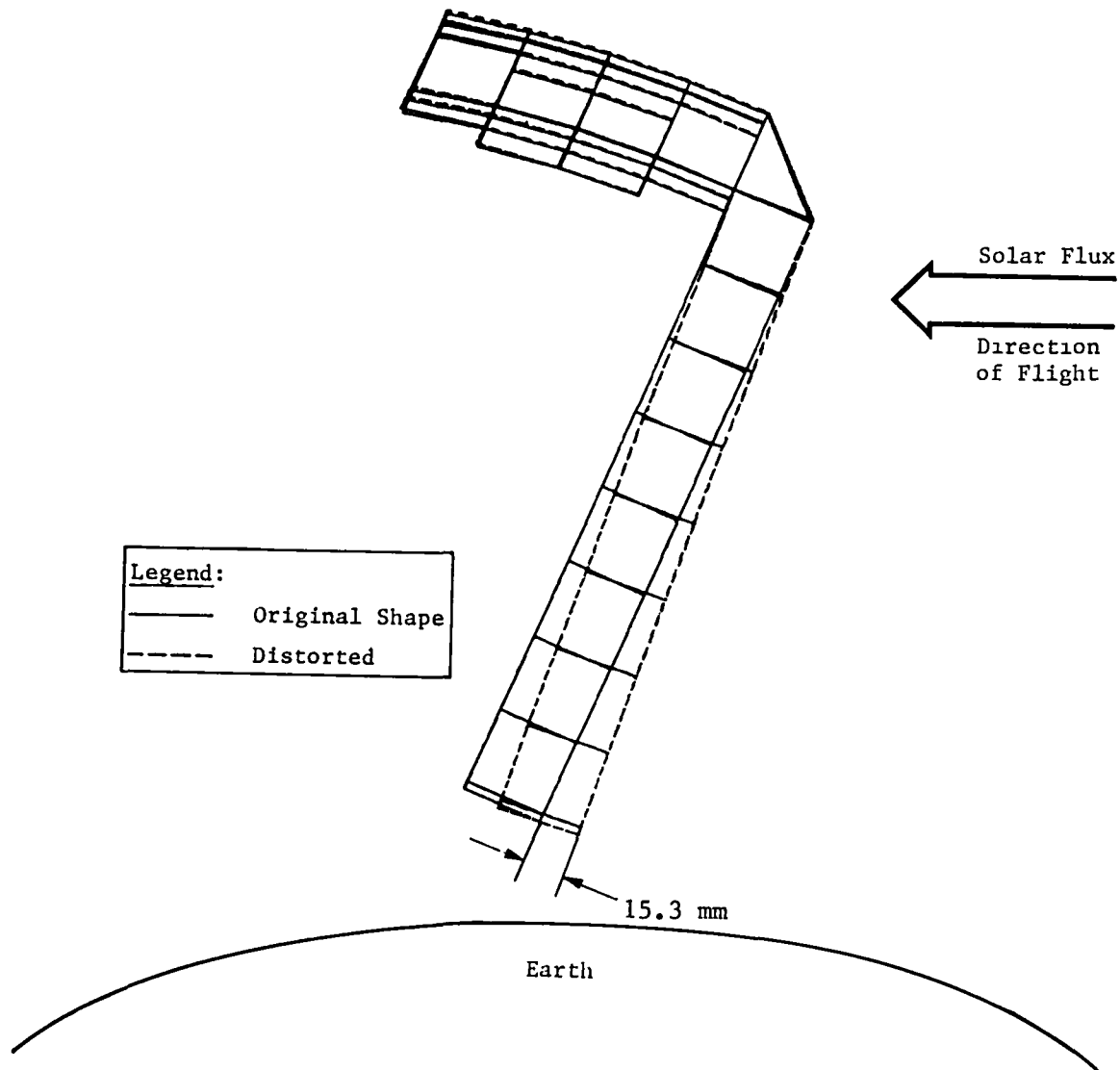
Figure 6-19   Thermoelastic Distortion at 90-deg Orbital Position

6.3.2 Thermal Distortions of Mesh Tie System

The ANSYS stress stiffening techniques were used to model the reflector
surface. The model used cable elements to represent the mesh tie sys-
tem. ANSYS cable elements can be initially strained before the stiff-
ness matrix is formed. This strain was determined by first assuming a
pretension in the mesh of 0.0178 N/cm. The 0.0178-N/cm pretension is
the minimum tension required to produce a flat reflective surface by
removing any wrinkles in the mesh caused by stowage constraints. Be-
cause pretension in the mesh is reacted by the surface cords, the sur-
face cords' tension is approximately 1.25 N for the surface cord spac-
ing of approximately 0.7 m. Because of the enormous number of cable
elements necessary to model the entire surface, a single representative
box truss section was used. The analysis cost of the mesh tie system
model was reduced even further by choosing a number of cable elements
to represent the surface. This reduction in elements did not give a
dramatic change in thermal distortions of the surface and gave a rea-
sonable initial estimate of thermal distortions in the mesh tie system.
The mesh box section selected (box 5, Fig. 3-21) had the worst-case
thermal environment, including shadowing effects, and therefore gives a
worst-case analysis for thermoelastic distortions of the mesh surface.
Figure 6-20 shows the node points for the ANSYS model. Because the
model's initial geometry was adjusted for prestrain deflections, when
the prestrain was applied to the cable elements, the mesh tie points
deflected to form the parabolic-toric surface required. Adjacent mesh
box sections were simulated by point loads at the standoff nodes. This
prestrained model was then subjected to three worst-case thermal envi-
ronments. The thermal cases also included the box truss standoff de-
flections caused by thermoelastic distortions of the antenna box struc-
ture. The first thermal case was the maximum solar flux position in
orbit. The second thermal case was the minimum solar flux in orbit.
The remaining thermal cases included local shadowing effects from the
SAR and/or from mesh shadowing mesh. Table 6-8 gives the average, max-
imum and minimum temperatures for each type of cord and each thermal
case.

Next, the surface area was divided into 20 pieces representing the ef-
fective surface area identified with each node point deflection. These
were used to determine a weighted area rms surface distortion. The ef-
fective areas were determined with quite a lot of conservatism because
the area of mesh around the standoffs will not be affected by the tie
system as much as by the box truss deflections. The box truss deflec-
tions cause systematic rather than random surface errors. Figure 6-21
shows how the surface was broken up and the effective area value for
each section. The three thermal cases were run on a mesh tie system
that used graphite cord with a modulus of 2.34×10^n N/m^2 and a CTE
of -0.4×10^{-6} m/m/°C.
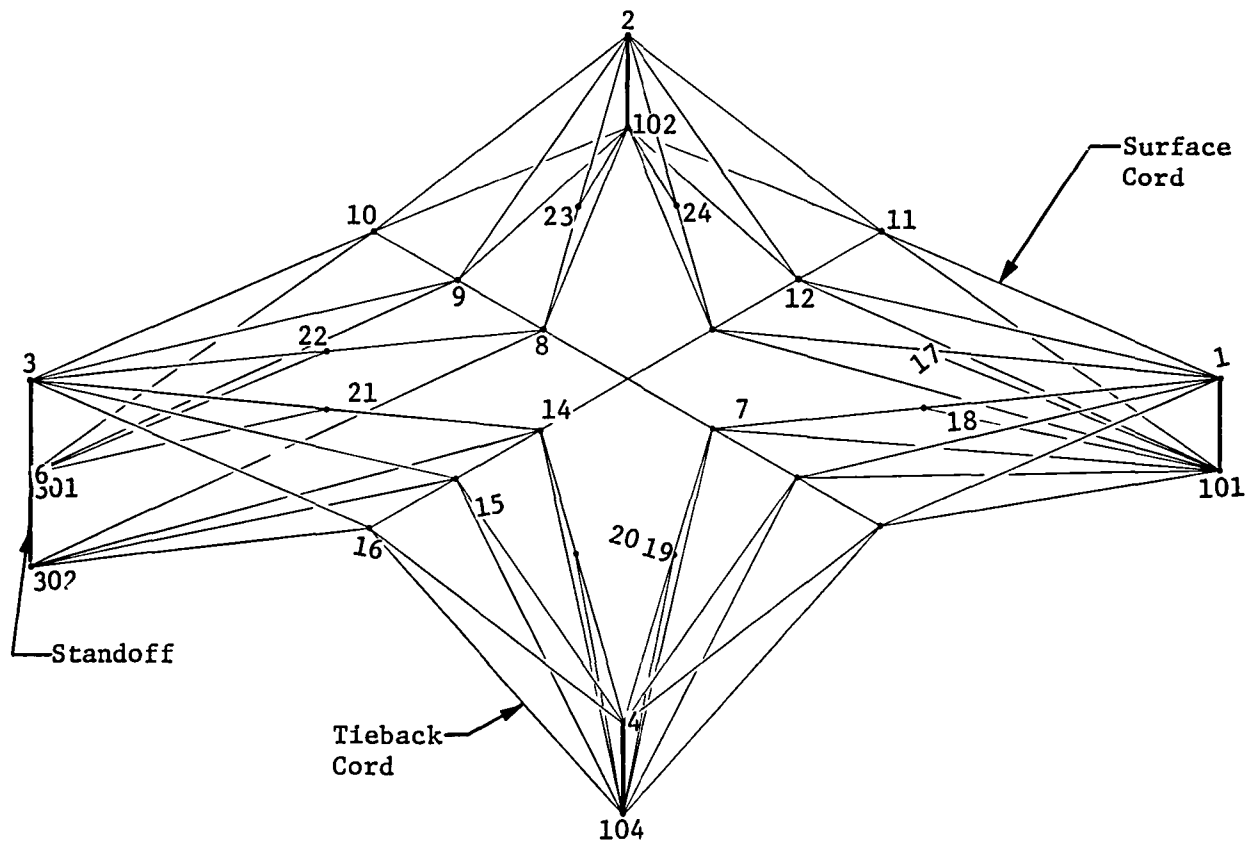
Figure 6-20 ANSYS Mesh Tie System Model Numbering System

Table 6-8 Temperature Values on Single Panel Mesh Support System

Thermal Case	Orbit Position, deg	Surface Cord Temperature, °C			Tieback Cord Temperature, °C		
		Average	Max	Min	Average	Max	Min
Max Solar Flux	0	45 0	47 01	41 86	43 5	47 88	32 63
Min Solar Flux	280	−89 6	−82 79	−93 03	−91 52	−89 11	−97.11
Local Shadow	270	− 0 695	30 62	−54 46	5 96	29 82	−25 22
Local Shadow	275	3 53	31 69	−42 81	8 88	29 42	−28 12
Local Shadow	285	15 26	34 61	−15 02	13 91	33 02	−74 57
Note Reference Temperature = 22 2°C							

Results showed the maximum deflection of the upper surface mesh tie system was 0.024 cm at node 7 with a rms surface distortion of 0.035 cm. This occurred with the minimum solar flux thermal case. Table 6-9 gives the maximum deflection and the rms surface distortions for all three thermal cases.

Legend:	
Node No.	Effective Area, m^2
5	12.80
6	12.80
7	6.40
8	6.40
9	12.80
10	12.80
11	12.80
12	12.80
13	6.40
14	6.40
15	12.80
16	12.80
17	12.80
18	12.80
19	12.79
20	12.79
21	12.80
22	12.80
23	12.80
24	12.80
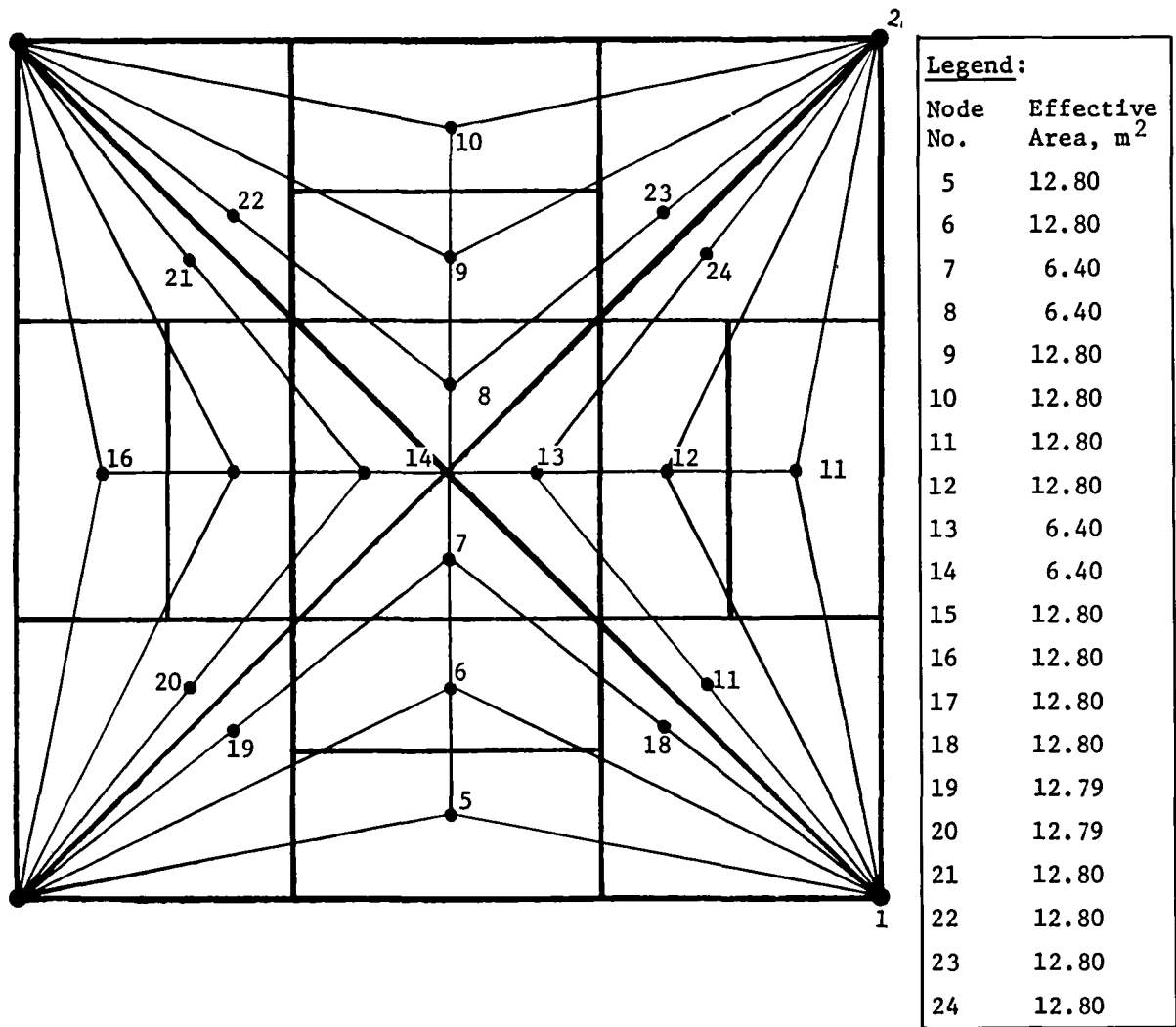
Figure 6-21   Effective Surface Area per Node Point

Table 6-9
Maximum and rms Distortion of Reflective Surface Caused by Temperature Change of the Box Truss Structure and the Mesh Tie System

Thermal Case	Maximum Deflection of Single Mesh Panel, cm	rms Distortion of Total Reflective Mesh, cm
Maximum Solar Flux	−0.021	0.030
Minimum Solar Flux	0.024	0.035
Local Shadow at 270 deg	0.007	0.007

6.3.3   Manufacturing Error Distortions

The manufacturing errors in the antenna support structure were determined from previous experience in building graphite/epoxy structures. The manufacturing errors are broken into two categories—random and

systematic. The random error of the EOS antenna support structure is 0.127 cm rms. In addition to the random error, the systematic error causes translations of the antenna support structure that effectively cause feed horn scanning and axial defocusing of the feeds. This systematic error is an approximately 0.508-cm peak at the outer apertures, reducing to 0.0 cm at the feed/mast attachment point. Section 6.6 discusses the dB loss due to these errors.

The manufacturing error of the mesh tie system is estimated to be 0.064 cm rms. This was derived from previously designed models of mesh tie systems such as shown in Figure 3-22.

6.3.4   Summary of Distortion Analysis

Table 6-10 summarizes the rms distortion of the EOS reflective mesh. These values are summed in a worst-case scenario to be evaluated in the rf analysis Section 6.6.

Table 6-10
Summary of Total Distortions of Total Reflector Mesh Caused by Pillowing and Thermal Effects, and Manufacturing Tolerances

Distortion	Magnitude, cm rms	Percent of Total Distortion
Saddling Distortions	0.021	8.5
Thermal (Truss and Mesh)	0.035	14.2
Manufacturing Truss	0.127	51.4
Manufacturing Mesh Tie System	0.064	25.9
Worst-Case Total rms	0.247 cm	
rss of rms	0.144 cm	

Table 6-11 tabulates the worst-case systematic errors. The table also includes the worst-case effective fixed scanning angle and axial defocus that results. Their impacts on the rf performance will be discussed in Section 6.6. Because distortion of the reflector surface can be analyzed as reflections of the feed, the distortions are presented as feed errors in Table 6-11. These angles and defocusing errors were calculated by fitting a parabola through the systematic surface distortions.

Table 6-11   Summary of Systematic Distortions

Distortions	Peak at reflector edge, cm	Effective feed scan angle, deg	Effective axial defocus, cm
Thermal	0.258	0.0025	2.3
Manufacturing Errors	0.503	0.0048	4.98

6.4 STRUCTURAL ANALYSIS

This section discusses the static loads analysis performed on EOS. The thermal loads were combined with the orbit transfer loads to determine the worst-case column compressive loads on the members. An analysis also investigated the necessary diagonal pretension levels. Another analysis was performed to determine the impact of normally distributed random length manufacturing error on the structure. The last section summarizes all the worst-case load conditions.

6.4.1 Thermal Loads and Orbit Transfer Loads

The goal of this investigation was to determine how fast the spacecraft can be accelerated (transferred) in the thermal environment without dramatically affecting structural design. The loads induced by the change in various member lengths to accommodate thermal gradients were combined with the orbit transfer acceleration loads. It was found, however, that some of the worst-case conditions could be attributed to thermal loads alone. The goal of this analysis was to determine the worst-case loads on structural members. A NASTRAN finite-element model was used in the analysis. The acceleration loads were scaled to determine maximum allowable acceleration.

The temperatures applied to the member were derived in Section 6.2. As in Section 6.3.1, nine thermal cases were run for the various orbital positions. Table 6-12 shows the maximum member loads for each of the 9 thermal cases when the maximum and minimum temperature are considered.

Table 6-12   Orbital Transfer and Thermal Compressive Loads, N

Thermal Case	Orbital Position, deg	Surface Members Load (Element No.)			Vertical Members Load (Element No.)		
		2 diag	3 diag	4 diag	2 diag	3 diag	4 diag
1	0	-57(202)	-68.4(215)	+	-78.1(465)	-35(462)	-99.8(449)
2	45	-268(202)	-305(203)	-171(155)	-122(438)	-131(433)	-23.6(461)
3	90	-147(202)	-188(215)	-156(135)	- 92(434)	-94.3(429)	-50(427)
4	115.8	-235(202)	-300(215)	-264(135)	-134(438)	-143(464)	-51(448)
5	116	-44.8(202)	-113(311)	+	- 75(438)	-38(464)	-70(461)
6	180	-144(202)	+	+	-175(438)	-103(462)	-129(461)
7	244	-345(202)	-360(216)	-164(136)	- 65(465)	- 18(431)	-112(461)
8	270	-238(202)	-216(225)	-130(135)	-212(438)	-184(464)	- 51(410)
9	315	-263(202)	-270(215)	-217(135)	-228(435)	-201(437)	- 41(410)
Orbit Transfer		-79(202)	- 70(215)	+	-143(438)	+	+
Maximum		-345(202)	-360(216)	-264(136)	-228(435)	-201(437)	-129(461)

The acceleration rate of the orbit transfer had a steady-state magnitude of 0.01 g and was applied to the structure along the Z-axis. This is the same direction of velocity vector at this point in the mission. Figure 6-22 depicts the direction of the acceleration and the deflection incurred under only the orbit transfer loads, which was 1.45 mm. The structure was constrained in the Z direction at nodes 4, 8, 34, and 38 (Fig. 6-2) where the orbit transfer nozzles were located. The spacecraft contained the full mass of the orbit transfer (819 kg) and slewing propellant (1265 kg), and all the subsystems.
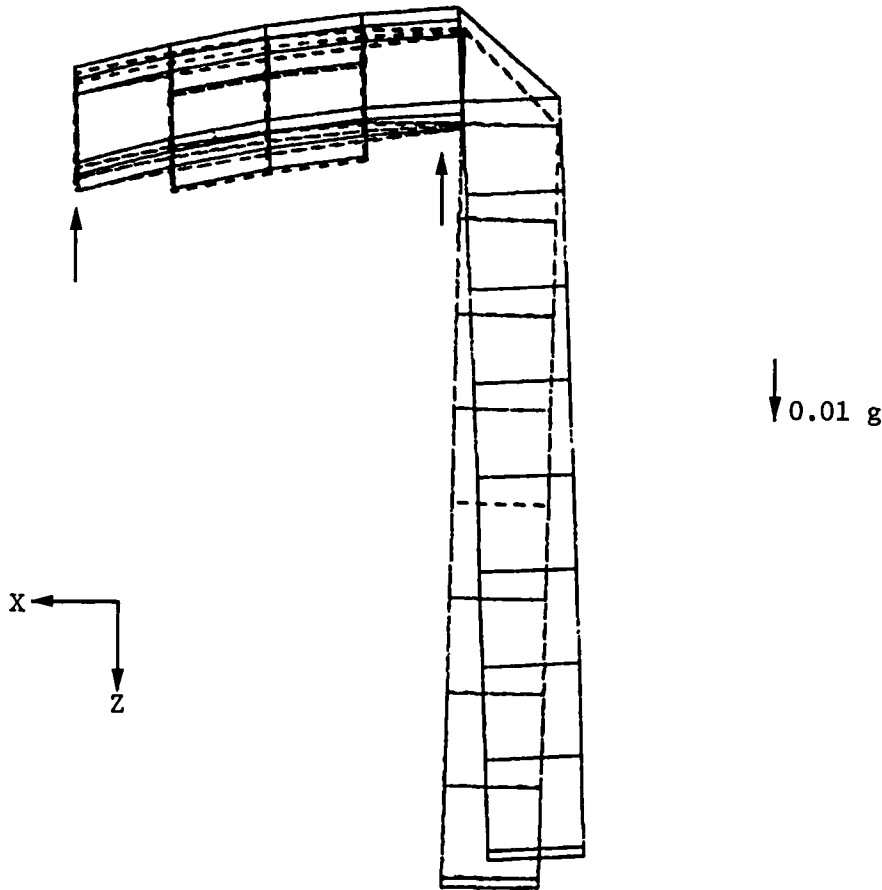
Figure 6-22   EOS Orbit Transfer Deflections

The results of the combined loading analysis are shown in Table 6-11. The member loads are broken down into how many sets of diagonals are reacting their pretension levels against the members.

A compressive load of -519 N occurs in the feed beam at the 90-deg orbital position. This member was modeled as a surface member and the loads would be different in a more detailed model. It is also likely that some sort of thermal control system for the feeds would be necessary, thus reducing the problem. Only the members' compressive loads were analyzed because their column load capability is much less than their ability to handle tension loads. The diagonal member loads were not analyzed in this section because they do not have to maintain a

tension load during orbit transfer. The worst case for member 135 occurs during an operational orbit with thermal load only because orbit transfer puts these members in tension. The next section will determine the amount of pretension necessary on the diagonal members during operational orbit. The loads in Table 6-12 will be further analyzed in the summary of Section 6.4.4.

6.4.2 Diagonal Pretension

Diagonal pretension is necessary in box truss structures to maintain rigidity, eliminate nonlinearity ^{or} sloppiness in the joints, and permit the use of linear analysis techniques. Pretension in the diagonal members loads the joints of the structure, thus eliminating joint sloppiness caused by clearances for pinned joints of the box truss. The pretension levels are determined in a tradeoff between a level high enough to maintain tension in the diagonals and yet minimize the compressive loads induced on the surface and vertical members. The diagonal member will be tensioned at final assembly in an iterative process of diagonally adjusting their length throughout the structure until the correct pretension level is reached.

The pretension level was determined using a worst-case scenario. The worst-case thermal load cases analyzed used the model described in Section 6.3.1. The results derived from the thermoelastic distortion computer run are shown in Table 6-13. The unloading of the diagonals in this analysis was actually a compressive load because all the static analysis was done with linear finite-element techniques, and the diagonal members were allowed to take compressive loads. The diagonal member would be pretensioned to a level higher than its worst-case combination, including safety margin pretension, and this level would vary throughout the structure to minimize compressive loads on the vertical and surface members.

Table 6-13   Thermally Induced Diagonal Member Loads

Orbital Positions, deg	Interior Diagonal		Exterior Diagonal	
	Element No.	Load (N)	Element No.	Load(N)
0	682	-103	1170	-150
45	610	- 87	1174	-25
90	606	-110	--	+
115.8	602	-143	--	+
116	602	- 86	1167	-130
180	683	- 16	1171	-150
244	656	-151	--	+
270	656	-150	1123	- 40.7
315	624	-138	1162	- 37.8

The highest untensioning was 151 N in both the exterior and interior diagonal member. Loads were higher in the feed, but these were discounted because the model did not account for the stiffness of the feed horn pentehedral truss. The diagonal pretension loads will be further analyzed in combination with other loads in Section 6.4.4.

6.4.3 Manufacturing Tolerance Analysis

An analysis investigating the loads and distortions generated by structural member length inaccuracies was performed on EOS. For a given manufacturing tolerance on the length of a member, the length disparities generate structural loads. The manufacturing tolerance of a member's length was fitted to a normal curve distribution and randomly applied to the vertical and surface members of the structure. The diagonal members were excluded because they have negligible length inaccuracies that produce loads because they are pretensioned to a set value during assembly and their length is a function of that pretension.

Using finite-element techniques, a half-symmetric model of the antenna truss was developed for the analysis. Member length disparities were input in the model through a temperature artifact. A pretension level was also applied to the diagonal members by this method. An iterative process of analyzing load levels in diagonal members after each computer run and adjusting tension (temperature) levels to obtain the prescribed pretension level was performed on the model. This process is presented in a flow chart in Figure 6-23. The procedure is analogous to the actual manufacturing process of setting tension levels at final assembly. Setting tension levels cannot be done in a single step because of (1) the absorption of strain energy by the structure, and (2) the unknown effect of member length inaccuracies on diagonal pretension levels. After about five iterations, the pretension levels of the diagonal members approach the desired tension level.
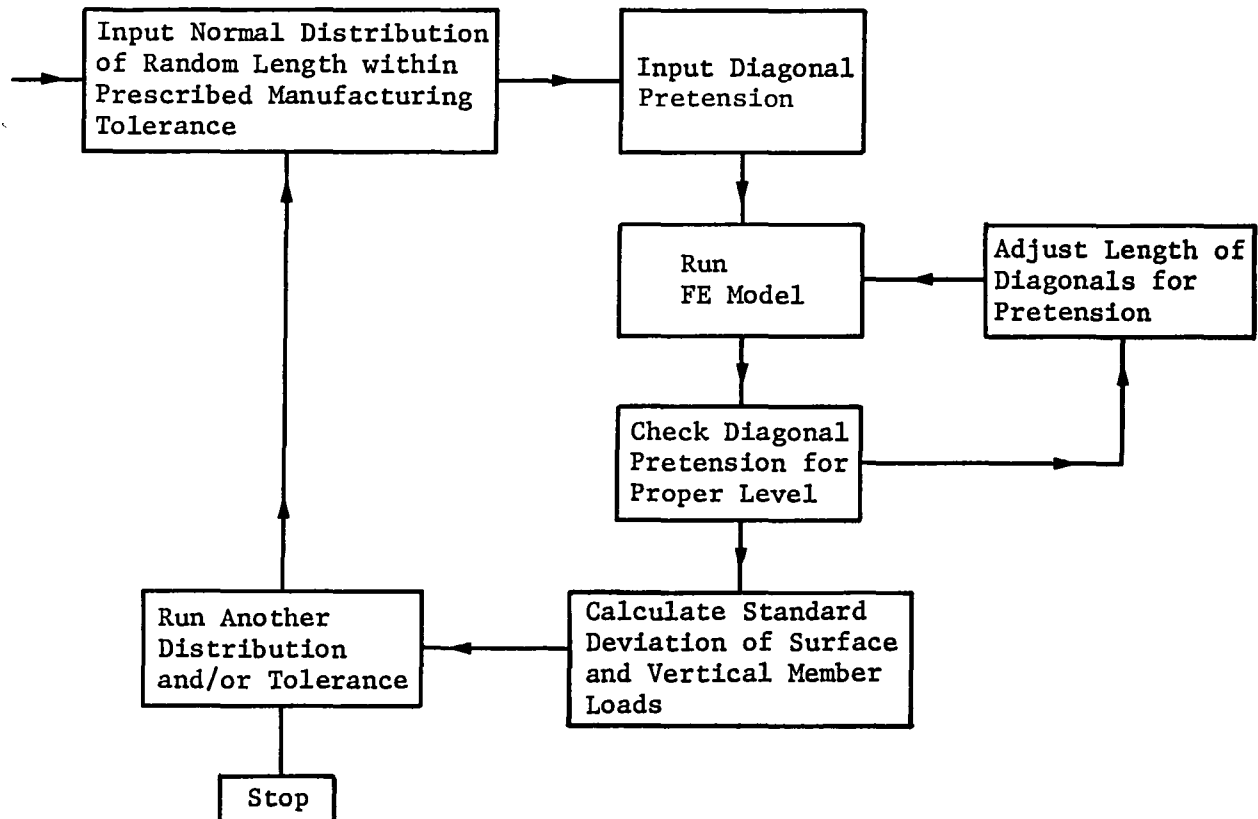
Figure 6-23   Flow Chart for Random Length Inaccuracies Analysis

Three cases of manufacturing tolerances (±0, ±0.25, and ±0.5 mm of the surface and vertical member lengths) were evaluated. The resulting loads were compared against a mean compression load induced by the diagonal pretension, and a standard deviation (σ) was calculated. These results are presented in Figure 6-24. Since a small sample was used in the analysis, a 4σ estimate is necessary to predict worst-case-induced loads. The actual loads on the members with a ±0.25-mm tolerance are shown in Figure 6-25. A tolerance of ±0.25 mm is possible with today's manufacturing techniques, and these loads will be discussed in the loads summary Section 6.4.4.
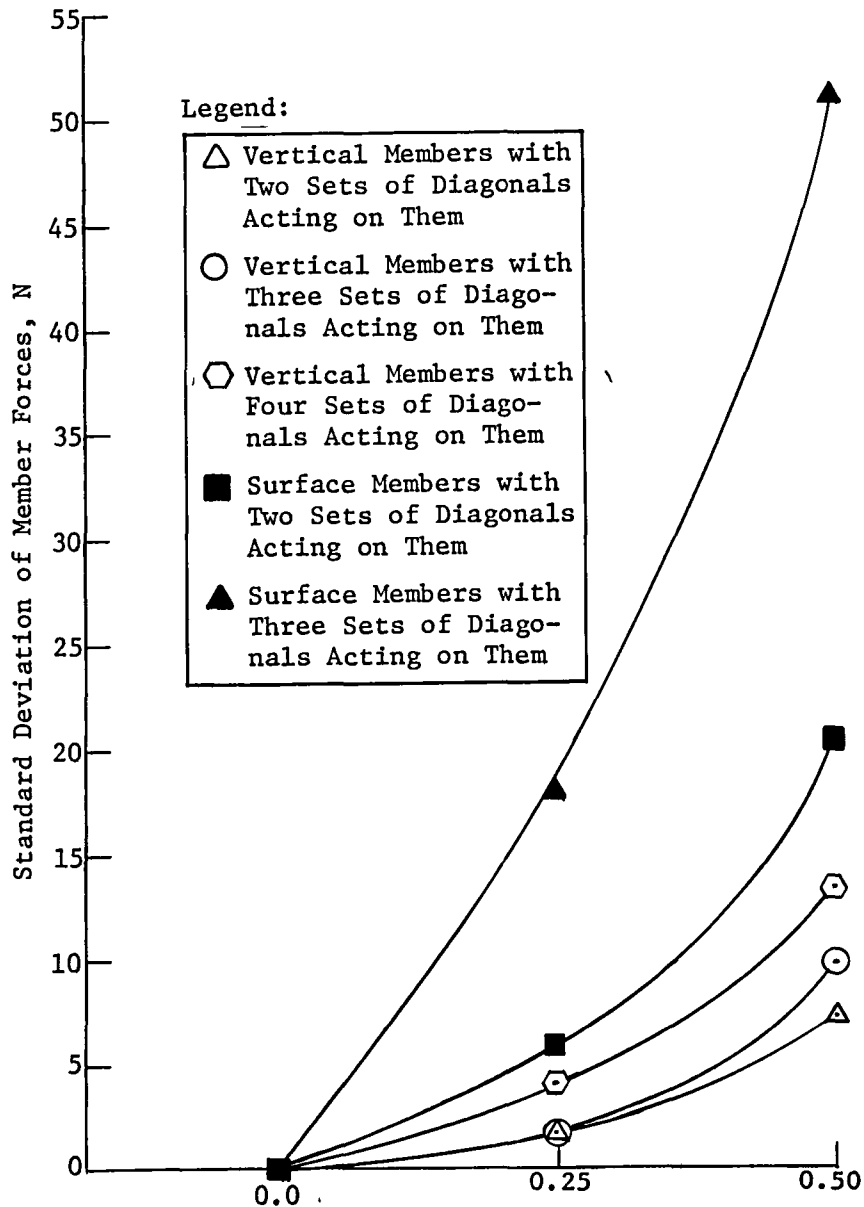
Figure 6-24
Standard Deviation of Manufacturing Length Error-Induced
Compressive Loads in Large Space Systems

139
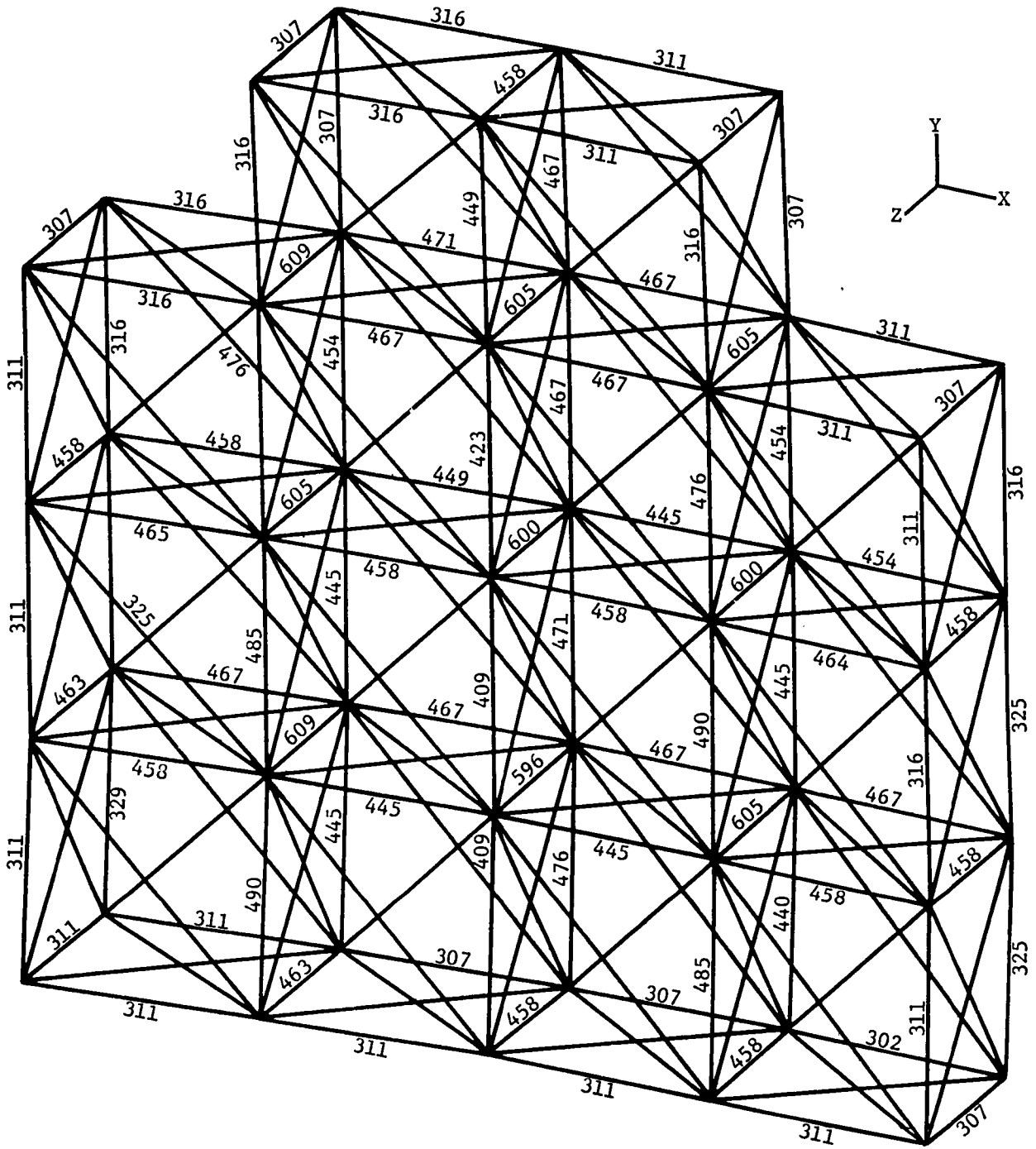
Figure 6-25
Vertical and Horizontal Member Compressive Loads Due to 222-N
Preload and +0.25-mm Manufacturing Tolerances

Other manufacturing-induced loads will exist in the structure. These would be caused by fixturing constraints and building the structure under a one-g environment. These loads will change once the spacecraft is located in orbit because the structure will assume a minimum strain energy state at zero-g. These loads can only be estimated at this time and are not included in this loads analysis.

6.4.4 Loads Summary

The compressive loads on the vertical and surface members were analyzed on a worst-case basis using a combination of (1) thermal loads, (2) orbit transfer loads, (3) manufacturing tolerance loads, and (4) diagonal pretension loads. The compressive loads are important in determining whether the column load capability of the member has been exceeded. These compressive loads were gleaned from the previous analyses discussed in this section. The reaction of the diagonal pretension on the vertical and surface members also causes a compressive load. This compressive load can be approximated by multiplying half the diagonal pretension level times the square root of 2 for each set of diagonals reacting on a member (as many as four sets of diagonals). Two surface members also have four sets of diagonals reacting upon them in the area of the feed mast interface. The compressive loads are summarized in Table 6-14.

Table 6-14 Summary of Worst-Case Loads, N

	Surface Members			Vertical Members		
	2 diag	3 diag	4 diag	2 diag	3 diag	4 diag
Thermal and Orbit Transfer	-345	-360	-264	-228	-201	-129
Diagonal Pretension Load $x\sqrt{2}/2 \times 160$ N	-226	-339	-453	-226	-339	-453
Manufacturing Tolerance Loads ($\pm$0.25 mm) 4	- 24	- 70	- 70	- 12	- 12	- 16
Totals	-595	-769	-790	-466	-553	-598

The highest compressive load was -790 N on member 135 in an operational orbital position of 115.8 deg. This first-cut design of the surface members has an allowable compressive load of -751 N, which includes a 25% margin of safety and a 10% knockdown factor for thermoelastic and manufacturing curvature and eccentric loading. During a second iterative stage of design, this negative margin member could easily be brought within the allowable limits through better matching and a value closer to zero for the various component member CTEs. The vertical members have an allowable load of 1549 N. It appears they may be overdesigned, but it should be noted that mesh loads on the vertical members were not included in this analysis. Also, their worst-case loading condition is probably during launch when they are the load-bearing members.

6.5 RIGID-BODY ANALYSIS

The approach used to determine the environmental forces and torques that must be compensated for to maintain attitude control and station-keeping was to constantly maintain the EOS in nadir pointing over the entire orbit. This eliminates any gravity gradient torques that would occur for any offset between the EOS principal axes and the rotating reference axes system. Once the environmental forces and torques were determined and locations selected on the EOS for placement of the electric thruster systems, the thruster system was sized to meet the attitude control and stationkeeping requirements.

This section discusses our rigid-body analysis of the EOS. The results were used to size the attitude control system (ACS) thrusters required to maintain attitude control and stationkeeping. The EOS was placed in a 700-km circular orbit about the earth, subjected to environment and vehicle interaction forces and torques and placed in a Z-local vertical mode (Fig. 6-26).
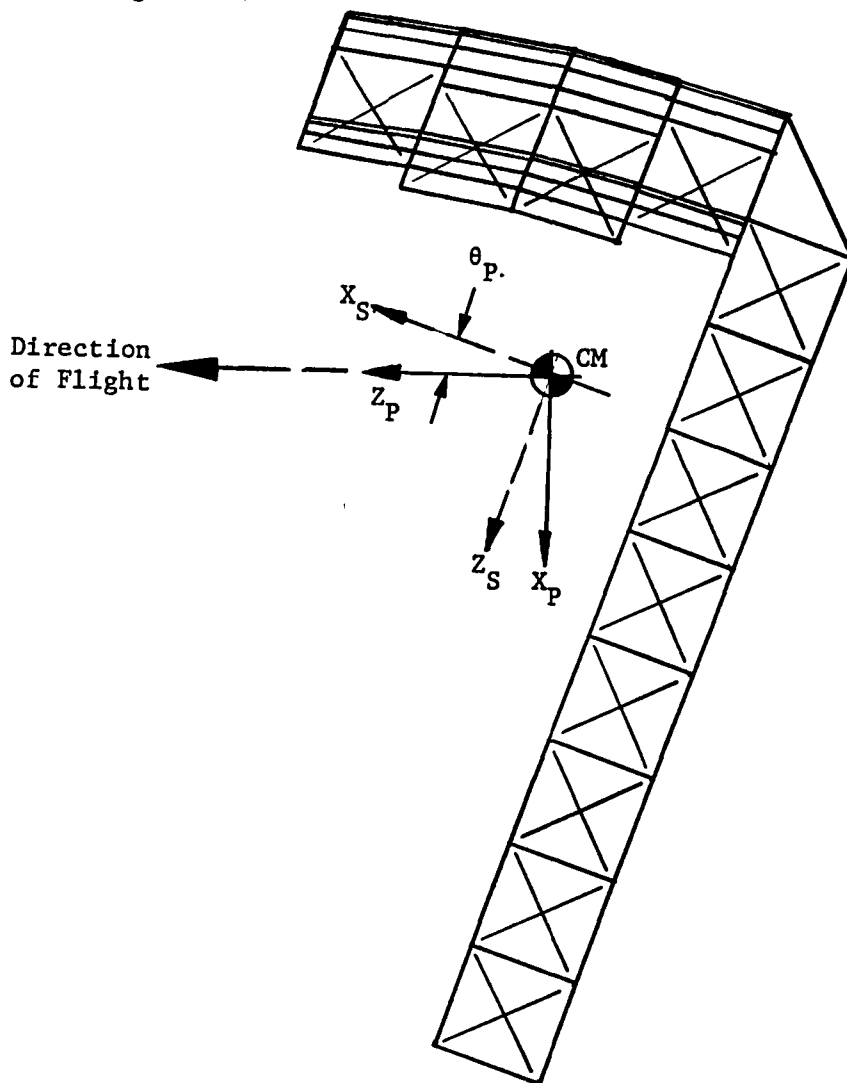
Figure 6-26 Flight Orientation with Respect to Principal Axis

6.5.1 Environmental Forcing Functions

The orbit, rotating reference, and inertial coordinate systems are shown in Figure 6-27, with the inertial reference coordinate system defined with respect to the earth's equatorial plane. The node line of a circular orbit regresses westward for each revolution of the spacecraft around the earth by the amount defined by

[1] $\quad \xi = 0.5856 \ (Re/Ro)^2 \cos i \quad (deg/orbit)$

[2] $\quad \tau = 2\pi R_o^{3/2} = \dfrac{2\pi}{\omega o} \quad s \quad$ where $\omega_o = \sqrt{\dfrac{\mu}{R_o^3}}, \ rad/s.$

Then the nodal regression rate of the orbit per day was determined by

[3] $\quad \omega_\lambda = \xi \ N \ (deg/day).$
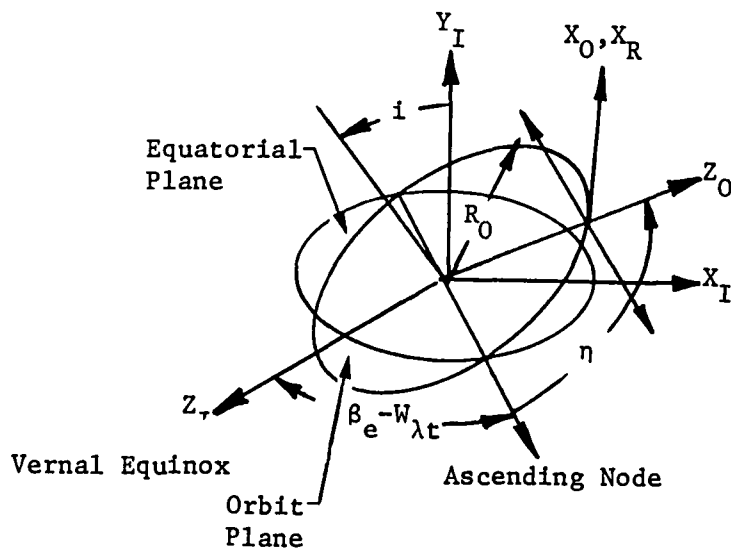
$Figure \ 6\text{-}27 \quad Orbit \ and \ Inertial \ Reference \ Coordinate \ Systems$

From the results of the mission analysis, it was concluded that the baseline EOS is to be placed in an orbit at an inclination angle of 98.17 deg. The number of orbits completed per day for a 700-km circular orbit is

[4] $\quad N = \dfrac{86400}{\tau} \quad (Orbits/Day)$

and for i = 98.17, the modal regression rate becomes

[5] $\quad \omega_\lambda = (-6.7599 \times 10^{-2} \ deg\text{-}Orbit)(14.58 \ Orbit/Days)$
$\qquad = -0.9856 \ deg/Day$

where the negative sign implies that the regression of the orbit is
eastward. The motion of the earth about the sun with respect to the
ecliptic plane is 0.9856 deg/day, which, when correlated with the nodal
regression rate, defines a sun-synchronous orbit. Three sun-synchro-
nous missions for the baseline EOS have been defined--the first, for β_e
= (0 deg $\pm$ 2.3 deg), which implies a noon equatorial crossing time, and
the second and third for β_e = -37.5 deg, ±2.3 deg, which produces a
9:30 a.m. equatorial crossing time. The angle β_e positions the orbit
plane with respect to the sun line, the result of which affects the
solar radiation pressure forces and torques and the occulted region of
the orbit. The fourth mission was flown at an orbit inclination of 60
deg, which produced a westward nodal regression rate equivalent to 5.26
deg/day.

The environmental forces and torques acting on the EOS over an orbit
will be presented as a function of the anomaly angle η_A. Figure 6-28
shows the anomaly angle η_A and its initial condition with respect to
the orbit and to the occulted region of the orbit.
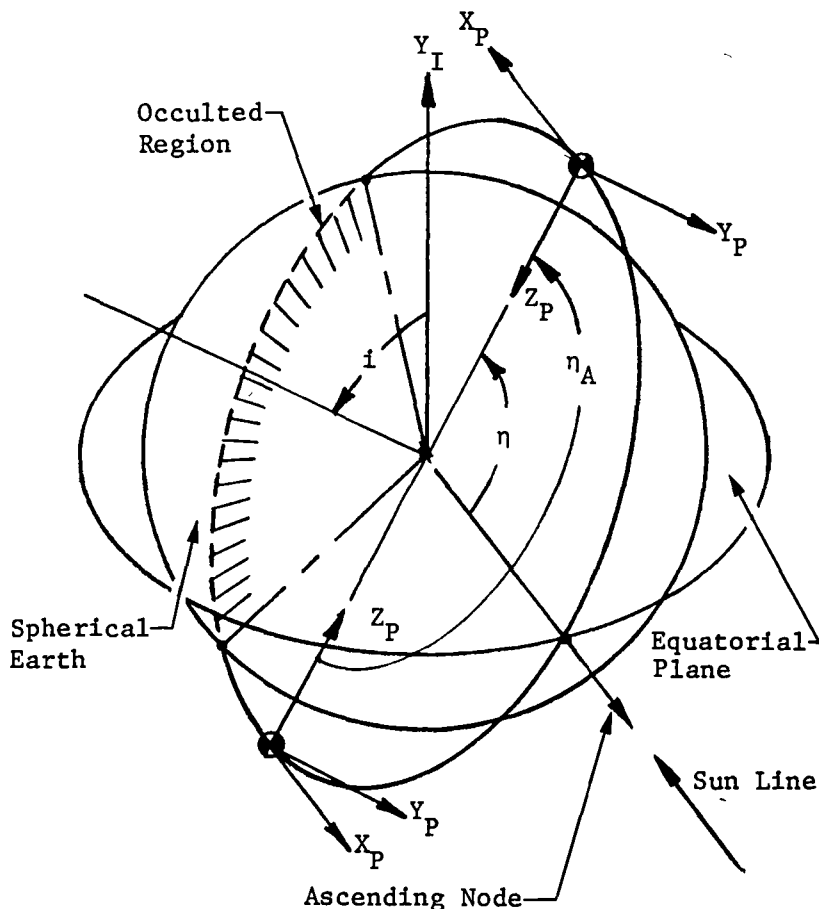
Figure 6-28
Occulted Region and Anomaly Angle, η_A,
Defined with Respect to an Orbit

A portion of the EOS structural configuration is shown in Figure 6-29 to illustrate location of the center of mass with respect to the zero datum. The centers of pressure for the aerodynamic and solar radiation pressure are located with respect to the EOS center of mass (CM). The baseline EOS mission was flown with respect to its principal axes system, which is offset from its X_s and Z_s structural axes by the angle θ_p, defined by

[6] $\quad \tan 2\theta_p = 2I_{xz}/\left(I_{zz} - I_{xx}\right)$.
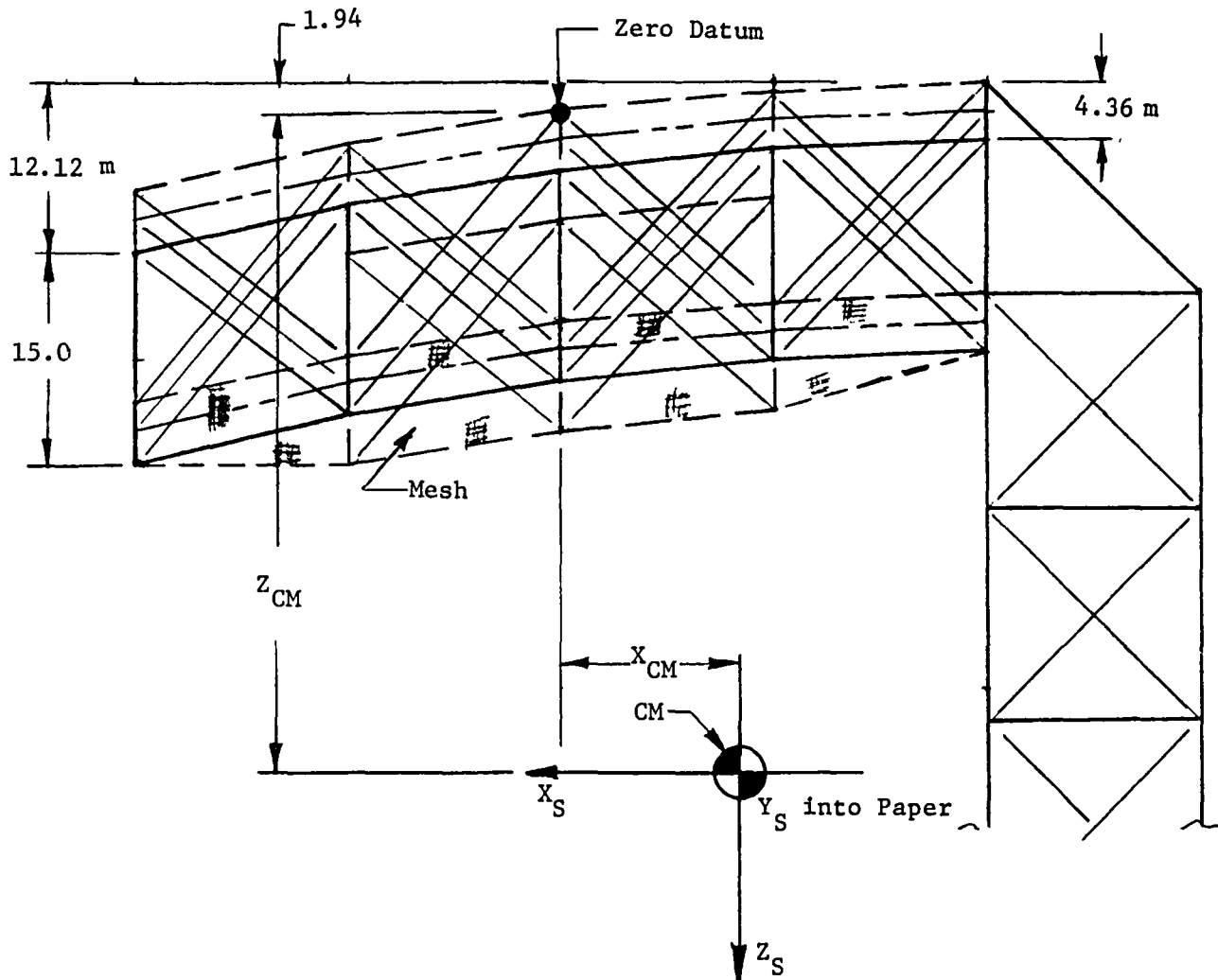
Figure 6-29 Location of Center of Mass

This requires that the X_s and Z_s axes form a plane of symmetry, which is the case because the EOS will be mass-balanced to achieve this condition. Figure 6-26 illustrates the EOS configuration in its flight orientation, which is achieved by commanding the EOS to rotate about its Y axis, θ_p. The EOS in this orientation eliminates the need to compensate the gravity gradient torque produced as a result of the I_{xz} cross product of inertia, and defined by

145

[7] $T = -3\omega^2 I$.

Considering a 700-km circular orbit and a representative value of 5.30 x 10^6 kg-m^2 for I_{xz}, the magnitude of the gravity gradient torque produced is 17.9 N-m in the old orientation, which is orders of magnitude larger than any of the torques produced as a result of the environment.

The projected areas required for computation of the solar pressure and aerodynamic forces were first determined with respect to the structural axes system and then transformed to the principal axes system. The mesh material that forms the antenna surface contributes the largest surface area projected in each axis. One m^2 of mesh is equivalent to a solid area of 0.1 m^2 when viewed normal to the area; such is the case with respect to the Z axis of the EOS. The appearance of the mesh, when viewed with respect to either the X or Y axis, approaches that of a more solid area. Figure 6-30 illustrates the projected areas of the antenna surface with respect to both the structural and principal axes systems. The projected area with any significant increases occurs with respect to the X_p axis while there is very little, if any, increase with respect to the Y_p and Z_p axes.
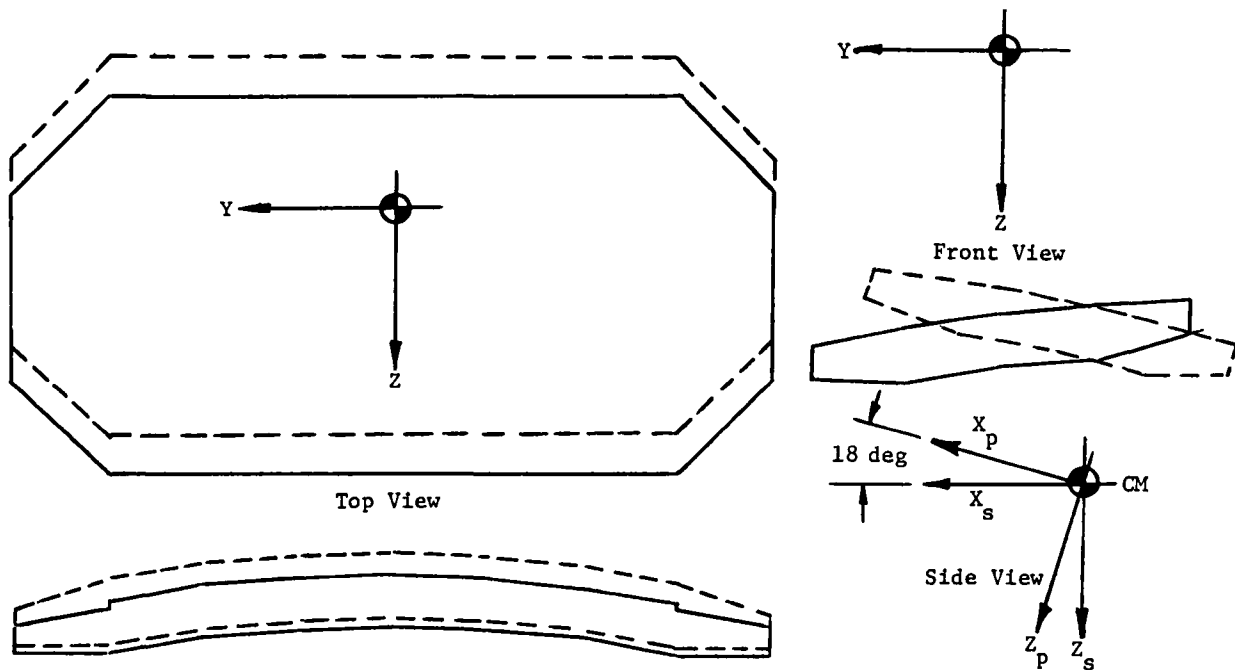
Figure 6-30   Projected Area of Antenna Surfaces

The four missions analyzed are described in detail in Section 2.2.4. Table 6-15 summarizes the mass moment of inertia values and the offset angle between the structural and principal axes systems for each of the four missions. The values of the spacecraft mass and the location of the center of mass with respect to the zero datum are shown in Table 6-16. The data presented in Table 6-16 clearly indicate that the plane formed by the X-Z axes is indeed a plane of symmetry. The variation in

the other parameters indicates that a redistribution of the masses that define a particular mission causes the offset angle, θ_p, to exhibit a 4.68-deg variation from Mission I to Mission IV EOS configurations.

Table 6-15   Mass Moments of Inertia

	Mass Moments of Inertia, kg-m^2						
Mission	I_{XX} x 10^7	I_{YY} x 10^7	I_{ZZ} x 10^7	I_{XY} x 10^{-9}	I_{XZ} x 10^6	I_{YZ} x 10^{-8}	θ_p, deg*
1	2.57	2.21	1.26	7.20	5.03	1.49	−18.76
2	2.59	2.26	1.30	7.92	5.26	1.49	−19.54
3	2.61	2.31	1.32	8.58	5.48	1.49	−20.24
4	2.26	2.25	1.29	7.70	5.19	1.49	−23.44
*See Equation [6].							

Table 6-16   Mass and Location of Center of Mass

Mission	Location of Center of Mass, m*			Mass, kg
	X_s	Y_s	Z_s	
1	−10.901	0.0	47.832	6558.9
2	−12.029	0.0	48.677	6738.9
3	− 9.8716	0.0	47.061	6911.9
4	−11.239	0.0	48.085	6683.9
*See Figure 6-30.				

The analysis of the thruster system follows. Solar pressure torques, total torque components, and total force components used for sizing the ACS are presented in Appendix D for each mission as a function of the anomaly angle.

6.5.2   Attitude Control System

The ACS uses the pulsed plasma thruster (PPT) for its baseline thruster. This thruster was chosen from concerns addressed in NASA Report 3522, Conceptual Design and Analysis of a Large Antenna Utilizing Electrostatic Membrane Managements. For example, long life and high I_{sp} were particularly important in choosing the correct thruster.

Packaging constraints initially dictated the size of the ACS 12 PPTs. These constraints were created when the EOS was folded into a package

that could be stowed in the shuttle bay. Moment arms and thrust vector structural interactions were considered when optimizing thruster placement. The volume constraints determined which thruster locations could be used.

In its folded package, the EOS had eight small volumes of space available at solid points on the EOS in which PPTs could be placed (Fig. 6-31). Four locations were large enough to contain twin PPTs on a gimbaling unit on the top side of the reflecting mesh (Fig. 6-32). Two locations on the sides of the receiving beam, and two locations on the rear, bottom side of the boom were only large enough to accommodate a single PPT and its gimbaling unit.

Front View   Side View
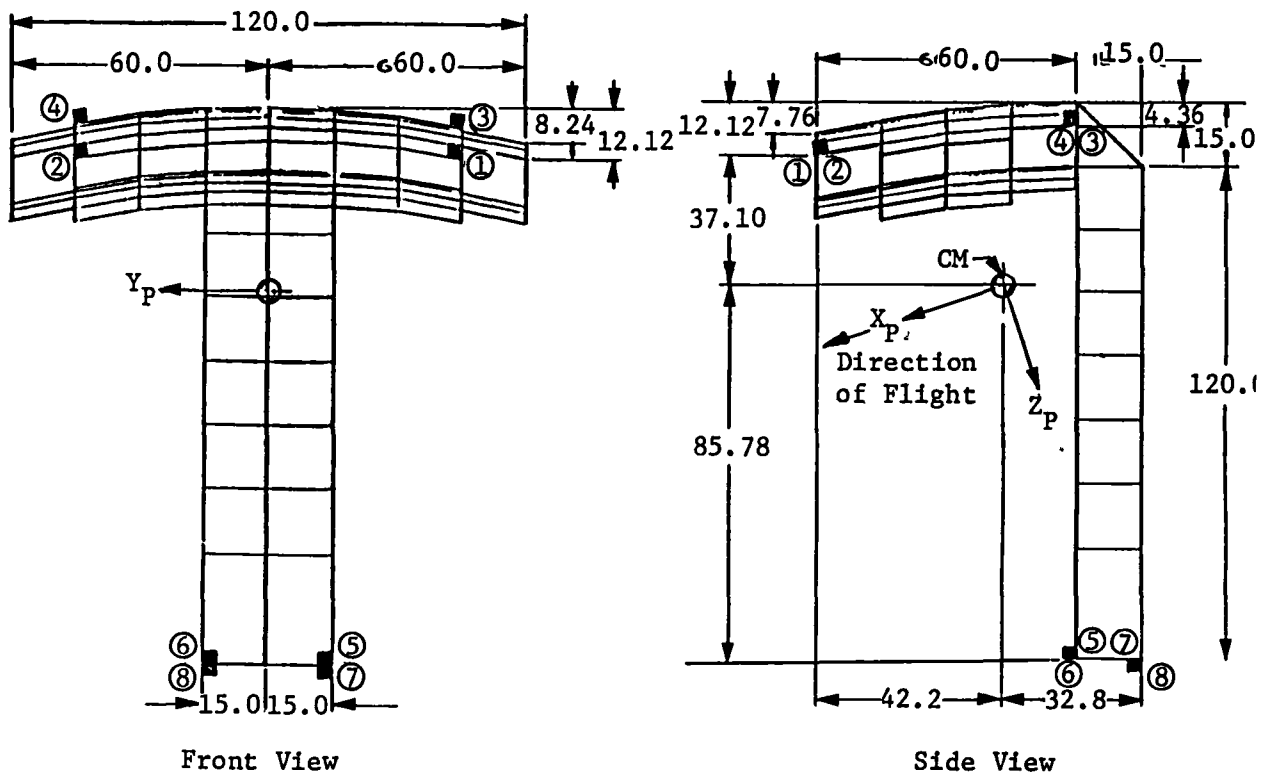
Note:

All dimensions are in meters.

Figure 6-31   Thruster Locations

148
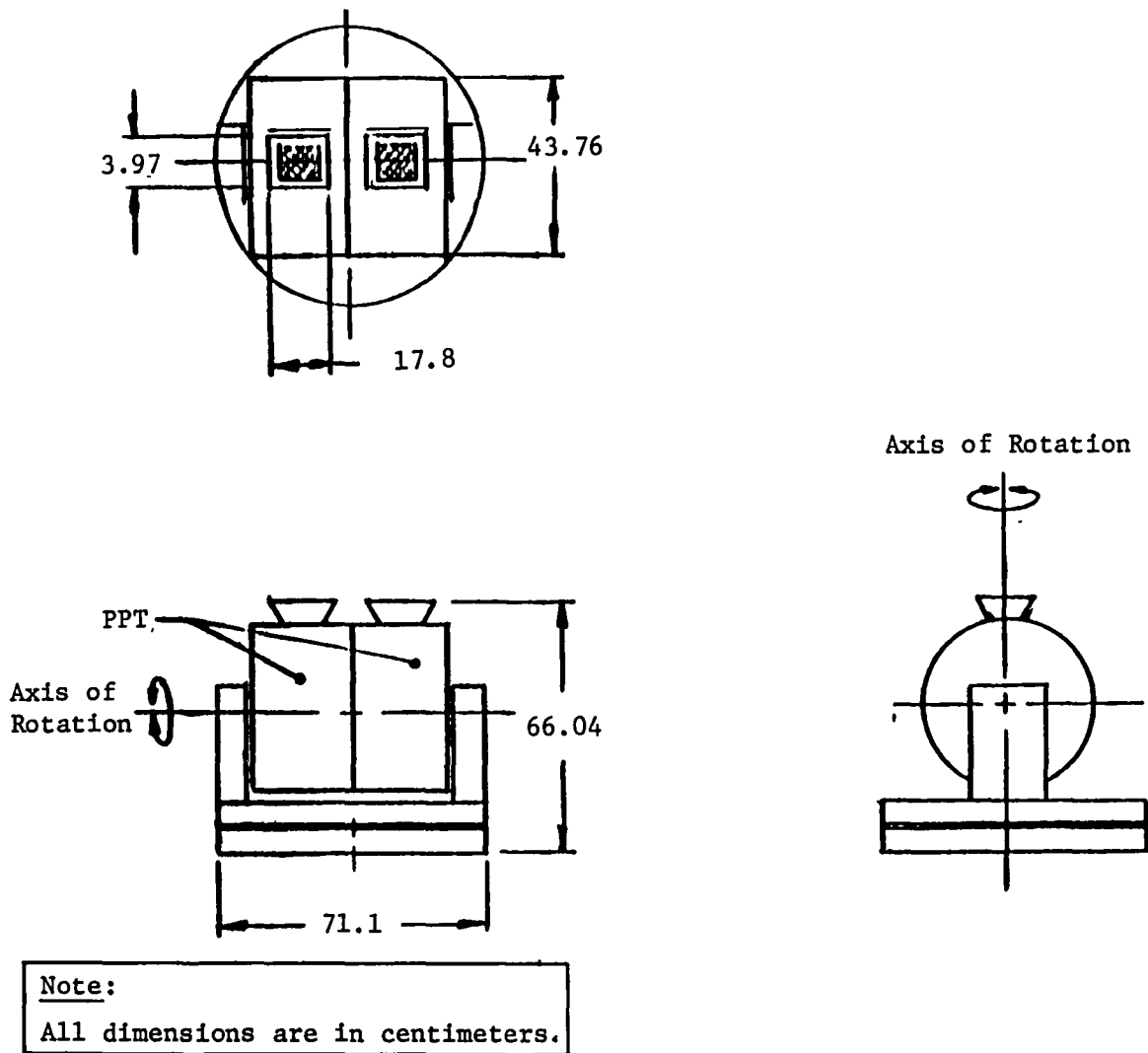
Figure 6-32   Twin PPT Unit

The maximum environmental forces and torques were compared with the maximum achievable thrust from the ACS to ensure the ACS had a sufficient force and torque capability. To uncouple the translational and rotational thrusting interactions, the two ACS functions were considered separately. The minimum impulse bit of the PPT and limit cycle rates were considered in development of the thruster firing order.

Translational effects were examined first. Thrusters were gimbaled to appropriate angles to give maximum translation without the thrusters, firing into the structure, which caused undesired rotation of the EOS. Then an inspection was performed to find the thrusters producing the most unwanted torque. These thrusters were throttled down until pure translation was achieved for the +X, -X, +Z, and -Z directions. The thruster-produced translational forces were then compared with the external forces to find the excess capability of the thruster system to cancel external forces. Next, the thrusters were gimbaled to appropriate angles to give maximum rotation without firing the thruster into

the structure causing unwelcome translation of the EOS. Then the thrusters that produced the most unwanted translation were found. These thrusters were throttled down until pure rotation was obtained for both the +θ and -θ rotations. Then the thruster-produced torques were compared with the external torques to find the excess capability of the thruster system to null external torques. The results showed that the thruster system had the least amount of excess capability to counter an external force in the +Z direction (266% extra capability). Table 6-17 presents the ACS' ability to null the external forces and torques acting on the EOS.

Table 6-17 Excess Capability of PPTs to Meet Torque Requirements

Thruster Locations Not Operating	$+\phi$, %*	$-\phi$, %*	$+\theta$, %	$-\theta$, %	$+\psi$, %*	$-\psi$, %*
(All Operating)	---	---	837	331	---	---
1 & 2	---	---	583	142	---	---
3 & 4	---	---	466	291	---	---
5 & 6	---	---	444	282	---	---
7 & 8	---	---	419	78.2	---	---

*No external torques. Negligble in sun synchronous orbit.

Note: There are two thrusters at locations 1, 2, 3, and 4, and one thruster at locations 5, 6, 7, and 8.

To find the redundancy of the ACS, all thrusters were sequentially shut down. The four thrusters on the top of the forward edge of the reflecting mesh were turned off, and the procedure for calculating the ability of the ACS to null external torques for +θ and -θ rotation was repeated to find the excess capability of the ACS (Table 6-17, row 2). Then the four thrusters on the top of the trailing edge of the mesh were turned off and the excess capability of the ACS determined for +θ and --θ rotation (Table 6-18, row 3). Next, the two thrusters on the sides of the feed beam were shut down and the excess capability found (Table 6-17, row 4). The two thrusters on the back side of the boom were shut down and the excess capability of the ACS was determined (Table 6-17, row 5). From this analysis, it was found that the ACS could meet the largest external force or torque with any two opposing thruster locations shut off. The thrusters on the back side of the boom were found to be the most critical to the ACS nulling capability because turning them off taxed the ACS' ability the most (excess capability of the ACS at that point was 78.2%).

Table 6-18 External Forces and Torques

	Forces						Torques					
	+X, N	−X, N	+Y, N	−Y, N	+Z, N	−Z, N	+ϕ, Nm	−ϕ, Nm	+θ, Nm	−θ, Nm	+ψ, Nm	−ψ, Nm
External, from the Integrated Analysis Program	0 116 x 10⁻²	−0 255 x 10⁻²	0		0 554 x 10⁻²	−0.139	0	0	0 316	−0 450	0	0
ACS-Produced to Null External	0 301 x 10⁻¹	−0 278 x 10⁻²	*	*	0 418 x 10⁻¹	−0 203 x 10⁻¹	*	*	1 94	−2.96	*	*
Excess Capability of ACS, %	2300	1080	*	*	266	2910	*	*	837	331	*	*

*Not considered since external force or torque was zero.

Note

+ϕ = rotation about X-axis,
+θ = rotation about Y-axis,
+ψ = rotation about Z-axis

The lifetime of the ACS was determined to complete the sizing of the ACS. The mass of fuel required per orbit was determined first. The average impulse per orbit experienced by the spacecraft was calculated to be 19.9 Ns. This was then divided by the specific impulse of the PPT (2200 s) and a gravitational constant (9.8 m/s^2) to give the mass of fuel required per orbit (9.22 x 10^{-4} kg). Then, assuming all the thrusters use all their fuel while stabilizing the spacecraft, approximation of the maximum ACS lifetime was calculated to be 36.7 years. In actuality, some thrusters, because of their position on the spacecraft, were oriented so they would have a higher duty cycle than others to stabilize the EOS and would run out of fuel before other thrusters. Therefore ACS lifetime would be less because it could not stabilize the EOS even though some thrusters had large amounts of fuel remaining and could still produce thrust. To determine the real lifetime of the ACS, a computer program was developed. The program first input the external forces and torques acting on the EOS calculated by the control module of the integrated analysis program. It then calculated the thrust necessary from each thruster to stabilize the EOS at 60 points in each orbit against the external forces and torques. It used this information to calculate the total impulse necessary from each thruster for an orbit. Then, by comparing the total impulse capability of each thruster, it calculated the length of time the ACS could null the external forces and torques acting on the EOS. The lifetime of the ACS was calculated to be 21 years.

This ACS thus met or exceeded the thrust, packaging, and lifetime (10 years with 3-year resupply) requirements for the EOS (Table 6-19). The ACS exceeded the pointing requirement of 0.07 deg because, by pulsing every 6 deg in an orbit, the maximum deviation from nadir pointing was 0.002 deg. Therefore this 12-thruster ACS met all the defined requirements and the sizing of the ACS was complete.

Table 6-19 *Pulsed Plasma Attitude Control System Characteristics*

Number of Thrusters Necessary	12
Total Power Requirement (PPT)	2040 W
Packaging Requirements	Satisfied
ACS Requirements	Satisfied
Lifetime Requirement (10 years)	Satisfied
Effects on Structure:	
I. Possible Contamination II. Disruptive Impulse III. Electromagnetic Interference	
Single PPT + Gimbaling Mechanism Weight	44 kg
Twin PPT + Gimbaling Mechanism Weight	84 kg
Total System Weight (4 Single & 4 Twin PPTs)	512 kg

6.6   RF ANALYSIS

The critical element in the feed design is to reduce the spillover and increase the edge taper of the feed pattern. Both of these aims are compatible except the volume available for the feed antennas is limited. The combination of the spillover loss and the power contained in the sidelobes due to the aperture distribution must be less than 0.5 dB to achieve 90% beam efficiency. In a space radiometer, most of the spillover power is pointed at the cool sky and it may be possible to discount some of the spillover.

Square corrugated horns are used in the two upper bands. Table 6-20 lists the design dimensions of the horns.

Table 6-20 *Horn Design Dimensions*

	5.5 GHz	10.68 GHz
Aperture Width	32.7 cm	16.8 cm
Axial Length	82.6	43.2
10-dB Beamwidth	22 deg	22 deg
Pattern Level at Spot Edge	-14.3 dB	-14.3 dB
Spillover Loss	0.24 dB	0.24 dB

The polar patterns of the feed horns are shown in Figures 6-33 and 6-34. A horn was designed at 1.41 GHz to give the same beamwidth, but its axial length (328 cm) was too long to package.

Angles, deg
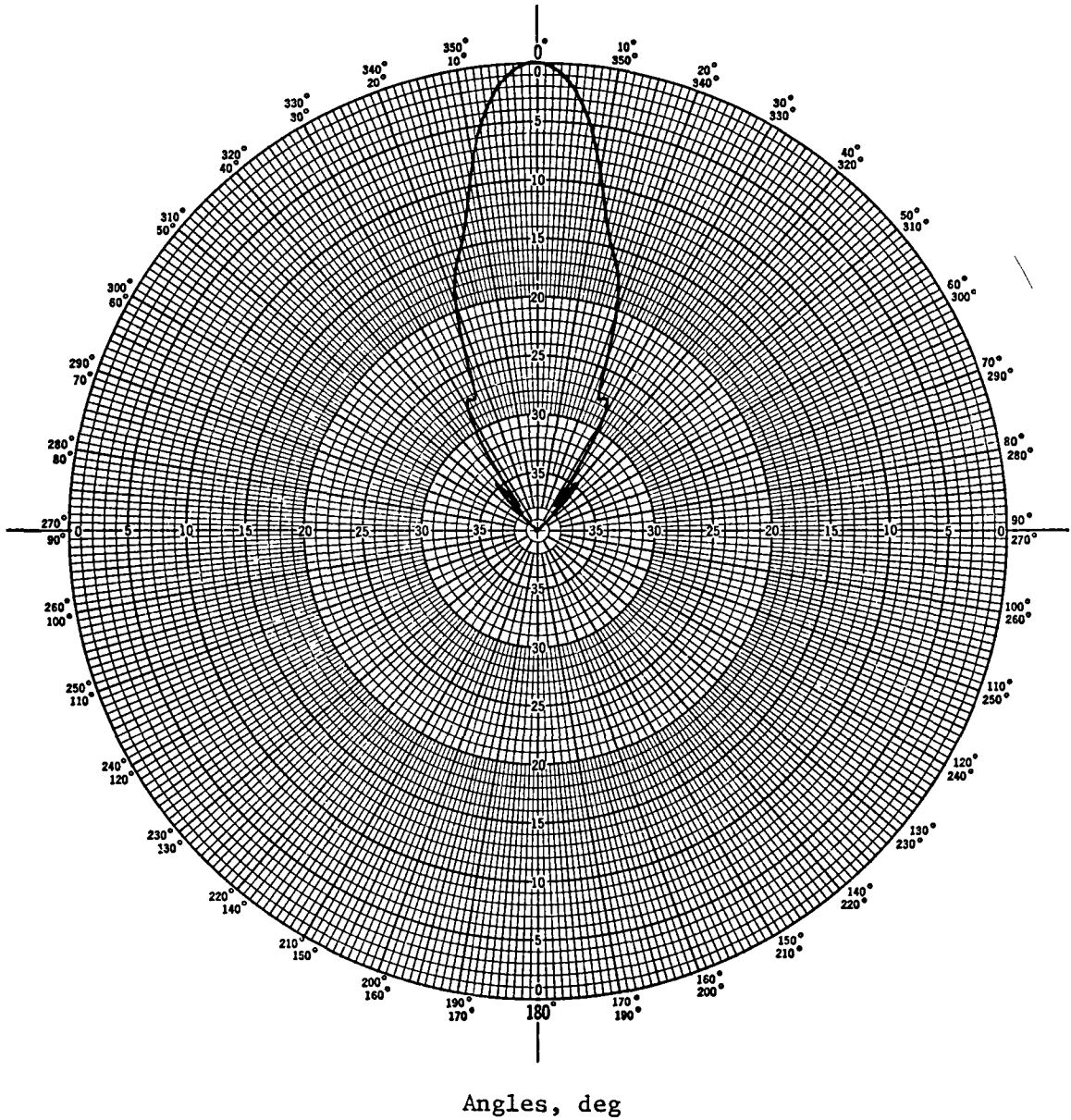
Figure 6-33   5.5-GHz Square Corrugated Horn Feed Pattern

Angles, deg
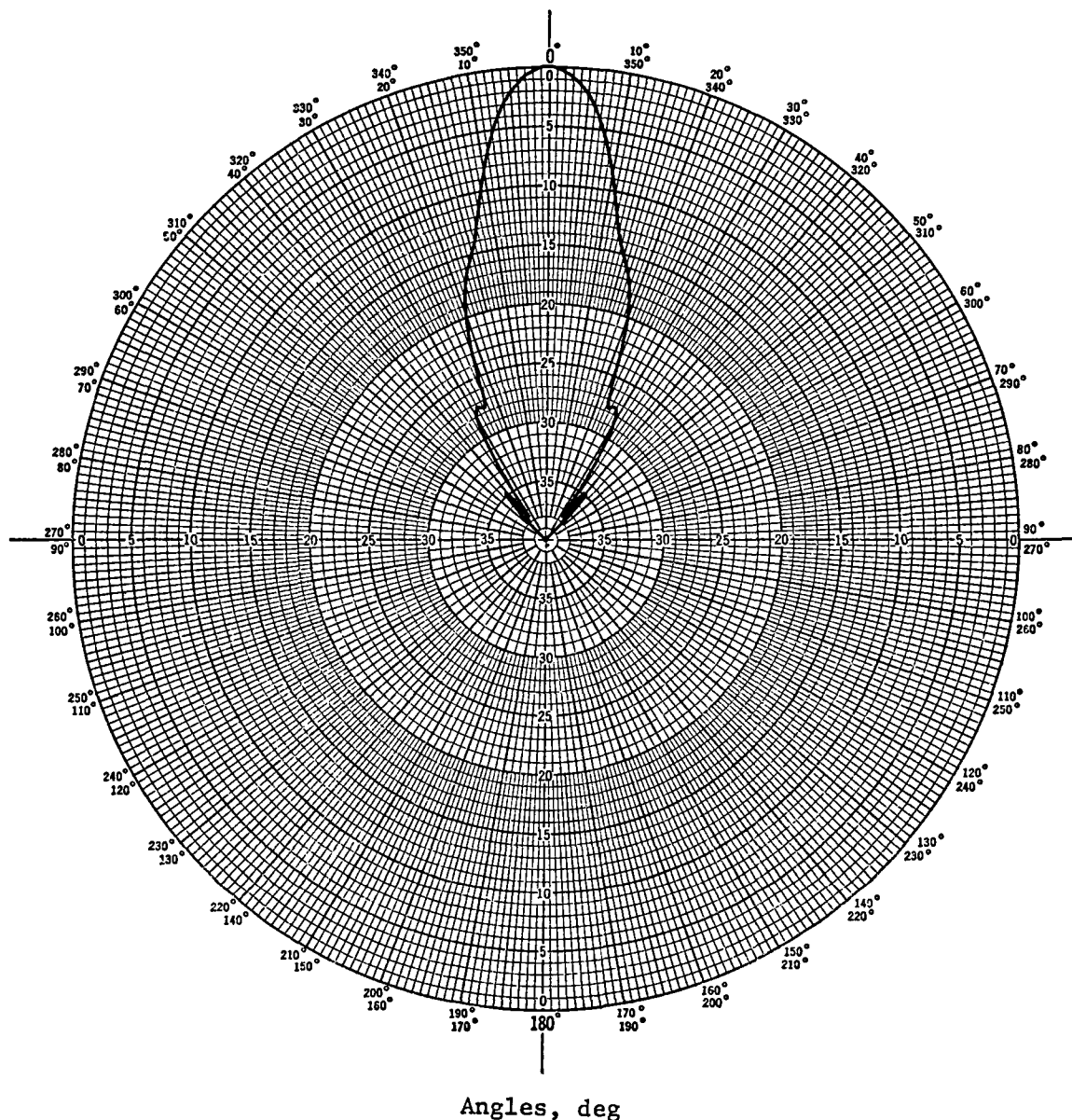
Figure 6-34   10.68-GHz Square Corrugated Horn Feed Pattern

To fit the packaging requirements, an array of small horns was designed
for the lowest frequency band (1.41 GHz). Each element aperture width
is 16.9 cm and uses smooth wall horns. The pattern is determined more
by the array than the horns. The differences between the E and H plane
beamwidths of the horn are masked by the array factor. Each spot is
formed by a 5 by 5 array. The four outer columns of elements are
shared with adjacent arrays so the centers of the arrays may be spaced
at 50.8 cm. The power distribution on the array is 1,3,4,3,1. A polar
pattern using this distribution and expected element beamwidths is
shown in Figure 6-35. Its beamwidth matches the corrugated horn pat-
terns (Figures 6-33 and 6-34). The spillover loss is slightly higher
than the horns (0.26 dB).

154

Angles, deg
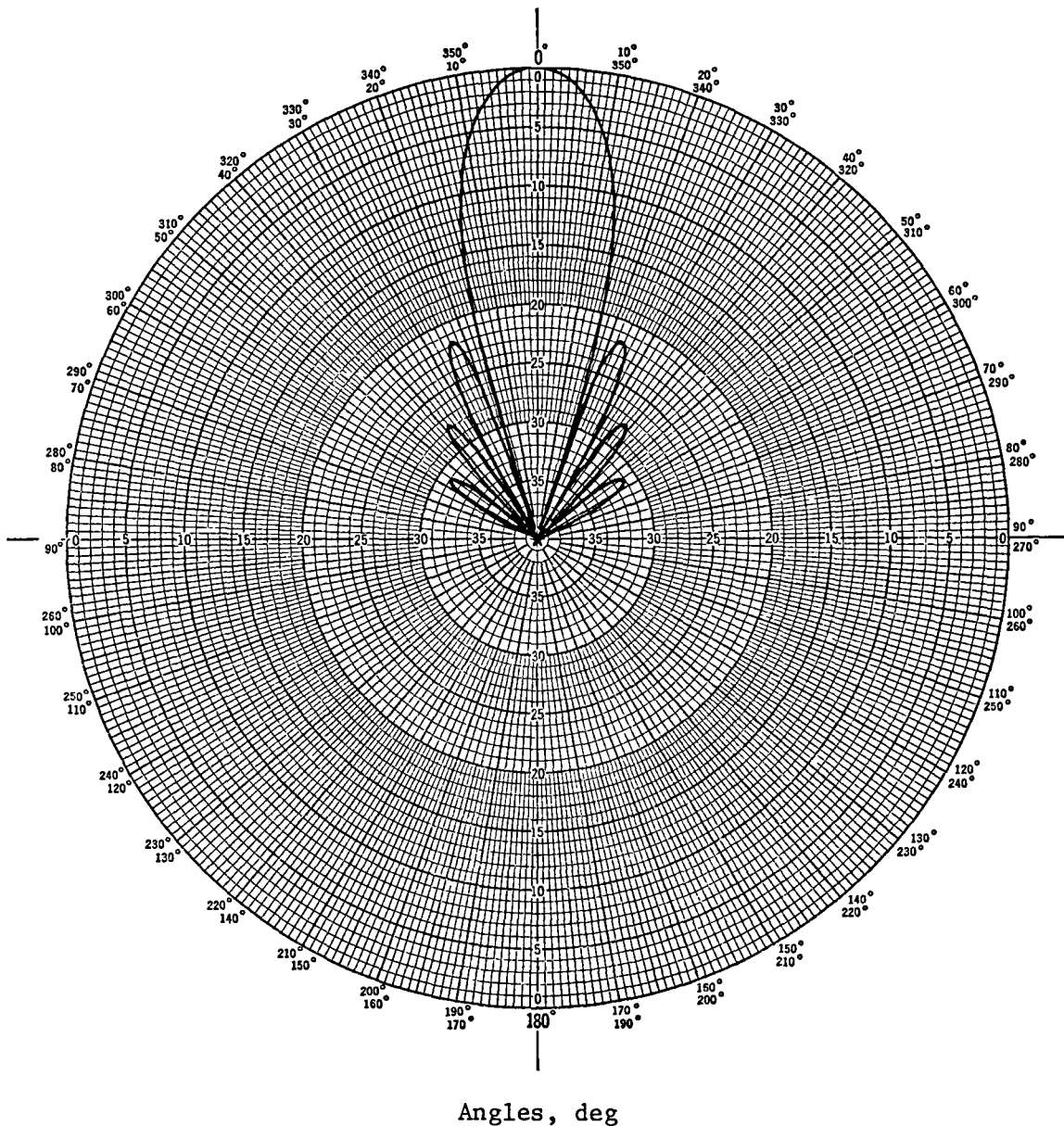
Figure 6-35 Five-Element, 1.1.41-GHz Array Feed Pattern

The feed network for this array will present a significant design problem. Since an array is being used, the pattern may be improved by matching the array to the focal plane fields and obtaining a better beam than with the square corrugated horns. This would complicate the feed network. No feed coefficients have been calculated to match focal plane fields. It may be trouble enough to design the network to share elements without significant crosscoupling between receivers. A second more significant problem is the isolation loads used in feed networks. They generate noise that may swamp out any attempt to calibrate the radiometer. The general system analysis of the calibration scheme must be worked out in conjunction with the feed network design.

155

Secondary patterns were generated for the design example reflector
using the feed patterns generated. A computer program was written by
Ohio State University under contract to Martin Marietta Corporation to
find the secondary patterns of toroidal reflectors. The program uses
aperture integration in the main beam and the geometrical theory of
diffraction for the peripheral sidelobes. The program can handle arbi-
trary rim shapes described by straight lines in the projected X-Y plane.
These patterns were generated assuming no reflector surface anomalies,
but the program can handle simple periodic surface variations. The
radius of curvature of the circle curve of the reflector is 234.8 m.
The focal length of the parabola curve is 116.1 m. The focal length of
the parabola does not match the paraxial focus of the circle curve.
The values were picked to minimize the difference between the surface
and a parabolic reflector.

The patterns generated are in the plane of the parabola and the plane
of the circle. Only the patterns for the central spot were generated,
and these have symmetry in the circle plane. The circle plane patterns
only show half the pattern. In all cases the parabolic plane patterns
have some squint. This can be removed by adjusting the difference be-
tween the focal length of the parabola and the radius of curvature of
the circle. The optimum may be found by rerunning the program with
different values. No attempt was made at this time to find the opti-
mum. Because the program is able to produce each pattern in about 2
minutes of VFX/VMS-11 computer time, it is quite reasonable to iterate
for a solution. The patterns are: 1.41 GHz (Fig. 6-36, 6-37), 5.5 GHz
(Fig. 6-38, 6-39), and 10.68 GHz (Fig. 6-40, 6-41).

No program has been written yet to calculate the beam efficiency of
these patterns. As frequency increases, the pattern performance de-
grades. The parabolic plane patterns (Fig. 6-36, 6-38, 6-40) show in-
creased coma and beam broadening as the frequency increases along with
squint. The coma increases faster than the squint and, of course, the
beam broadening is caused by the first sidelobe moving into the main
beam. The pattern in the circle plane also degrades with increasing
frequency. The first sidelobe (Fig. 6-37, 6-39, 6-41) increases from
30 dB at 1.41 GHz to 25 dB at 5.5 GHz, and finally to 20 dB at 10.68
dB. Additional work is necessary to optimize the feed positions to
establish the possibility of achieving 90% aperture efficiency.

The distortions of the antenna surface contribute to the ultimate rf
performance of the antenna. The nature and distribution of the errors
influence the changes in the desired radiation pattern and beam effi-
ciency. The scattering of energy caused by deviations from a desired
shape and localized imperfections tend to widen the main beam and raise
the sidelobe level.

The effects of surface distortions on the rf pattern are difficult to
quantify. Past investigators of tolerance theory have usually consid-
ered random errors   with small correlation lengths. The correlation
length of the disturbances represents the area and mutual coupling of
the errors. Bates (1959)* demonstrated that the effects on the pattern

*R. H. T. Bates: "Random Errors in Aperture Distributions," IRE Trans Antennas
and Propagation, Vol AP-9, October 1959, p 369.

are more proportional to the radius of correlation than their amplitude, indicating that errors should be kept small in proportion to wavelength.
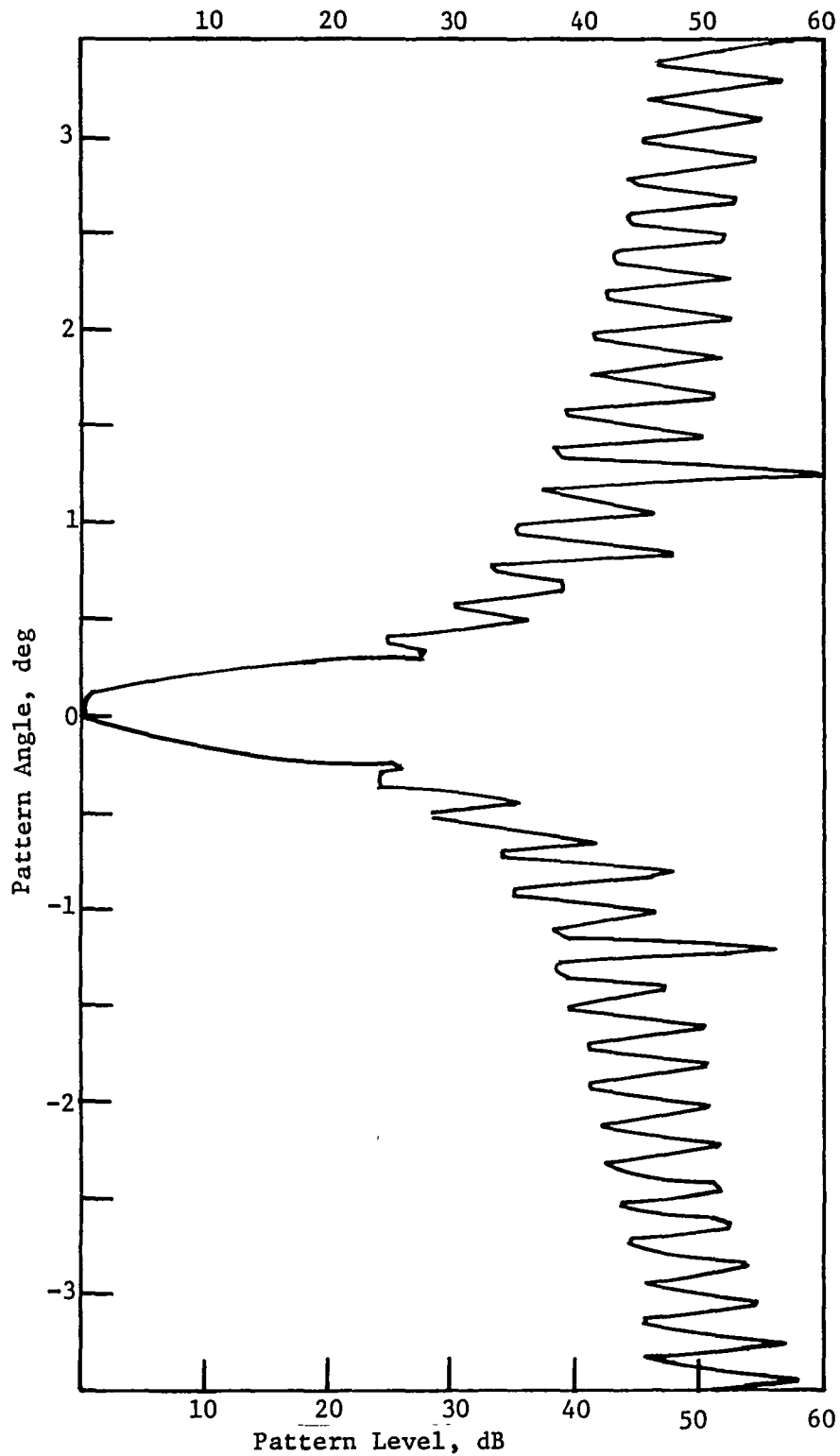
Figure 6-36   Parabolic Plane Pattern at 1.41 GHz
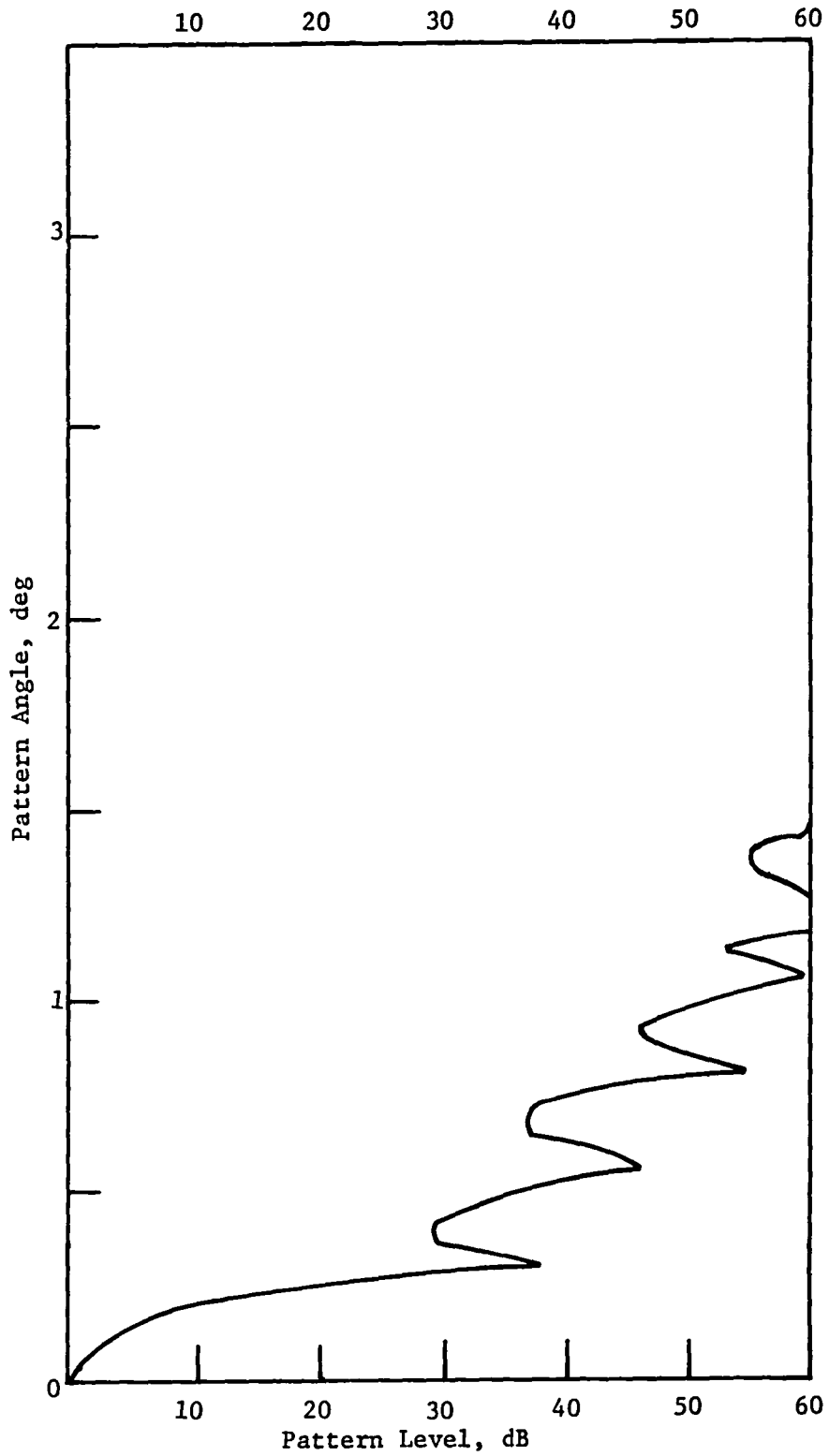
Figure 6-37   Circular Plane Pattern at 1.41 GHz
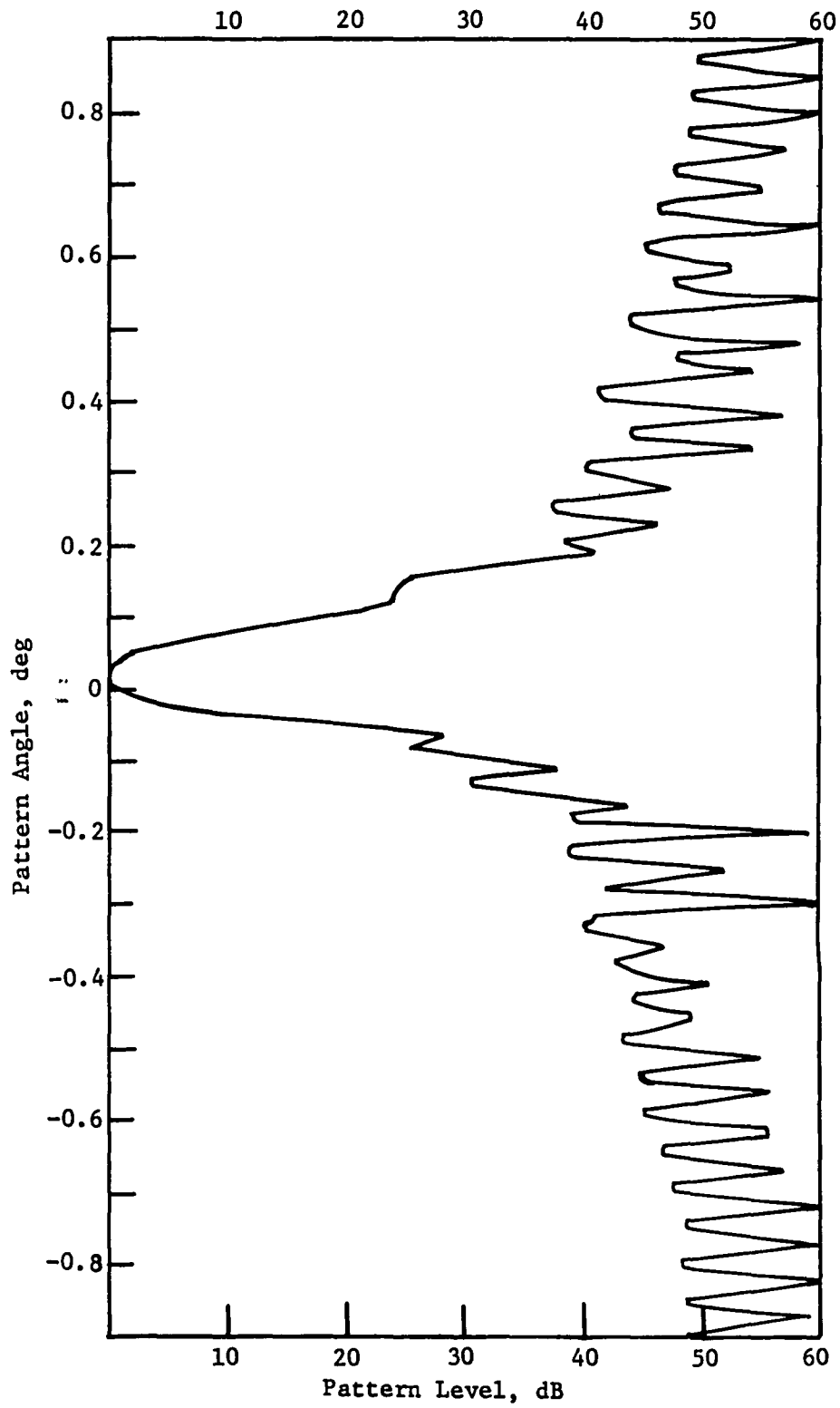
Figure 6-38 Parabolic Plane Pattern at 5.5 GHz

159
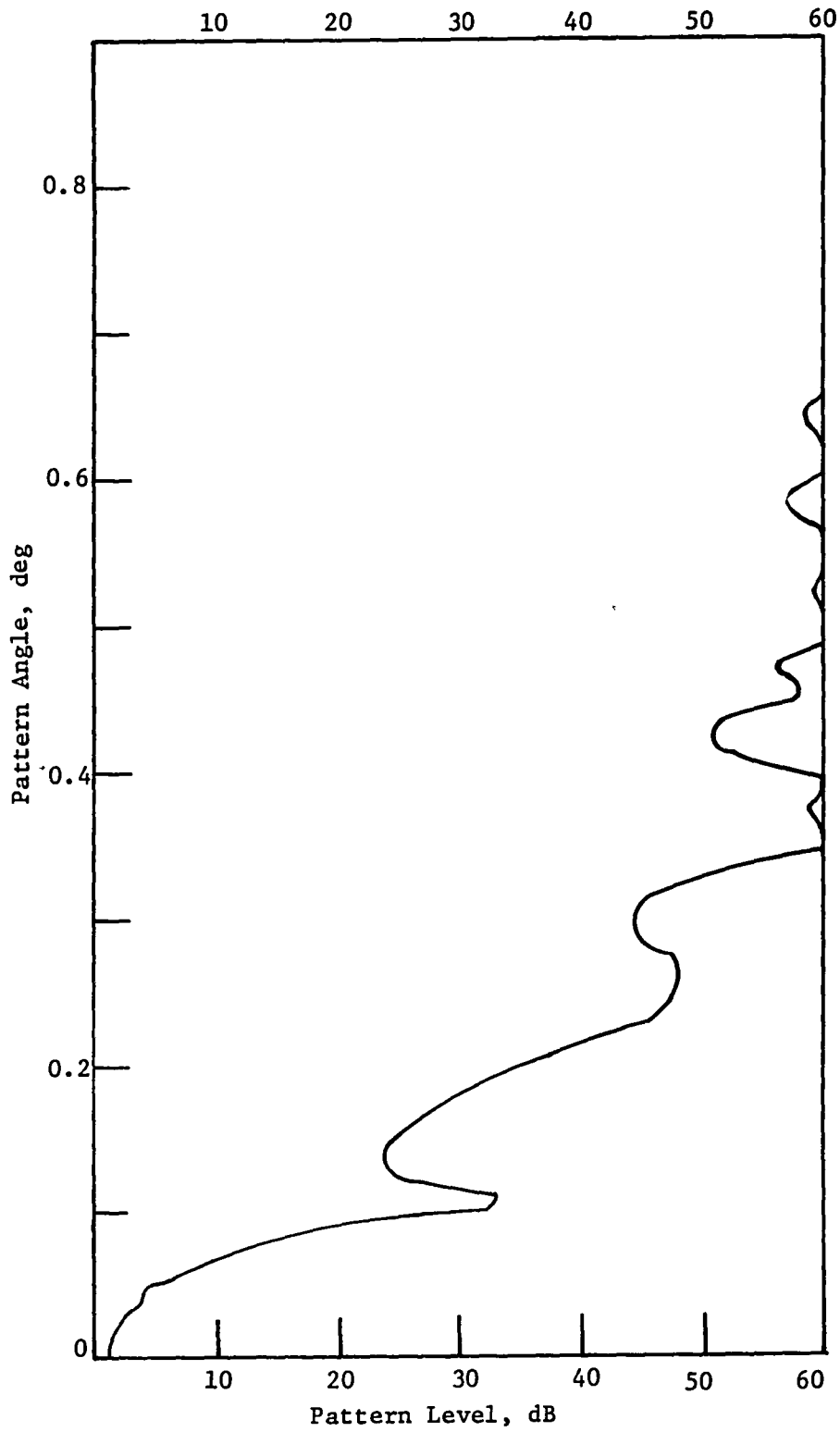
Figure 6-39 Circular Plane Pattern at 5.5 GHz
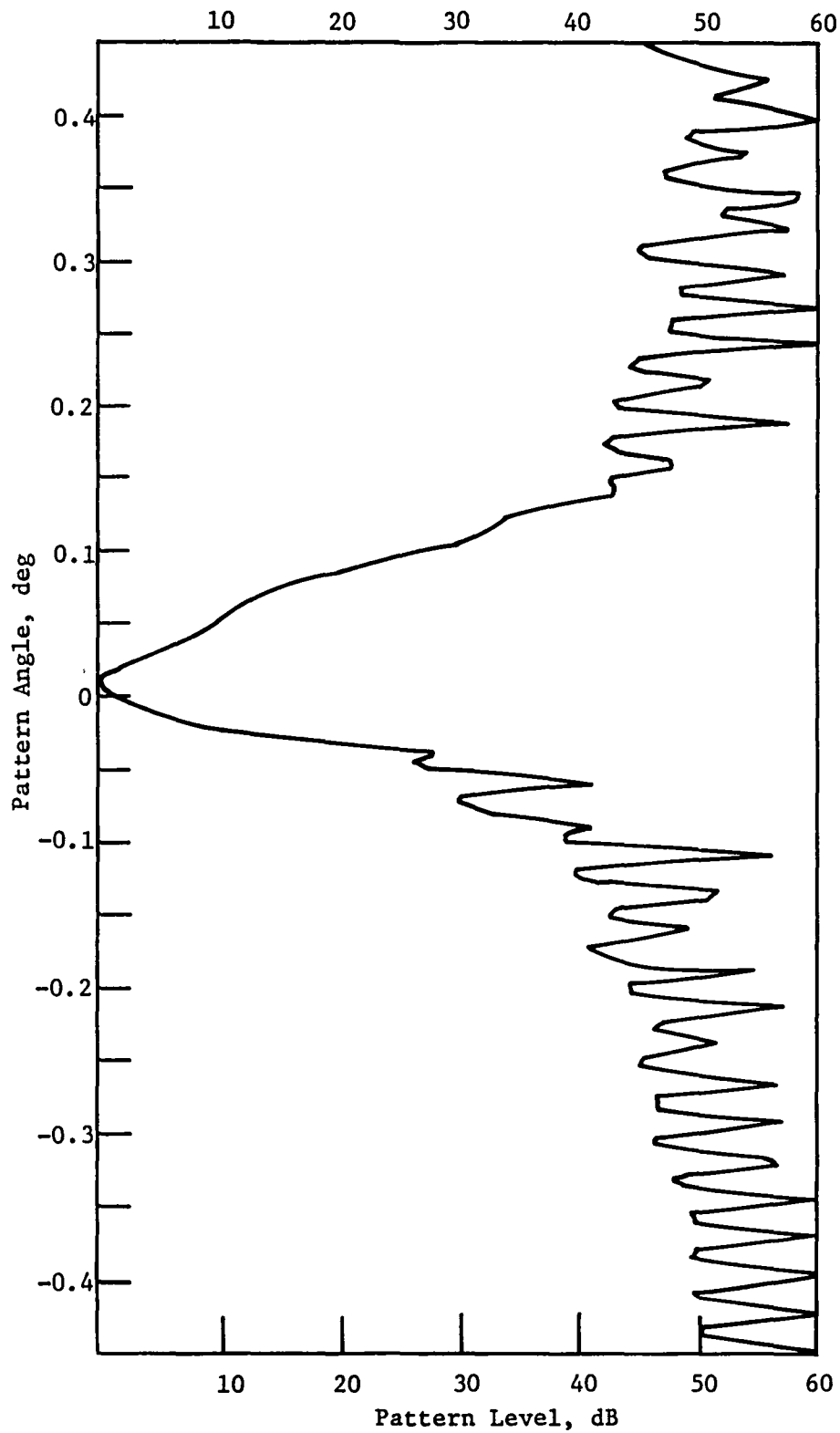
Figure 6-40   Parabolic Plane Pattern at 10.68 GHz
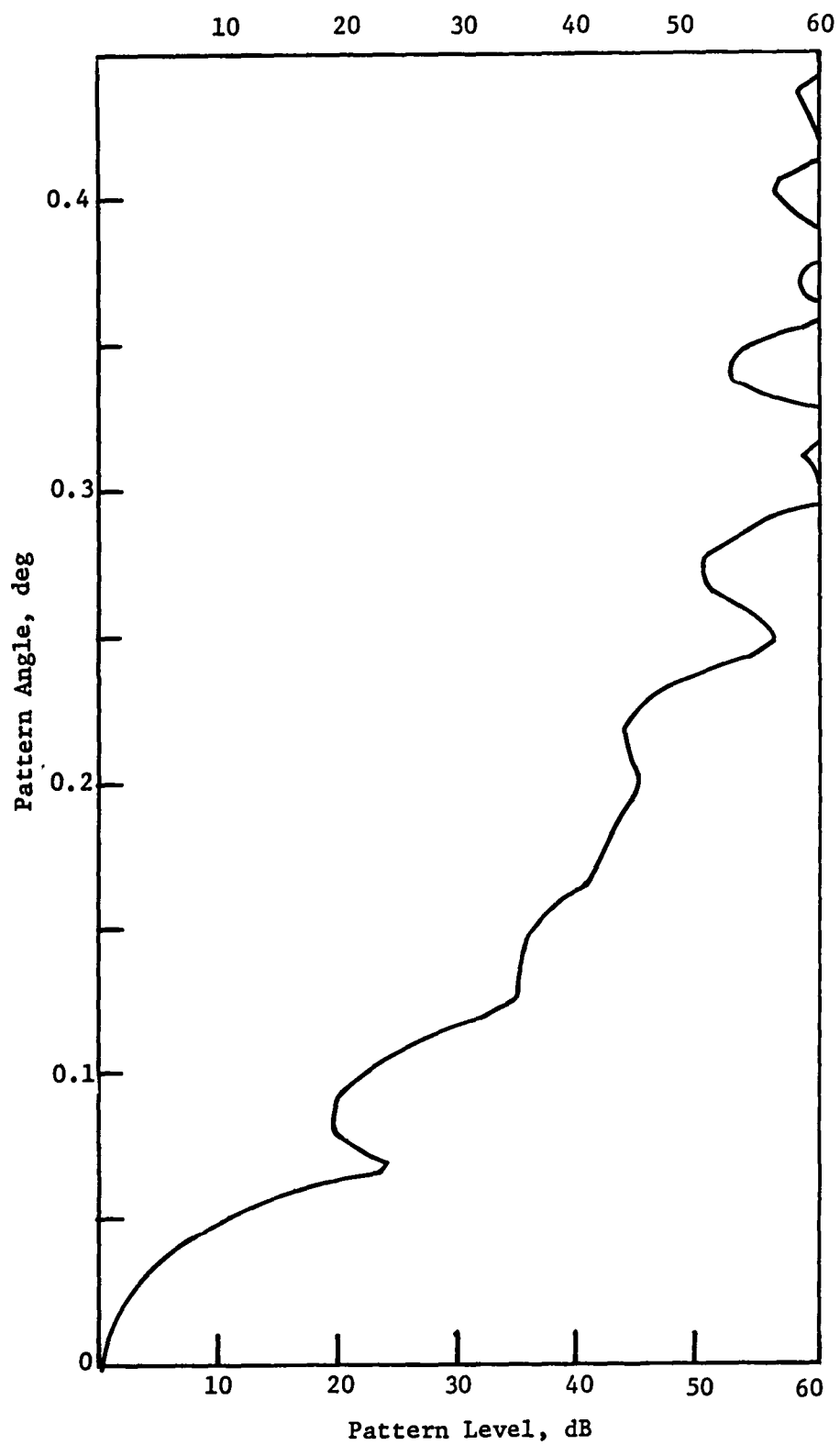
Figure 6-41 Circular Plane Pattern at 10.68 GHz

The geometric saddling effects (pillowing) of the mesh are illustrated in Figure 3-23. The correlation length for the EOS mesh is on the order of a meter. This result can significantly affect antenna performance and further analysis is required to quantify the effects of pillowing. The theoretical development of surface errors is not sufficiently conclusive to provide detailed antenna performance predictions. Antenna performance predictions incorporating surface errors is done numerically using surface current integration techniques and a mathematical model of the surface. This method can become very expensive.

The systematic errors are primarily caused by thermal and manufacturing errors and produce phase errors in the aperture distribution. Distortions of the reflector surface can be analyzed as reflections of the feed, so the distortions are presented as feed errors. Systematic errors include the effects that produce either a translation or axial displacement of the feed. These effects have different consequences on performance.

Translation of the feed produces phase errors that are essentially linear with the motion of the feed. The effect is to move or "squint" the beam a maximum of 0.007 deg off the boresight of the antenna, which will have only a minor effect on the total shape of the antenna pattern.

Axial displacement of the feed produces quadratic phase errors. The primary effect is to decrease the beam efficiency of the antenna. A reduction of the beam efficiency is proportional to the phase error. A phase error of 1.0 rad produces a corresponding decrease in beam efficiency of approximately 10%. The worst-case combination of thermal and manufacturing errors results in a displacement of 0.75 cm, and corresponds to a reduction in beam efficiency of 2.2%. The degradation becomes progressively worse at the higher frequencies.

6.7 SLEWING

This section will develop the rationale and present analyses that show the enhancement of mission performance with slewing. A general mission requirement for the LMR is to have full contiguous ground coverage with a revisit time of one to three days. The geographic coverage, which governs revisit time, depends on the ground track and swathwidth of the instrument, with the ground pattern fixed by orbit parameters. The EOS spacecraft has also been considered as a platform for other earth-imaging sensors that require sun-synchronous orbits, which immediately imposes additional constraints on the orbit. Having the slewing capability onboard the EOS can provide increased flexibility and overcome some of the constraints.

In the sun-synchronous orbit, the orbital precession rate is set equal to the average solar precession rate, and is a function of both altitude and inclination. Thus we are trying to reconcile two independent constraints—the correct precession rate and the repetitive ground coverage.

The revisit interval is the time required to retrace the ground path for a particular day. The interval tends to determine the swath required, with short intervals requiring wider swaths. This is because less time is permitted to image intermediate points between the approximately 24 deg between tracks. Table 6-21 summarizes the situation. These orbits are sun-synchronous with specified revisit periods.

Table 6-21   Orbit and Revisit Time Parameters

Q-Factor	Altitude, km	Orbit Repeat Interval, days	Swathwidth Required	Field of View, deg
14 1/2	720	2	1381	74
14 1/3	775	3	931	61
14 1/4	802	4	700	41
14 1/9	850	9	315	19.6
14 1/14	863	14	203	13
14 9/16	705	16	175	14
Note: Only descending nodes were considered.				

The geographic ground coverage is the result of a combination of orbit and instrument parameters. Assuming no perturbations, the westward longitude displacement of the descending node is the result of the earth rotating underneath an unperturbed Keplerian orbit during one anomalistic period. These displacements are on the order of 24 deg at the equator, but vary primarily with altitude. Because the altitude must be maintained to retain sun-synchronization, not much can be done to change the size of the displacements and, as a consequence, the revisit time.

The complexity and size of the antenna and feed structure is related to the resolution and swath required (recall that revisit time also depended on swathwidth). The minimum resolution acceptable for missions of this type is 10 km, with 1 km or less very desirable. Ten-km resolution requires approximately 138 and 93 feed horns for a two- or three-day revisit time, respectively, or 500 feed horns for a 1-km resolution. Very wide swaths with high resolution will require very large feed arrays. Therefore the tradeoff becomes either large swaths with low resolution, or a narrower swath with higher resolution. The EOS structure is capable of a 3-km resolution of 200-km swaths. The tradeoff is temporal resolution because smaller swaths necessitate longer times (more revolutions) to fill in the longitude displacements previously discussed.

6.7.1   Slewing As a Solution

To maintain the high spatial resolution and packageability in one orbiter bay, a longer revisit time is required, which is augmented with a slewing capability. Operating in this regime, a new set of alternatives is possible. For this analysis, orbits enabling contiguous coverage with swaths on the order of 200 km were selected. It is beneficial to investigate how mission performance can be improved by slewing.

164

The factor Q represents the number of satellite revolutions divided by the number of revolutions of a particular point on the earth. For sun-synchronous orbits, Q is identical to the number of nodal (equatorial) crossings per day. An orbit with a Q = 14 9/16 or 14.56 orbits per day at an altitude of 705 km was selected for analysis. This selection was made because it is lower than other orbits, ensuring good resolution, and is similar to the orbit of LANDSAT-4. This fact is instrumental when considering the radiometer as a platform for other earth-imaging sensors.

The ground track for this orbit is schematically illustrated in Figure 6-42. Successive equatorial passes from right to left are indicated. For example, the second equatorial crossing on day one is at 90.58 deg, the third at 116.16 deg, etc, and returns on day two at 75.80 deg. The original ground track repeats itself every 16 days. The ground coverage pattern alternates on a two-day interval, such as between day four and six. The separation between centers is 350 km, indicating a gap in coverage assuming a 200-km swath. This intermediate point is imaged again on day 13.

The temporal resolution can be greatly improved with a slewing capability. An object in swath A requires 16 days to be overflown again or revisited assuming the normal ground track progression. This time can be shortened to two days if a 14-deg maneuver is effected during pass B. The spacecraft is then returned to follow path B again. An object intermediate between two successive swaths (marked A and B) could be successfully imaged with a one-day interval by slewing approximately 17 deg off nadir during pass A and another 17 deg during pass B. The same point will be reviewed on day 16 because of the natural progression of the orbit. The technical aspects involved in slewing are discussed in Section 6.7.2. This slewing scenario requires a prior knowledge of objects, with an increased interest and need for immediate reimaging.

Another tasking scenario can be developed using the orbit suggested in The Microwave Radiometer Spacecraft (NASA 1981). In this orbit, adjacent swaths are imaged on successive days and require 14 days for the pattern to repeat itself. Contiguous global coverage is possible with 200-km swaths, and one-day reimaging is possible with a single 13-deg slewing maneuver.

The requirements to have a wide swath and good temporal and spatial resolution conflict with the desirability to package the spacecraft in one shuttle bay and to reduce antenna feed complexity. A swathwidth of 200 km with 1-km ground resolution appears to be the limit of practicality for this class of instruments. Slewing appears to be a viable solution to reimage selective objects in the desired timeframes.
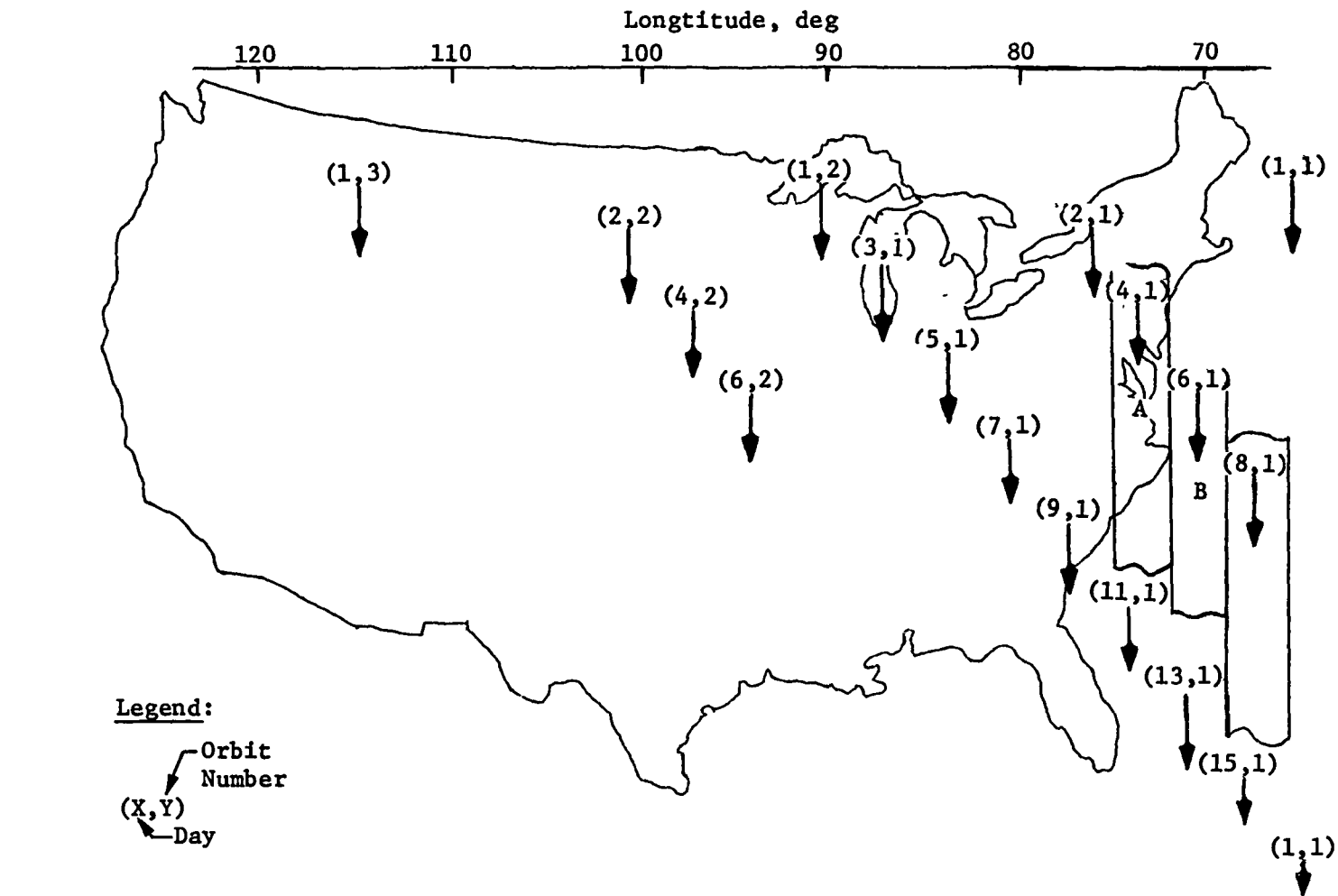
Figure 6-42   Orbit Ground Track

6.7.2 Analysis of the Thruster System Required to Perform an EOS Out-of-Plane Maneuver

This section presents an analysis conducted to determine the size and type of thruster system required to slew the EOS about its X_p-axis. Considering only the baseline EOS configuration and mission, the only thruster system available for the 15-deg maneuver requirement consists of the pulsed plasma thrusters (PPTs). The PPT system can only produce 2.0 Nm of torque with which to perform the slew maneuver. Figure 6-43 shows the torque, rate, and angle profiles as a function of the time required to perform the maneuver.
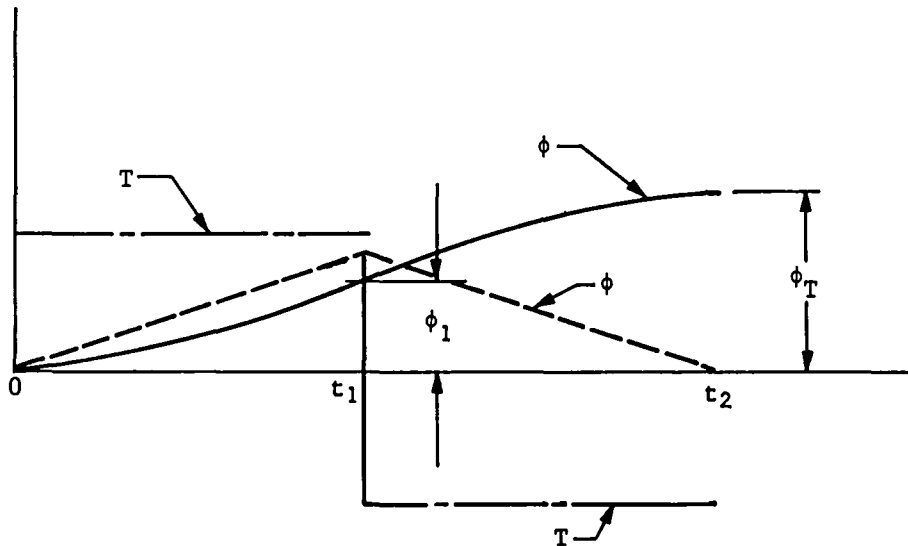
Figure 6-43   Torque, Rate, and Angle Profiles

The total time required for the maneuver is given by

[1] $t_T = t_1 + t_2 = 2t_1, \quad t_1 = t_2$

and the torque magnitude required is given by

[2] $T = \dfrac{2\phi_T \ I_{XP}}{t_T^2}$

where $\theta_T = 2\theta_1$. The time required to maneuver the EOS using the PPT system is determined by solving equation [2] for the total time t_T. Hence

$$t_T = \sqrt{\dfrac{2(15 \ \text{deg}) \ (2.36 \ \times \ 10^7 \ \text{kg-m}^2)}{(2 \ \text{Nm}) \ (57.3 \ \text{deg})}}$$

$$= 2485.6 \ \text{s}$$

$$= 42.42 \ \text{min}$$

The time required to maneuver when compared to the orbit period, which is 98.80 minutes, has been determined to be unsatisfactory. This conclusion necessitated considering a chemical thruster system. The first approach is to consider a thruster system similar to the orbit transfer propulsion system, which in its conceptual design stage will allow both translational and rotational maneuvers to be performed. The location of the thruster system required to perform the slew maneuver is shown in Figure 6-44. The initial thruster system with individual thrust levels of 26 to 5 N has a gimbaled nozzle system that will allow the positioning of the thrust vectors parallel to the Z_p axis, thus eliminating a rotation about the pitch axis.
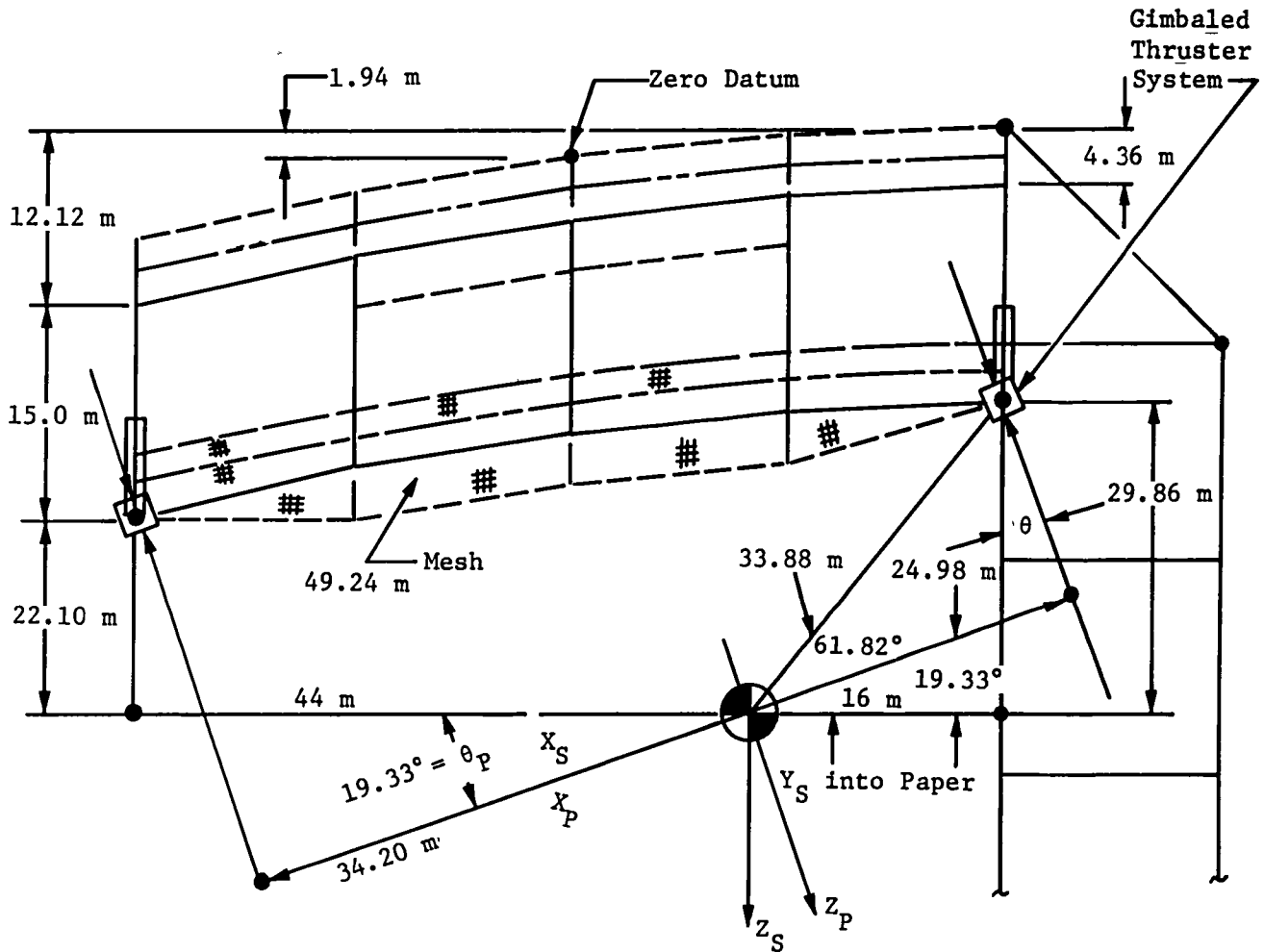
Figure 6-44 Thruster System Location for Slew Maneuvers

The time to complete the out-of-plane maneuver will be a minimum when the maximum thrust level is used. Using 26 N of thrust from each of the four thruster systems, the minimum time to maneuver is

$$t_T(min) = \sqrt{\frac{2(15)(2.36 \times 10^7)}{(57.3)(52)(90)}} = 51.38 \text{ s}$$

The maximum time will occur when the thrust level is 5 N from each of the four thruster systems. Maximum time to maneuver is

$$t_T(max) = \sqrt{\frac{2(15)(2.36 \times 10^7)}{(57.3)(10)(90)}} = 117.17s$$

The torque required to produce the maneuver must be able to compensate the gravity gradient torque resulting from misalignment of the spacecraft's principal axes with respect to the rotating reference axes. The gravity gradient torque produced about the X_p axis is

[3]
$$T_{ggXp} = \frac{3 \omega_o^2}{2} (I_{Zp} - I_{\lambda p}) \sin 2\phi.$$

Figure 6-45 shows a graph of the magnitude of $TggX_p$ as a function of the roll angle (ϕ), indicating an almost linear variation for the range of maneuver angles considered. The maximum gravity gradient torque produced is 9.52 Nm for an angle of 15 deg. When this value is compared to the maximum and minimum torque available, the following percentage values result

$$\text{Percent (max Torque)} = \left(\frac{9.52 - \text{Nm}}{4680 - \text{Nm}}\right)100$$

$$= 0.20\%$$

$$\text{Percent (min Torque)} = \left(\frac{9.52 - \text{Nm}}{900 - \text{Nm}}\right)100$$

$$= 1.06\%$$

These results imply that the gradient torques do not have a significant effect on the performance of the maneuver.

The effect of the maneuver, with respect to the angular accelerations produced, on the structural integrity of the spacecraft must be analyzed. The maximum and minimum values of angular acceleration are

$$\ddot{\phi}_{max} = \frac{4680 \text{ Nm}}{3.02 \times 10^7 \text{ kg-m}^2} = 1.55 \times 10^{-4} \text{ rad/s}^2$$

$$\ddot{\phi}_{min} = \frac{900 \text{ Nm}}{3.02 \times 10^7 \text{ kg-m}^2} = 2.98 \times 10^{-5} \text{ rad/s}^2.$$
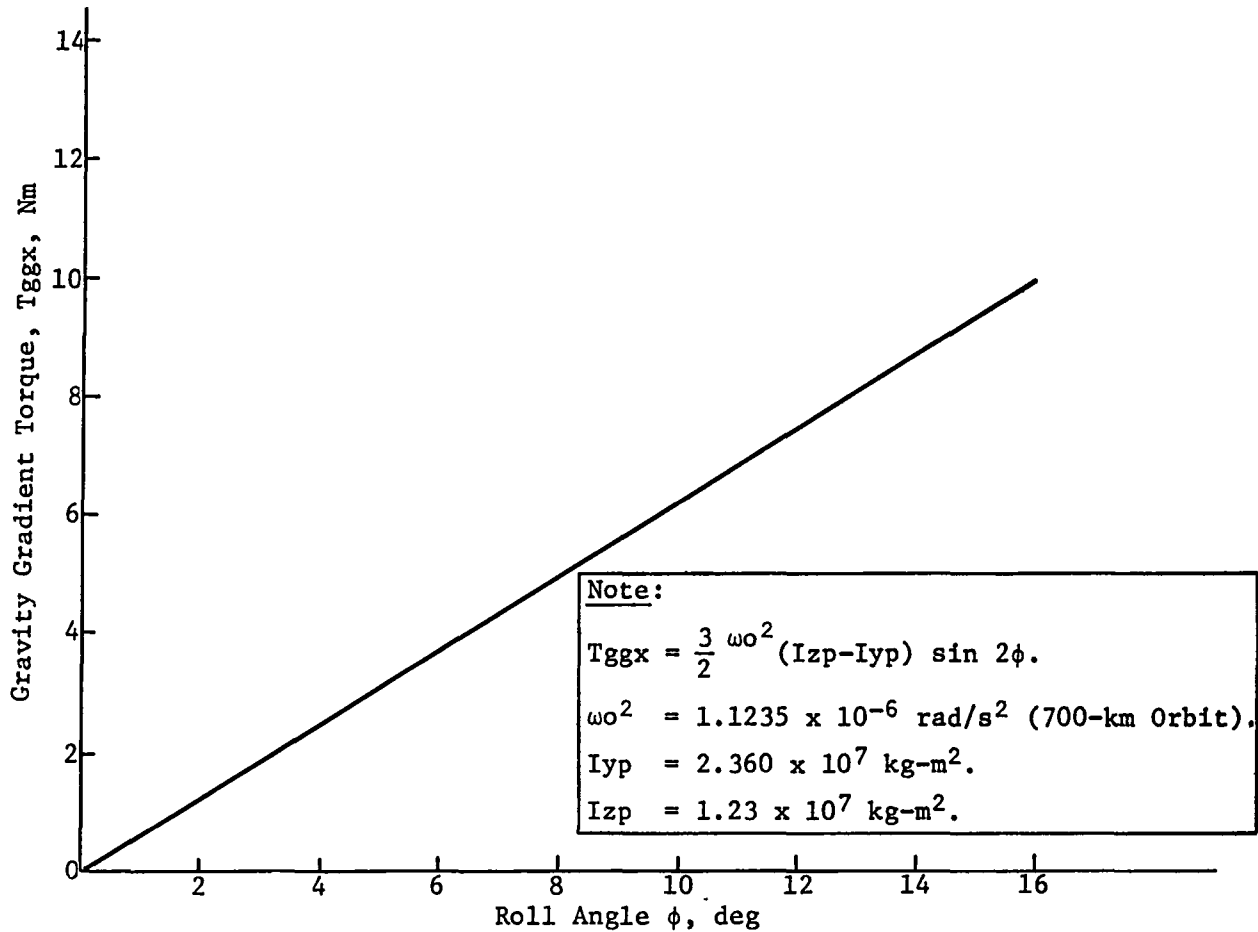
Figure 6-45 Gravity Gradient Torques

It has been determined that the EOS can withstand an acceleration level of 0.01 g, which is equivalent to 0.1 m/s^2. Using a maximum moment arm of 93.0 m, the level of linear acceleration produced for the maximum angular acceleration is

$$a = \ell_{max} \, \ddot{\phi}_{max} = (93.0 \text{ m})(1.55 \times 10^{-4} \text{ rad/s}^2)$$

$$= 1.44 \times 10^{-2} \text{ m/s}^2,$$

which is less than the tolerable acceleration level.

The mass of fuel required can be determined from the following equation:

[4] $$m = \frac{I_t}{I_{sp}g}$$

where

I_{sp} = specific impulse, 225 s,
g   = acceleration of gravity, 9.81 m/s^2,
I_t = total mass impulse, Ns,
m   = mass of fuel, kg.

Table 6-22 summarizes the fuel required to complete the total maneuver, i.e., out-of-plane and back into the plane.

Table 6-22 Fuel Requirements to Perform Out-of-Plane Maneuver

Thruster No.	Level of Thrust, Newtons		Total Impulse, Ns		Fuel Mass, kg		Total Fuel Mass, kg	
	Max	Min	Max	Min	Max	Min	Max	Min
1	26	5	1335.88	585.85	0.61	0.27	1.22	0.54
2	26	5	1335.88	585.85	0.61	0.27	1.22	0.54
3	26	5	1335.88	585.85	0.61	0.27	1.22	0.54
4	26	5	1335.88	585.85	0.61	0.27	1.22	0.54

Considering the average fuel consumption to perform the complete maneuver to be

$$M_{ave} = \frac{4.88 + 2.16}{2} = 3.52 \text{ kg/Maneuver}$$

and the total fuel available to be 1200 kg, which is 300 kg for each thruster system, the average number of maneuvers capable of being conducted is

$$N = \frac{1200 \text{ kg}}{3.52 \text{ kg/Maneuver}} = 340.91 \text{ Maneuvers}.$$

The pointing requirement about the X_p-axis is ± 0.07 deg whether in or out of the orbit plane as shown in Figure 6-46.

There is some latitude in the length of time the spacecraft can remain in the out-of-plane position. A practical minimum time is about 10 seconds, which will allow imaging special areas for a length of 70 km on the earth's surface. A maximum duration is derived from the desire not to use the thruster system to maintain position. The angle the spacecraft rotates toward the orbit plane is determined by

[5] $$\phi = \frac{\alpha t^2}{2}$$

where α is the angular acceleration determined from the gravity gradient torque, which is nearly constant over 0.07 (0.001 rad) deg. Then rearranging [5]

$$\phi = \frac{9.52 \text{ Nm}}{3.02 \times 10^7 \text{ kg-m}^2} \frac{(10 \text{ s})^2}{2}$$

$$= 1.5762 \times 10^{-5} \text{ rad}$$

$$= 9.03 \times 10^{-4} \text{ deg} < 0.07 \text{ deg}$$
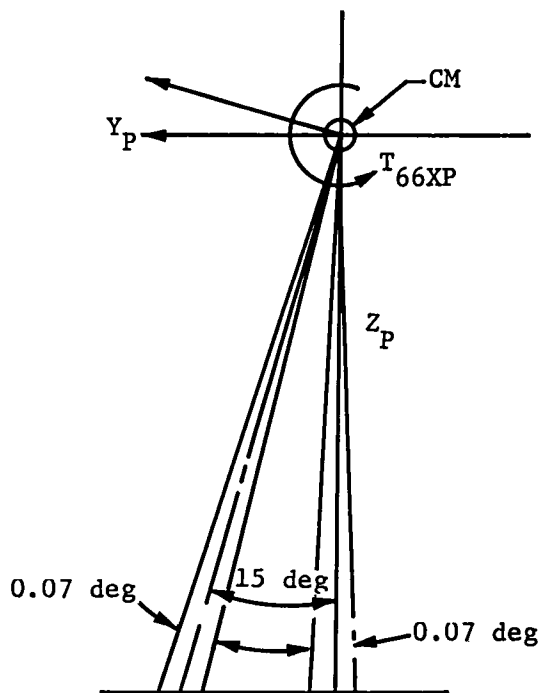
Figure 6-46
In and Out of Orbit Plane
Pointing Requirement

This result implies that the gravity gradient-restoring torque need not be compensated for because the rotation angle produced is well within the pointing requirement.

Almost 90 seconds can elapse before the pointing accuracy requirement is exceeded.

This conceptual thruster system can be integrated into the baseline EOS in addition to the primary orbit transfer system. It would be located on the same vertical tube member allocated for the orbital transfer propulsion system.

7.0 TECHNOLOGY DEVELOPMENT REQUIREMENTS

Technology development requirements were identified and classified regarding their value in enabling and enhancing multidiscipline missions. These requirements were identified for the spacecraft and associated sensors, including the LMR, and for analytical and testing techniques. Each of the technology development items is discussed along with its state-of-the-art impact on EOS program development. Section 7.8 presents Martin Marietta's near-term IR&D program to start addressing these technology issues.

7.1 SURFACE ACCURACY

According to Keafer's et al. report* on radiometer mission requirements, radiometers must have a surface accuracy of 1/55 of a wavelength or less to ensure that the loss of efficiency produced by random surface error is within acceptable limits of 5% or less. EOS has a high operating frequency requirement of 10.68 GHz, which gives a wavelength of 2.81 cm or a required surface accuracy of 0.051 cm rms. The present design of EOS has a worst-case total surface distortion of 0.308 cm rms (Table 6-9). This meets the surface accuracy requirement at an operating frequency of 1.8 GHz. Projecting technology improvements to the late 1980s could improve the total rms surface distortion by first reducing the thermal distortions (i.e., by reducing the CTE of the graphite/epoxy members used to build the truss and mesh tie system or by adding thermal coatings on the truss members to reduce their temperature variations). However, this accounts for only 30% of the total distortion. Over 60% of the distortion comes from manufacturing error estimates, showing the need for high-precision manufacturing techniques of truss structures and mesh surfaces. Thus the second improvement is to reduce the manufacturing errors from 0.2 cm to less than 0.04 cm.

The manufacturing problems fall into three categories. The first problem relates to the one-g and fixturing-induced loads in the structure. Although these loads can be reduced by zero-g fixturing and the predicted onorbit deflections produced by these loads compensated for during manufacturing, the residual errors are still projected to exceed the EOS requirements.

The second problem relates to individual member manufacturing errors and the resultant deflections and internal loads they produce. Analysis indicates this problem is not as severe as the fixturing and one-g problem. However, if these random manufacturing errors happen to be assembled in a worst-case condition, deflections can become excessive. This potential tolerance buildup is a definite technology problem. The third problem relates to material uncertainties. Microcracking, microstrain, aging, creep, moisture effects, and CTE changes must be understood to meet the high-precision requirements.

---

*L. S. Keafer, P. Swanson, and J. Eckerman: "Radiometer Mission Requirements for Large Space Antenna Systems," NASA TM-84478, 1982.

Consideration of onorbit adjustment to achieve the required surface accuracy should be included in the overall solution of these problems. Although this raises a whole new set of problems (e.g., sensors and adjustment devices), the cost-benefit should be traded off to decide whether pushing manufacturing methods or onorbit adjustment, or a combination of both, is the most reliable and cost effective method.

7.2   MESH PERFORMANCE AS USED IN A RADIOMETER

Tricot-knitted gold-plated molybedenum wire has not been verified for use as a reflective surface for space radiometers. Many concerns exist because of the possible changes in the radiation efficiency (η_ℓ) or ohmic losses of the mesh surface. The increased surface resistance (ohmic loss) not only reduces the amount of energy reflected into the feeds, but more importantly increases the amount of self-emitted radiation by the mesh. These losses must be quantitatively known at any particular point in orbit to preclude introducing an intractable bias in the signal that will adversely affect the measurement accuracy.

These changes are caused by tension field variations and/or changes in the wires' resistivity because of the extreme thermal environments in space. Reduction or increase in the tension field on the mesh can allow changes in the wire-to-wire contact that affect radiation efficiency.

The power "seen" by the radiometer feeds is related to a quantity known as the radiometric antenna temperature (T_a). The influence of the radiation efficiency on this quantity is given by the equation

$$T_a = \eta_\ell \eta_m T_{m\ell} + \eta_\ell (1 - \eta_\ell) T_{s\ell} + (1 - \eta_\ell) T_o$$

where

T_a = Total radiometeric antenna temperature,
$T_{m\ell}$ = radiometric temperature of the mainlobe,
$T_{s\ell}$ = radiometric temperature of the sidelobes,
T_o = physical temperature of the mesh,
η_ℓ = radiation efficiency of the antenna,
η_m = main beam efficiency of the antenna.

Unlike communication applications, the accuracy and precision of radiometric measurements are governed in part by T_a and the accuracy to which it is known.

7.3   DEPLOYMENT VERIFICATION AND ANALYSIS

A critical issue of large deployable space systems is the analysis and qualification of deployment. The issue revolves around the fact that

174

the total structure cannot be effectively qualified on the ground be-
cause of three factors—large size, flexible gossamer structures and
one-g effects. Another problem is the understanding of the effects of
nonsymmetric, worst-case loading during deployment and the latchup
transient phase.

To resolve these issues, a combination of analysis, ground test and
space testing is required. New deployment analysis methods need to be
developed to analyze the total deployment phase, including the effects
of coupling of dynamic bodies by multiple deploying members, and to
provide positions, rates, accelerations, and loads in a cost effective
method. Cost effectiveness is critical because of the large number of
deployment simulations that must be performed to demonstrate positive
margins and successful deployment during a variety of symmetric and
nonsymmetric worst-case conditions. Reliability tests of latches would
also be included in these tests.

A combination of multicube scale model testing and full-scale cube
testing is also required to validate the analytical simulations and
demonstrate successful deployment. But this is only the first step to
test qualification of the structure. Subsequent flight tests will
probably be required.

7.4   DEFICIENCIES IN CRYOGENIC COOLING SYSTEMS FOR IR SENSORS

The increased use of high-performance IR sensors such as the limb scan-
ning spectrometer on EOS Mission IV motivates the need for cryogenic
systems that will attain lower temperatures, have higher thermal capac-
ity, and have significantly longer lifetimes than currently attainable.
Various existing cryogenic systems can provide some, but not all, of
the three necessary attributes just described.

The temperature requirement is approximately 10 K for detectors and 30
K for the instrument itself, which imposes a thermal load of several
watts. Lifetimes greater than five years are necessary. Table 7-1
illustrates the development of applicable cryogenic technologies.

Table 7-1 Cryogenic Systems Capability

Type	Temperature Range, °C	Capacity	Lifetime
Radiant Cooler	No	No	Yes
Solid Cryogen	Yes	Yes	No
Mechanical	Yes	Yes	Potential

Mechanical systems such as the Vuilleumier cooler and turbo-refrigera-
tor (reverse Brayton cycle) are perhaps the two most developed technol-
ogies available for satisfying the cooling problem.

7.5 OPERATIONAL EOS MAINTENANCE/SERVICING

Three factors combine to make the EOS a likely candidate for operational maintenance/servicing (M/S): (1) long life, (2) complex sensors and support subsystems, and (3) its potential to be used as a facility in which new instruments can be installed as they become available. Numerous studies have addressed low earth orbit M/S with manned and unmanned vehicles. Approaches have been well defined for various teleoperator M/S spacecraft ranging from small-payload maneuvering systems usable at or near the shuttle to longer range, higher payload systems. However, no major program commitment has been made to procure M/S hardware applicable to an EOS-class system nor has the EOS been thoroughly defined with M/S in mind. Accordingly, EOS-class M/S technology is best defined as being in the conceptual stage supplemented by a reasonable number of laboratory-demonstrated M/S tools, maneuvering platforms and docking devices. A total package of EOS M/S technology clearly does not exist and therefore this must be classified as a technology need for EOS-class systems.

7.6 DATA MANAGEMENT/STORAGE TECHNOLOGY NEEDS

Data management and storage would not be a technology factor in the development of EOS subsystems if a dedicated, high-speed (150- to 300-Mbps) return link service were established at all times in orbit. This would allow the data obtained during any remote sensing scenario to be returned to earth in real time for processing.

This is not a viable operating alternative because TDRSS, which can handle this data rate, is used on a priority or scheduled basis and approximately 15% of the EOS orbit would be in the exclusion zone and constitute lost data. This restriction limits EOS usage of the available high data rate channels. Thus a reliable, high-speed and high-capacity data storage/playback medium must be used in conjunction with an innovative data management system. The present maturity of storage technology cannot fulfill these requirements.

The primary concern is long-lifetime operation. Electromechanical devices such as tape recorders have the necessary read/write capability, but not the specified lifetime performance. A possible solution is to further develop a space-qualified magnetic bubble storage medium and qualify it for spacecraft use. Prototypes available today have an estimated reliability of 0.9 over five years.

7.7 DYNAMIC VERIFICATION

Understanding the dynamic performance of a large space structure is critical in designing an attitude control system that will stabilize

176

and point the system and in defining the dynamic response of the structure to the environmental and onboard forcing functions. The critical parameters that are difficult to test in the ground environment are damping characteristics of the structure, effective stiffness of the multimember structure, and any nonlinear characteristics. Ground test difficulties are the same as for deployment verification (large size, gossamer, and one-g effects).

A technology development program would consist of ground testing, space testing, and analytical upgrading and verification.

7.8   PLANNED NEAR-TERM DEVELOPMENT WORK

To address the technology needs of large space systems, Martin Marietta Denver Aerospace has maintained four independent research and development (IR&D) projects in design, analysis, controls and propulsion that have totaled over a million dollars during the last two years. Starting in 1983, the IR&D program emphasis will be on addressing two technology needs discussed earlier: (1) manufacturing of high-precision truss structures, and (2) deployment of a multicube truss structure. The following paragraphs discuss the IR&D activities to address these technology needs.

7.8.1 Hardware Fabrication and Test

The long-range objective of the box truss development task is to demonstrate and validate the performance of a box truss structure that will eventually lead to a qualified space structure by the mid to late 1980s. The specific objective of this task for 1983 is to demonstrate the performance of a multicube deployable box truss structure when stowed, during deployment, and deployed. A demonstration and validation of the sequential-orthogonal deployment will be included. This validation will include demonstration of all phases of deployment to understand symmetric and asymmetric deployment, latchup transients, loads and deflections and local lumped masses on the cube corner fittings. Manufacturing methods, processes, and precision will also be demonstrated.

A prototype scale model (approximately 6-ft cubes) of a four-bay by five-bay, 60x120-m box truss, offset-fed parabolic reflector will be fabricated in 1983 to demonstrate multibay truss design, performance, packaging, deployment, and the parabolic design approaches developed in 1982. An integrated offset-fed mast will be included in the scale model. Manufacturing and assembly procedures will be representative of flight hardware to demonstrate and validate these procedures and to determine the precision of the complete article. The design of the deployment testing fixture will be based on the best possible means for simulating zero-g conditions.

The model will be functionally, structurally, and kinematically similar to the flight article except for the material selection and the use of nonflight-qualified components. Metallic parts have been selected instead of graphite/epoxy because of cost considerations. In spite of the material change, all required test results can be realized. The model will be fabricated in a fixture similar to one used for flight fabrication. After completion of the structure, the structure will be removed from the assembly fixture and the precision measured. This will determine if any fixture-induced loads/distortions were produced in the structure. These data will be valuable in extrapolating loads/distortions to LSS flight articles.

This model will also be compatible with future additions of mesh surfaces, subsystem and cable integration, and have the potential for refurbishment and qualification as a low-cost flight experiment. This flight experiment would not only provide insight into the behavior of the structure in the zero-g space environment, but also give insight into the rigorousness of the ground test methods.

The deployment testing will include varying the deployment forces ($\pm$10%) in a variety of deployment members, varying the latch release times ($\pm$2-s variation), varying the mass distribution of the deploying structure ($\pm$5%), and varying the resistance forces ($\pm$50%). These variations will provide insight into the effects of nonsymmetric deployment on rates, loads, and deployment transients. These parameters are most critical because of the difficulty in analyzing these nonsymmetric effects.

7.8.2 Deployment Kinematics and Dynamics

Mathematical modeling of the deployment of large space structures requires an understanding of the kinematics and dynamics of deploying members. Because space-deployable structures must be lightweight, they are inherently flexible and, as a result, susceptible to damage from large dynamic forces. Therefore a thorough knowledge of rigid-body/elastic motion interaction, damping characteristics, and nonlinear large deflection dynamic analysis methods is required to develop optimum deployable structures. This knowledge also needs to be applied in the development of analytical simulations of the deployment process.

Based on results of the study performed by The Charles Stark Draper Laboratories, Inc. report CSDL-R-1558 released in May 1982, "There are currently no computer simulations available which can be used, without major modifications and extensions, to study the deployment dynamics of large, flexible, deployable satellites..."

It is desirable to develop or modify an existing computer code to model the dynamic behavior of the EOS during deployment. Through comparison with test data, computer simulation of deployment will be refined resulting in an accurate and inexpensive model. This model will provide insight concerning the determination of which parameters have a controlling influence on EOS design.

The following approach will be taken under IR&D D-12R to develop a computer simulation of deployment:

1) A computer code known as automatic dynamic analysis of mechanical systems (ADAMS) will be purchased. This program has a three-dimensional design capability for static analysis, large displacement nonlinear transient analysis, and small displacement analysis around a static solution or at any solution point in time. The Gear implicit integration is used for transient solutions, a so-called "stiff" integration formula avoiding the possibility of numerical instability caused by widely split Eigenvalues. Near-term studies will involve the comparison of IMP and ADAMS modeling capabilities of a simplified one-cube deployment model. The most suitable code will be modified to take into account the effects of instantaneous introduction of structural stiffening and the flexibility of the appendages;

2) The enhanced computer code will be used to develop a model that simulates the interaction between cubes during various deployment stages. Parametric studies will be undertaken to determine the effect of deployment stored energy, which is a function of spring stiffness, on deployment time and dynamic loads for a given appendage size. Other parameters to be studied include damping and joint friction;

The following unresolved areas of difficulty exist in computer simulation of deployment:

1) Determination of frictional joint loads;

2) Determination of structural and nonstructural damping coefficients:

3) Modeling uncontrolled deployment,

    a) Interaction between several members achieving locked positions simultaneously or randomly,

    b) Coupling interaction between rigid-body and elastic-body dynamics as a function of particular deployment methods.

A successful ground-based test (in a one-g environment) is a necessary first step in verification of large, lightweight flexible structures in space deployment. The test articles should include a small-scale model of EOS as well as a portion of the full-scale model. Gravity effects, errors in gravity compensation devices, air lubrication and air damping can mask the parameters being measured. Methods must be devised to obtain the test information pertinent to space deployment.

A successful ground-based test can be used to verify the accuracy of the computer simulation of deployment in a one-g environment. The next step would be to test EOS components whose actual behavior can only be determined in the zero-g environment. This could be accomplished in a flight test of the EOS scale model. The computer simulation could then be modified to represent a more realistic representation of deployment in space.

7.8.3 Dynamic Verification

Because large, lightweight deployable structures are generally more flexible than conventional structures, their dynamic behavior becomes a critical parameter in their control. As stability and control requirements become more severe because of the pointing requirement for large systems, and as structural frequencies become lower because of the size of the systems, deleterious structure dynamics and control interaction can occur. Therefore the ability to accurately test and predict the dynamic behavior of the LSS is a critical requirement in designing the structure and attitude control system.

The goal of dynamic verification is to establish the relationships between analysis, scaled ground-based system or element testing, and the dynamic behavior of the large space structure in flight.

The near-term objective of this task is to completely define the configuration, constraints, and test requirements for a flight experiment to verify the onorbit dynamics. A key objective is to design an experiment that will establish the relationship between analysis, ground test and measured onorbit dynamics. Specific objectives for dynamic verification are:

1) Define system requirements in terms of key parameters, e.g., deployment method, cantilevered modes and frequencies, damping, etc;

2) Develop analytical approaches to focus on simulating the major effects expected during each of the configuration phases of stow--age, deployment, and onorbit deployment;

3) Define testing philosophies, procedures, and instrumentation requirements for both zero-g and one-g environments. This will involve identifying both component and system test requirements that will support and validate the analytical models;

4) Define or develop the methods by which zero-g and one-g data may be correlated, and the way in which the test data can be used to validate the analysis model and assumptions for LSS dynamics.

The approach to achieving objectives 1 and 2 would be to employ and improve existing analytical tools and implement new techniques. The NASTRAN finite-element program would be used to analyze the configuration in the stowed and deployed conditions. Significant dynamic response characteristics such as mode shapes, frequencies and damping will be computed and used to predict the transient responses caused by selected input forcing functions.

Objective 3, definition of testing philosophies, will be approached by incorporating and improving state-of-the-art testing techniques and hardware. The general problem of test verification applies to three categories of tests--component tests, one-g scaled representations, and orbital demonstrations.

Objective 4, the development of zero-g to one-g test data correlation, will be approached by developing specific mast experiment definitions and data recovery requirements.

Ground testing obviously presents formidable difficulties in represent-
ing the zero-g conditions of the entire system. Combinations of full-
scale sections of the system, small-scale models of sections, and
small-scale models of the entire system will be tested in both the air
and vacuum environments. Particular attention will be directed toward
investigating appropriate zero-g devices and configurations.

EOS is intended to be a multifaceted earth remote sensing platform. It employs deployable large space system technology and is stowed in a single shuttle bay for transport. This section is intended to highlight and summarize the important developments, conclusions, and mission profiles produced under this study. The salient characteristics of the EOS system are summarized in Tables 8-1, 8-2, and 8-3.

Table 8-1   Spacecraft Summary

Reflector Dimensions	58 x 116 m
Focal Length	116.1 m
Spherical Radius	234.8 m
Total System Wt.	7635 kg
Fundamental Dynamic Mode	1.09 Hz
Stowed Envelope	4.25-m Diagonal x 17.8 m

Table 8-2   Orbit Parameters

Mission	Inclination, deg	Equatorial Altitude, km	Crossing	Synchronous
I-Baseline	98	705	12:00	Yes
II-Land	98	705	9:30	Yes
III-Ocean	98	705	12:00 or 9:30	Yes
IV-Atmospheric	60	705	None	No

Table 8-3   Ground Geometry

Frequency, GHz	Ground Resolution, km		Maximum No. Horns	Swathwidth, km
	Optimistic	Conservative		
1.4	2.95	14.75	58	173
5.5	0.88	4.5	90	350
10.68	0.41	2.06	88	18

8.1   LAUNCH AND DEPLOYMENT

The EOS will be launched from Vandenberg to achieve a near polar orbit. The spacecraft will be supported by a cradle in the STS cargo bay. EOS nearly fills the entire cargo bay with a stowed dimension of 4.28 m diameter by 17.8 m and the total system weight is 7635 kg. Once in orbit at an altitude of approximately 200 km, the EOS would be removed from the STS by the cradle ejection mechanisms. The spacecraft would then

start deployment in sequential, orthogonal steps. The deployment is controlled by STS astronauts via remote control. Once deployed, the EOS is boosted to a higher orbit using the integral propulsion system with an acceleration rate of 0.01 g.

During orbit transfer, many of the component members see their highest compression loading, with member 135 sustaining a load of 650 N.

At operational orbit, the spacecraft will circle the earth once every 90 minutes at an altitude of 700 km. The orbit is a noon sun-synchronous polar orbit.

8.2   ORBIT OPERATION

EOS represents a major advancement in the capability, completeness and approach to earth orbiting remote sensing platforms that use a large microwave radiometer as the "core" instrument. The organization of the missions began with user-defined measurement needs and the capability of the LMR. These capabilities were then augmented with the inclusion of auxiliary sensors that provide, expand and augment the LMR. The final result was a system demonstrating a holistic approach in the design of satellite-based remote sensing platforms.

Each of these missions represents a viable and compatible ensemble of sensors. Observables, orbits, and sensors have been selected to yield an efficient end-to-end remote sensing platform, with a completeness of measurements beyond the present capability. This approach to the mission planning development for future LMR has never been addressed from this perspective before. Table 8-2 summarizes the orbit parameters for each of the missions.

This study defined four distinct missions based on the observables. They have been categorized as EOS Mission I – baseline, Mission II – land, Mission III – ocean, and Mission IV – atmospheric. Each mission has a set of sensors specifically tailored for the intended mission. Table 8-4 summarizes the missions, sensors and observables. Both active and passive sensor are employed, and cover a wide spectral range.

Table 8-4 Sensor Summary

Mission	Observables	Sensors	Note
I Baseline	— Soil Moisture — Ocean Surface — Ice/Snowpack	— Microwave Radiometers, — Synthetic Aperture Radar,	— X-Band, 25-m Ground Resolution
II Land	— Crop Monitoring — Land Studies — Geology — Ocean Surface	— Microwave Radiometers, — Synthetic Aperture Radar, — Multispectral Imagers, — Multispectral IR Imagers	— X-Band, 25-m Ground Resolution — Visible and Near IR — Operates at 8 to 12 μm
III Ocean	— Ocean Surface — Soil Moisture	— Microwave Radiometers, — Radar Altimeter, — Radar Scatterometer, — Multispectral Imagers,	— 10-cm Precision — Sea State — Designed for Ocean Color Measurement
IV Atmospheric	— Chemical Species — Temperature — Clouds	— Survey Spectrometers, — Correlation Interferometer, — Filter Radiometer, — Atmospheric Temperature	— Trospheric Species — Stratosphere — Stratosphere — Temperature Profiling, CO_2 Bands

The missions analysis task of this study defined several important in-
novations, including:

1) Developed a unified approach to the future mission planning of LMR;

2) Identified potential problems in retrieval of remotely sensed data;

3) Defined sensor sets for each mission that compensate for retrieval
    ambiguities and also maximize the remote sensing capability;

4) Identified the usefulness of having a slewing capability for the
    LMR spacecraft.

8.3   STRUCTURE AND SUBSYSTEMS

The advantages of the box truss structure are numerous. This truss
system is inherently stiff, which reduces the control problems asso-
ciated with the spacecraft by increasing the structure's fundamental
frequency. The fundamental frequency before orbit transfer and at
operational orbit with and without slewing propellant is 0.711, 0.911,
and 1.09 Hz respectively. The vertical members provide an excellent
attachment point for sensors, thrusters, tankage, solar panels, and
battery packs. The box truss also lends itself to easy attachment of a
feed mast. The mast is rigidly attached to the truss system and re-
quires no special guywires or appendages. Because of this rigid at-
tachment, the rf performance is greatly improved because of negligible
movement between the feed and the reflective surface. The truss con-
figurations feature very compact stowage as demonstrated by stowage of
the entire EOS system in the STS. The box truss also has the advantage
of sequential, orthogonal deployment. Extensions of the vertical mem-
bers provide an ideal attachment point for the mesh tie system.

The mesh tie system is a direct tieback system. The tie system is sim-
ple in concept, but has numerous tie points to pull the reflective sur-
face to the desired shape. A very accurate reflective surface is nec-
essary for a 10.65-GHz radiometric antenna to perform well. Random
surface errors are inversely proportional to the number of mesh tie
points because of the pillowing between these points. In other words,
the more tie points, the closer the surface fits the parabola and the
lower the rms error. A double catenary system was considered for this
application but Martin Marietta models have shown that this system has
more coupling problems than the direct tieback systems. Each mesh tie
box can be tied independently of other boxes and at final assembly the
reflective mesh section will be sewn together.

The thermoelastic distortions of the EOS structure were minimized by
using graphite/epoxy members. This material features very small CTEs.
Thermal distortions and loads can be further minimized by matching the
CTEs of the various component members.

184

8.4   CONTINUED EFFORTS

This section describes the future work to be done on the EOS. Because analyses were beyond the present contract's scope, they were not performed. The list is not all inclusive nor is it itemized by priority.

1) Build scale model,

   a) Develop manufacturing techniques,

   b) Identify and qualify manufacturing errors,

   c) Gain better understanding of rf performance,

   d) Investigate mesh dynamics.

2) Further optimize member materials and sectional properties.

3) Conduct a transient thermal analysis of the structure for a variety of potential orbits.

4) Conduct a rigorous multibay mesh tie system model analysis to investigate the interactions between box truss bays.

5) Perform a rigorous attitude controls analysis.

6) Perform a rigorous nonlinear dynamic analysis of the structure during and after deployment.

7) Refine mesh distortion theory in an effort to inexpensively determine how mesh distortions will affect rf performance for preliminary analysis.

8) Perform detailed analysis for mesh using the surface current distribution method as verification (FIRE computer program).

9) Investigate observation-correcting feed systems and their influence on total system design.

10) Conduct a feasibility study employing active figure control of the mesh using actuators in the mesh standoffs.

11) Consider radiometer electronics and processing requirements in more detail.

12) Continue development of the subsystem designs.

13) Compile list of forcing functions that might excite structural modes while in orbit and determine what the dynamic response is.

14) Continue investigation of feed types, horns and other items and their integration with structure.

15) Investigate initial calibration of radiometer and thermal/vacuum tests.

16) Analyze mesh for suitabilty as a reflecting surface in a radiometer antenna.

Appendix A—Member Properties

t = 0.066 cm

OD = 8.33 cm

Area = 1.72 cm^2

$I_{YY} = I_{ZZ} = 14.65$ cm^4

$J = 29.3$ cm^4
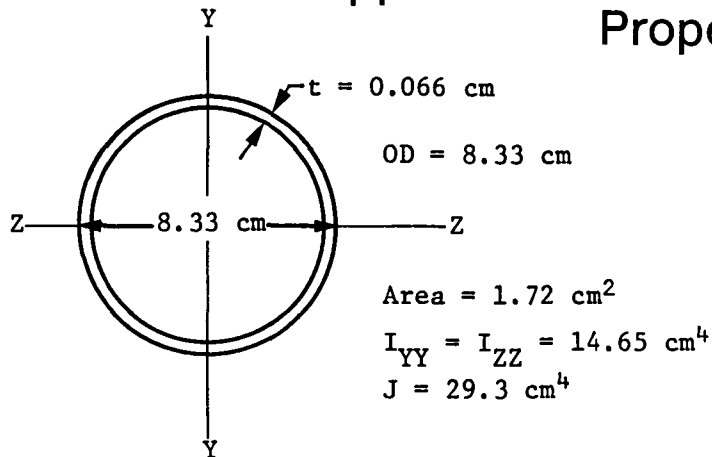
Member 1

Layup [OF/OT$_2$/45F]   T = Tape
                        F = Fabric

Material Used
- Tape - Pitch 75
- Fabric - T300

E_L = 1.66 x 10^{11} N/m^2 E_L = Longitudinal Modulus

E_T = 0.291 x 10^{11} N/m^2 E_T = Transverse Modulus

G_{LT} = 0.131 x 10^{11} N/m^2 G_{LT} = Shear Modulus

ν_{LT} = 0.193 ν_{LT} = Poisson's Ratio

CTE_L = 0.252 x 10^{-6} m/m/°C CTE_L = Coefficient of Thermal Expansion in Longitudinal Direction

ϵ_{ULT} = 0.001 m/m

$F_{TU} = F_{CU}$ = 1.66 x 10^8 N/m^2

Figure A-1
EOS Member Definition - Surface Member (Member 1)

187

Area = 3.81 cm^2

$I_{YY} = I_{ZZ}$ = 27.53 cm^4

J = 55.06 cm^4

Member 2

Layup [45F/OT$_3$/45F$_2$/OT$_3$/45F]   T = Tape
F = Fabric

Material Used
- Tape - Pitch 75
- Fabric - T300

E_L = 1.82 x 10^{11} N/m^2

E_T = 0.219 x 10^{11} N/m^2

G_{LT} = 0.143 x 10^{11} N/m^2

ν_{LT} = 0.35

CTE_L = -0.522 x 10^{-6} m/m/C°

ε_{ULT} = 0.001

$F_{TU} = F_{CU}$ = 1.82 x 10^8 N/m^2

Note:

See Member 1 for nomenclature.

Figure A-2
EOS Member Definition - Vertical Member (Member 2)

188
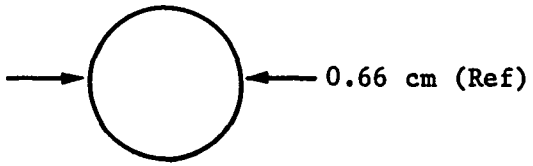
0.66 cm (Ref)   Area = 0.348 cm^2

Member 5

Material Used
75-12000 Tow Celion Cords

E_L = 2.34 x 10^{11} N/m^2

CTE = -0.4 x 10^{-6} m/m/C°

Figure A-3
EOS Member Definition - Diagonal Member (Member 5)

Area = 0.52 cm^2

←———0.81 cm (Ref)
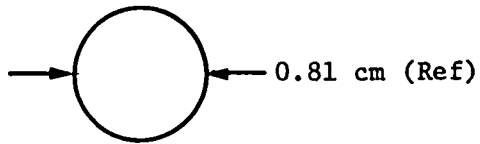
Member 6

Material Used
113-12000 Tow Celion Cords

E_L = 2.34 x 10^{11} N/m^2

CTE = -0.4 x 10^{-6} m/m/C°

Figure A-4
EOS Member Definition - Diagonal Member (Member 6)

Y

t = 0.127 cm

OD = 8.33 cm

Z———8.33 cm———Z
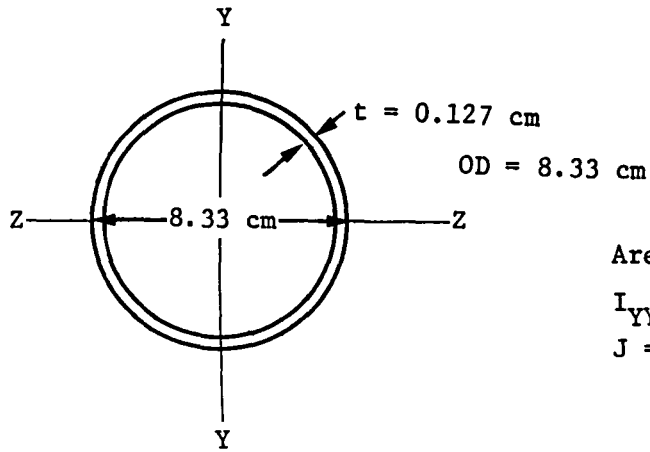
Area = 3.271 cm^2

$I_{YY} = I_{ZZ} = 27.55$ cm^4

$J = 55.1$ cm^4

Y

Member 51

Layup [45F/OT$_2$/OF/OT$_2$/OF/OT$_2$/OF]   T = Tape
                                          F = Fabric

Materials Used
- Tape - Pitch 75
- Fabric - T300

E_L = 1.88 x 10^{11} N/m^2

E_T = 0.251 x 10^{11} N/m^2

G_{LT} = 0.105 x 10^{11} N/m^2

ν_{LT} = 0.154

CTE_L = -0.335 x 10^{-6} m/m/C°

ε_{ULT} = 0.001

$F_{TU} = F_{CU}$ = 1.88 x 10^8 N/m^2

Note:
See Member 1 for nomenclature.

Figure A-5
EOS Member Definition - Surface Member (Member 51)
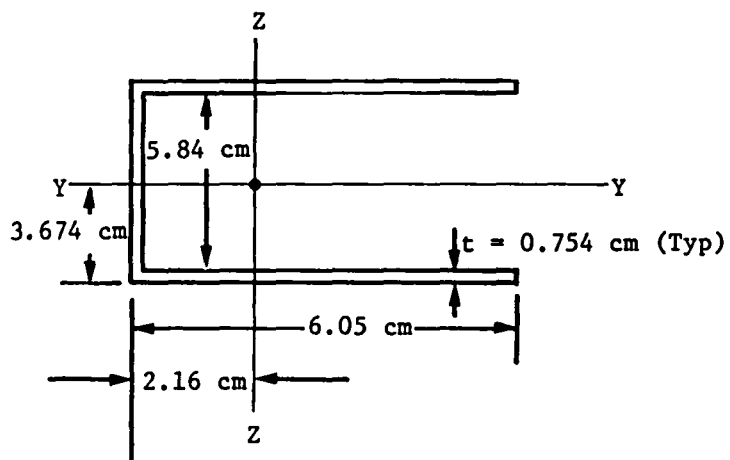
$Area = 13.53 \ cm^2$

$I_{YY} = 112.1 \ cm^4 \quad I_{ZZ} = 48.78 \ cm^4$

$J = 2.57 \ cm^4$

Member 53

Layup $[(45F/0T_2/0F/0T_2/0F/0T_2/45F)_6]$

Materials Used
- Tape - Pitch 75
- Fabric - T300

$E_L = 1.87 \times 10^{11} \ N/m^2$

$E_T = 0.242 \times 10^{11} \ N/m^2$

$G_{LT} = 0.115 \times 10^{11} \ N/m^2$

$\nu_{LT} = 0.198$

$CTE_L = -0.378 \times 10^{-6} \ m/m/C°$

$\varepsilon_{ULT} = 0.001$

$F_{TU} = F_{CU} = 1.87 \times 10^8 \ N/m^2$

Note:

See Member 1 for nomenclature.

Figure A-6
EOS Member Definition - Channel Member (Member 53)

192

$$Area = 4.24 \text{ cm}^2 \begin{pmatrix} \text{Normalized to} \\ E_L = 1.89 \times 10^{11} \text{ N/m}^2 \end{pmatrix}$$

$I_{YY} = 22.28 \text{ cm}^4$ $I_{ZZ} = 25.28 \text{ cm}^4$

$J = 0.026 \text{ cm}^4$
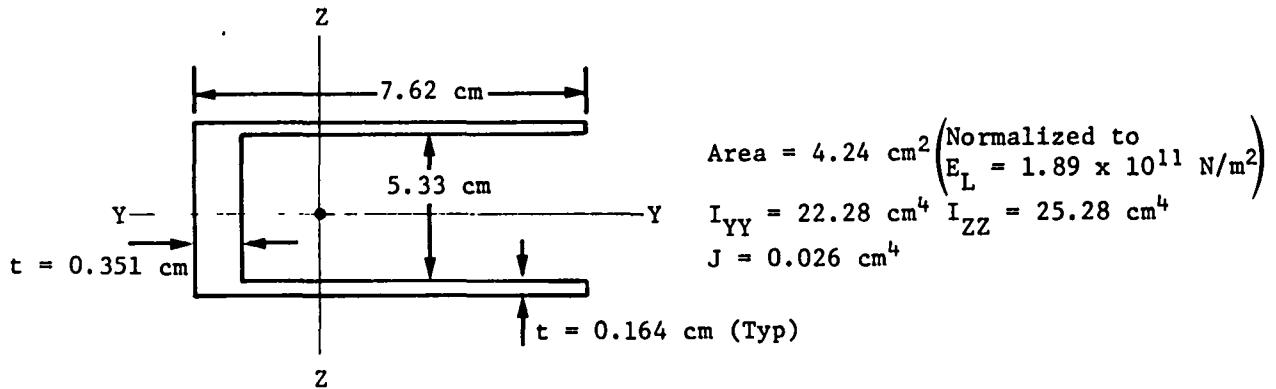
Member 54

Layup
- Flange [45F/0T$_2$/90F/0T$_2$/45F/0T$_2$/90F/0T$_2$/45F]
- Web   [(45F/0T$_2$/90F/0T$_2$/45F)$_4$]

Material Used
- Tape - Pitch 75
- Fabric - T300

Flange	Web
E_L = 1.89 x 10^{11} N/m^2	E_L = 1.79 x 10^{11} N/m^2
E_T = 0.23 x 10^{11} N/m^2	E_T = 0.247 x 10^{11} N/m^2
G_{LT} = 0.117 x 10^{11} N/m^2	G_{LT} = 0.131 x 10^{11} N/m^2
ν_{LT} = 0.225	ν_{LT} = 0.243
CTE_L = -0.414 x 10^{-6} m/m/C°	CTE_L = -0.379 x 10^{-6} m/m/C°
ε_{ULT} = 0.001	ε_{ULT} = 0.001
F_{TU} = F_{CU} = 1.89 x 10^8 N/m^2	F_{TU} = F_{CU} = 1.79 x 10^8 N/m^2

Figure A-7
EOS Member Definition - Channel Member (Member 54)

t = 0.278 cm
(Typ)

Area = 5.34 cm^2

$I_{YY} = I_{ZZ}$ = 20.60 cm^4

J = 30.80 cm^4

5.08 cm
(Typ)
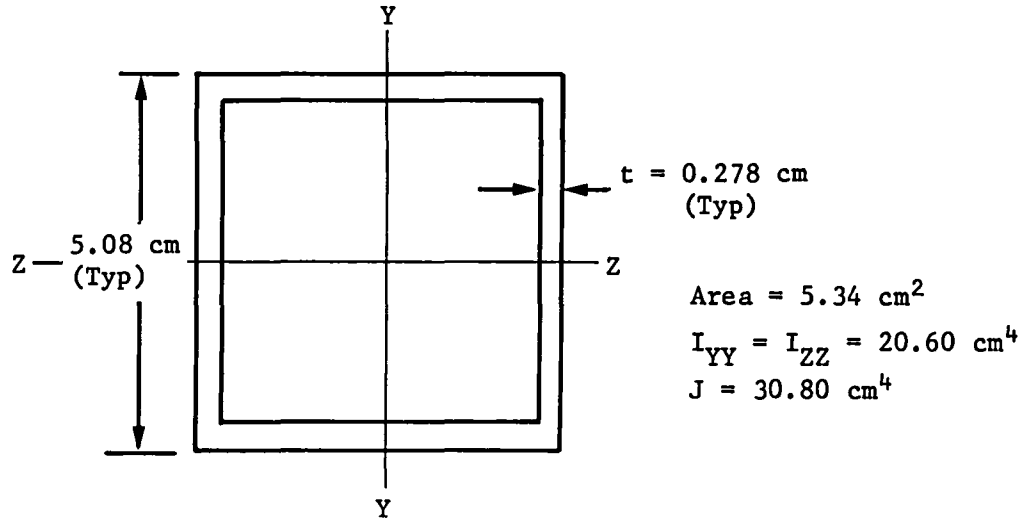
Member 58

Layup [45F/(OT$_2$/OF)$_6$/OT$_2$/45F]

Material Used
- Tape - Pitch 75
- Fabric - T300

E_L = 1.96 x 10^{11} N/m^2

E_T = 0.237 x 10^{11} N/m^2

G_{LT} = 0.096 x 10^{11} N/m^2

ν_{LT} = 0.136

CTE_L = -0.36 x 10^{-6} m/m/C°

ε_{ULT} = 0.001

$F_{TU} = F_{CU}$ = 1.96 x 10^8 N/m^2

Figure A-8

EOS Member Definition - Feed Mast Brace Member (Member 58)

```
t = 0.142 cm                                    Area = 3.27 cm²
      (Typ)                                     I_YY  = 18.08 cm⁴
                    5.9 cm                       I_ZZ  = 18.08 cm⁴
    Z               (Typ)                       J     = 36.2 cm⁴
```

$t = 0.142$ cm (Typ)

5.9 cm (Typ)
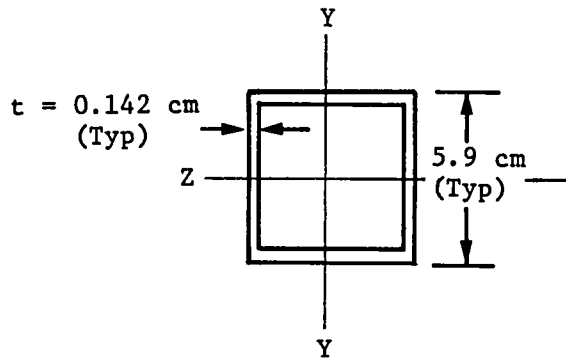
Area $= 3.27$ cm^2

$I_{YY} = 18.08$ cm^4

$I_{ZZ} = 18.08$ cm^4

$J = 36.2$ cm^4

Member 59

Layup $[45F/0T_2/0F/0T_2/0F/0T_2/45F]$ T = Tape
                                         F = Fabric

Materials Used
- Tape - Pitch 75
- Fabric - T300

$E_L = 1.87 \times 10^{11}$ N/m^2

$E_T = 0.24 \times 10^{11}$ N/m^2

$G_{LT} = 0.12 \times 10^{11}$ N/m^2

$\nu_{LT} = 0.198$

$CTE_L = -0.4 \times 10^{-6}$ m/m/C°

$\varepsilon_{ULT} = 0.001$

$F_{TU} = F_{CU} = 1.87 \times 10^8$ N/m^2

> Note:
> See Member 1 for nomenclature

Figure A-9

EOS Member Definition - Surface Member (Member 59)

Y

t = 0.389 cm (Typ)

Area = 6.64 cm²

I_{YY} = 17.29 cm⁴

I_{ZZ} = 23.3 cm⁴

J = 40.6 cm⁴

Z ———— Z

4.23 cm

←———— 5.08 cm ————→

Y
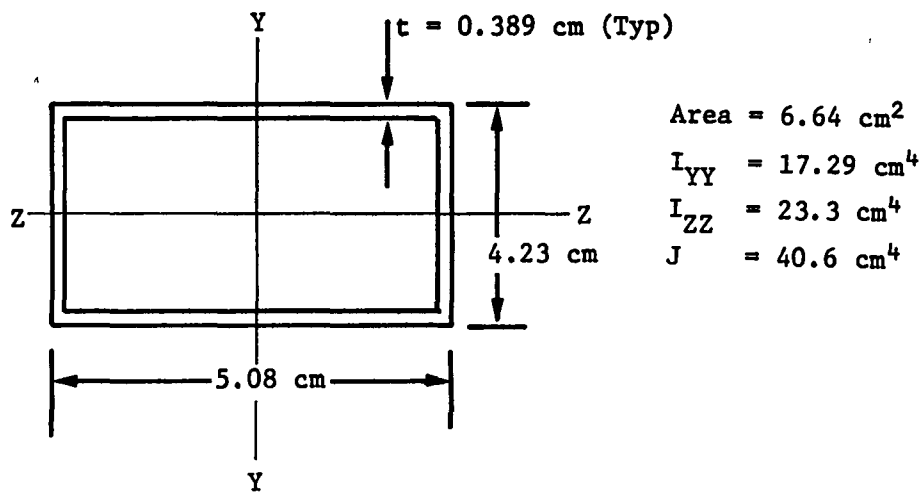
Member 60

Layup [45F/(OT₂/OF)₁₀/OT₂/45F]

Material Used
- Tape - Pitch 75
- Fabric - T300

E_L = 1.96 x 10¹¹ N/m²

E_T = 0.237 x 10¹¹ N/m²

G_{LT} = 0.096 x 10¹¹ N/m²

ν_{LT} = 0.136

CTE_L = -0.36 x 10⁻⁶ m/m/C°

ϵ_{ULT} = 0.001

F_{TU} = F_{CU} = 1.96 x 10⁸ N/m²

Note:
See Member 1 for nomenclature.

Figure A-10

EOS Member Definition - Surface Member (Member 60)

N A S T R A N   E X E C U T I V E   C O N T R O L   D E C K   E C H O

```
    ID. MSDA,DYNAMIC
    CHKPNT YES
    SOL 24
    TIME 30
    DIAG 8,9,13,14,19,21,22
    CEND
```

ECHO OF FIRST CARD IN CHECKPOINT DICTIONARY TO BE PUNCHED OUT FOR THIS PROBLEM

    RESTART   MSDA   .DYNAMIC . 2/26/83.   4858.

C A S E   C O N T R O L   D E C K   E C H O

CARD
COUNT
```
 1      TITLE= EOS THERMOLELASTIC   AND ORBIT TRANSFER
 2      SUBTITLE=MODEL 8        O1G
 3      DISP=ALL
 4      ELFORCE=ALL
 5      SPCFORCE=ALL
 6      SPC=11
 7      SET 11=19
 8      SUBCASE=7
 9      LABEL=244 6 DEG ORBIT POSITION
10       TEMP(LOAD)=7
11      BEGIN BULK

          INPUT BULK DATA CARD COUNT =    7740
```

CARD COUNT	1	2	3	4	5	6	7	8	9	10
1-	CBAR	101	1	1	2	1.	O	1.		+101
2-	+101	6	6							
3-	CBAR	102	1	2	3	1	O	1		+102
4-	+102	6	6							
5-	CBAR	103	1	39	40	1	O.	1		+103
6-	+103	6	6							
7-	CBAR	104	1	40	41	1	O	1		+104
8-	+104	6	6							
9-	CBAR	105	1	4	5	1	O	1.		+105
10-	+105	6	6							
11-	CBAR	106	1	5	6	1	O	1		+106
12-	+106	6	6							
13-	CBAR	107	1	6	7	1	O	1		+107
14-	+107	6	6							
15-	CBAR	108	1	7	8	1	O.	1		+108
16-	+108	6	6							
17-	CBAR	109	1	9	10	1.	O.	1		+109
18-	+109	6	6							
19-	CBAR	110	1	10	11	1	O	1		+110
20-	+110	6	6							
21-	CBAR	111	1	11	12	1	O	1		+111
22-	+111	6	6							
23-	CBAR	112	1	12	13	1	O	1		+112
24-	+112	6	6							
25-	CBAR	113	51	14	15	1	O.	1		+113
26-	+113	6	6							
27-	CBAR	114	1	15	16	1	O	1.		+114
28-	+114	6	6							
29-	CBAR	115	1	16	17	1	O	1.		+115
30-	+115	6	6							
31-	CBAR	116	1	17	18	1	O	1		+116
32-	+116	6	6							
33-	CBAR	117	51	19	20	1	O	1		+117
34-	+117	6	6							
35-	CBAR	118	1	20	21	1	O	1		+118
36-	+118	6	6							
37-	CBAR	119	1	21	22	1	O	1		+119
38-	+119	6	6							
39-	CBAR	120	1	22	23	1	O	1		+120
40-	+120	6	6							
41-	CBAR	121	51	24	25	1	O	1		+121
42-	+121	6	6							
43-	CBAR	122	1	25	26	1.	O	1.		+122
44-	+122	6	6							
45-	CBAR	123	1	26	27	1	O	1.		+123
46-	+123	6	6							
47-	CBAR	124	1	27	28	1	O.	1.		+124
48-	+124	6	6							
49-	CBAR	125	1	29	30	1.	O.	1.		+125
50-	+125	6	6							

SORTED   BULK   DATA   ECHO

CARD COUNT	1	2	3	4	5	6	7	8	9	.. 10
51-	CBAR	126	1	30	31	1.	O	1.		+126
52-	+126	6	6							
53-	CBAR	127	1	31	32	1	O.	1		+127
54-	+127	6	6							
55-	CBAR	128	1	32	33	1	O	1		+128
56-	+128	6	6							
57-	CBAR	129	1	34	35	1	O	1		+129
58-	+129	6	6							
59-	CBAR	130	1	35	36	1	O	1		+130
60-	+130	6	6							
61-	CBAR	131	1	36	37	1	O	1.		+131
62-	+131	6	6							
63-	CBAR	132	1	37	38	1	O	1		+132
64-	+132	6	6							
65-	CBAR	133	1	4	9	O	1	1.		+133
66-	+133	6	6							
67-	CBAR	134	1	9	14	O	1	1		+134
68-	+134	6	6							
69-	CBAR	135	1	14	19	O	1	1		+135
70-	+135	6	6							
71-	CBAR	136	1	19	24	O	1.	1		+136
72-	+136	6	6							
73-	CBAR	137	1	24	29	O	1	1		+137
74-	+137	6	6							
75-	CBAR	138	1	29	34	O	1	1		+138
76-	+138	6	6							
77-	CBAR	139	1	8	13	O	1	1		+139
78-	+139	6	6							
79-	CBAR	140	1	13	18	O	1	1		+140
80-	+140	6	6							
81-	CBAR	141	1	18	23	O	1	1.		+141
82-	+141	6	6							
83-	CBAR	142	1	23	28	O	1	1		+142
84-	+142	6	6							
85-	CBAR	143	1	28	33	O	1	1		+143
86-	+143	6	6							
87-	CBAR	144	1	33	38	O	1	1.		+144
88-	+144	6	6							
89-	CBAR	145	1	5	10	O	1	1		+145
90-	+145	6	6							
91-	CBAR	146	1	10	15	O	1	1.		+146
92-	+146	6	6							
93-	CBAR	147	1	15	20	O	1.	1.		+147
94-	+147	6	6							
95-	CBAR	148	1	20	25	O.	1	1		+148
96-	+148	6	6							
97-	CBAR	149	1	25	30	O	1	1.		+149
98-	+149	6	6							
99-	CBAR	150	1	30	35	O	1	1.		+150
100-	+150	6	6							

CARD COUNT	1	2	3	4	5	6	7	8 ..	9 .	10
101-	CBAR	151	1	6	11	O	1.	1		+151
102-	+151	6	6							
103-	CBAR	152	1	11	16	O	1.	1		+152
104-	+152	6	6							
105-	CBAR	153	1	16	21	O	1.	1		+153
106-	+153	6	6							
107-	CBAR	154	1	21	26	O	1	1		+154
108-	+154	6	6							
109-	CBAR	155	1	26	31	O	1	1.		+155
110-	+155	6	6							
111-	CBAR	156	1	31	36	O	1	1		+156
112-	+156	6	6							
113-	CBAR	157	1	7	12	O	1.	1.		+157
114-	+157	6	6							
115-	CBAR	158	1	12	17	O	1	1.		+158
116-	+158	6	6							
117-	CBAR	159	1	17	22	O	1	1		+159
118-	+159	6	6							
119-	CBAR	160	1	22	27	O	1.	1		+160
120-	+160	6	6							
121-	CBAR	161	1	27	32	O.	1	1.		+161
122-	+161	6	6							
123-	CBAR	162	1	32	37	O	1	1.		+162
124-	+162	6	6							
125-	CBAR	163	1	1	5	O	1	1		+163
126-	+163	6	6							
127-	CBAR	164	1	2	6	O	1	1		+164
128-	+164	6	6							
129-	CBAR	165	1	3	7	O.	1	1		+165
130-	+165	6	6							
131-	CBAR	166	1	35	39	O.	1.	1		+166
132-	+166	6	6							
133-	CBAR	167	1	36	40	O.	1.	1		+167
134-	+167	6	6							
135-	CBAR	168	1	37	41	O.	1.	1		+168
136-	+168	6	6							
137-	CBAR	169	1	42	43	1.	O.	1		+169
138-	+169	6	6							
139-	CBAR	170	1	43	44	1.	O	1		+170
140-	+170	6	6							
141-	CBAR	171	1	80	81	1	O	1.		+171
142-	+171	6	6							
143-	CBAR	172	1	81	82	1.	O	1.		+172
144-	+172	6	6							
145-	CBAR	173	1	45	46	1	O.	1.		+173
146-	+173	6	6							
147-	CBAR	174	1	46	47	1	O.	1		+174
148-	+174	6	6							
149-	CBAR	175	1	47	48	1	O.	1.		+175
150-	+175	6	6							

SORTED BULK DATA ECHO

	1	.. 2	.. 3	.. 4	5	.. 6	.. 7	.. 8	.. 9	. 10
151-	CBAR	176	1	48	49	1.	0.	1.		+176
152-	+176	6	6							
153-	CBAR	177	1	50	51	1.	0.	1.		+177
154-	+177	6	6							
155-	CBAR	178	1	51	52	1.	0.	1		+178
156-	+178	6	6							
157-	CBAR	179	1	52	53	1.	0.	1.		+179
158-	+179	6	6							
159-	CBAR	180	1	53	54	1.	0	1.		+180
160-	+180	6	6							
161-	CBAR	181	51	55	56	1	0.	1.		+181
162-	+181	6	6							
163-	CBAR	182	1	56	57	1.	0.	1.		+182
164-	+182	6	6							
165-	CBAR	183	1	57	58	1.	0	1.		+183
166-	+183	6	6							
167-	CBAR	184	1	58	59	1.	0.	1.		+184
168-	+184	6	6							
169-	CBAR	185	51	60	61	1.	0	1.		+185
170-	+185	6	6							
171-	CBAR	186	1	61	62	1	0.	1.		+186
172-	+186	6	6							
173-	CBAR	187	1	62	63	1	0.	1.		+187
174-	+187	6	6							
175-	CBAR	188	1	63	64	1	0	1.		+188
176-	+188	6	6							
177-	CBAR	189	51	65	66	1	0.	1.		+189
178-	+189	6	6							
179-	CBAR	190	1	66	67	1.	0.	1.		+190
180-	+190	6	6							
181-	CBAR	191	1	67	68	1	0.	1.		+191
182-	+191	6	6							
183-	CBAR	192	1	68	69	1	0.	1.		+192
184-	+192	6	6							
185-	CBAR	193	1	70	71	1.	0	1.		+193
186-	+193	6	6							
187-	CBAR	194	1	71	72	1	0	1.		+194
188-	+194	6	6							
189-	CBAR	195	1	72	73	1	0	1.		+195
190-	+195	6	6							
191-	CBAR	196	1	73	74	1	0.	1		+196
192-	+196	6	6							
193-	CBAR	197	1	75	76	1.	0.	1.		+197
194-	+197	6	6							
195-	CBAR	198	1	76	77	1	0	1		+198
196-	+198	6	6							
197-	CBAR	199	1	77	78	1.	0	1.		+199
198-	+199	6	6							
199-	CBAR	200	1	78	79	1	0	1.		+200
200-	+200	6	6							

CARD COUNT	1	2	3	4	5	6	7	8	9	10
201-	CBAR	201	1	45	50	O	1	1		+201
202-	+201	6	6							
203-	CBAR	202	1	50	55	O	1	1.		+202
204-	+202	6	6							
205-	CBAR	203	1	55	60	O	1	1		+203
206-	+203	6	6							
207-	CBAR	204	1	60	65	O	1	1.		+204
208-	+204	6	6							
209-	CBAR	205	1	65	70	O	1	1		+205
210-	+205	6	6							
211-	CBAR	206	1	70	75	O	1	1.		+206
212-	+206	6	6							
213-	CBAR	207	1	49	54	O	1	1.		+207
214-	+207	6	6							
215-	CBAR	208	1	54	59	O.	1.	1.		+208
216-	+208	6	6							
217-	CBAR	209	1	59	64	O	1	1.		+209
218-	+209	6	6							
219-	CBAR	210	1	64	69	O.	1	1.		+210
220-	+210	6	6							
221-	CBAR	211	1	69	74	O	1.	1.		+211
222-	+211	6	6							
223-	CBAR	212	1	74	79	O	1.	1.		+212
224-	+212	6	6							
225-	CBAR	213	1	46	51	O	1	1.		+213
226-	+213	6	6							
227-	CBAR	214	1	51	56	O	1.	1.		+214
228-	+214	6	6							
229-	CBAR	215	1	56	61	O	1	1		+215
230-	+215	6	6							
231-	CBAR	216	1	61	66	O.	1.	1.		+216
232-	+216	6	6							
233-	CBAR	217	1	66	71	O	1.	1.		+217
234-	+217	6	6							
235-	CBAR	218	1	71	76	O.	1	1.		+218
236-	+218	6	6							
237-	CBAR	219	1	47	52	O	1.	1.		+219
238-	+219	6	6							
239-	CBAR	220	1	52	57	O.	1	1		+220
240-	+220	6	6							
241-	CBAR	221	1	57	62	O	1.	1.		+221
242-	+221	6	6							
243-	CBAR	222	1	62	67	O	1.	1.		+222
244-	+222	6	6							
245-	CBAR	223	1	67	72	O.	1.	1.		+223
246-	+223	6	6							
247-	CBAR	224	1	72	77	O	1.	1.		+224
248-	+224	6	6							
249-	CBAR	225	1	48	53	O.	1.	1.		+225
250-	+225	6	6							

S O R T E D   B U L K   D A T A   E C H O

CARD COUNT	. 1	2	3	4	5	. 6 .. 7	8	. 9 . 10 .
251-	CBAR 226	1	53	58	O.	1. 1		+226
252-	+226 6	6						
253-	CBAR 227	1	58	63	O	1. 1		+227
254-	+227 6	6						
255-	CBAR 228	1	63	68	O	1 1		+228
256-	+228 6	6						
257-	CBAR 229	1	68	73	O	1 1.		+229
258-	+229 6	6						
259-	CBAR 230	1	73	78	O.	1 1		+230
260-	+230 6	6						
261-	CBAR 231	1	42	46	O	1 1		+231
262-	+231 6	6						
263-	CBAR 232	1	43	47	O	1 1.		+232
264-	+232 6	6						
265-	CBAR 233	1	44	48	O.	1 1		+233
266-	+233 6	6						
267-	CBAR 234	1	76	80	O.	1 1.		+234
268-	+234 6	6						
269-	CBAR 235	1	77	81	O.	1. 1		+235
270-	+235 6	6						
271-	CBAR 236	1	78	82	O	1. 1		+236
272-	+236 6	6						
273-	CBAR 237	51	83	84	O	1. 1		+237
274-	+237 6	6						
275-	CBAR 238	51	84	85	O.	1 1		+238
276-	+238 6	6						
277-	CBAR 239	51	14	86	-1.	O 1.		+239
278-	+239 6	6						
279-	CBAR 240	51	19	87	-1	O 1		+240
280-	+240 6	6						
281-	CBAR 241	51	24	88	-1.	O 1		+241
282-	+241 6	6						
283-	CBAR 242	51	83	89	-1	O 1		+242
284-	+242 6	6						
285-	CBAR 243	51	84	90	-1	O 1.		+243
286-	+243 6	6						
287-	CBAR 244	51	85	91	-1.	O 1.		+244
288-	+244 6	6						
289-	CBAR 245	51	86	92	-1	O 1.		+245
290-	+245 6	6						
291-	CBAR 246	51	87	93	-1	O 1		+246
292-	+246 6	6						
293-	CBAR 247	51	88	94	-1	O 1.		+247
294-	+247 6	6						
295-	CBAR 248	51	89	95	-1	O 1		+248
296-	+248 6	6						
297-	CBAR 249	51	90	96	-1.	O 1.		+249
298-	+249 6	6						
299-	CBAR 250	51	91	97	-1.	O. 1.		+250
300-	+250 6	6						

CARD COUNT	1	..	2	3	4	5	6	7	8	9	.	10
301-	CBAR	251	1	92	98	-1	O	1				+251
302-	+251	6	6									
303-	CBAR	252	1	93	99	-1	O	1				+252
304-	+252	6	6									
305-	CBAR	253	1	94	100	-1	O	1				+253
306-	+253	6	6									
307-	CBAR	254	1	95	101	-1	O.	1				+254
308-	+254	6	6									
309-	CBAR	255	1	96	102	-1	O	1				+255
310-	+255	6	6									
311-	CBAR	256	1	97	103	-1.	O	1				+256
312-	+256	6	6									
313-	CBAR	257	1	98	104	-1	O.	1				+257
314-	+257	6	6									
315-	CBAR	258	1	99	105	-1	O	1				+258
316-	+258	6	6									
317-	CBAR	259	1	100	106	-1.	O	1				+259
318-	+259	6	6									
319-	CBAR	260	1	101	107	-1	O.,	1.				+260
320-	+260	6	6									
321-	CBAR	261	1	102	108	-1	O	1				+261
322-	+261	6	6									
323-	CBAR	262	1	103	109	-1	O	1				+262
324-	+262	6	6									
325-	CBAR	263	1	104	110	-1	O	1.				+263
326-	+263	6	6									
327-	CBAR	264	1	105	111	-1	O.	1				+264
328-	+264	6	6									
329-	CBAR	265	1	106	112	-1	O	1.				+265
330-	+265	6	6									
331-	CBAR	266	1	107	113	-1	O	1.				+266
332-	+266	6	6									
333-	CBAR	267	1	108	114	-1	O.	1				+267
334-	+267	6	6									
335-	CBAR	268	1	109	115	-1	O	1				+268
336-	+268	6	6									
337-	CBAR	269	1	110	116	-1	O	1				+269
338-	+269	6	6									
339-	CBAR	270	1	111	117	-1	O.	1				+270
340-	+270	6	6									
341-	CBAR	271	1	112	118	-1	O.	1.				+271
342-	+271	6	6									
343-	CBAR	272	1	113	119	-1	O	1.				+272
344-	+272	6	6									
345-	CBAR	273	1	114	120	-1	O	1				+273
346-	+273	6	6									
347-	CBAR	274	1	115	121	-1	O.	1				+274
348-	+274	6	6									
349-	CBAR	275	1	'16	122	-1	O	1.				+275
350-	+275	6	6									

SORTED BULK DATA ECHO

	1	2	3	4	5	6	7	8	9	10
351-	CBAR	276	1	117	123	-1.	O.	1.		+276
352-	+276	6	6							
353-	CBAR	277	1	118	124	-1	O	1.		+277
354-	+277	6	6							
355-	CBAR	278	1	119	125	-1.	O	1		+278
356-	+278	6	6							
357-	CBAR	279	1	120	126	-1	O	1		+279
358-	+279	6	6							
359-	CBAR	280	1	121	127	-1	O.	1.		+280
360-	+280	6	6							
361-	CBAR	281	1	122	128	-1	O	1.		+281
362-	+281	6	6							
363-	CBAR	282	1	123	129	-1	O	1		+282
364-	+282	6	6							
365-	CBAR	283	1	124	130	-1.	O.	1		+283
366-	+283	6	6							
367-	CBAR	284	1	125	131	-1	O.	1.		+284
368-	+284	6	6							
369-	CBAR	285	1	126	132	-1	O.	1		+285
370-	+285	6	6							
371-	CBAR	286	1	127	133	-1	O.	1.		+286
372-	+286	6	6							
373-	CBAR	287	1	86	87	1.	1	O		+287
374-	+287	6	6							
375-	CBAR	288	1	87	88	1	1.	O.		+288
376-	+288	6	6							
377-	CBAR	289	1	89	90	1.	1	O.		+289
378-	+289	6	6							
379-	CBAR	290	1	90	91	1.	1.	O.		+290
380-	+290	6	6							
381-	CBAR	291	1	92	93	1	1.	O.		+291
382-	+291	6	6							
383-	CBAR	292	1	93	94	1.	1.	O		+292
384-	+292	6	6							
385-	CBAR	293	1	95	96	1	1.	O.		+293
386-	+293	6	6							
387-	CBAR	294	1	96	97	1.	1.	O.		+294
388-	+294	6	6							
389-	CBAR	295	1	98	99	1.	1.	O		+295
390-	+295	6	6							
391-	CBAR	296	1	99	100	1	1.	O.		+296
392-	+296	6	6							
393-	CBAR	297	1	101	102	1	1.	O.		+297
394-	+297	6	6							
395-	CBAR	298	1	102	103	1.	1.	O.		+298
396-	+298	6	6							
397-	CBAR	299	1	104	105	1	1.	O.		+299
398-	+299	6	6							
399-	CBAR	300	1	105	106	1.	1.	O		+300
400-	+300	6	6							

CARD COUNT	1	.	2	3	4	5	6	7	.	8	.	9	10
401-	CBAR	301	1		107	108	1	1	O				+301
402-	+301	6	6					.					
403-	CBAR	302	1		108	109	1	1	O.				+302
404-	+302	6	6										
405-	CBAR	303	1		110	111	1	1	O				+303
406-	+303	6	6										
407-	CBAR	304	1		111	112	1	1	O				+304
408-	+304	6	6										
409-	CBAR	305	1		113	114	1	1	O.				+305
410-	+305	6	6										
411-	CBAR	306	1		114	115	1	1	O				+306
412-	+306	6	6										
413-	CBAR	307	1		116	117	1	1	O				+307
414-	+307	6	6										
415-	CBAR	308	1		117	118	1	1	O.				+308
416-	+308	6	6										
417-	CBAR	309	1		119	120	1	1	O.				+309
418-	+309	6	6										
419-	CBAR	310	1		120	121	1	1	O				+310
420-	+310	6	6										
421-	CBAR	311	1		122	123	1	1	O				+311
422-	+311	6	6										
423-	CBAR	312	1		123	124	1	1.	O				+312
424-	+312	6	6										
425-	CBAR	313	1		125	126	1	1.	O.				+313
426-	+313	6	6										
427-	CBAR	314	1		126	127	1	1	O				+314
428-	+314	6	6										
429-	CBAR	315	21		128	129	1	1	O				+315
430-	+315	6	6										
431-	CBAR	316	21		129	130	1	1	O				+316
432-	+316	6	6										
433-	CBAR	317	1		131	132	1	1	O				+317
434-	+317	6	6										
435-	CBAR	318	1		132	133	1	1	O				+318
436-	+318	6	6										
437-	CBAR	319	1		128	134	-1	O	1				+319
438-	+319	6	6										
439-	CBAR	320	1		129	135	-1	O	1				+320
440-	+320	6	6										
441-	CBAR	321	1		130	136	-1	O	1				+321
442-	+321	6	6										
443-	CBAR	322	1		131	137	-1	O	1				+322
444-	+322	6	6										
445-	CBAR	323	1		132	138	-1	O	1				+323
446-	+323	6	6										
447-	CBAR	324	1		133	139	-1	O	1				+324
448-	+324	6	6										
449-	CBAR	325	21		134	135	1	1	O				+325
450-	+325	6	6										

SORTED BULK DATA ECHO

CARD COUNT	1	2	.	3	.	4	5	.	6	7	.	8	.	9	.	10	.
451-	CBAR	326	21		135	136	1.		1.	O						+326	
452-	+326	6	6														
453-	CBAR	327	1		137	138	1.		1.	O						+327	
454-	+327	6	6														
455-	CBAR	328	1		138	139	1.		1.	O						+328	
456-	+328	6	6														
457-	CBAR	401	20		1	42	1		O.	-1.							
458-	CBAR	402	2		2	43	1.		O.	-1.							
459-	CBAR	403	20		3	44	1.		O.	-1.							
460-	CBAR	404	20		39	80	1.		O.	-1.							
461-	CBAR	405	2		40	81	1		O.	-1.							
462-	CBAR	406	20		41	82	1.		O.	-1.							
463-	CBAR	407	2		5	46	1.		O	-1.							
464-	CBAR	408	2		10	51	1		O	-1.							
465-	CBAR	409	2		15	56	1		O	-1.							
466-	CBAR	410	2		20	61	1.		O	-1.							
467-	CBAR	411	2		25	66	1.		O.	-1.							
468-	CBAR	412	2		30	71	1.		O.	-1.							
469-	CBAR	413	2		35	76	1		O	-1.							
470-	CBAR	414	2		6	47	1.		O	-1							
471-	CBAR	415	2		11	52	1		O.	-1.							
472-	CBAR	416	2		16	57	1		O	-1.							
473-	CBAR	417	2		21	62	1		O.	-1.							
474-	CBAR	418	2		26	67	1		O	-1							
475-	CBAR	419	2		31	72	1.		O	-1.							
476-	CBAR	420	2		36	77	1.		O	-1							
477-	CBAR	421	2		7	48	1.		O	-1							
478-	CBAR	422	2		12	53	1		O.	-1.							
479-	CBAR	423	2		17	58	1.		O	-1.							
480-	CBAR	424	2		22	63	1		O	-1							
481-	CBAR	425	2		27	68	1		O	-1							
482-	CBAR	426	2		32	73	1		O	-1.							
483-	CBAR	427	2		37	78	1.		O	-1.							
484-	CBAR	428	25		8	49	1		O	-1							
485-	CBAR	429	2		13	54	1		O	-1.							
486-	CBAR	430	2		18	59	1		O.	-1							
487-	CBAR	431	2		23	64	1		O	-1.							
488-	CBAR	432	2		28	69	1		O.	-1							
489-	CBAR	433	2		33	74	1.		O.	-1.							
490-	CBAR	434	25		38	79	1		O.	-1.							
491-	CBAR	435	29		4	45	1		O	-1							
492-	CBAR	436	2		9	50	1		O	-1.							
493-	CBAR	437	2		29	70	1		O.	-1.							
494-	CBAR	438	29		34	75	1		O	-1.							
495-	CBAR	439	2		86	89	-1		O.	1							
496-	CBAR	440	2		87	90	-1		O	1							
497-	CBAR	441	2		88	91	-1		O	1							
498-	CBAR	442	2		92	95	-1		O	1							
499-	CBAR	443	2		93	96	-1		O	1							
500-	CBAR	444	2		94	97	-1		O	1							

CARD COUNT	1	. 2	. 3	. 4	5	6	7	8	. 9	. 10
501-	CBAR	445	2	98	101	-1	O	1.		
502-	CBAR	446	2	99	102	-1	O.	1.		
503-	CBAR	447	2	100	103	-1	O	1		
504-	CBAR	448	2	104	107	-1	O	1.		
505-	CBAR	449	2	105	108	-1	O.	1.		
506-	CBAR	450	2	106	109	-1	O	1.		
507-	CBAR	451	2	110	113	-1	O	1.		
508-	CBAR	452	2	111	114	-1	O	1		
509-	CBAR	453	2	112	115	-1	O	1.		
510-	CBAR	454	2	116	119	-1	O	1.		
511-	CBAR	455	2	117	120	-1	O	1		
512-	CBAR	456	2	118	121	-1	O	1		
513-	CBAR	457	2	122	125	-1	O	1		
514-	CBAR	458	2	123	126	-1	O.	1.		
515-	CBAR	459	2	124	127	-1	O	1		
516-	CBAR	460	20	128	131	-1.	O	1		
517-	CBAR	461	2	129	132	-1	O	1.		
518-	CBAR	462	20	130	133	-1	O	1		
519-	CBAR	463	2	134	137	-1.	O	1.		
520-	CBAR	464	22	135	138	-1.	O	1.		
521-	CBAR	465	2	136	139	-1	O.	1.		
522-	CBAR	501	54	14	83	-1	O	1.		+501
523-	+501	6	6							
524-	CBAR	502	54	19	84	-1	O.	1.		+502
525-	+502	6	6							
526-	CBAR	503	54	24	85	-1	O	1		+503
527-	+503	6	6							
528-	CBAR	504	53	14	55	1.	O	-1		
529-	CBAR	505	53	19	60	1	O.	-1		
530-	CBAR	506	53	24	65	1	O	-1		
531-	CBAR	551	58	55	83	- 5	O	1.		+551
532-	+551	6	6							
533-	CBAR	552	58	60	84	- 5	O	1		+552
534-	+552	6	6							
535-	CBAR	553	58	65	85	- 5	O.	1.		+553
536-	+553	6	6							
537-	CONM2	2001	1	O	4 810					
538-	CONM2	2002	2	O	6 170					
539-	CONM2	2003	3	O	4 810					
540-	CONM2	2004	4	O	4 810					
541-	CONM2	2005	5	O	11 317					
542-	CONM2	2006	6	O	11 317					
543-	CONM2	2007	7	O	11 317					
544-	CONM2	2008	8	O	4 810					
545-	CONM2	2009	9	O	6 170					
546-	CONM2	2010	10	O	11 317					
547-	CONM2	2011	11	O	11 317					
548-	CONM2	2012	12	O	11 317					
549-	CONM2	2013	13	O	6 170					
550-	CONM2	2014	14	O	6 317					

SORTED   BULK   DATA   ECHO

CARD COUNT		1	2	3	4	5	6 ..	7	8 .	9 .	10
551-		CONM2	2015	15	O	11 317					
552-		CONM2	2016	16	O	11 317					
553-		CONM2	2017	17	O	11 317					
554-		CONM2	2018	18	O	6 170					
555-		CONM2	2019	19	O	6 317					
556-		CONM2	2020	20	O	11 317					
557-		CONM2	2021	21	O	11 317					
558-		CONM2	2022	22	O	11 317					
559-		CONM2	2023	23	O	175 317					
560-		CONM2	2024	24	O	6 317					
561-		CONM2	2025	25	O	11 317					
562-		CONM2	2026	26	O	11 317					
563-		CONM2	2027	27	O	11 317					
564-		CONM2	2028	28	O	6 170					
565-		CONM2	2029	29	O	6 170					
566-		CONM2	2030	30	O	11 317					
567-		CONM2	2031	31	O	11 317					
568-		CONM2	2032	32	O	11 317					
569-		CONM2	2033	33	O	6 170					
570-		CONM2	2034	34	O	4.810					
571-		CONM2	2035	35	O	11 317					
572-		CONM2	2036	36	O	11.317					
573-		CONM2	2037	37	O	11 317					
574-		CONM2	2038	38	O	4 810					
575-		CONM2	2039	39	O	4 810					
576-		CONM2	2040	40	O	6 170					
577-		CONM2	2041	41	O	4 810					
578-		CONM2	2042	42	O	223					
579-		CONM2	2043	43	O	332					
580-		CONM2	2044	44	O	223					
581-		CONM2	2045	45	O	84 223					
582-		CONM2	2046	46	O	479					
583-		CONM2	2047	47	O	479					
584-		CONM2	2048	48	O	.479					
585-		CONM2	2049	49	O	84 223					
586-		CONM2	2050	50	O	332					
587-		CONM2	2051	51	O	479					
588-		CONM2	2052	52	O	479					
589-		CONM2	2053	53	O	479					
590-		CONM2	2054	54	O	332					
591-		CONM2	2055	55	O	706					
592-		CONM2	2056	56	O	479					
593-		CONM2	2057	57	O	479					
594-		CONM2	2058	58	O	479					
595-		CONM2	2059	59	O	332					
596-		CONM2	2060	60	O	706					
597-		CONM2	2061	61	O	479					
598-		CONM2	2062	62	O	479					
599-		CONM2	2063	63	O	479					
600-		CONM2	2064	64	O	332					

CARD COUNT	. 1	. 2	. 3	. 4	. 5	6	7 .	8	9	10
601-	CONM2	2065	65	O	.706					
602-	CONM2	2066	66	O	479					
603-	CONM2	2067	67	O	479					
604-	CONM2	2068	68	O	479					
605-	CONM2	2069	69	O	332					
606-	CONM2	2070	70	O	332					
607-	CONM2	2071	71	O	479					
608-	CONM2	2072	72	O	479					
609-	CONM2	2073	73	O	479					
610-	CONM2	2074	74	O	332					
611-	CONM2	2075	75	O	84 223					
612-	CONM2	2076	76	O	479					
613-	CONM2	2077	77	O	.479					
614-	CONM2	2078	78	O	479					
615-	CONM2	2079	79	O	84 223					
616-	CONM2	2080	80	O	223					
617-	CONM2	2081	81	O	332					
618-	CONM2	2082	82	O	223					
619-	CONM2	2083	83	O	332					
620-	CONM2	2084	84	O	479					
621-	CONM2	2085	85	O	332					
622-	CONM2	2086	86	O	332					
623-	CONM2	2087	87	O	479					
624-	CONM2	2088	88	O	.332					
625-	CONM2	2089	89	O	332					
626-	CONM2	2090	90	O	479					
627-	CONM2	2091	91	O	332					
628-	CONM2	2092	92	O	332					
629-	CONM2	2093	93	O	479					
630-	CONM2	2094	94	O	332					
631-	CONM2	2095	95	O	332					
632-	CONM2	2096	96	O	.479					
633-	CONM2	2097	97	O	332					
634-	CONM2	2098	98	O	332					
635-	CONM2	2099	99	O	479					
636-	CONM2	2100	100	O	332					
637-	CONM2	2101	101	O	332					
638-	CONM2	2102	102	O	479					
639-	CONM2	2103	103	O	332					
640-	CONM2	2104	104	O	332					
641-	CONM2	2105	105	O	.479					
642-	CONM2	2106	106	O	332					
643-	CONM2	2107	107	O	332					
644-	CONM2	2108	108	O	479					
645-	CONM2	2109	109	O	332					
646-	CONM2	2110	110	O	332					
647-	CONM2	2111	111	O	.479					
648-	CONM2	2112	112	O	332					
649-	CONM2	2113	113	O	332					
650-	CONM2	2114	114	O	479					

SORTED BULK DATA ECHO

CARD COUNT	1	. 2	3	. 4	. 5	.. 6	. 7	. 8	. 9	.. 10	.
651-	CONM2	2115	115	0	.332						
652-	CONM2	2116	116	0	332						
653-	CONM2	2117	117	0	479						
654-	CONM2	2118	118	0	332						
655-	CONM2	2119	119	0	.332						
656-	CONM2	2120	120	0	479						
657-	CONM2	2121	121	0	332						
658-	CONM2	2122	122	0	.332						
659-	CONM2	2123	123	0	.479						
660-	CONM2	2124	124	0	.332						
661-	CONM2	2125	125	0	332						
662-	CONM2	2126	126	0	479						
663-	CONM2	2127	127	0	332						
664-	CONM2	2128	128	0	332						
665-	CONM2	2129	129	0	479						
666-	CONM2	2130	130	0	332						
667-	CONM2	2131	131	0	332						
668-	CONM2	2132	132	0	479						
669-	CONM2	2133	133	0	332						
670-	CONM2	2134	134	0	44 223						
671-	CONM2	2135	135	0	70 332						
672-	CONM2	2136	136	0	44 223						
673-	CONM2	2137	137	0	44 223						
674-	CONM2	2138	138	0	332						
675-	CONM2	2139	139	0	44 223						
676-	CROD	601	5	1	43						
677-	CROD	602	5	42	2						
678-	CROD	603	5	2	44						
679-	CROD	604	5	43	3						
680-	CROD	605	5	39	81						
681-	CROD	606	5	80	40						
682-	CROD	607	5	40	82						
683-	CROD	608	5	81	41						
684-	CROD	609	5	4	46						
685-	CROD	610	5	45	5						
686-	CROD	611	5	5	47						
687-	CROD	612	5	46	6						
688-	CROD	613	5	6	48						
689-	CROD	614	5	47	7						
690-	CROD	615	5	7	49						
691-	CROD	616	5	48	8						
692-	CROD	617	5	9	51						
693-	CROD	618	5	50	10						
694-	CROD	619	5	10	52						
695-	CROD	620	5	51	11						
696-	CROD	621	5	11	53						
697-	CROD	622	5	52	12						
698-	CROD	623	5	12	54						
699-	CROD	624	5	53	13						
700-	CROD	625	5	14	56						

CARD COUNT	1	2	3	4	5	6	7	8	9	10
701-	CROD	626	5	55	15					
702-	CROD	627	5	15	57					
703-	CROD	628	5	56	16					
704-	CROD	629	5	16	58					
705-	CROD	630	5	57	17					
706-	CROD	631	5	17	59					
707-	CROD	632	5	58	18					
708-	CROD	633	5	19	61					
709-	CROD	634	5	60	20					
710-	CROD	635	5	20	62					
711-	CROD	636	5	61	21					
712-	CROD	637	5	21	63					
713-	CROD	638	5	62	22					
714-	CROD	639	5	22	64					
715-	CROD	640	5	63	23					
716-	CROD	641	5	24	66					
717-	CROD	642	5	65	25					
718-	CROD	643	5	25	67					
719-	CROD	644	5	66	26					
720-	CROD	645	5	26	68					
721-	CROD	646	5	67	27					
722-	CROD	647	5	27	69					
723-	CROD	648	5	68	28					
724-	CROD	649	5	29	71					
725-	CROD	650	5	70	30					
726-	CROD	651	5	30	72					
727-	CROD	652	5	71	31					
728-	CROD	653	5	31	73					
729-	CROD	654	5	72	32					
730-	CROD	655	5	32	74					
731-	CROD	656	5	73	33					
732-	CROD	657	5	34	76					
733-	CROD	658	5	75	35					
734-	CROD	659	5	35	77					
735-	CROD	660	5	76	36					
736-	CROD	661	5	36	78					
737-	CROD	662	5	77	37					
738-	CROD	663	5	37	79					
739-	CROD	664	5	78	38					
740-	CROD	665	5	1	46					
741-	CROD	666	5	42	5					
742-	CROD	667	5	2	47					
743-	CROD	668	5	43	6					
744-	CROD	669	5	3	48					
745-	CROD	670	5	44	7					
746-	CROD	671	5	35	80					
747-	CROD	672	5	76	39					
748-	CROD	673	5	36	81					
749-	CROD	674	5	77	40					
750-	CROD	675	5	37	82					

SORTED BULK DATA ECHO

CARD COUNT		1	2		3	4	5	6	7	8	9	10
751-	CROD	676	5		78	41						
752-	CROD	677	5		4	50						
753-	CROD	678	5		45	9						
754-	CROD	679	5		9	55						
755-	CROD	680	5		50	14						
756-	CROD	681	5		14	60						
757-	CROD	682	5		55	19						
758-	CROD	683	5		19	65						
759-	CROD	684	5		60	24						
760-	CROD	685	5		24	70						
761-	CROD	686	5		65	29						
762-	CROD	687	5		29	75						
763-	CROD	688	5		70	34						
764-	CROD	689	5		5	51						
765-	CROD	690	5		46	10						
766-	CROD	691	5		10	56						
767-	CROD	692	5		51	15						
768-	CROD	693	5		15	61						
769-	CROD	694	5		56	20						
770-	CROD	695	5		20	66						
771-	CROD	696	5		61	25						
772-	CROD	697	5		25	71						
773-	CROD	698	5		66	30						
774-	CROD	699	5		30	76						
775-	CROD	700	5		71	35						
776-	CROD	701	5		6	52						
777-	CROD	702	5		47	11						
778-	CROD	703	5		11	57						
779-	CROD	704	5		52	16						
780-	CROD	705	5		16	62						
781-	CROD	706	5		57	21						
782-	CROD	707	5		21	67						
783-	CROD	708	5		62	26						
784-	CROD	709	5		26	72						
785-	CROD	710	5		67	31						
786-	CROD	711	5		31	77						
787-	CROD	712	5		72	36						
788-	CROD	713	5		7	53						
789-	CROD	714	5		48	12						
790-	CROD	715	5		12	58						
791-	CROD	716	5		53	17						
792-	CROD	717	5		17	63						
793-	CROD	718	5		58	22						
794-	CROD	719	5		22	68						
795-	CROD	720	5		63	27						
796-	CROD	721	5		27	73						
797-	CROD	722	5		68	32						
798-	CROD	723	5		32	78						
799-	CROD	724	5		73	37						
800-	CROD	725	5		8	54						

CARD COUNT		1	2	.	3	4	5	6	7	.	8	.	9	10
801-	CROD	726	5		49	13								
802-	CROD	727	5		13	59								
803-	CROD	728	5		54	18								
804-	CROD	729	5		18	64								
805-	CROD	730	5		59	23								
806-	CROD	731	5		23	69								
807-	CROD	732	5		64	28								
808-	CROD	733	5		28	74								
809-	CROD	734	5		69	33								
810-	CROD	735	5		33	79								
811-	CROD	736	5		74	38								
812-	CROD	737	5		14	89								
813-	CROD	738	5		83	86								
814-	CROD	739	5		19	90								
815-	CROD	740	5		84	87								
816-	CROD	741	5		24	91								
817-	CROD	742	5		85	88								
818-	CROD	743	5		89	92								
819-	CROD	744	5		86	95								
820-	CROD	745	5		90	93								
821-	CROD	746	5		87	96								
822-	CROD	747	5		91	94								
823-	CROD	748	5		88	97								
824-	CROD	749	5		95	98								
825-	CROD	750	5		92	101								
826-	CROD	751	5		96	99								
827-	CROD	752	5		93	102								
828-	CROD	753	5		97	100								
829-	CROD	754	5		94	103								
830-	CROD	755	5		101	104								
831-	CROD	756	5		98	107								
832-	CROD	757	5		102	105								
833-	CROD	758	5		99	108								
834-	CROD	759	5		103	106								
835-	CROD	760	5		100	109								
836-	CROD	761	5		107	110								
837-	CROD	762	5		104	113								
838-	CROD	763	5		108	111								
839-	CROD	764	5		105	114								
840-	CROD	765	5		109	112								
841-	CROD	766	5		106	115								
842-	CROD	767	5		113	116								
843-	CROD	768	5		110	119								
844-	CROD	769	5		114	117								
845-	CROD	770	5		111	120								
846-	CROD	771	5		115	118								
847-	CROD	772	5		112	121								
848-	CROD	773	5		119	122								
849-	CROD	774	5		116	125								
850-	CROD	775	5		120	123								

SORTED BULK DATA ECHO

	. 1	2	3 .	4 .	5 ..	6 ..	7 ..	8 ..	9	10
851-	CROD	776	5	117	126					
852-	CROD	777	5	121	124					
853-	CROD	778	5	118	127					
854-	CROD	779	5	125	128					
855-	CROD	780	5	122	131					
856-	CROD	781	5	126	129					
857-	CROD	782	5	123	132					
858-	CROD	783	5	127	130					
859-	CROD	784	5	124	133					
860-	CROD	785	5	83	19					
861-	CROD	786	5	14	84					
862-	CROD	787	5	19	85					
863-	CROD	788	5	84	24					
864-	CROD	789	5	86	90					
865-	CROD	790	5	89	87					
866-	CROD	791	5	87	91					
867-	CROD	792	5	90	88					
868-	CROD	793	5	92	96					
869-	CROD	794	5	95	93					
870-	CROD	795	5	93	97					
871-	CROD	796	5	96	94					
872-	CROD	797	5	98	102					
873-	CROD	798	5	101	99					
874-	CROD	799	5	99	103					
875-	CROD	800	5	102	100					
876-	CROD	801	5	104	108					
877-	CROD	802	5	107	105					
878-	CROD	803	5	105	109					
879-	CROD	804	5	108	106					
880-	CROD	805	5	110	114					
881-	CROD	806	5	113	111					
882-	CROD	807	5	111	115					
883-	CROD	808	5	114	112					
884-	CROD	809	5	116	120					
885-	CROD	810	5	119	117					
886-	CROD	811	5	117	121					
887-	CROD	812	5	120	118					
888-	CROD	813	5	122	126					
889-	CROD	814	5	125	123					
890-	CROD	815	5	123	127					
891-	CROD	816	5	126	124					
892-	CROD	817	5	128	132					
893-	CROD	818	5	131	129					
894-	CROD	819	5	129	133					
895-	CROD	820	5	132	130					
896-	CROD	821	5	55	84					
897-	CROD	822	5	83	60					
898-	CROD	823	5	60	85					
899-	CROD	824	5	84	65					
900-	CROD	825	5	131	134					

CARD COUNT	1	. 2	3	4	5	6	7	. 8	.. 9	10
901-	CROD	826	5	128	137					
902-	CROD	827	5	132	135					
903-	CROD	828	5	129	138					
904-	CROD	829	5	133	136					
905-	CROD	830	5	130	139					
906-	CROD	831	5	134	138					
907-	CROD	832	5	137	135					
908-	CROD	833	5	135	139					
909-	CROD	834	5	138	136					
910-	CROD	1001	6	1	6					
911-	CROD	1002	6	2	5					
912-	CROD	1003	6	3	6					
913-	CROD	1004	6	2	7					
914-	CROD	1005	6	35	40					
915-	CROD	1006	6	36	39					
916-	CROD	1007	6	37	40					
917-	CROD	1008	6	36	41					
918-	CROD	1009	6	4	10					
919-	CROD	1010	6	5	9					
920-	CROD	1011	6	9	15					
921-	CROD	1012	6	10	14					
922-	CROD	1013	6	14	20					
923-	CROD	1014	6	15	19					
924-	CROD	1015	6	19	25					
925-	CROD	1016	6	20	24					
926-	CROD	1017	6	24	30					
927-	CROD	1018	6	25	29					
928-	CROD	1019	6	29	35					
929-	CROD	1020	6	30	34					
930-	CROD	1021	6	5	11					
931-	CROD	1022	6	6	10					
932-	CROD	1023	6	10	16					
933-	CROD	1024	6	11	15					
934-	CROD	1025	6	15	21					
935-	CROD	1026	6	16	20					
936-	CROD	1027	6	20	26					
937-	CROD	1028	6	21	25					
938-	CROD	1029	6	25	31					
939-	CROD	1030	6	26	30					
940-	CROD	1031	6	30	36					
941-	CROD	1032	6	31	35					
942-	CROD	1033	6	6	12					
943-	CROD	1034	6	7	11					
944-	CROD	1035	6	11	17					
945-	CROD	1036	6	12	16					
946-	CROD	1037	6	16	22					
947-	CROD	1038	6	17	21					
948-	CROD	1039	6	21	27					
949-	CROD	1040	6	22	26					
950-	CROD	1041	6	26	32					

CARD COUNT	. 1 .. 2	. 3 .. 4 .. 5 .. 6 . 7 .. 8 .. 9 .. 10 .

CARD COUNT					
951-	CROD	1042	6	27	31
952-	CROD	1043	6	31	37
953-	CROD	1044	6	32	36
954-	CROD	1045	6	7	13
955-	CROD	1046	6	8	12
956-	CROD	1047	6	12	18
957-	CROD	1048	6	13	17
958-	CROD	1049	6	17	23
959-	CROD	1050	6	18	22
960-	CROD	1051	6	22	28
961-	CROD	1052	6	23	27
962-	CROD	1053	6	27	33
963-	CROD	1054	6	28	32
964-	CROD	1055	6	32	38
965-	CROD	1056	6	33	37
966-	CROD	1057	6	42	47
967-	CROD	1058	6	43	46
968-	CROD	1059	6	44	47
969-	CROD	1060	6	43	48
970-	CROD	1061	6	76	81
971-	CROD	1062	6	77	80
972-	CROD	1063	6	78	81
973-	CROD	1064	6	77	82
974-	CROD	1065	6	45	51
975-	CROD	1066	6	46	50
976-	CROD	1067	6	50	56
977-	CROD	1068	6	51	55
978-	CROD	1069	6	55	61
979-	CROD	1070	6	56	60
980-	CROD	1071	6	60	66
981-	CROD	1072	6	61	65
982-	CROD	1073	6	65	71
983-	CROD	1074	6	66	70
984-	CROD	1075	6	70	76
985-	CROD	1076	6	71	75
986-	CROD	1077	6	46	52
987-	CROD	1078	6	47	51
988-	CROD	1079	6	51	57
989-	CROD	1080	6	52	56
990-	CROD	1081	6	56	62
991-	CROD	1082	6	57	61
992-	CROD	1083	6	61	67
993-	CROD	1084	6	62	66
994-	CROD	1085	6	66	72
995-	CROD	1086	6	67	71
996-	CROD	1087	6	71	77
997-	CROD	1088	6	72	76
998-	CROD	1089	6	47	53
999-	CROD	1090	6	48	52
1000-	CROD	1091	6	52	58

CARD COUNT	. 1	2	. 3	.. 4	. 5	6	. 7 .	8 ..	9 .. 10
1001-	CROD	1092	6	53	57				
1002-	CROD	1093	6	57	63				
1003-	CROD	1094	6	58	62				
1004-	CROD	1095	6	62	68				
1005-	CROD	1096	6	63	67				
1006-	CROD	1097	6	67	73				
1007-	CROD	1098	6	68	72				
1008-	CROD	1099	6	72	78				
1009-	CROD	1100	6	73	77				
1010-	CROD	1101	6	48	54				
1011-	CROD	1102	6	49	53				
1012-	CROD	1103	6	53	59				
1013-	CROD	1104	6	54	58				
1014-	CROD	1105	6	58	64				
1015-	CROD	1106	6	59	63				
1016-	CROD	1107	6	63	69				
1017-	CROD	1108	6	64	68				
1018-	CROD	1109	6	68	74				
1019-	CROD	1110	6	69	73				
1020-	CROD	1111	6	73	79				
1021-	CROD	1112	6	74	78				
1022-	CROD	1113	6	14	87				
1023-	CROD	1114	6	19	86				
1024-	CROD	1115	6	87	24				
1025-	CROD	1116	6	19	88				
1026-	CROD	1117	6	83	90				
1027-	CROD	1118	6	89	84				
1028-	CROD	1119	6	84	91				
1029-	CROD	1120	6	90	85				
1030-	CROD	1121	6	86	93				
1031-	CROD	1122	6	92	87				
1032-	CROD	1123	6	87	94				
1033-	CROD	1124	6	93	88				
1034-	CROD	1125	6	89	96				
1035-	CROD	1126	6	95	90				
1036-	CROD	1127	6	90	97				
1037-	CROD	1128	6	96	91				
1038-	CROD	1129	6	92	99				
1039-	CROD	1130	6	98	93				
1040-	CROD	1131	6	93	100				
1041-	CROD	1132	6	99	94				
1042-	CROD	1133	6	95	102				
1043-	CROD	1134	6	101	96				
1044-	CROD	1135	6	96	103				
1045-	CROD	1136	6	102	97				
1046-	CROD	1137	6	98	105				
1047-	CROD	1138	6	104	99				
1048-	CROD	1139	6	99	106				
1049-	CROD	1140	6	105	100				
1050-	CROD	1141	6	101	108				

SORTED BULK DATA ECHO

CARD COUNT	1	2	3	4	. 5 .	6 ..	7 ..	8 ..	9 .. 10 .
1051-	CROD	1142	6	107	102				
1052-	CROD	1143	6	102	109				
1053-	CROD	1144	6	108	103				
1054-	CROD	1145	6	104	111				
1055-	CROD	1146	6	110	105				
1056-	CROD	1147	6	105	112				
1057-	CROD	1148	6	111	106				
1058-	CROD	1149	6	107	114				
1059-	CROD	1150	6	113	108				
1060-	CROD	1151	6	108	115				
1061-	CROD	1152	6	114	109				
1062-	CROD	1153	6	110	117				
1063-	CROD	1154	6	116	111				
1064-	CROD	1155	6	111	118				
1065-	CROD	1156	6	117	112				
1066-	CROD	1157	6	113	120				
1067-	CROD	1158	6	119	114				
1068-	CROD	1159	6	114	121				
1069-	CROD	1160	6	120	115				
1070-	CROD	1161	6	116	123				
1071-	CROD	1162	6	122	117				
1072-	CROD	1163	6	117	124				
1073-	CROD	1164	6	123	118				
1074-	CROD	1165	6	119	126				
1075-	CROD	1166	6	125	120				
1076-	CROD	1167	6	120	127				
1077-	CROD	1168	6	126	121				
1078-	CROD	1169	6	122	129				
1079-	CROD	1170	6	128	123				
1080-	CROD	1171	6	123	130				
1081-	CROD	1172	6	129	124				
1082-	CROD	1173	6	125	132				
1083-	CROD	1174	6	131	126				
1084-	CROD	1175	6	126	133				
1085-	CROD	1176	6	132	127				
1086-	CROD	1177	6	128	135				
1087-	CROD	1178	6	134	129				
1088-	CROD	1179	6	129	136				
1089-	CROD	1180	6	135	130				
1090-	CROD	1181	6	131	138				
1091-	CROD	1182	6	137	132				
1092-	CROD	1183	6	132	139				
1093-	CROD	1184	6	138	133				
1094-	GRAV	30	0	.098066	0	0.			
1095-	GRID	1	0	15 161	-60.000	7.197			
1096-	GRID	2	0	30.250	-60.000	8.670			
1097-	GRID	3	0	45.214	-60 000	11.100			
1098-	GRID	4	0	0.000	-45 214	3.353			
1099-	GRID	5	0	15 161	-45 214	3.845			
1100-	GRID	6	0	30 250	-45 214	5 317			

CARD COUNT	1	2	3	4	5	. 6	. 7	8	9	10
1101-	GRID	7	0	45 214	-45 214	7.747				
1102-	GRID	8	0	60.000	-45 214	11 128				
1103-	GRID	9	0	0 000	-30 250	919				
1104-	GRID	10	0	15 161	-30 250	1 411				
1105-	GRID	11	0	30 250	-30 250	2 884				
1106-	GRID	12	0	45 214	-30.250	5 313				
1107-	GRID	13	0	60.000	-30 250	8 694				
1108-	GRID	14	0	0 000	-15 161	-1 053				
1109-	GRID	15	0	15 161	-15 161	- 561				
1110-	GRID	16	0	30 250	-15 161	912				
1111-	GRID	17	0	45 214	-15 161	3 341				
1112-	GRID	18	0	60 000	-15 161	6.722				
1113-	GRID	19	0	0.000	0 000	-1 053				
1114-	GRID	20	0	15.161	0 000	- 561				
1115-	GRID	21	0	30 250	0 000	912				
1116-	GRID	22	0	45 214	0 000	3 341				
1117-	GRID	23	0	60 000	0 000	6 722				
1118-	GRID	24	0	0 000	15.461	-1.053				
1119-	GRID	25	0	15 161	15 161	- 561				
1120-	GRID	26	0	30 250	15 161	912				
1121-	GRID	27	0	45 214	15 161	3 341				
1122-	GRID	28	0	60 000	15 161	6 722				
1123-	GRID	29	0	0 000	30 250	919				
1124-	GRID	30	0	15 161	30 250	1 411				
1125-	GRID	31	0	30 250	30 250	2 884				
1126-	GRID	32	0	45 214	30 250	5 313				
1127-	GRID	33	0	60 000	30 250	8 694				
1128-	GRID	34	0	0.000	45.214	3 353				
1129-	GRID	35	0	15.161	45 214	3 845				
1130-	GRID	36	0	30.250	45 214	5.317				
1131-	GRID	37	0	45 214	45.214	7 747				
1132-	GRID	38	0	60 000	45 214	11.128				
1133-	GRID	39	0	15 161	60 000	7.197				
1134-	GRID	40	0	30 250	60 000	8 670				
1135-	GRID	41	0	45 214	60.000	11 100				
1136-	GRID	42	0	15 161	-60 000	-7.833				
1137-	GRID	43	0	30 250	-60 000	-6 353				
1138-	GRID	44	0	45.214	-60 000	-3 915				
1139-	GRID	45	0	0 000	-45 214	-11 685				
1140-	GRID	46	0	15 161	-45 214	-11 186				
1141-	GRID	47	0	30 250	-45 214	-9 705				
1142-	GRID	48	0	45 214	-45 214	-7.268				
1143-	GRID	49	0	60 000	-45 214	-3 911				
1144-	GRID	50	0	0 000	-30 250	-14 119				
1145-	GRID	51	0	15 161	-30 250	-13 620				
1146-	GRID	52	0	30 250	-30 250	-12.139				
1147-	GRID	53	0	45 214	-30 250	-9 701				
1148-	GRID	54	0	60 000	-30 250	-6 345				
1149-	GRID	55	0	0.000	-15 161	-16 091				
1150-	GRID	56	0	15 161	-15 161	-15.592				

SORTED BULK DATA ECHO

	1	.	2	3	4	5	.	6	.	7	.	8	.	9	10	.

CARD COUNT								
1151-	GRID	57	O		30 250	-15 161	-14.111	
1152-	GRID	58	O		45 214	-15 161	-11.673	
1153-	GRID	59	O		60 000	-15 161	-8 317	
1154-	GRID	60	O		0 000	0 000	-16 091	
1155-	GRID	61	O		15 161	0 000	-15.592	
1156-	GRID	62	O		30.250	0 000	-14.111	
1157-	GRID	63	O		45 214	0 000	-11 673	
1158-	GRID	64	O		60.000	0 000	-8.317	
1159-	GRID	65	O		0.000	15 161	-16 091	
1160-	GRID	66	O		15.161	15 161	-15 592	
1161-	GRID	67	O		30.250	15 161	-14 111	
1162-	GRID	68	O		45.214	15 161	-11.673	
1163-	GRID	69	O		60.000	15 161	-8.317	
1164-	GRID	70	O		0 000	30 250	-14.119	
1165-	GRID	71	O		15.161	30 250	-13 620	
1166-	GRID	72	O		30.250	30 250	-12 139	
1167-	GRID	73	O		45.214	30 250	-9.701	
1168-	GRID	74	O		60.000	30 250	-6.345	
1169-	GRID	75	O		0.000	45 214	-11.685	
1170-	GRID	76	O		15.161	45 214	-11.186	
1171-	GRID	77	O		30 250	45 214	-9.705	
1172-	GRID	78	O		45.214	45.214	-7 268	
1173-	GRID	79	O		60.000	45 214	-3.911	
1174-	GRID	80	O		15 161	60.000	-7 833	
1175-	GRID	81	O		30.250	60 000	-6.353	
1176-	GRID	82	O		45 214	60.000	-3.915	
1177-	GRID	83	O		-15.04	-15 16	-1 20	
1178-	GRID	84	O		-15.04	0.00	-1.20	
1179-	GRID	85	O		-15.04	15 16	-1 20	
1180-	GRID	86	O		- 14	-15.16	13 54	
1181-	GRID	87	O		- 14	0 00	13.54	
1182-	GRID	88	O		-.14	15 16	13.54	
1183-	GRID	89	O		-15.18	-15.16	13.39	
1184-	GRID	90	O		-15 18	0 00	13 39	
1185-	GRID	91	O		-15 18	15 16	13.39	
1186-	GRID	92	O		- 29	-15 16	28.13	
1187-	GRID	93	O		- 29	0 00	28 13	
1188-	GRID	94	O		- 29	15 16	28.13	
1189-	GRID	95	O		-15 32	-15.16	27.98	
1190-	GRID	96	O		-15 32	0 00	27.99	
1191-	GRID	97	O		-15.32	15 16	27.99	
1192-	GRID	98	O		-.43	-15 16	42 72	
1193-	GRID	99	O		- 43	0 00	42 72	
1194-	GRID	100	O		- 43	15 16	42 72	
1195-	GRID	101	O		-15 46	-15 16	42 58	
1196-	GRID	102	O		-15 46	0 00	42 58	
1197-	GRID	103	O		-15.46	15.16	42 58	
1198-	GRID	104	O		- 57	-15 16	57 32	
1199-	GRID	105	O		- 57	0 00	57 32	
1200-	GRID	106	O		-.57	15 16	57 32	

CARD COUNT	. 1	. 2	3	4	. 5	6	.. 7	8	. 9	. 10
1201-	GRID	107	O	-15.61	-15 16	57 17			
1202-	GRID	108	O	-15.61	O OO	57.17			
1203-	GRID	109	O	-15.61	15 16	57 17			
1204-	GRID	110	O	- 71	-15 16	71 91			
1205-	GRID	111	O	- 71	O OO	71 91			
1206-	GRID	112	O	- 71	15 16	71 91			
1207-	GRID	113	O	-15 75	-15 16	71 76			
1208-	GRID	114	O	-15 75	O OO	71.76			
1209-	GRID	115	O	-15.75	15 16	71.76			
1210-	GRID	116	O	- 86	-15 16	86.50			
1211-	GRID	117	O	- 86	O OO	86.50			
1212-	GRID	118	O	- 86	15 16	86.50			
1213-	GRID	119	O	-15.89	-15 16	86.35			
1214-	GRID	120	O	-15.89	0.00	86 36			
1215-	GRID	121	O	-15.89	15 16	86 36			
1216-	GRID	122	O	-1.00	-15 16	101 09			
1217-	GRID	123	O	-1 00	O OO	101 09			
1218-	GRID	124	O	-1.00	15.16	101.09			
1219-	GRID	125	O	-16.03	-15.16	100.94			
1220-	GRID	126	O	-16 03	O OO	100.95			
1221-	GRID	127	O	-16 03	15 16	100.95			
1222-	GRID	128	O	-1.14	-15.16	115 68			
1223-	GRID	129	O	-1 14	O OO	115.68			
1224-	GRID	130	O	-1 14	15 16	115 68			
1225-	GRID	131	O	-16.18	-15 16	115 54			
1226-	GRID	132	O	-16.18	O OO	115 54			
1227-	GRID	133	O	-16 18	15 16	115.54			
1228-	GRID	134	O	-1 16	-15 16	117.19			
1229-	GRID	135	O	-1 16	0.00	117 19			
1230-	GRID	136	O	-1.16	15 16	117.19			
1231-	GRID	137	O	-16 19	-15.16	117.04			
1232-	GRID	138	O	-16.19	0.00	117.04			
1233-	GRID	139	O	-16.19	15 16	117.04			
1234-	MAT1	1		1.66E11	1.31E10	193	1605 43	- 252E-6	22.22
1235-	MAT1	2		1.82E11	1.43E10	35	1716 15	-.522E-6	22.22
1236-	MAT1	11		2.34E11	O.	O.	1662 28	- 396E-6	22.22
1237-	MAT1	51		1.879E11	1.055E10	154	1605.43	-.335E-6	22.22
1238-	MAT1	53		1.866E11	1.15E10	198	1716 15	- 378E-6	22.22
1239-	MAT1	54		1 889E11	1.17E10	.225	1716.15	-.414E-6	22.22
1240-	MAT1	58		1.956E11	9.59E9	.136	1716.15	- 36E-6	22 22
1241-	PARAM	ASING	-1						
1242-	PARAM	COUPMASS	1						
1243-	PARAM	GRDPNT	O						
1244-	PARAM	NEWSEQ	3						
1245-	PARAM	SEQOUT	1						
1246-	PBAR	1	1	1 715E-4	1.471E-7	1.471E-7	2.941E-7	.03	
1247-	PBAR	2	2	3.806E-4	2 753E-7	2.753E-7	5.506E-7		
1248-	PBAR	20	2	7.000E-4	2 081E-6	2.081E-6	5.506E-7	9 333	
1249-	PBAR	21	1	7.000E-4	2 081E-6	2.081E-6	2.941E-7	11.492	
1250-	PBAR	22	2	7 000E-4	2 081E-6	2 081E-6	5 506E-7	7.333	

```
CARD
COUNT       .  1  .   2       3   .  4        5   .  6       7  ..  8    .  9  .  10
1251-    PBAR    25      2          7.000E-42 081E-62 081E-65 506E-728 431
1252-    PBAR    29      2          7.000E-42 081E-62.081E-65 506E-743.243
1253-    PBAR    51     51          3 271E-42 755E-72.755E-75 569-7
1254-    PBAR    53     53          1 353E-34 88E-7 1.12E-6 2 568E-8
1255-    PBAR    54     54          4 238E-42 23E-7 2.528E-73 E-10
1256-    PBAR    58     58          5.340E-42.06E-7 2 060E-73.08E-7
1257-    PROD     5     11          3.486E-50.      0.
1258-    PROD     6     11          5.230E-50       0
1259-    SPC     11     19          123456  O
1260-    TEMPRB   1    101          11.82    11 82
1261-    TEMPRB   1    102          11 36    11 36
1262-    TEMPRB   1    103          11 82    11 82
1263-    TEMPRB   1    104          11.36    11 36
1264-    TEMPRB   1    105          12 11    12 11
1265-    TEMPRB   1    106          11 82    11 82
1266-    TEMPRB   1    107          11 36    11 36
1267-    TEMPRB   1    108          10 21    10.21
1268-    TEMPRB   1    109          12.38    12 38
1269-    TEMPRB   1    110          12.19    12.19
1270-    TEMPRB   1    111          11.67    11.67
1271-    TEMPRB   1    112          10.69    10.69
1272-    TEMPRB   1    113          12 53    12 53
1273-    TEMPRB   1    114          12 43    12 43
1274-    TEMPRB   1    115          11 87    11 87
1275-    TEMPRB   1    116          10 95    10 95
1276-    TEMPRB   1    117          12.50    12 50
1277-    TEMPRB   1    118          12.45    12 45
1278-    TEMPRB   1    119          11.90    11 90
1279-    TEMPRB   1    120          10 90    10 90
1280-    TEMPRB   1    121          12 53    12 53
1281-    TEMPRB   1    122          12 43    12 43
1282-    TEMPRB   1    123          11 87    11 87
1283-    TEMPRB   1    124          10 95    10 95
1284-    TEMPRB   1    125          12 39    12 39
1285-    TEMPRB   1    126          12 19    12 19
1286-    TEMPRB   1    127          11·67    11 67
1287-    TEMPRB   1    128          10 70    10.70
1288-    TEMPRB   1    129          12 11    12 11
1289-    TEMPRB   1    130          11 82    11 82
1290-    TEMPRB   1    131          11.36    11 36
1291-    TEMPRB   1    132          10.21    10 21
1292-    TEMPRB   1    133          12 65    12 65
1293-    TEMPRB   1    134          12 65    12 65
1294-    TEMPRB   1    135          12 65    12 65
1295-    TEMPRB   1    136          12 65    12 65
1296-    TEMPRB   1    137          12.65    12 65
1297-    TEMPRB   1    138          12 65    12 65
1298-    TEMPRB   1    139          11 07    11 07
1299-    TEMPRB   1    140          11.07    11 07
1300-    TEMPRB   1    141          11.07    11 07
```
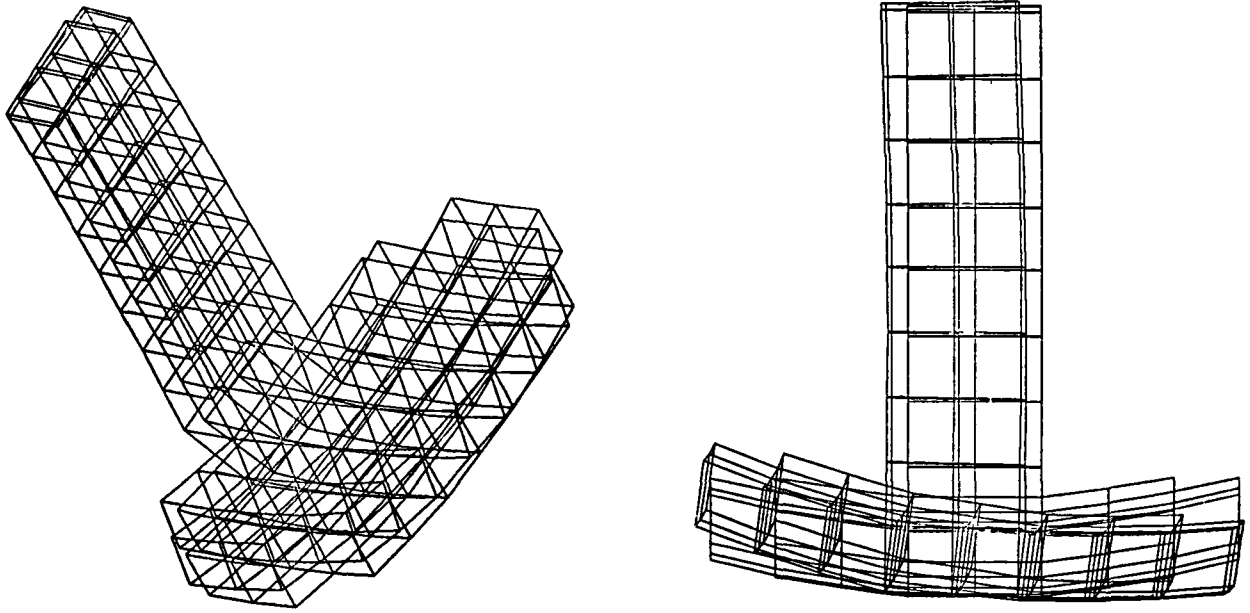
Figure C-1   Third Mode Shape with Slewing and Orbit Transfer (Freq of 0.765 Hz)
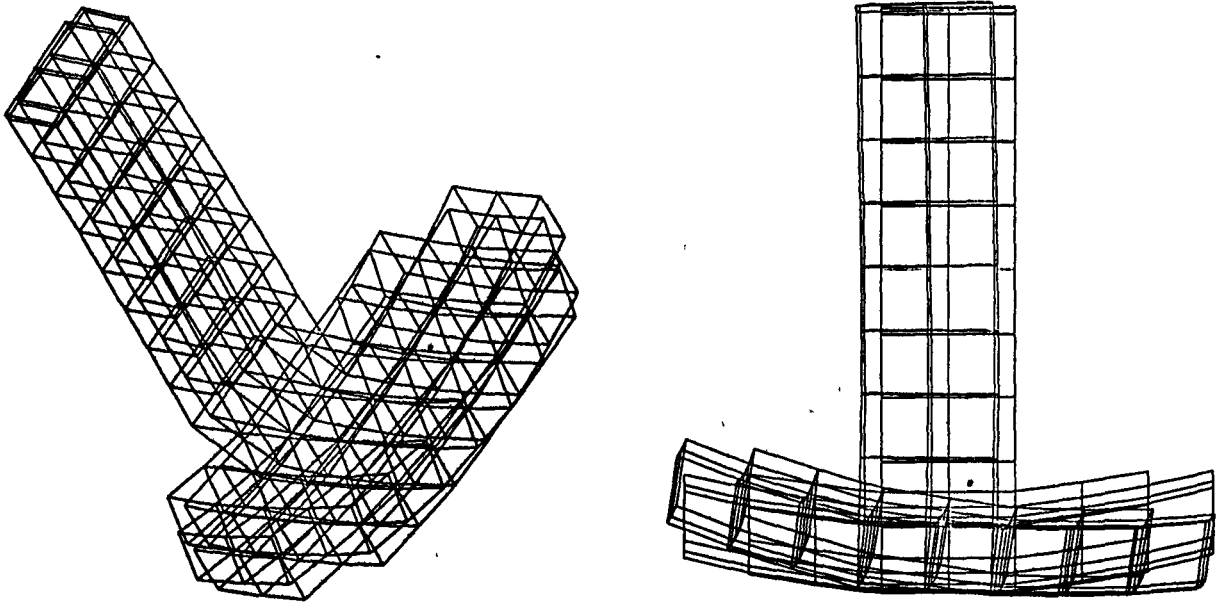
Figure C-2
Fourth Mode Shape with Slewing and Orbit Transfer (Freq of 0.781 Hz)
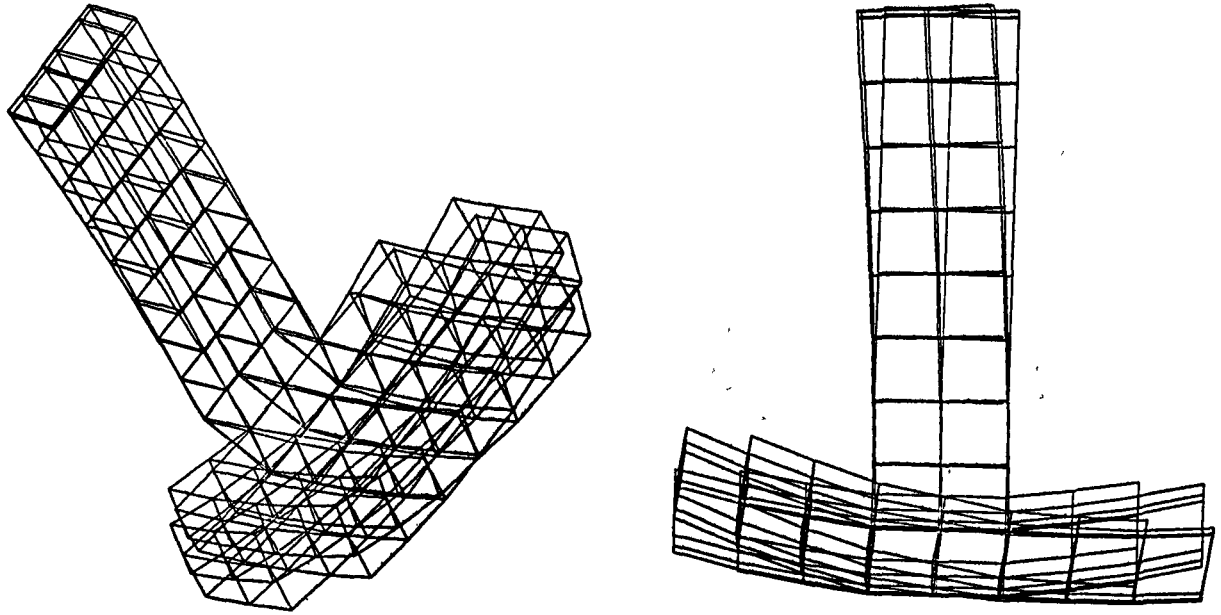
Figure C-3
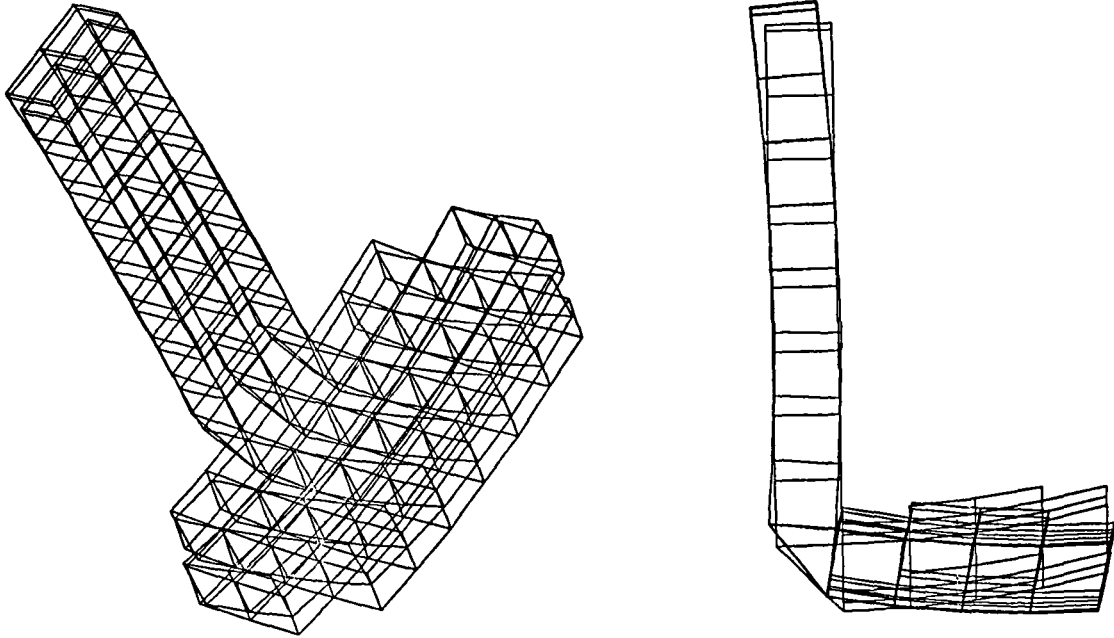*Fifth Mode Shape with Slewing and Orbit Transfer (Freq of 0.844 Hz)*
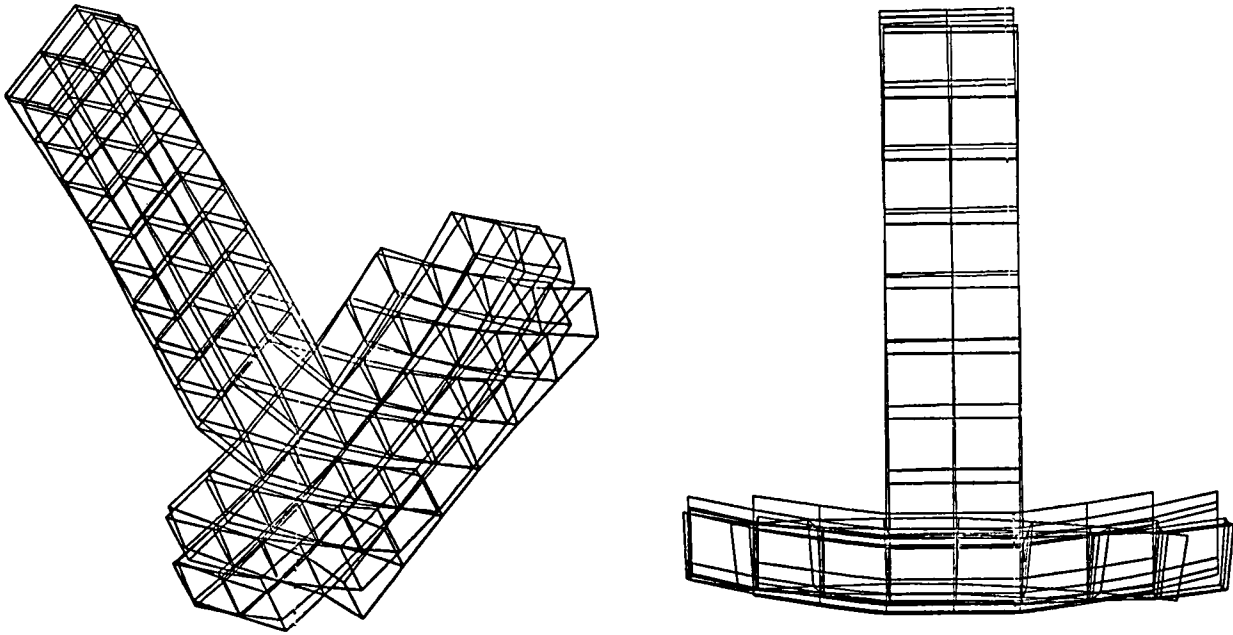
Figure C-4   Sixth Mode Shape with Slewing and Orbit Transfer (Freq of 0.871)
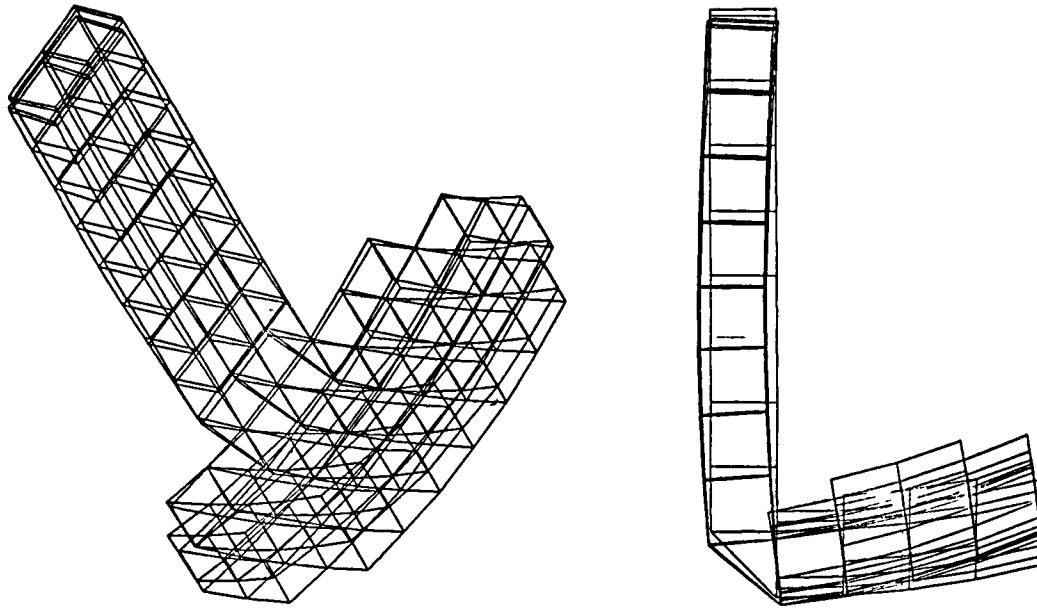
Figure C-5
Third Mode Shape without Slewing or Orbit Transfer (Freq of 1.137 Hz)
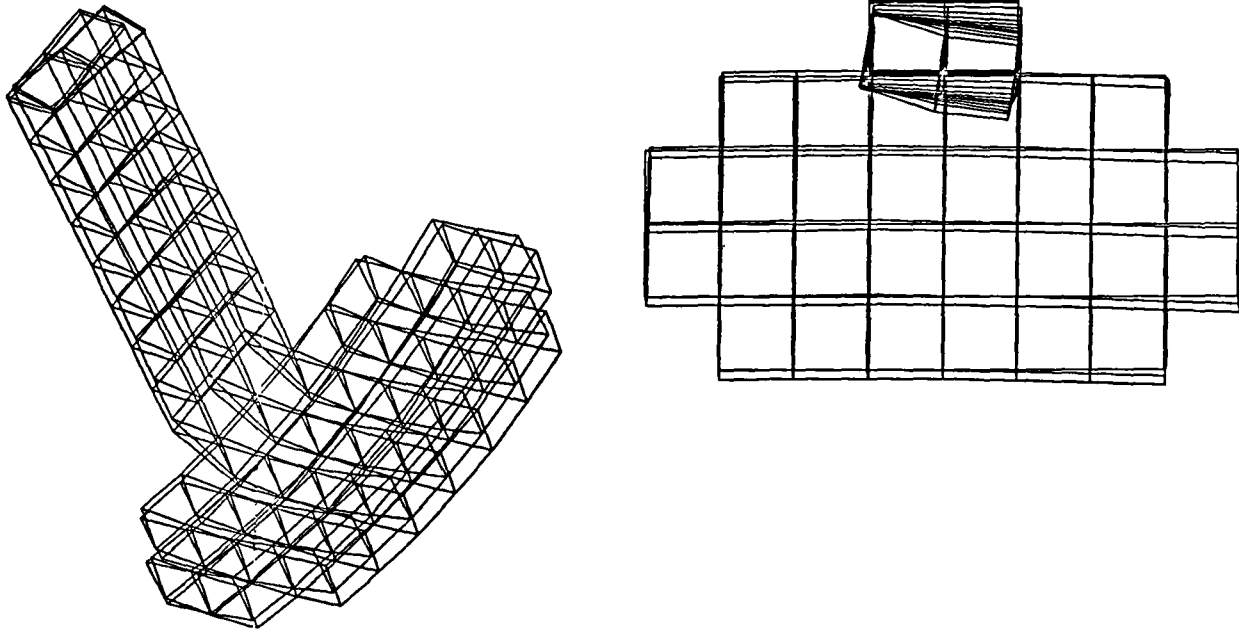
Figure C-6
Fourth Mode Subcase without Slewing or Orbit Transfer (Freq of 1.315 Hz)
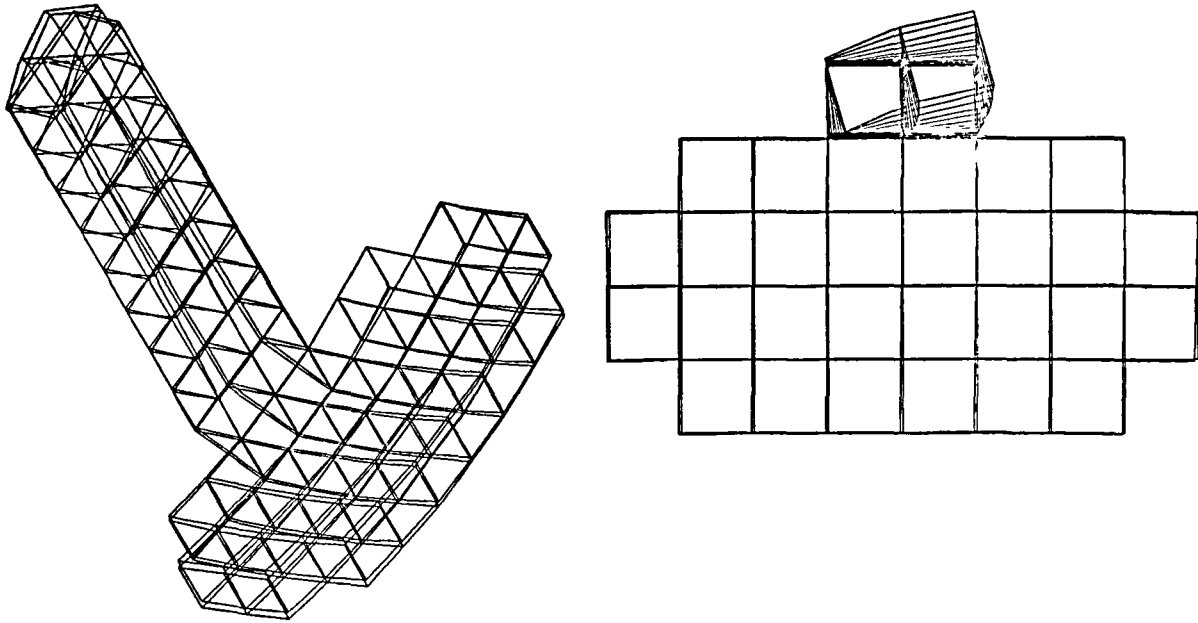
Figure C-7
Fifth Mode Subcase without Slewing or Orbit Transfer (Freq of 1.377 Hz)
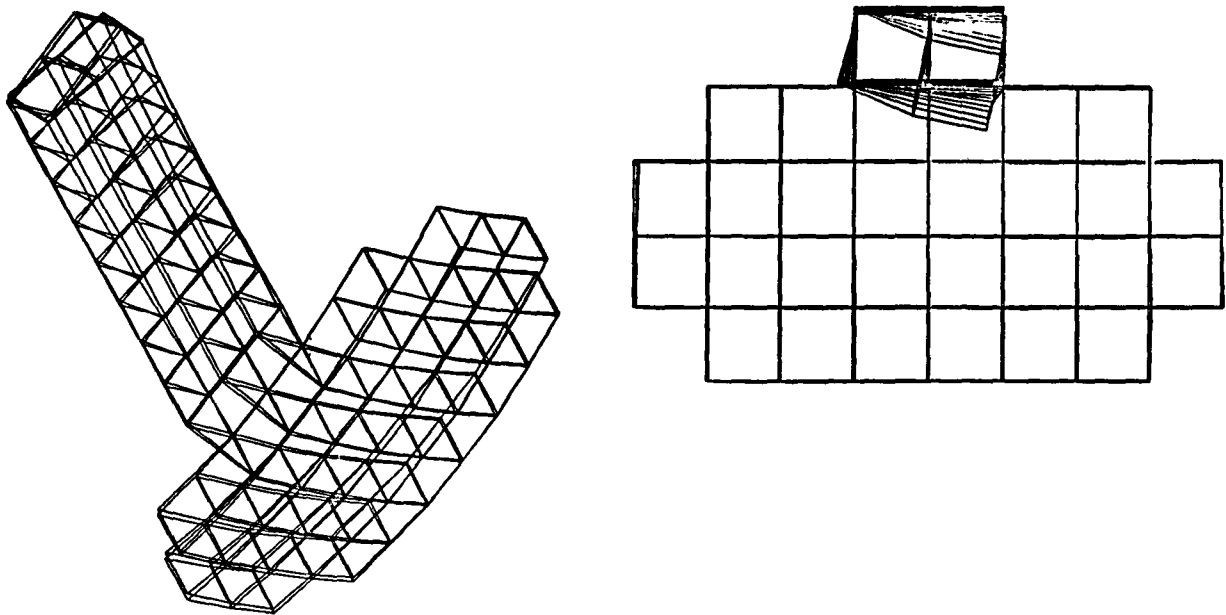
Figure C-8
Sixth Mode Subcase without Slewing or Orbit Transfer (Freq of 1.391 Hz)
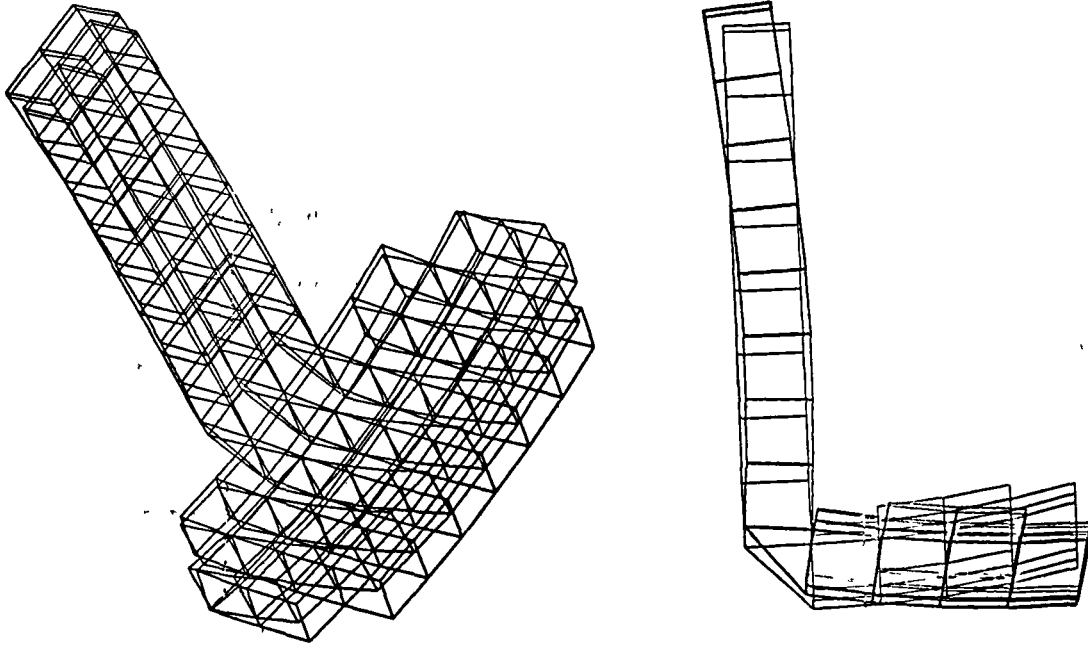
Figure C-9
Third Mode with Slewing and without Orbit Transfer (Freq of 0.969 Hz)
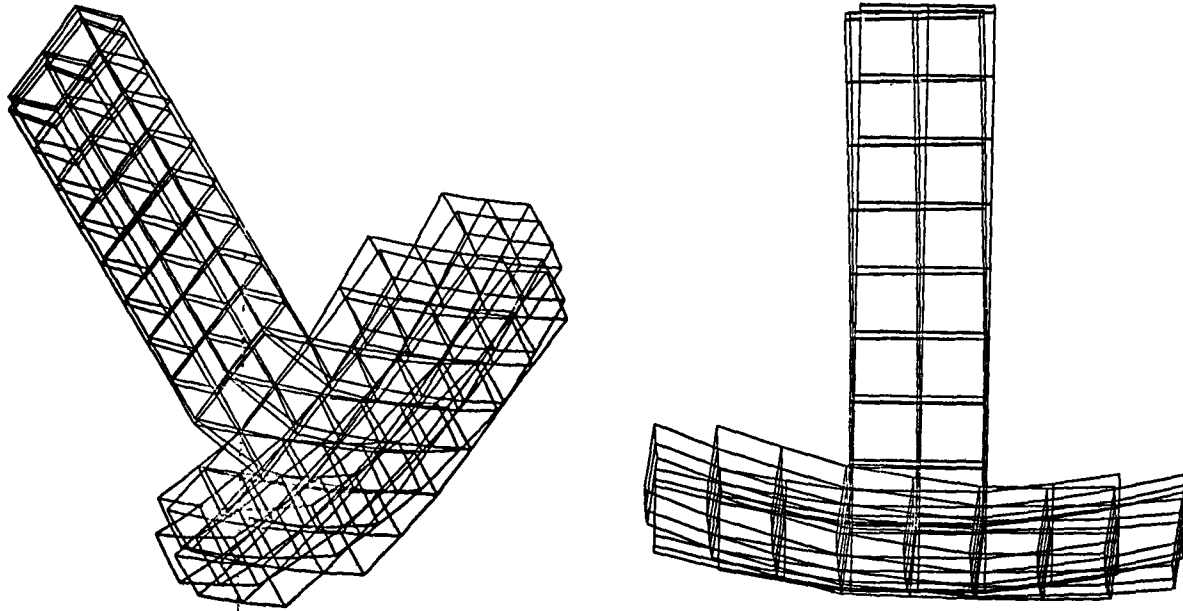
Figure C-10
Fourth Mode with Slewing and without Orbit Transfer (Freq of 0.972 Hz)
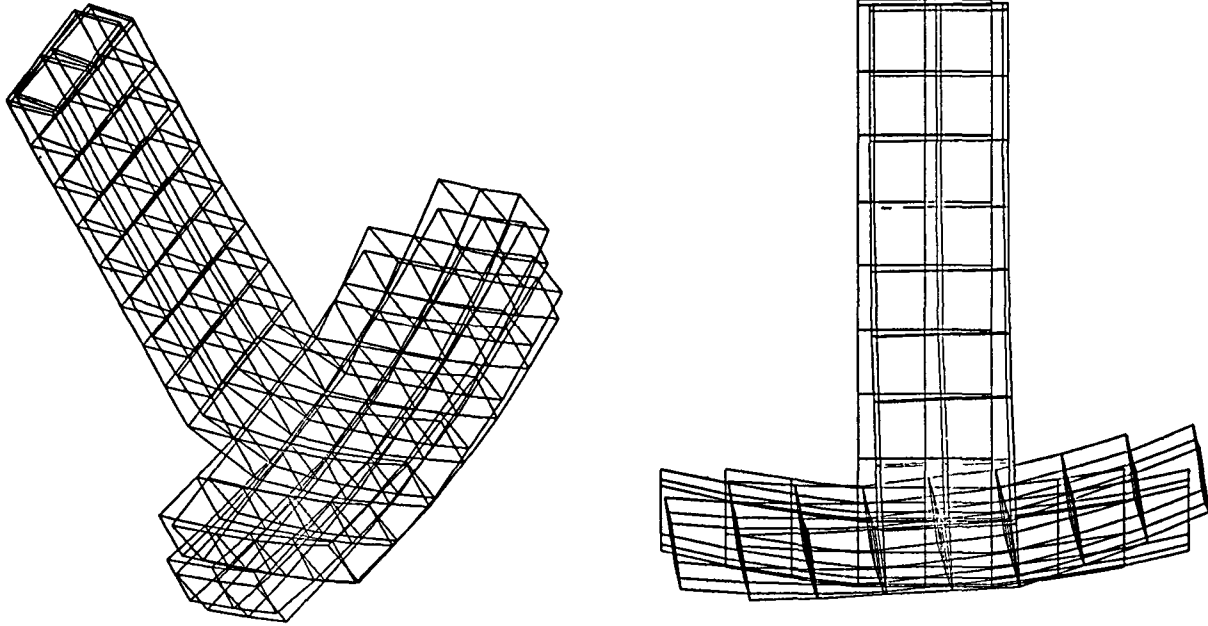
Figure C-11
Fifth Mode with Slewing and without Orbit Transfer (Freq of 0.990 Hz)

Figure C-12
Sixth Mode with Slewing and without Orbit Transfer (Freq of 0.998 Hz)

236
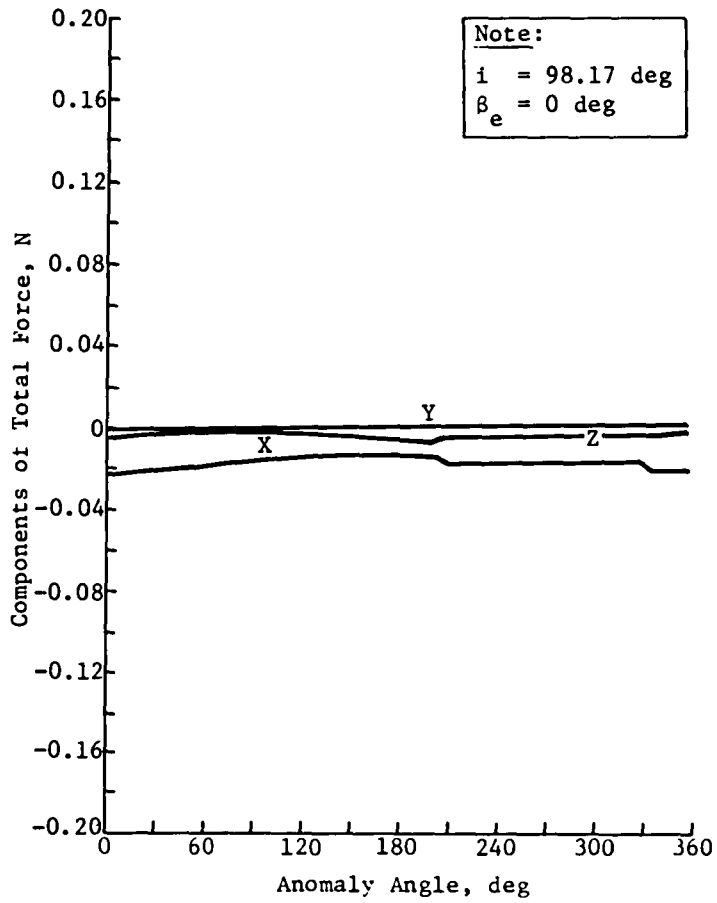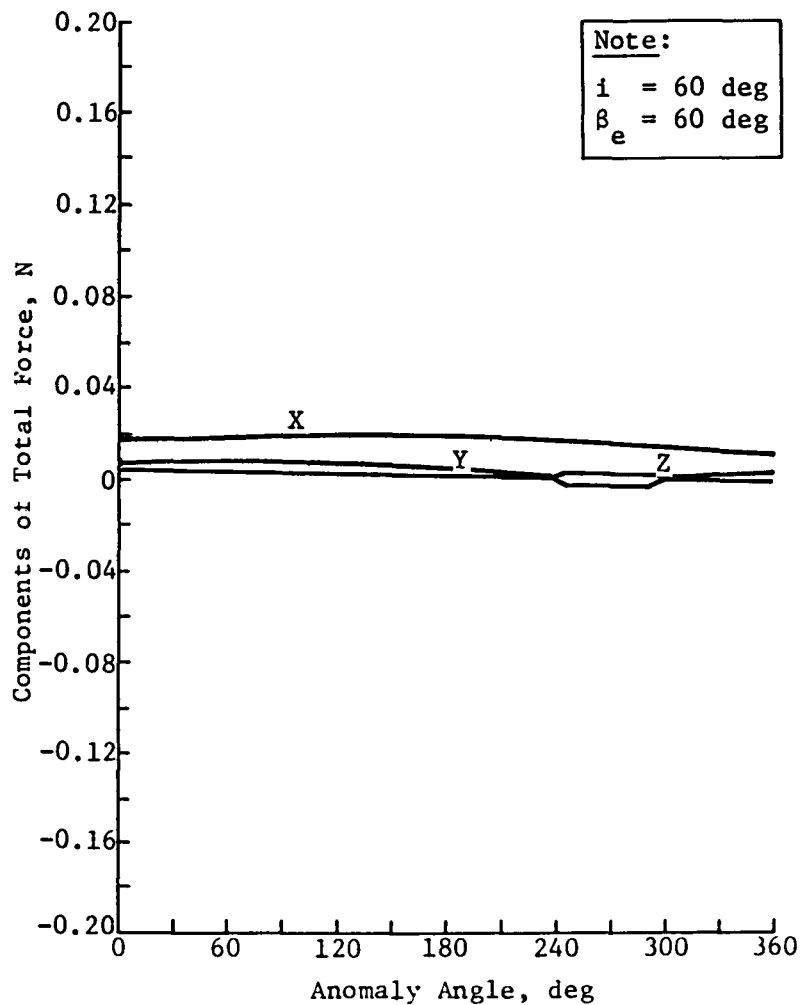
Figure D-1
Components of Total Force versus
Anomaly Angle - Mission 1
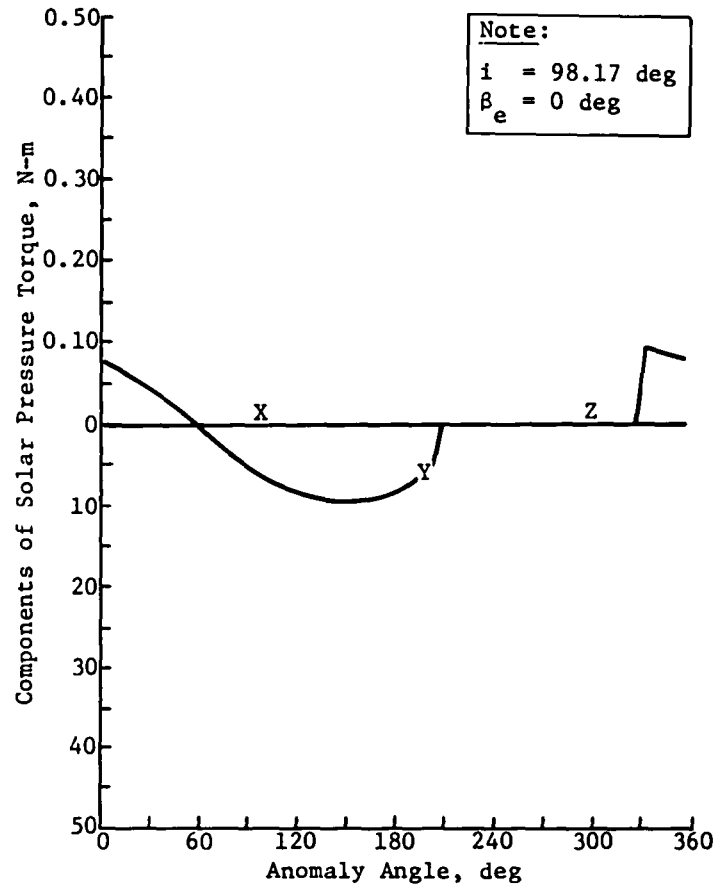
Figure D-2
Components of Solar Pressure Torque
versus Anomaly Angle - Mission 1
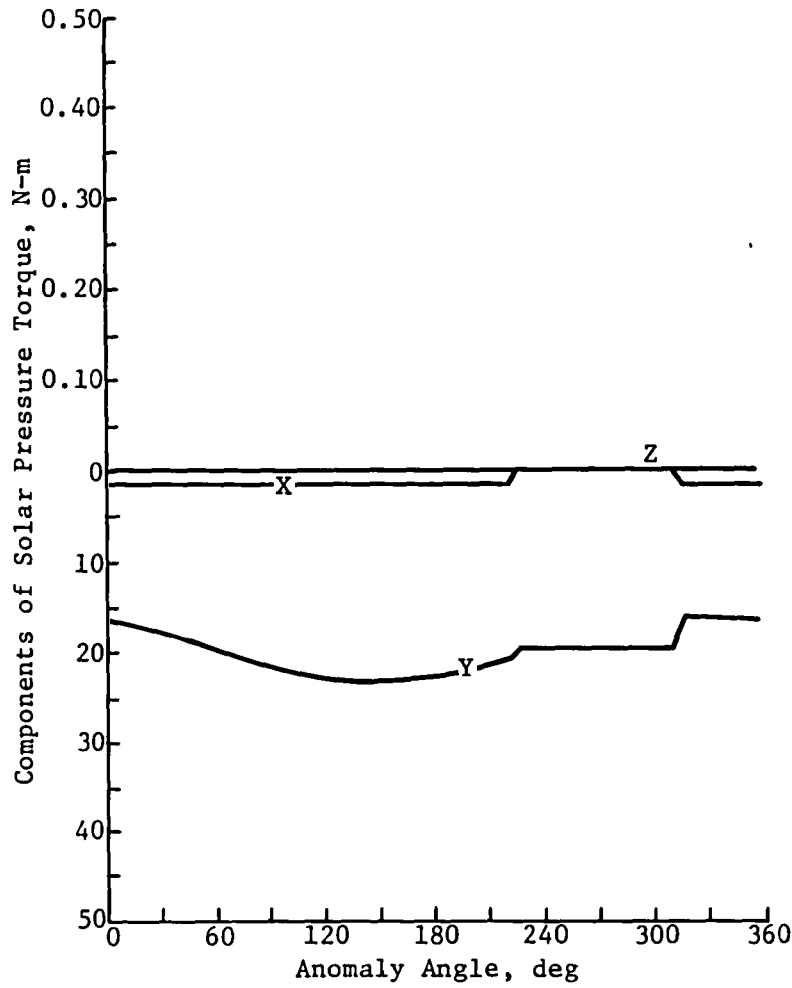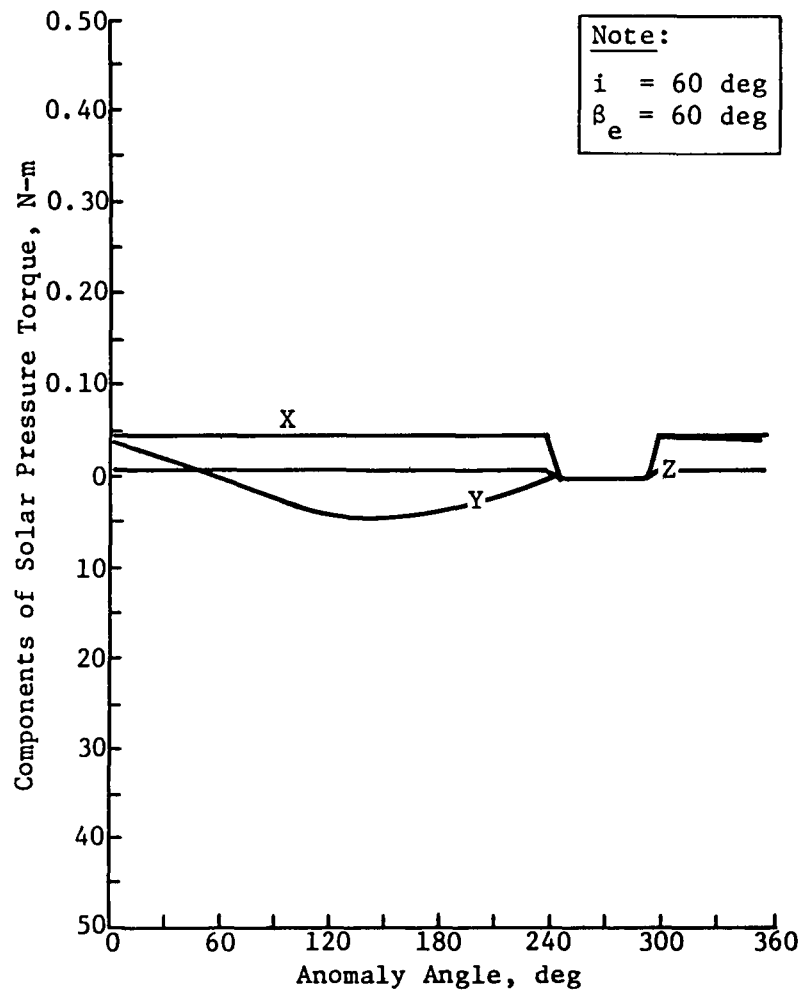
Figure D-3
Components of Solar Pressure Torque
versus Anomaly Angle - Mission 2
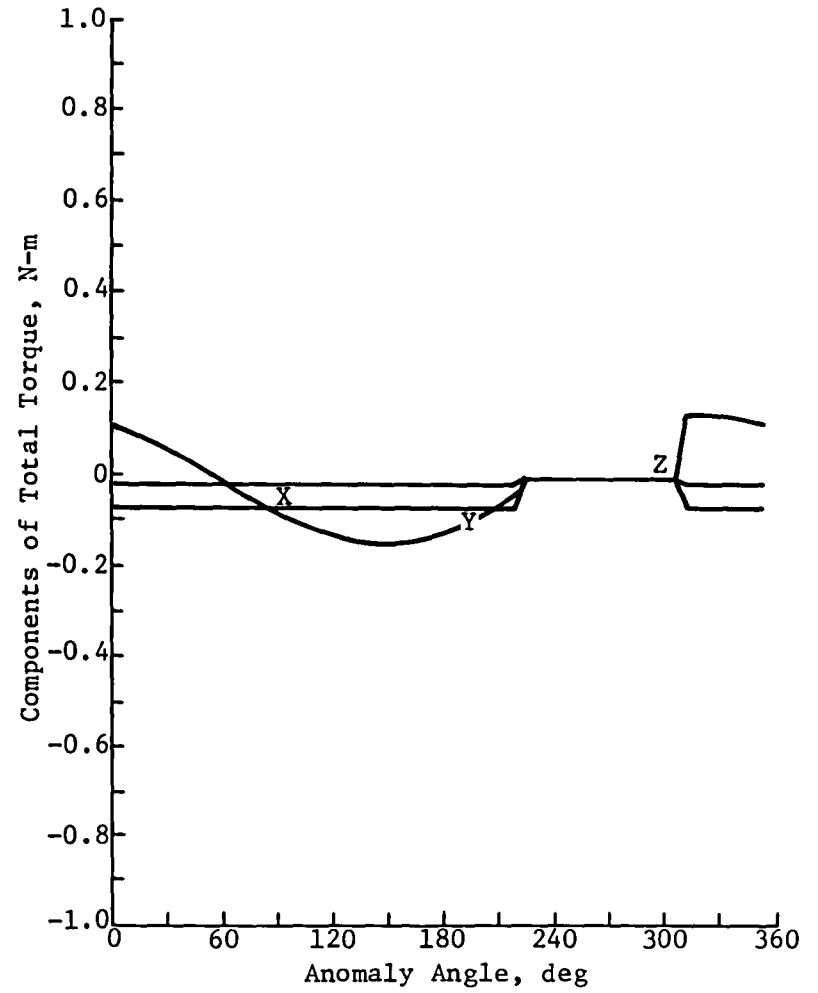
Figure D-4
Components of Total Torque versus
Anomaly Angle - Mission 2
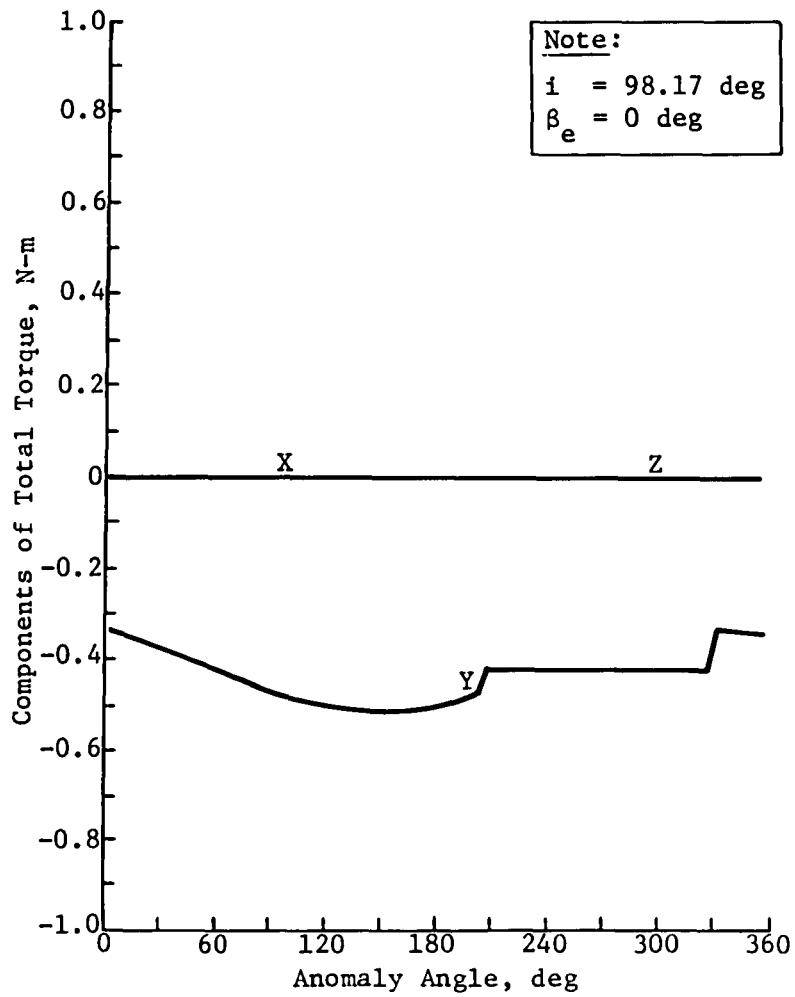
Figure D-5
Components of Total Torque versus
Anomaly Angle - Mission 1
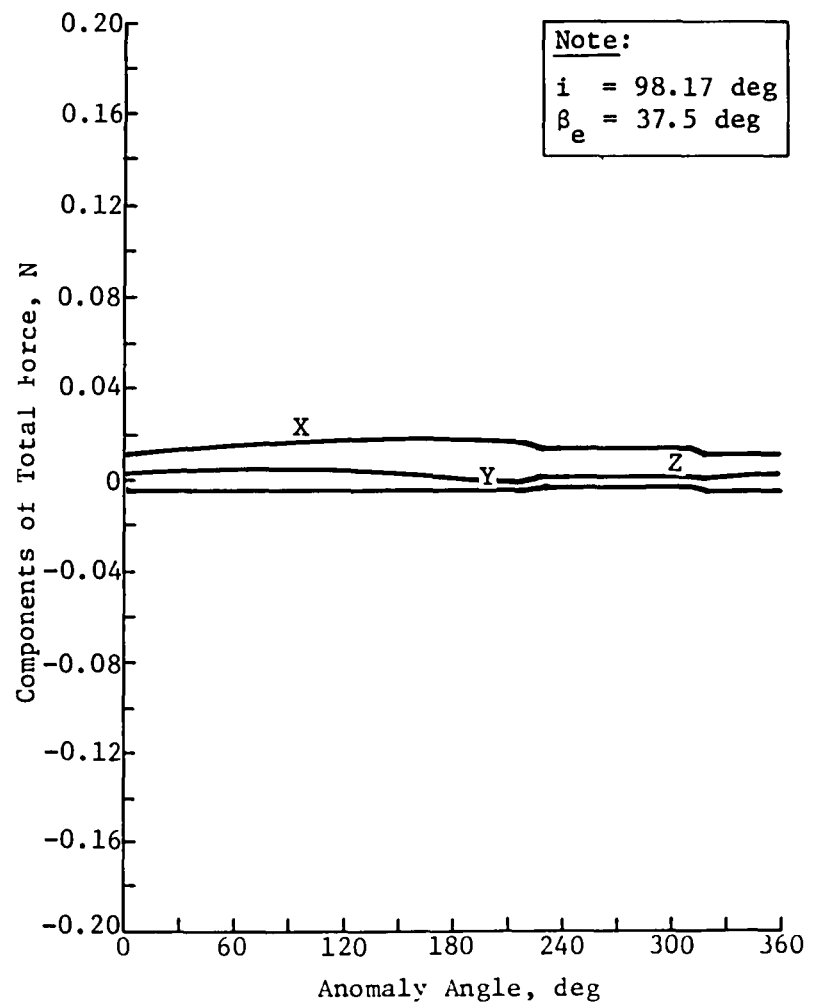
Figure D-6
Components of Total Force versus
Anomaly Angle - Mission 2
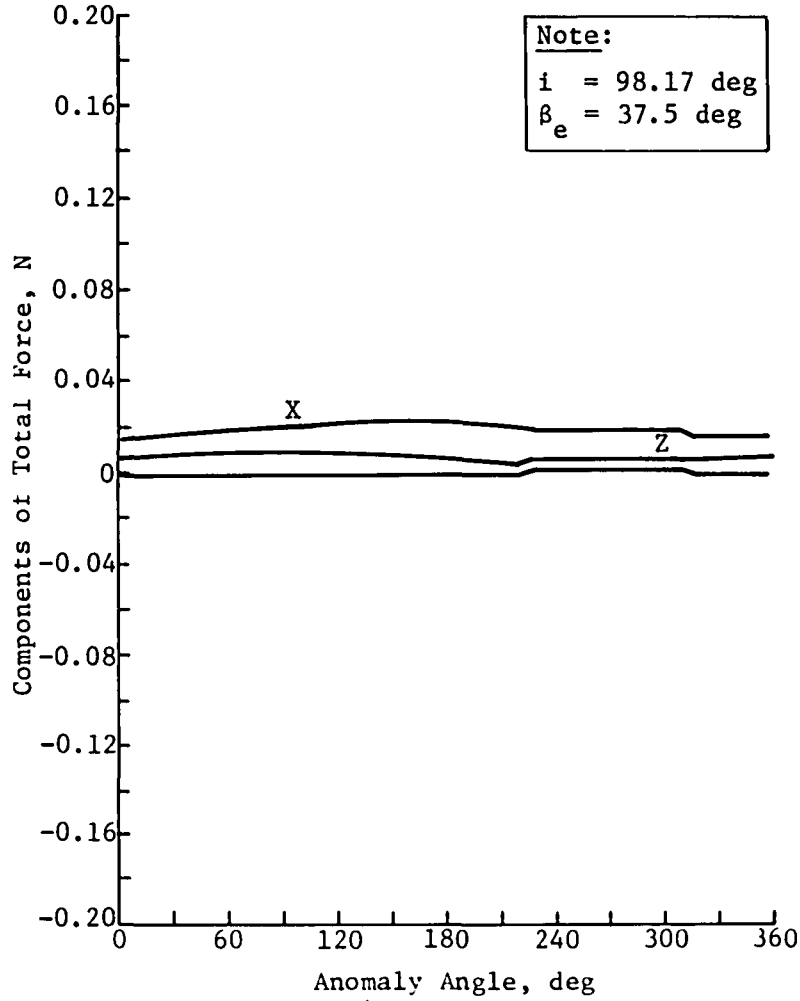
Figure D-7
Components of Total Force versus
Anomaly Angle - Mission 3
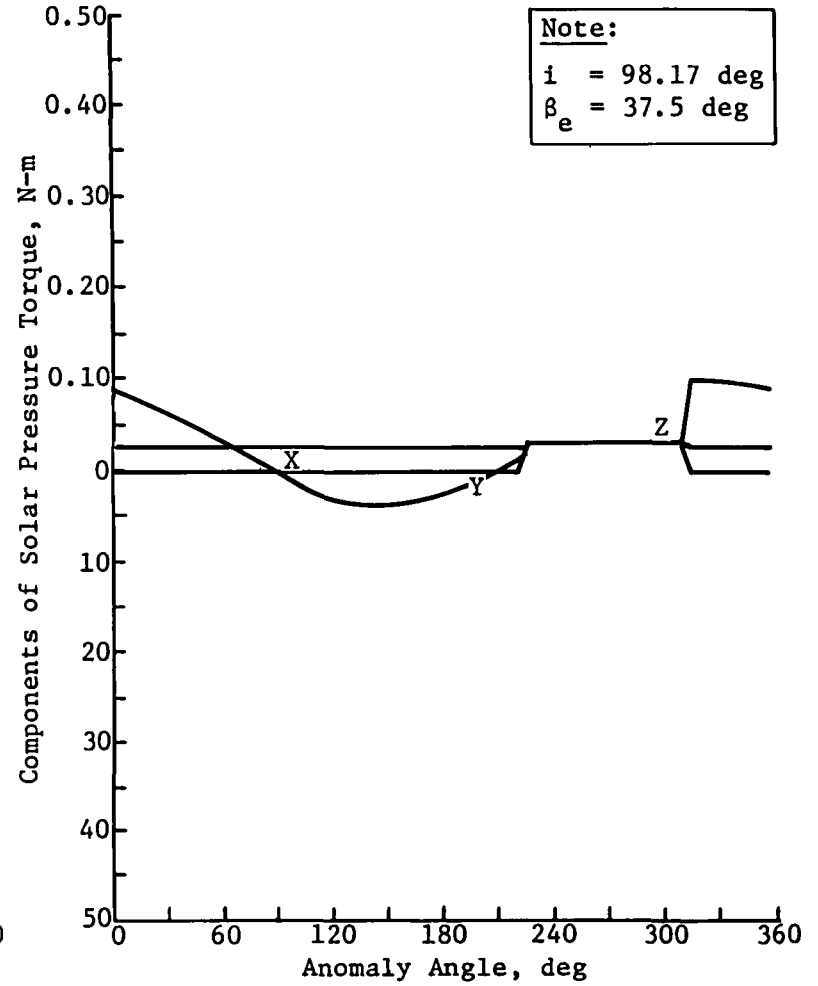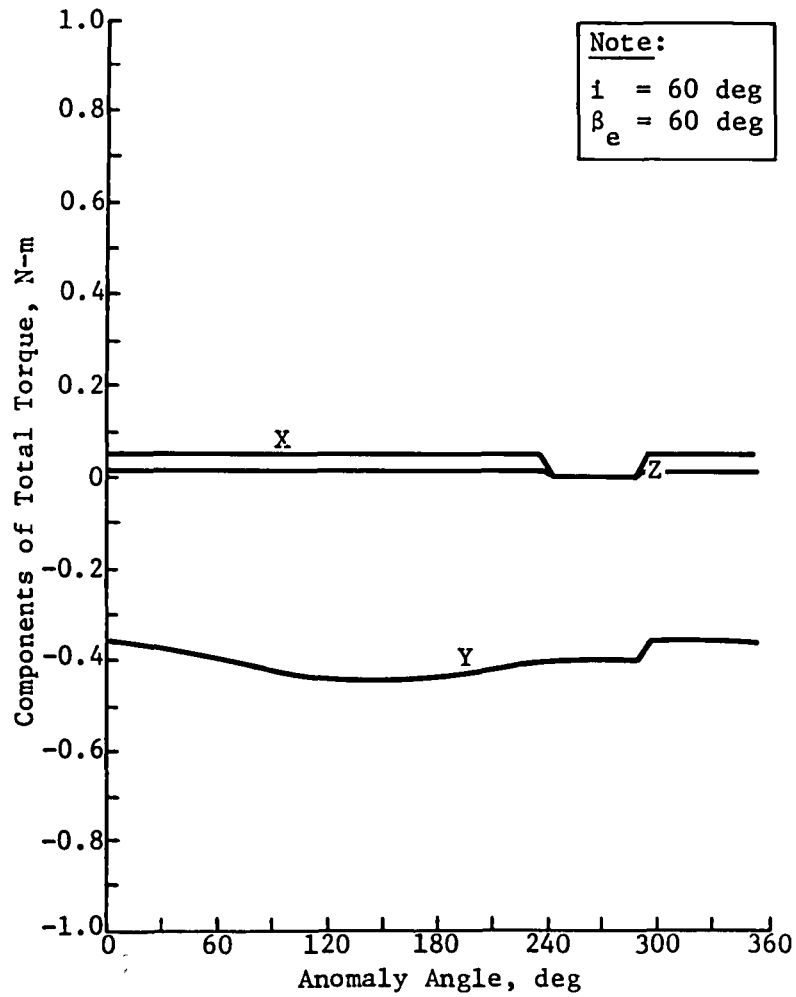

Figure D-8
Components of Solar Torque versus
Anomaly Angle - Mission 3
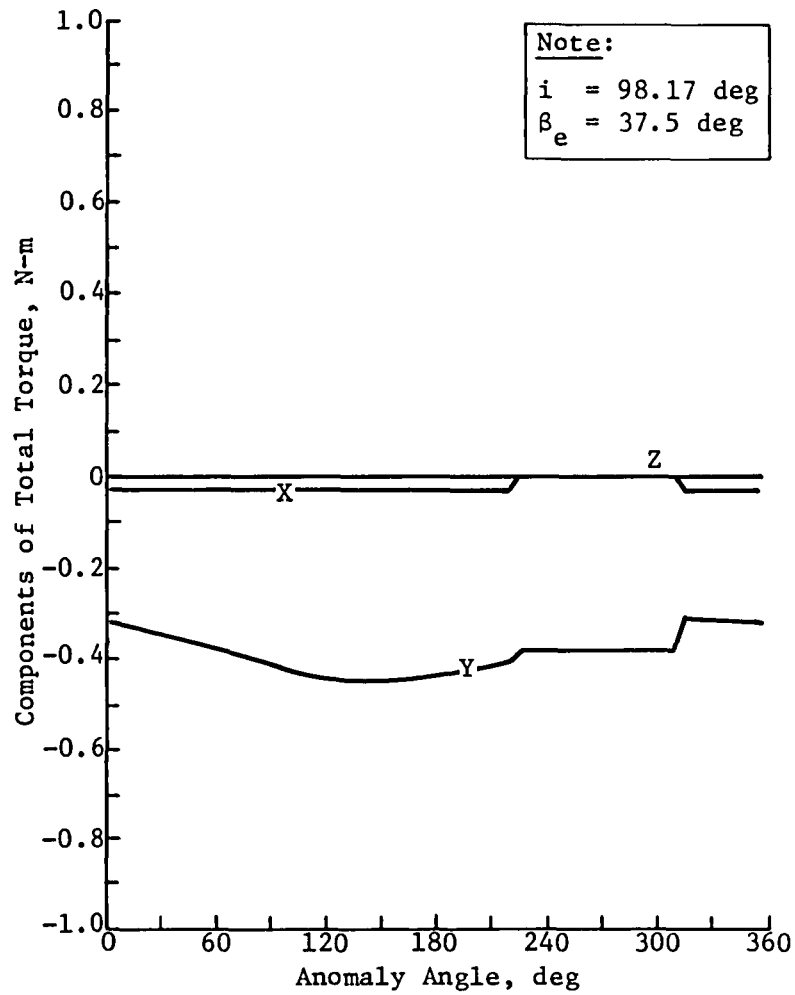
Figure D-9
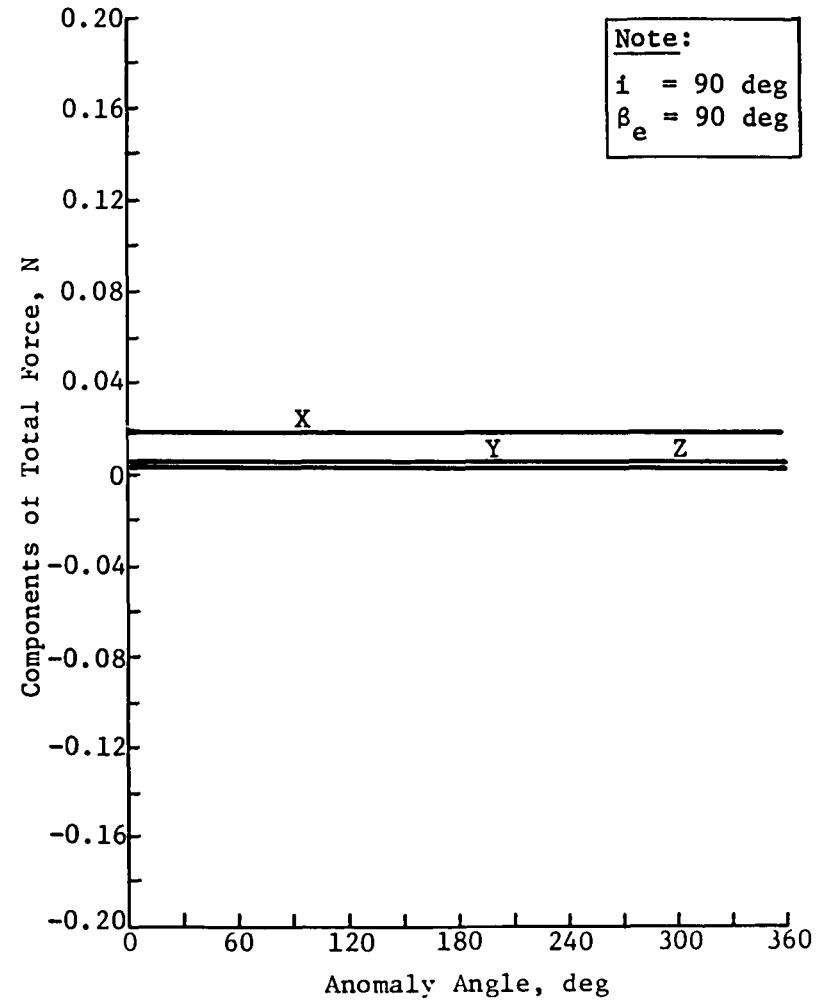Components of Total Torque versus
Anomaly Angle - Mission 3
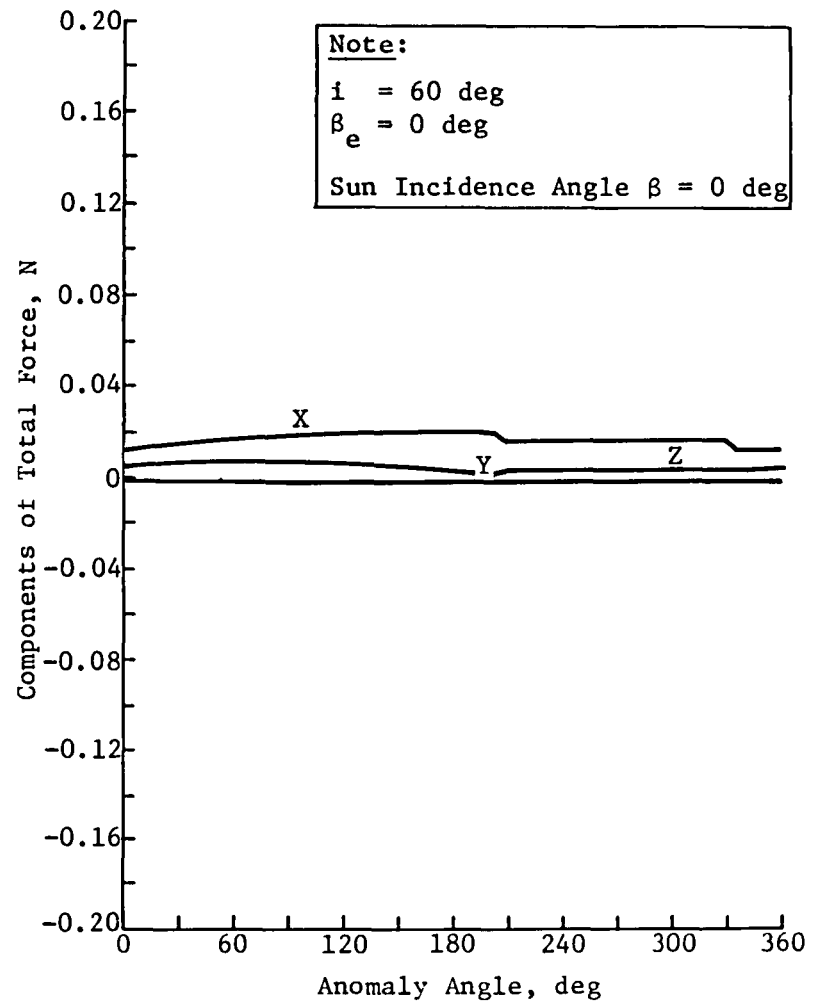
Figure D-10
Components of Total Force versus
Anomaly Angle - Mission 4
(β = 0 deg)
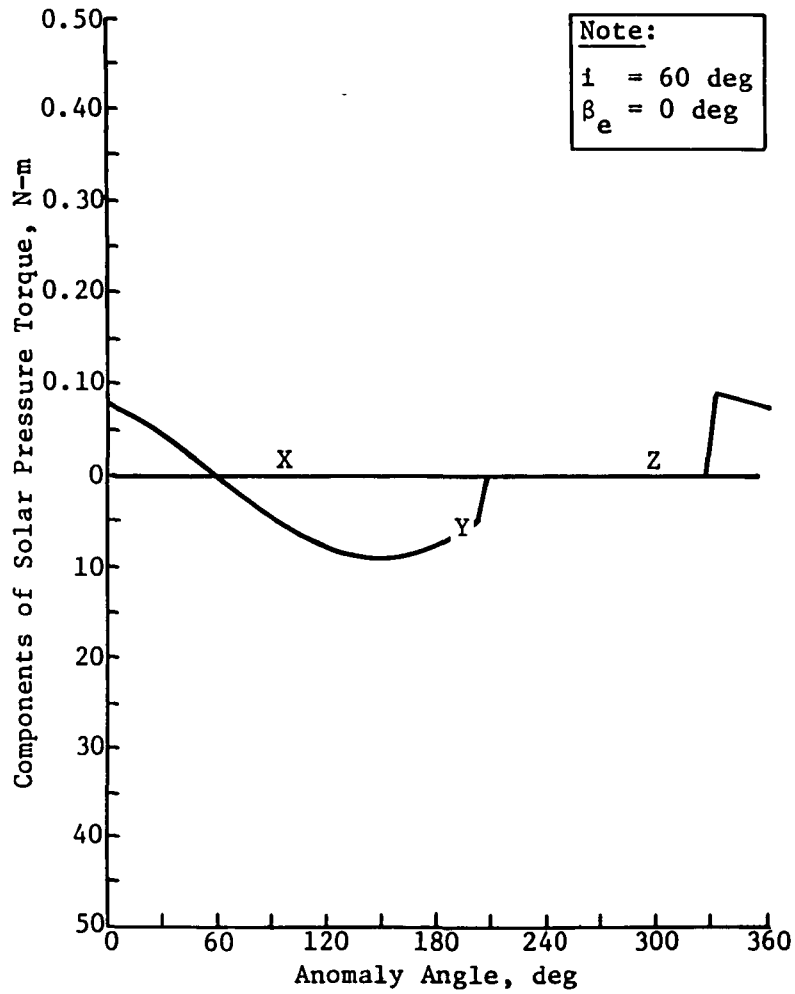
Figure D-11
Components of Solar Pressure Torque
versus Anomaly Angle - Mission 4
(β = 0 deg)
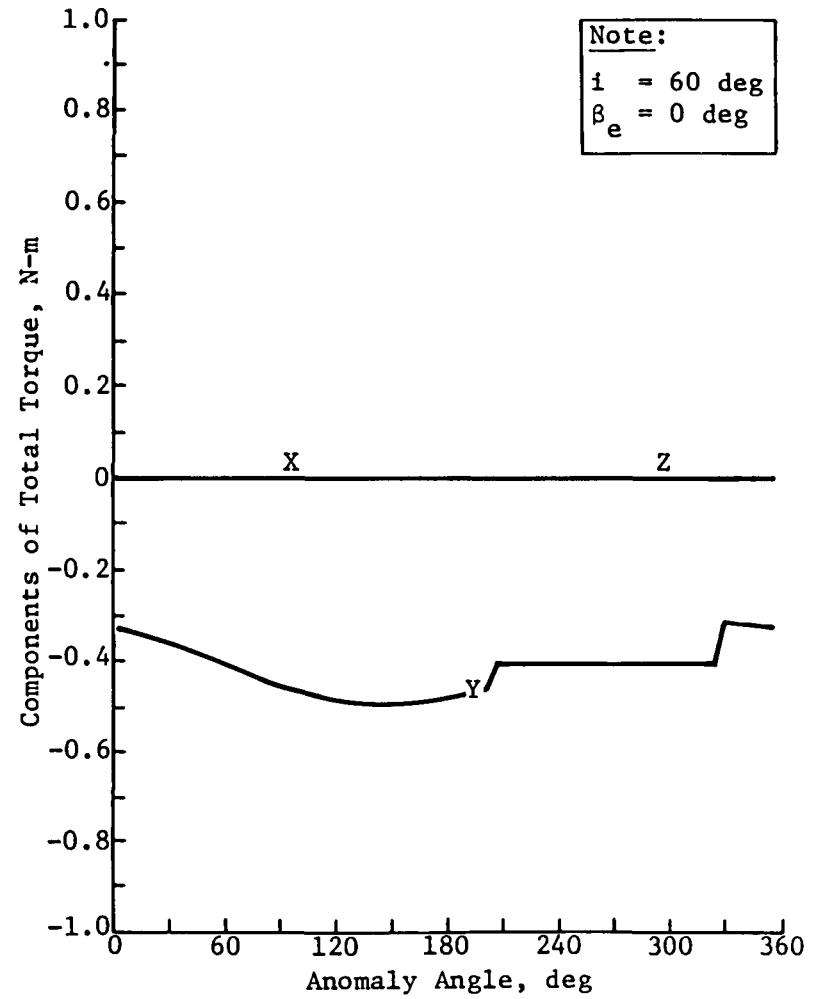
Figure D-12
Components of Total Torque versus
Anomaly Angle - Mission 4
(β = 0 deg)

Figure D-13
Components of Total Force versus
Anomaly Angle - Mission 4
(β = 60 deg)

Figure D-14
Components of Solar Pressure Torque
versus Anomaly Angle - Mission 4
(β = 60 deg)

Figure D-15
Components of Total Torque versus
Anomaly Angle - Mission 4
(β = 60 deg)

Figure D-16
Components of Total Force versus
Anomaly Angle - Mission 4
(β = 90 deg)
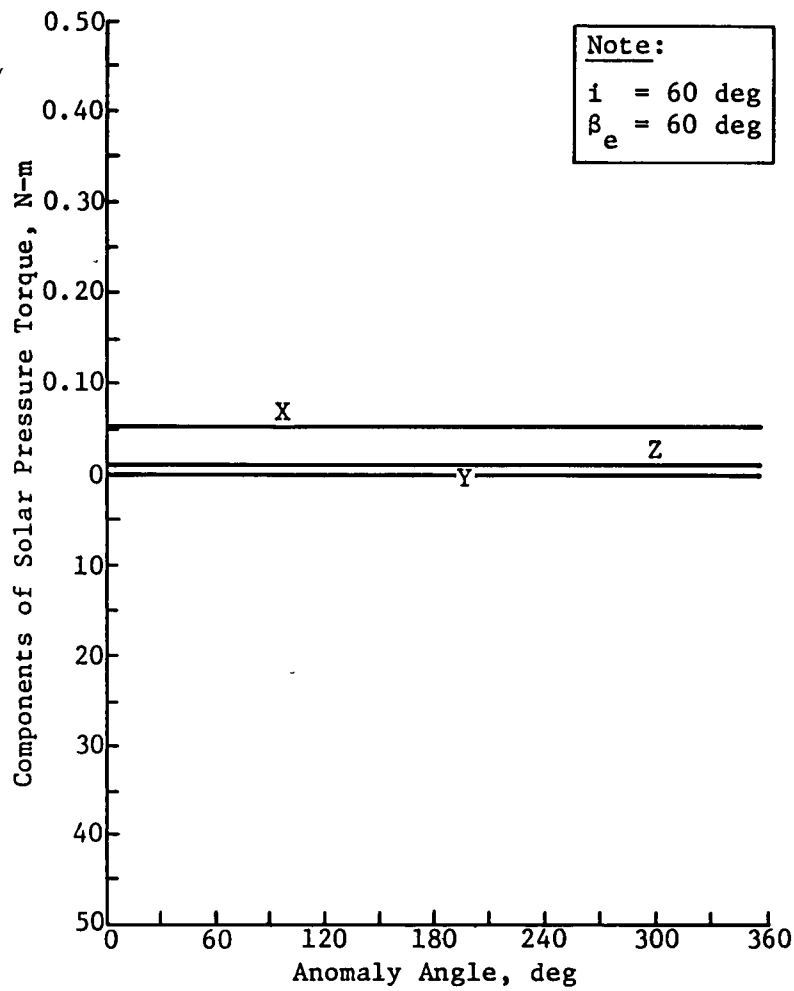
Figure D-17
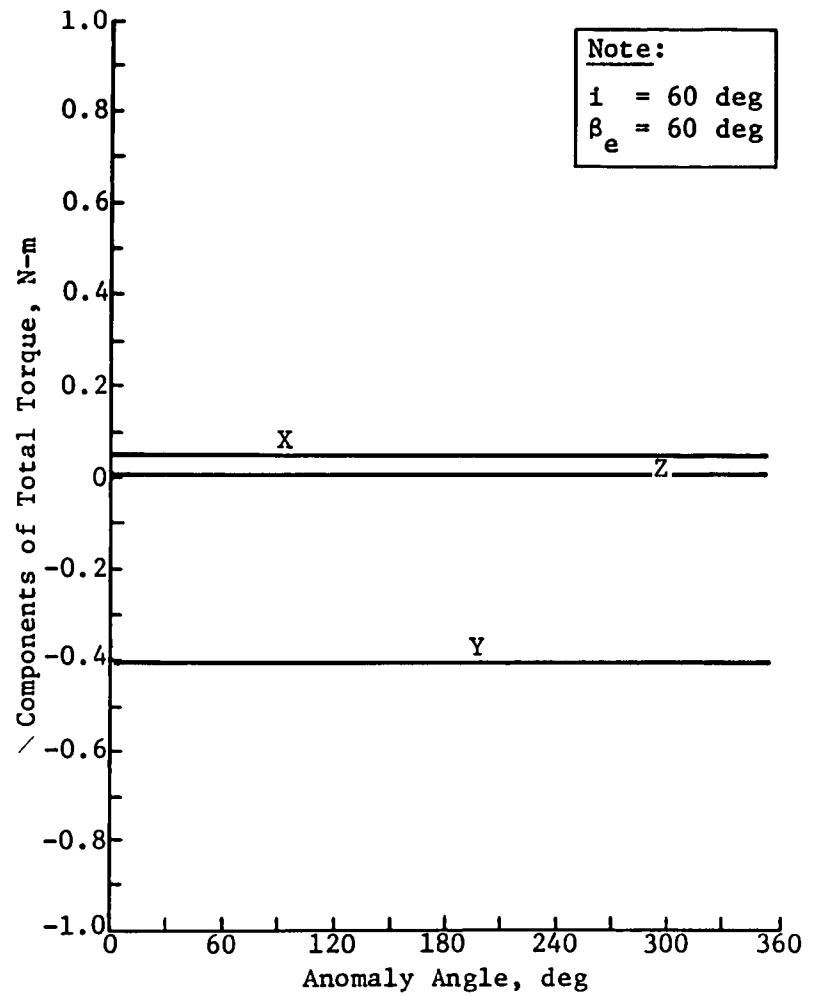Components of Solar Pressure Torque
versus Anomaly Angle - Mission 4
(β = 90 deg)

Figure D-18
Components of Total Torque versus
Anomaly Angle - Mission 4
(β = 90 deg)

1 Report No NASA CR-3698	2 Government Accession No	3 Recipient's Catalog No

4 Title and Subtitle	5 Report Date
TECHNOLOGY NEEDS OF ADVANCED EARTH OBSERVATION SPACECRAFT	January 1984
	6 Performing Organization Code

7 Author(s) James J. Herbert, J. R. Postuchow, Wilfred A. Schartel	8 Performing Organization Report No MCR-81-630
	10 Work Unit No
9 Performing Organization Name and Address Martin Marietta Aerospace Denver Aerospace P. O. Box 179 Denver, CO 80201	11 Contract or Grant No NAS1-16756
	13 Type of Report and Period Covered Contractor Report
12 Sponsoring Agency Name and Address National Aeronautics and Space Administration Washington, DC 20546	14 Sponsoring Agency Code

15 Supplementary Notes

Langley Technical Monitor: U. M. Lovelace
Final Report

16 Abstract

Remote sensing missions have been synthesized which could contribute significantly to the understanding of global environmental parameters. Instruments capable of sensing important land and sea parameters are combined with a large antenna designed to passively quantify surface emitted radiation at several wavelengths. A conceptual design for this large deployable antenna has been developed. All subsystems required to make the antenna an autonomous spacecraft have been conceptually designed. The entire package, including necessary orbit transfer propulsion, is folded to package within the Space Transportation System (STS) cargo bay. After separation the antenna, its integral feed mast, radiometer receivers, power system, and other instruments are automatically deployed and transferred to the operational orbit. The design resulted in an antenna with a major antenna dimension of 120 meters, weighing 7650 kilograms, and operating at an altitude of 700 kilometers.

17 Key Words (Suggested by Author(s))	18 Distribution Statement
Large Antenna Microwave Radiometer Deployable Spacecraft Advanced Concepts	Unclassified – Unlimited Subject Category 18

19 Security Classif (of this report)	20 Security Classif (of this page)	21 No of Pages	22 Price
Unclassified	Unclassified	260	A12

N-305

End of Document